

Synthesis and Characterization of
Copper Hexacyanoferrate and its Analogues
as Cathode Material for Aqueous Zinc-Ion Batteries

Vom Fachbereich Produktionstechnik

der

UNIVERSITÄT BREMEN

zur Erlangung des Grades
Doktor-Ingenieur
genehmigte

Dissertation

von

M.Sc. Ghoncheh Kasiri Bidhendi

Gutachter:

Prof. Fabio La Mantia

Prof. Riccardo Ruffo (University of Milano-Bicocca)

Tag der mündlichen Prüfung: 17.05.2019

Abstract

There is a current global need of clean energy sources to replace the non-renewable fossil fuels due to the global warming and environmental impacts. Therefore, renewable energy sources such as solar and wind have attracted wide attention as clean energy to meet the worldwide energy demand. Since these resources are inherently intermittent, a scalable low-cost energy storage system with long lifetime is needed to integrate these sources to the grid-scale. Among different energy storage technologies, batteries are the best choice for the integration in renewable energy systems. Thereby, the main goal of energy storage development is to select a battery which is stable, affordable, and reliable with high energy efficiency. In the last decades, among rechargeable batteries, aqueous metal-ion batteries provide lower cost, are environmentally friendly, safe, and nontoxic systems. This makes them a potential choice for grid-scale energy storage.

This study is a follow-up work of Trócoli et al. in 2015 in which a low-cost, environmentally friendly, nontoxic, aqueous zinc-ion battery (ZIB) based on copper hexacyanoferrate (CuHCF) as a cathode material has been introduced. It has been shown that the battery reached 96.3% of its specific charge after 100 cycles with an average discharge potential of 1.73 V at a 1C current rate. Although the system offered a good cyclability and rate capability, the standard CuHCF active material degrades upon cycling. Therefore, in this Ph.D. work the focus is on the development of an aqueous ZIB based on derivatives of the Prussian blue family that can provide high specific energy and power. Transition-metal hexacyanometallates known as Prussian blue analogues (PBAs) have attracted significant interest for their wide range of applicability and nontoxic properties. Besides, they have facile synthesis procedures and low production costs. Their characteristics make PBAs a good candidate for large-scale energy storage applications.

The motivation of this Ph.D. work is improving the performance of this system and to prevent or postpone the aging mechanism of standard CuHCF. For this purpose, the effect of different parameters such as the nature and the concentration of the electrolyte as well as the current rate on the electrochemical performance of this battery have been examined. The investigations have been carried out by the means of galvanostatic cycling with potential limitation (GCPL), inductively coupled plasma mass spectrometry (ICP-MS), and X-ray diffractometer (XRD). With the help of these techniques the obtained results illustrated that the electrochemical performance of standard CuHCF is strongly dependent on the nature and the concentration of the electrolyte. When the electrolyte's concentration is higher the degradation of standard CuHCF is occurring faster. In addition, the aging of standard CuHCF also has a relation with the current rate. In other words, the lower the current rate the faster the degradation happens. The results also revealed that the degradation of standard CuHCF upon cycling is followed by a

phase transformation. The phase transformation mechanism suggests that upon cycling standard CuHCF in a zinc salt solution with high concentration, zinc ions intercalate through the standard CuHCF structure and occupy the interstitial 'A sites'. When critical amounts of intercalated zinc are reached in the lattice, the zinc ions occupy $[\text{Fe}(\text{CN})_6]$ vacancies and lead to lattice distortion and poor electrochemical performance. This occupancy can be followed by nucleating CuZnHCF mixture and/or ZnHCF. Since upon phase transformation, not only the interstitial sites are occupied by zinc ions but also the regular crystal sites, it will be an interesting study to substitute zinc ions during synthesis into the CuHCF lattice. For this purpose, different mixtures of CuZnHCF were synthesized in which copper was partially substituted with zinc, namely with Cu:Zn at the following ratios: 85:15, 90:10, 93:7, 95:5, and 98:2. Among them, the CuZnHCF mixture with a Cu:Zn ratio of 93:7 showed a high specific charge retention of 98.12% and 86.26% in 20 mM and 100 mM ZnSO_4 after 500 cycles, respectively. Furthermore, the phase transformation in $\text{Cu}_{0.93}\text{Zn}_{0.07}\text{HCF}$ mixture was less favorable during cycling and postponed to higher numbers of cycles. Although this mixture showed better electrochemical performance in both solutions after 500 cycles, appearance of new phase(s) was observed by means of crystallography techniques (XRD). In order to have a deeper insight on the composition of the new formed phase(s), the cycled samples were analyzed by scanning electron microscopy (SEM) in combination with energy dispersive X-ray spectroscopy (EDX). The obtained results proved that optimizing CuHCF by substituting zinc in the CuHCF structure during synthesis successfully postponed the phase transformation mechanism, although at high concentration the $\text{Cu}_{0.93}\text{Zn}_{0.07}\text{HCF}$ mixture did not perform as well as in 20 mM ZnSO_4 . This can be explained by formation of new phases which had different compositions in comparison with the ones regarding standard CuHCF. To fulfill the main goal of this study and in order to obtain an active material with high power density and long life cycle, another alternative would be to act on the synthesis procedure. Therefore, the effects of the pumping speed, temperature, and atmosphere during synthesis on the electrochemical performance of the final product were investigated. The results revealed that the argon atmosphere had a huge impact on the performances of the CuHCF, increasing the energy retention after 1000 cycles from 81% to 87%. That means that the battery could be stable up to 1500 cycles, thus reaching the performances of a classic high power LIB. This new synthesis condition provides a new perspective to develop materials for rechargeable ZIBs for stationary applications and for short-time storage of solar and wind power with high energy. Besides the original Ph.D. goals, a 1 Wh ZIB based on standard CuHCF was constructed. Different cell designs and attempts have been done in order to reach this goal. Although, each design had some drawbacks, the general idea of a low-cost and environmentally friendly aqueous ZIB with an energy of 1 Wh has a potential to be manufactured in different sizes and designs for stationary applications.

Kurzfassung

Der globale Bedarf an erneuerbaren Energien steigt stetig an. Nur mit Hilfe erneuerbarer Energien können fossile Brennstoffe ersetzt werden, um den negativen Einfluss dieser auf die globale Erwärmung oder die Natur zu vermindern. Um die weltweiten Bedürfnisse nach sauberer Energie zu befriedigen, hat die Aufmerksamkeit bezüglich erneuerbaren Energieressourcen, wie Wind- und Sonnenenergie an Bedeutung gewonnen. Da die Stromerzeugung mittels erneuerbarer Energiequellen, stark tageszeit- und wetterabhängig ist, wird ein skalierbares und kostengünstiges Energiespeichersystem mit langer Laufzeit benötigt, um den erzeugten Strom in das Stromnetz einzuspeisen. Neben vielen möglichen Energiespeichern, zeichnen sich besonders Akkumulatoren aus, um erneuerbare Energien zu integrieren. Hierbei ist das Hauptziel einen Akku zu finden, welcher bei hohen Energiedichten stabil, bezahlbar und zuverlässig ist. In den letzten Jahrzehnten stellen gerade wässrige Metallionen-Akkumulatoren, aufgrund ihrer niedrigen Kosten, hohen Umweltverträglichkeit und Sicherheit einen potentiellen Kandidaten als Energiespeichermedium für die Stromeinspeisung dar.

Diese Arbeit ist ein Nachfolgeprojekt der Arbeit von Trócoli et al. von 2015. Hier wurde ein kostengünstiger, umweltfreundlicher und ungiftiger, wässriger Zinkionen-Akkumulator (ZIB) mit Kupferhexacyanoferrat (CuHCF) als Kathode eingeführt. Das vorgestellte System erreichte nach 100 Zyklen 96,3% der Anfangskapazität bei einer C-Rate von 1 und einem durchschnittlichen Entladepotential von 1,73 V. Trotz guter Zyklenstabilität und Ratenperformance, neigte das Aktivmaterial beim Zyklisieren zur Degradation. Der Fokus dieser Doktorarbeit liegt in der Entwicklung eines wässrigen ZIB mit hohen Energie- und Leistungsdichten, basierend auf Derivaten des Preußisch Blau. Übergangsmetall-Hexacyanometallate, auch Preußisch Blau Analoge (PBAs) genannt, haben aufgrund ihres großen Anwendungsbereichs und ihrer ungiftigen Eigenschaften große Aufmerksamkeit erregt. Dazu können PBAs über einfache Syntheserouten hergestellt werden und besitzen geringe Produktionskosten. Diese Eigenschaften machen sie zu einem exzellenten Kandidaten für großskalige Energiespeicheranwendungen.

Die Motivation dieser Arbeit ist die Leistung des oben genannten Systems zu verbessern, sowie den Alterungsmechanismus von reinem CuHCF zu verhindern oder zumindest zu verlangsamen. Zu diesem Zweck, wurden verschiedene Parameter, wie die Art und Konzentration des eingesetzten Elektrolyten sowie die verwendete Stromrate überprüft und deren Einfluss auf die elektrochemische Performance untersucht. Die Untersuchungen wurden mittels galvanostatischem Zyklisierens (GCPL), Massenspektrometrie mit induktiv gekoppeltem Plasma (ICP-MS) und Pulverröntgendiffraktometrie (XRD) durchgeführt. Mit Hilfe dieser analytischen Methoden wurde ermittelt, dass die elektrochemische Performance von reinem

CuHCF stark von der Art und der Konzentration des verwendeten Elektrolyten abhängig ist. Hierbei schreitet der Alterungsprozess mit steigender Konzentration schneller voran. Zusätzlich besteht ein Zusammenhang zwischen Stromrate und der Degradation des Aktivmaterials, so gilt: je niedriger die Stromrate, desto schneller die Alterung. Anhand der Ergebnisse wurde festgestellt, dass die Degradation des reinen CuHCF mit einer Phasenumwandlung einhergeht. Hierbei, wurde anhand eines Phasenumwandlungsmechanismus dargestellt, dass während des Zyklisierens von reinem CuHCF in hoch konzentriertem Zinksalzelektrolyt, Zinkionen Zwischengitterplätze (A sites) der reinen CuHCF Struktur besetzen. Erreicht die Anzahl an eingebauten Zinkionen eine kritische Masse, so besetzen Zinkionen zusätzlich $[\text{Fe}(\text{CN})_6]$ Vakanzen, was zu Gitterverzerrung und final zu schlechteren elektrochemischen Eigenschaften führt. Dieser Prozess kann zusätzlich zur Ausbildung von weiteren Phasen, wie CuZnHCF oder ZnHCF oder zu einer Mischung aus allen führen. Da bei der Phasenumwandlung nicht nur Zwischengitterplätze, sondern auch reguläre CuHCF Positionen besetzt werden, stellen der Einsatz von Zinkionen während der Synthese und die damit verbundene Substitution von Zinkionen in das CuHCF Gitter eine interessante, wissenschaftliche Fragestellung dar. Zu diesem Zweck wurden verschiedene CuZnHCF Verbindungen mit unterschiedlichem Cu zu Zn Verhältnissen synthetisiert. Hierbei wurden fünf Cu:Zn Verhältnisse, namentlich 85:15, 90:10, 93:7, 95:5, und 98:2, getestet. Unter diesen zeichnete sich besonders die 93:7 Mischung durch geringe Kapazitätsverluste nach 500 Zyklen aus. So konnten in 20 mM ZnSO_4 98,12% und in 100 mM ZnSO_4 noch 86,26% der ursprünglichen Kapazität erreicht werden. Zusätzlich konnte die Nebenphasenbildung für die $\text{Cu}_{0,93}\text{Zn}_{0,07}\text{HCF}$ Mischung zu höheren Zyklenzahlen verschoben werden. Trotz der besseren elektrochemischen Ergebnisse, konnten mit Hilfe von kristallographischen Methoden (XRD) innerhalb von 500 Zyklen neue Phasen nachgewiesen werden. Um ein besseres Verständnis für den vorliegenden Phasenbestand und deren Zusammensetzung zu bekommen, wurden die zyklisierten Proben mit Hilfe eines Rasterelektronenmikroskops (REM), welches mit einem energiedispersiven Röntgendetektor (EDX) gekoppelt war, untersucht. Mittels der erhaltenen Ergebnisse, konnte bewiesen werden, dass durch den Einbau von Zink in die CuHCF Struktur die Phasenumwandlung erfolgreich unterdrückt werden konnte. Die schlechtere Performance der $\text{Cu}_{0,93}\text{Zn}_{0,07}\text{HCF}$ Mischung bei höher konzentrierten Elektrolytlösungen konnte dabei auf die Ausbildung von Nebenphasen mit unterschiedlichen Zusammensetzungen zurückgeführt werden.

Um das Hauptziel dieser Arbeit, ein Aktivmaterial mit hoher Leistungsdichte und langer Lebensdauer, zu erreichen, wurden zusätzlich Syntheseparameter geändert. Zu diesem Zweck wurden einzelne Parameter, wie die Pumpgeschwindigkeit, die Synthesetemperatur sowie die Syntheseatmosphäre untersucht. Diese Untersuchungen zeigten, dass die verwendete Argonatmosphäre einen hohen Einfluss hatte. So konnte die verbliebene Kapazität nach

1000 Zyklen von 81% auf 87% gesteigert werden, sodass der Akkumulator über 1500 Zyklen stabil laufen könnte und somit an die Leistung einer klassischen Lithiumionenbatterie heranreicht. Diese neuen Syntheseparameter zeigen einen neuen Weg, Materialien für wieder aufladbare ZIBs zu entwickeln, welche in der Lage sind größere Mengen an Energie, aus stationären oder Kurzzeitspeichern für Sonnen- und Windenergie, zu speichern.

Neben den Hauptzielen dieser Arbeit, wurde versucht eine 1 Wh ZIB, welche auf reinem CuHCF basiert, zu konstruieren. Hierfür wurden unterschiedliche Zelldesigns getestet, um dieses Ziel zu erreichen. Obwohl jedes Design Nachteile aufwies, ist es durchaus denkbar eine kostengünstige und umweltfreundliche, wässrige ZIB mit einer Energie von 1 Wh zu bauen. Diese Batterie hat das Potential in unterschiedlichen Größen und Designs produziert zu werden, um sie anschließend als stationären Speicher zu nutzen.

Acknowledgements

This Ph.D. work would not have been possible without the help, inspiration and support of many people. Herein, I would like to pay special thanks and appreciation to the persons below who made this journey possible and assisted me at every point to cherish my goals in scientific and private life.

I owe my deepest gratitude to my doctoral advisor Prof. Fabio La Mantia. Without his optimism concerns, encouragements, supports, and valuable comments this work would have not been completed. His guidance helped me not only in the professional scientific fields but also my personal growth and developments. He provided constructive criticisms which helped me to develop a broader perspective to my thesis. Additionally, it is an honor for me to have Prof. Riccardo Ruffo with his valuable knowledge and experiences as my second supervisor.

I am grateful to all of those with whom I have had the pleasure to work during past years. I would like to show my gratitude to my friends and colleagues: Dr. Dorian Brogioli, Dr. Anastasia Dushina, Dominique Koster, Collins Erinmwingbovo, Maria Sofia Palagonia, Miriam Gutjahr, and Kurt Neumeister.

I want to thank Dr. Rafael Trócoli for his support and assistance. Without his supervision it was hardly possible to achieve this Ph.D. work.

I am indebted to many of my colleagues at Fraunhofer IFAM institute as well as at Bremen University. I want to thank all the members of the innovative sensor and functional materials (ISFM) group. In particular, Dr. Robert Kun, Dr. Ingo Bardenhagen, Dr. Frederieke Langer, Jens Glenneberg, Michael Gockeln, Elena Crespo, and Sebastian Jentsch for lending me their expertise and intuition to my scientific problems.

It is a pleasure for me to thank the directors of the advanced energy systems (AES), the late Prof. Dr. Stefan Gößling-Reisemann, Prof. Dr. Edwin Zondervan, Prof. La Mantia, and all of their group members.

I would also like to thank my friend and former colleague Dr. Amir Bani Hashemi and his kind wife Maryam Sasani for their priceless friendship, support and encouragement.

At last I would like to express my deep and sincere gratitude to my mom and dad, without whom I would have not been able to keep on going along this path. I acknowledge their continuous and selfless love, care and support. Additionally, I am grateful to my one and only sister Hama for always being there as a friend, for her understanding and encouragement.

Contents

1. Introduction	- 1 -
1.1. Energy – Challenges and Perspectives	- 1 -
1.2. Secondary Batteries	- 5 -
1.2.1. Lead-Acid Battery	- 6 -
1.2.2. Lithium-Ion Batteries	- 6 -
1.2.3. Ni-based Batteries	- 9 -
1.2.4. Molten-Salt Batteries	- 10 -
1.2.4.1. Na-S Batteries	- 10 -
1.2.4.2. Sodium Metal Chloride Batteries	- 10 -
1.2.5. Redox Flow Batteries	- 10 -
1.2.6. Metal-Air (Li, Na, Zn) Batteries	- 12 -
1.2.6.1. Lithium-Oxygen (Li-O ₂) Batteries	- 12 -
1.2.6.2. Sodium-Oxygen (Na-O ₂) Batteries	- 13 -
1.2.6.3. Zinc-Air Batteries	- 13 -
1.2.7. Sodium-Ion Batteries	- 14 -
1.2.7.1. Cathodes	- 14 -
1.2.7.2. Anodes	- 15 -
1.2.8. Aqueous Metal-Ion Batteries	- 16 -
1.2.8.1. Aqueous Lithium-Ion Batteries	- 17 -
1.2.8.2. Aqueous Sodium-Ion Batteries	- 17 -
1.2.8.3. Aqueous Aluminum-Ion Batteries	- 18 -
1.2.8.4. Aqueous Zinc-Ion Batteries	- 19 -
1.2.8.4.1. Cathodes	- 20 -
1.2.8.4.2. Anodes	- 23 -
1.3. Prussian Blue and its Analogues (PB and PBAs)	- 24 -
1.4. Aim of the Work	- 29 -
2. Experimental	- 31 -
2.1. Materials and Instruments	- 31 -
2.2. Synthesis of Materials	- 32 -
2.2.1. Synthesis of Standard Copper Hexacyanoferrate (CuHCF)	- 32 -
2.2.2. Synthesis of Copper Zinc Hexacyanoferrate Mixtures (CuZnHCF)	- 33 -
2.2.3. Synthesis of Copper Hexacyanoferrate Based on different Dropping Speeds	- 33 -
2.2.4. Synthesis of Copper Hexacyanoferrate Based on different Temperatures	- 33 -
2.2.5. Synthesis of Copper Hexacyanoferrate Based on different Atmospheres and Temperatures	- 34 -
2.2.6. Synthesis of ZnHCF	- 34 -
2.3. Electrode Fabrication	- 34 -
2.4. Electrochemical Cells	- 35 -
2.5. Characterization Techniques	- 36 -
2.5.1. Galvanostatic Cycling with Potential Limitation	- 36 -
2.5.2. Thermodynamic and Kinetic Analysis	- 36 -
2.5.3. X-Ray Diffraction	- 44 -
2.5.4. Scanning Electron Microscopy and Energy Dispersive X-Ray Spectroscopy	- 45 -
2.5.5. Inductively Coupled Plasma Mass Spectrometry	- 45 -

3. Investigation of the Effects of the Electrolyte and Current Rate on the Aging of Standard CuHCF	- 46 -
3.1. Effects of the Nature of the Electrolyte	- 47 -
3.2. Effects of the Electrolyte Concentration	- 49 -
3.3. Effects of the Current Rate	- 57 -
3.4. Phase Transformation Mechanism	- 60 -
4. Optimizing the Standard CuHCF Structure by Adding a Co-Ion.....	- 63 -
5. Electrochemical and Crystallographic Performances of Standard CuHCF and the Cu_{0.93}Zn_{0.07}HCF Mixture in Different Electrolytes.....	- 78 -
5.1. Electrochemical Characterization of Standard CuHCF and the Cu _{0.93} Zn _{0.07} HCF Mixture in 20 mM ZnSO ₄	- 78 -
5.2. Crystallographic Characterization of Standard CuHCF and Cu _{0.93} Zn _{0.07} HCF Mixture Before and After Cycling in 20 mM ZnSO ₄	- 82 -
5.3. Electrochemical Characterization of Standard CuHCF and the Cu _{0.93} Zn _{0.07} HCF Mixture in 100 mM ZnSO ₄	- 91 -
5.4. Crystallographic Characterization of Standard CuHCF and Cu _{0.93} Zn _{0.07} HCF Mixture Before and After Cycling in 100 mM ZnSO ₄	- 94 -
6. Controlling Synthesis Parameters	- 108 -
6.1. Effect of Dropping Speed.....	- 108 -
6.2. Effect of Temperature	- 111 -
6.3. Effect of Argon and Temperature.....	- 114 -
7. Discussion and Results Comparison.....	- 120 -
8. Construction of 1 Wh Zinc-Ion Battery Based on PBAs	- 127 -
9. Conclusions and Outlook.....	- 135 -
10. References	- 137 -
11. Appendix	- 144 -
11.1. Influence of other Synthesis Parameters	- 144 -
11.2. List of Figures	- 146 -
11.3. List of Tables.....	- 150 -
11.4. Abbreviations & Symbols	- 152 -
12. Publications and Conference Contributions.....	- 156 -
12.1. Published peer-reviewed Papers.....	- 156 -
12.2. Oral Presentations at International Conferences.....	- 156 -
12.3. Posters at International Conferences	- 157 -
Declaration.....	- 158 -

1. Introduction

1.1. Energy – Challenges and Perspectives

Fossil fuels are a significant source to provide electricity for industry and household applications. Major difficulties that are arising along with the energy development include a shortage of fossil fuels as well as the production of carbon dioxide (CO₂) and other greenhouse gases (GHGs) such as methane (CH₄), nitrous oxide (N₂O), and fluorinated gases. Due to the scarcity of natural resources, massive numbers of clean, renewable and in parallel nuclear energy resources have been developed.^[1] To prevent climate change and global warming, a reduction of the greenhouse emissions is of primary importance.^[1,2] It is the main goal to provide the overall worldwide energy consumption, i.e. 549 quadrillion British thermal units in 2012 (1 quad BTU = 293 TWh),^[3] with the help of renewable resources such as wind, water, and solar power.

The use of nuclear energy resources is controversial due to several environmental and political reasons. Extracted enriched uranium resources may be abused and increase the risk of national disaster. Additionally, nuclear energy sources emit 9 to 25 times more carbon than wind energy, which has a huge effect on the climate change. Another important concern regarding nuclear energy sources are safety issue of nuclear power plants, especially due to the performance of the reactors or the risk of releasing radioactive material into the environment. The Fukushima Daiichi nuclear disaster can be mentioned as an example of a nuclear accident in the recent years, which caused critical environmental problems as well as negative health impacts. In addition, the toxic radioactive wastes produced by nuclear power are also a serious topic. Therefore, nuclear energy cannot be the best choice to be used as a long-term global energy source.^[2]

In recent years, solar photovoltaics (PVs), as a clean renewable energy source, have been employed as a rooftop PV power station at residential houses for solar lights, solar cars, or as utility-scale solar PV power plants.^[2] Between 2008 and 2016, the price of solar power modules has dropped from 3 US\$ W⁻¹ to 0.5 US\$ W⁻¹.^[4] The future goal is to decrease the cost of PV electricity to 0.03 US\$ kWh⁻¹ with high module efficiency (module efficiency is the percentage of sunlight that hits the solar panel, which can be converted to the applicable electricity), a longer lifetime (more than 35 years), and less efficiency loss (<0.3% per year).^[1]

Solar and wind power are great potential sources of electricity to mediate grid connection problems.^[5] During one hour of solar radiation energy towards earth, the worldwide energy demand for almost one year can be supplied. In addition, capturing potential wind energy can contribute to the need for universal energy demand. Since solar and wind power are inherently intermittent, they can cause several challenges for the electric grid.^[6-9] Renewable energy

sources are localized and the electrical grid is used to transport the electricity from a power plant to the demanding location. Therefore, to integrate these renewable energy sources to the grid-scale (stationary application), a scalable electrical energy storage (EES) with low capital cost (<250 US\$ kWh⁻¹), long life cycle (>15 years), long calendar life (>4000 deep cycles for energy application),^[10,11] and minimum maintenance is needed. To develop an EES based on the market requirements, certain features should be considered. These factors are the ratio of power to energy, discharge time, charge/discharge rates (response time), capital cost, life cycle, reliability, durability, and safety.^[6] By considering the aforementioned factors and how the electrical energy is stored, a possible classification of the EES systems is proposed (Fig. 1-1).

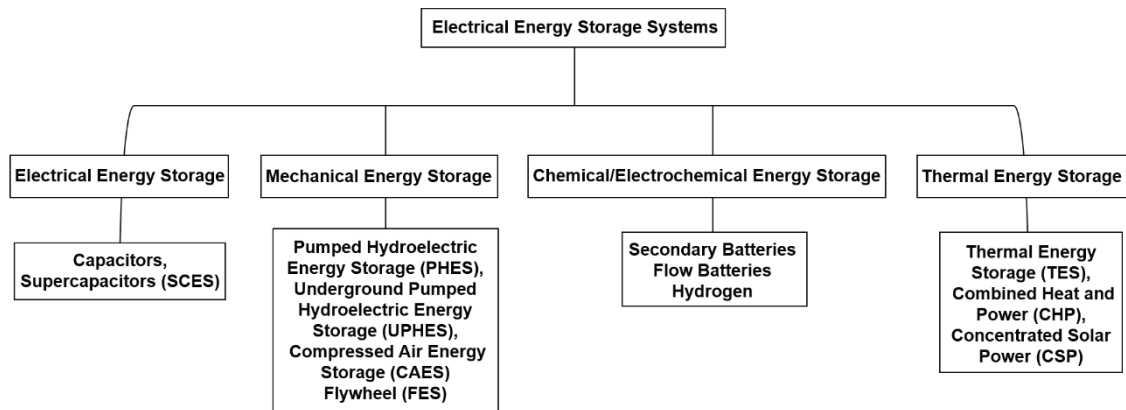


Figure 1-1. Schematic of the electrical energy storage systems classification (adapted from [6]).

Furthermore, a brief comparison for some of the energy storage technologies and their advantages and disadvantages are reported in Table 1-1.

Table 1-1. Brief comparison of the energy storage technologies.^[12,13,22,23,14-21]

Energy storage type	Advantages	Disadvantages
CAES	Low-cost Flexible sizing Mature technology Large storage capability Long lifetime (reservoir, compressor, turbine) Small footprint on surface (underground storage)	Geologically limited Adverse effect on environment High investment cost Low efficiency due to round-trip conversion
PHES	Mature technology High power capacity Moderate access time	Geographical restrictions Long construction time Low energy efficiency High surface footprint Adverse effect on environment
SCES	Low-cost Flexible sizing Long lifetime Fast charging	Low energy density Few power system applications High self-discharge Low voltage cells Voltage balancing is needed

Energy storage type	Advantages	Disadvantages
FES	High power density and scalability for short duration technology Short access time Low maintenance effort Compact design	Low energy capacity Sensitive to vibration High heat generation Rotor tensile strength limitations
LIB	Light weight Long life cycle High energy/power density Low maintenance Low self-discharge rate	Expensive Safety issues (explosive) Aging
TES	Low-cost Flexible sizing Long distance transport available Highly compact energy storage	Adverse effect on environment High capital cost Technically complex

A good form for representing the specific energy density of various electrical energy conversion systems as a function of their specific power density (or vice versa) is the Ragone plot (Fig. 1-2). Energy density is the amount of energy that can be stored per unit volume or mass. In addition, the term of power density describes the amount of power output per unit volume. Since most of the current studies focus on developing a safe, low-cost, and long-life energy storage device with high specific energy and power, it is important to compare the present EES technologies based on their specific power and energy.

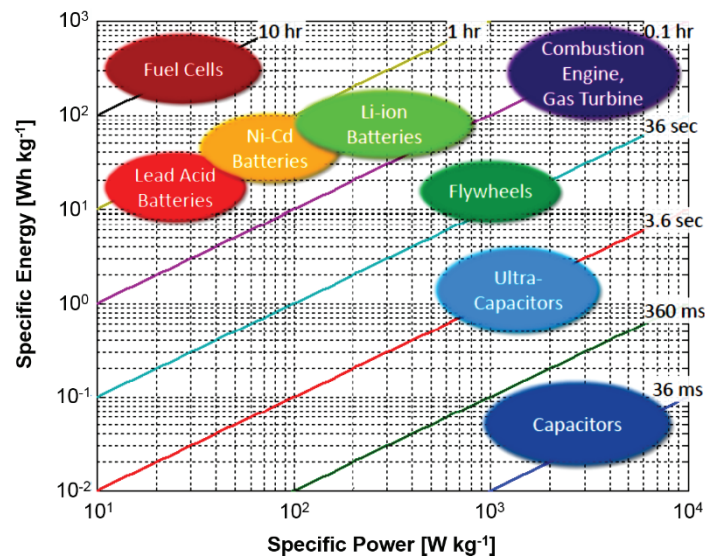


Figure 1-2. Ragone plot comparing different energy storage technologies with regard to their gravimetric power density and gravimetric energy density including their charge times (adapted from [24]).

Among these technologies, batteries are the best choice for the integration in renewable energy systems. The ideal energy storage device should have a long life cycle and be composed of cheap and abundant materials. The challenge for using energy storage systems are not only the technological restrictions but also the economic and abundance constraints of the elements that are utilized in these systems. Therefore, it is important to review the abundance of the elements

in the earth's cluster and their cost per kilogram (kg). In Fig. 1-3, the relative abundance of the different chemical elements in the earth's cluster is shown.

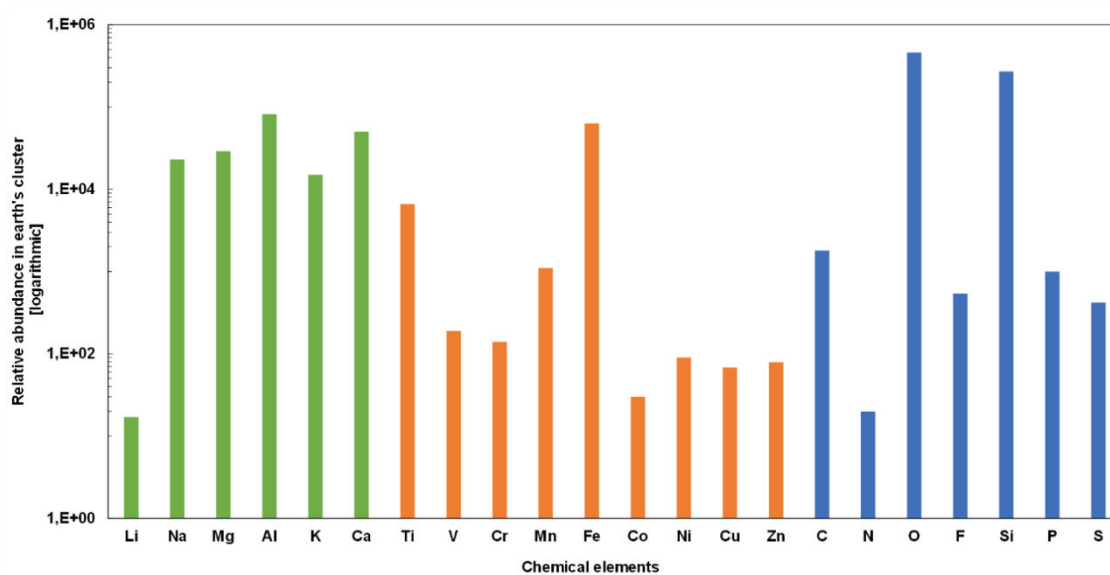


Figure 1-3. Relative abundance of chemical elements in the earth's cluster. Alkali metals and alkaline earth metals are shown in green, transition-metals in orange, and main group elements in blue (extracted and modified from [11,25]).

Although some of the elements have shown a high relative abundance, it does not mean that those elements can be mined and produced.^[26–28] In Table 1-2, the costs of pure and chemical elements at market (US\$ kg⁻¹), owing to their abundance in the earth's crust (ppm), are reported for consideration in developing a suitable EES.

Table 1-2. Abundance of chemical elements in the earth's crust.^[25,29,30]

Chemical element	Abundance in Earth's crust [ppm]	Cost of pure element [US\$ kg ⁻¹]	Cost of chemical elements by market price [US\$ kg ⁻¹]
Li	17	270	115.7
Na	23000	250	3.04
K	15000	1000	13.02
Mg	29000	37	2.26
Ca	50000	200	5.93
Al	82000	157.2	1.91
Ti	6600	6610	3.77
V	190	2200	22.6
Cr	140	320	7.64
Mn	1100	65	2.06
Fe	63000	72	0.08
Co	30	210	59.5
Ni	90	77	9.19
Cu	68	976	5.9
Zn	79	53	2.83
C	1800	24	24
Si	270000	54	1.91
Ge	1.4	3600	1825
N	20	4	2.77
P	1000	300	300

Chemical element	Abundance in Earth's crust [ppm]	Cost of pure element [US\$ kg ⁻¹]	Cost of chemical elements by market price [US\$ kg ⁻¹]
O	460000	3	0.64
S	420	500	0.1
F	540	1900	1900

These results are leading the researches and developments of new EES systems in which the price of their raw materials, as well as their abundance, are playing an important role. Since batteries have the great potential for being used in stationary applications the main focus of this work will be on this specific EES. Batteries and electrochemical cells are classified in four different categories namely primary, secondary, reserve batteries, and fuel cells. Primary or non-rechargeable batteries are usually in small sizes and do not need a great deal of power. They are intended to be discharged once and then discarded. Most of the primary cells consisting of absorbent or separator material, with no free liquid electrolyte. These are called dry cells. The main disadvantages of this type of battery are its short lifetime, disposal pollution, and the high cost of continues replacement. Secondary or rechargeable batteries are employed as energy storage devices and can be recharged for reuse. These batteries are usually recharged electrically by passing current through them which reverses the chemical reactions that take place during its use. Some of the secondary batteries have high power density, high discharge rate, and good performance at low temperatures. These batteries in comparison with primary batteries generally have low energy densities and poorer charge retention but the capacity which was lost on standing for secondary batteries could be restored by recharging. The third type of batteries is called reserve batteries which are a primary battery. In this battery, the key component of the cell is separated from other components until the battery needs to be used. This battery eliminates the possibility of self-discharge and chemical deterioration and is compatible for long-term storage. In particular is used in timing, pressure, and temperature sensitive detonation devices. Fuel cell is an electrochemical cell, which converts the chemical energy to electrical energy through an electrochemical reaction. Fuel cells are similar to batteries except for the fact that the active materials are fed into the fuel cell from an external source and its function continues as long as the active materials are fed to the electrodes, otherwise its operation is stopping.^[31]

Since the secondary batteries can provide the requirements for an EES, in the following sections an overview of the different types of secondary batteries and their characteristics are noted.

1.2. Secondary Batteries

In recent year, renewable energy sources are an important technology as an alternative to fossil fuels. In order to balance the fluctuations of renewable energy sources and to integrate them into

the electrical grid, effective EESs are needed. Among these technologies, secondary batteries have played a critical role in technological progress.^[5,32,33] Rechargeable batteries are used in electric vehicles (EV), portable electronic devices, and large-scale electrical storage in grids.^[1] To integrate the renewable resources, it is possible to use EV batteries as EES, a strategy known as vehicle-to-grid (V2G).^[34] The current lithium-ion batteries (LIBs) for EVs provide a driving range of about 200 km.^[32,35] Based on this, clean transportation technologies are under further development. Only by increasing the number of electrical vehicles, the goal of the US Department of Energy to decrease the cost for EV battery packs to 125 US\$ kWh⁻¹ until 2022 can be reached. The Battery 500 Consortium suggested that the current EV battery cells with a specific energy of 200-250 Wh kg⁻¹ should reach 500 Wh kg⁻¹ with a lifetime of more than 10 years.^[1] In grid-storage applications, high energy density is not mandatory, while stability of performance and more than 4000 cycles with a lifetime of 20 years is a matter of importance.^[1,36] There are several options for storing the energy of sustainable energy sources for load-leveling applications such as lead-acid batteries, redox flow batteries, sodium-sulfur (Na-S) batteries, and LIBs. In this chapter, a brief description of these batteries is discussed.

1.2.1. Lead-Acid Battery

The lead-acid battery is known as the oldest type of rechargeable battery invented in 1859 by the French chemist Gaston Planté. This type of battery is used in current mobile (automobile, electric bikes, and buses) and stationary applications. Although this battery is cheap, recyclable, and has a high surge-to-weight ratio (can deliver a high jolt of electricity in an instant), has a short life cycle (life cycle is the number of charge/discharge cycles that a battery can reach before its capacity falls under 80% of its initial capacity), and has environmental concerns due to the toxic lead (Pb), has a low energy density and a limited depth of discharge, and require a high loading time. Lead-acid batteries are based on the electrochemical conversion of Pb and lead oxide (PbO₂) to lead sulfate (PbSO₄). Sulfuric acid (H₂SO₄), which is used as an electrolyte in this type of battery, acts as a reactant for the battery. This battery can deliver a nominal cell voltage (nominal voltage is measured at the mid-point between fully charged and fully discharged) of 2 V per cell. The lead-acid system is a popular low-cost secondary battery since the raw materials are abundant. They have mature technology and can provide a high current, available in large quantities (different sizes and designs), with great durability and resistance to temperature variations.^[37,38]

1.2.2. Lithium-Ion Batteries

In the 1990s, LIBs were commercially introduced by Sony, and so far, they have been used for portable electronics and transportation. A schematic illustration of a LIB is shown in Fig. 1-4.

The usual LIB consists of a lithium intercalation compound cathode, usually a transition-metal oxide in a low oxidation state which can (de-)intercalate lithium ion at high potential (lithium metal oxides), or sulfides and a graphite anode.^[1,36] Copper and aluminum sheets are used as the current collector at the anode and cathode sides, respectively.^[39] The electrochemical reaction that occurs in LIBs is the reversible intercalation of lithium ions from the cathode to the anode upon charging and vice versa during discharging. LIB has a high energy density (at a 1C rate of 75-200 Wh kg⁻¹), low energy loss, high life cycle, and can provide a voltage in the range of 2 to 4.2 V per cell, depending on the chemistry.^[32,36] In addition to the application of LIBs in hand-held devices, they are being used in grid-connected storage systems. As an example of LIB utilization in grid-scale energy storage, the AES Corporation facility developed a 1 MW LIB (250 kWh LIB) that can be fully charged/discharged in 15 minutes at a 4C rate.^[40,41]

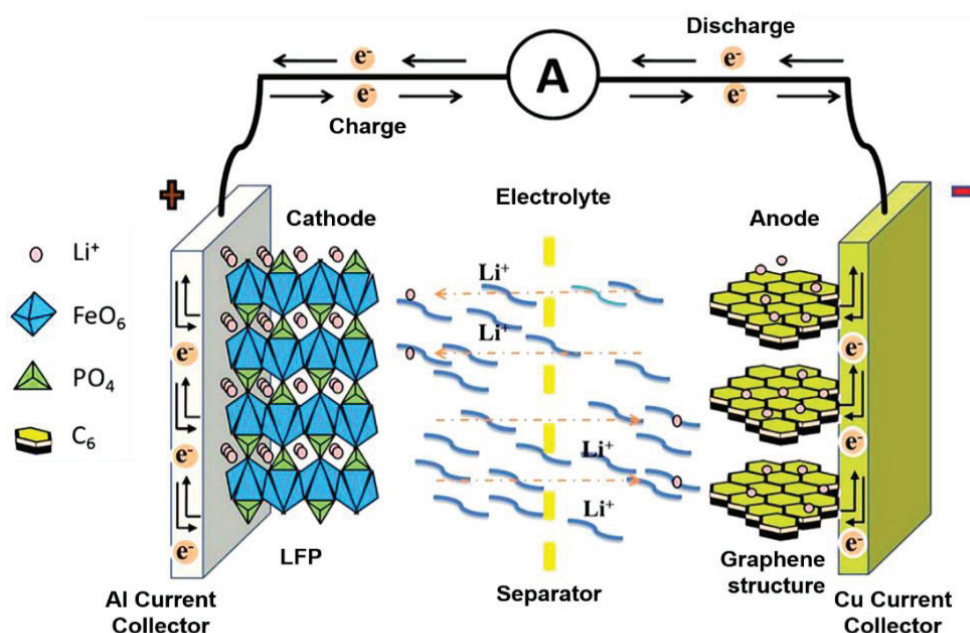


Figure 1-4. Schematic representation of a Li-ion battery (adapted from [42]).

There are different possible materials that can be used as a cathode in LIBs. The first commercial cathode materials for LIBs were layered lithium metal oxides, which are still employed in portable electronic devices. Lithium nickel oxide (LiNiO₂), besides its safety issues, has shown poor cyclability and low stability, in particular at high temperatures. Lithium cobalt oxide, LiCoO₂ (LCO), has a practical specific capacity of 140 mAh g⁻¹ and can provide high charge/discharge rates. Spinel lithium manganese oxides, LiMn₂O₄ (LMO), with a theoretical specific capacity of 148 mAh g⁻¹, offers a high rate capability and high electrical conductivity, but it loses capacity upon cycling. As a combination of the above materials, layered lithium nickel manganese cobalt oxide, LiNi_xCo_yMn_zO₂ (NMC), with a specific capacity of 250 mAh g⁻¹ is another alternative cathode material in LIBs, although its chemical and structural stability should be studied more. Olivine lithium iron phosphate (LiFePO₄, LFP) is the

most common cathode material in LIBs, and it can provide a theoretical specific capacity of 170 mAh g^{-1} .^[36,39,43] In addition, sulfur and oxygen cathodes with a high specific capacity of 1700 mAh g^{-1} are other cathode materials for LIBs, but they suffer from short-term stability. However, it is possible to improve their life cycle with the help of nanostructured architectures (sulfur/mesoporous carbon material).^[44,45]

Graphite is the most used anode material in commercial LIBs. Graphite is an abundant environmentally friendly material and due to its structure, it allows a reversible (de-)intercalation of lithium ions. In addition to graphite, lithium titanate ($\text{Li}_4\text{Ti}_5\text{O}_{12}$, LTO) is also used as anode in LIBs. The LTO has been used in electric buses owing to its fast charging, but it delivers low energy densities.^[45] With a higher specific capacity (4200 mAh g^{-1}) than graphite (372 mAh g^{-1}), silicon has also been used as an anode in LIBs, but due to its volume expansion upon charging/discharging, it causes mechanical breakdown. Therefore, recent research has been focused on overcoming this limitation using nanoscale design, electrolyte additives, solid-state electrolytes, and confining the lithium anode into the layered reduced graphene.^[46,47]

Ion conducting electrolyte materials for LIBs can be divided into three major classes, i.e. liquid, solid and gel electrolytes (GE). The liquid electrolytes comprise organic liquid electrolytes (OLEs), ionic liquid electrolytes (ILEs), and aqueous liquid electrolytes (ALEs). Liquid electrolytes inherit better ionic conductivity than other electrolytes and can provide a stable contact with the electrodes. OLEs are the most common electrolytes due to their excellent properties in ionic conductivity and their stability in contact with electrodes. Classic lithium salts such as lithium perchlorate (LiClO_4), lithium hexafluorophosphate (LiPF_6), and lithium bis(trifluoromethanesulfonyl)imide (LiTFSI) can be used by solving in different organic solvents, e.g. ethylene carbonate (EC), propylene carbonate (PC), dimethyl carbonate (DMC), and ethyl methyl carbonate (EMC) among others. For determining a suitable salt and solvent, different factors should be considered. The important parameters for the lithium salts are their cost, electrochemical stability, their solubility into the solvent and environmental impact. Besides, the viscosity, melting and/or boiling point, safety, and dielectric constant of the organic solvent should be considered. ILEs have several remarkable properties such as high electrochemical and thermal stability, low volatility, and non-flammability. On the other hand, they suffer from low rate capability and poor cycle performance that limits their application as high-performance electrolytes. Solid electrolytes can be in the form of solid polymer electrolytes (SPEs) or inorganic solid electrolytes (ISEs). SPEs and ISEs have excellent performances due to their safety and mechanical properties. GEs have a state between solid and liquid. They have high ionic conductivity and good mechanical properties.^[48]

The advantages of LIBs are their low weight, high energy density, low self-discharge, and excellent rate capability. However, they have high production costs, safety issues, reliability problems due to heat management issues, and small temperature ranges for operation.^[37]

In Table 1-3, the estimated costs are reported for manufacturing different LIBs based on different cathode materials, their cycle life, calendar life (calendar life is the time without usage after which the battery loses 20% of its initial capacity due to its aging), and their applications.^[34,49]

Table 1-3. Manufacturing costs and cycle life of different Li-ion batteries (LIBs).^[34,49]

Positive electrode	LIB			
	NCA	NMC	NCA	NMC
MC [$\$ \text{kWh}^{-1}$]	210-330	210-330	350-860	350-860
Cycle life [DoD]	>3200	~3000	>400000	~3000
Calendar life [years]	>12	>10	>20	>10
Application	EV	EV	HEV	HEV

NCA = Lithium nickel cobalt aluminum oxide (LiNiCoAlO_2), NMC = Lithium nickel cobalt manganese oxide (LiNiCoMnO_2), MC = manufacturing costs, DoD = depth of discharge = inverse of the state of charge (SOC), EV = Electric vehicle (operates with medium power and high energy), HEV = Hybrid electric vehicle (operates with high power and medium energy)

1.2.3. Ni-based Batteries

There are different nickel-based batteries, such as nickel-cadmium (Ni-Cd), nickel-zinc (Ni-Zn), nickel-hydrogen (Ni-H₂), nickel-iron (Ni-Fe), and nickel metal hydride (Ni-MH). Nickel oxide hydroxide (NiOOH) has been used as the positive electrode in all of the mentioned batteries. Among all, Ni-Cd and Ni-MH are common types that are used for portable electronic devices. Although Ni-Cd batteries provide moderate energy densities and coulombic efficiencies, good performances at low temperature, flexibility in size and design, and high discharge rates, they suffer due to the toxicity of Cd, and memory effects (short life cycle). The battery memory effect usually occurs in both Ni-Cd and Ni-MH rechargeable batteries in which the battery partially discharged before recharging and lead to have less charge and poor lifetime.^[31,37,50] The electrochemical reaction in Ni-Cd batteries is a redox reaction between NiOOH (positive electrode) and Cd (negative electrode). As an electrolyte, alkaline solutions such as potassium hydroxide (KOH) are used. Ni-MH has been commercially used since the 1990s in portable electronics and power tools due to the high capacity, high energy and power, and environmental friendliness compared to Ni-Cd batteries. However, LIBs, due to their excellent cycling performance and high gravimetric energy densities, have overtaken the role of Ni-MH and Ni-Cd in the market.^[37,50]

1.2.4. Molten-Salt Batteries

1.2.4.1. Na-S Batteries

Due to the high abundance of sodium and its low-cost (as shown in Fig. 1-3, Table 1-2), it is possible to use this material as an anode for batteries. Sodium-sulfur batteries (Na-S) convert electrical energy to chemical potential, utilizing sodium (usually molten sodium) as anode material and sulfur as cathode material.^[6,51] Nowadays, Na-S batteries are a promising candidate for grid-scale applications and are able to smooth the output of renewable energy sources. In this battery, molten sulfur is used as a cathode, molten sodium as an anode, and Na⁺ conducting ceramic as a separator. Usually, this separator consists of β'' -alumina (β'' -Al₂O₃). The battery is able to work at high temperatures (300°C–350°C) with zero self-discharge and high electrical efficiency (electrical efficiency is the ratio between the useful power output to the total consumed electrical power). A novel room temperature Na-S battery, consisting of solid sulfur/metal sulfide as a cathode, solid sodium as an anode, liquid glyme/carbonate as an electrolyte, and a Celgard separator, has a discharge capacity of 489 mAh g⁻¹.^[40] Although its capacity is close to the high-temperature Na-S battery, it degrades fast upon cycling. Advantages of high temperature Na-S batteries are their long life cycle with high energy densities. In addition, they show fast response with high columbic efficiencies. However, they suffer from a highly corrosive behavior, require thermal management and high operation temperatures. Moreover they have safety and security issues due to hazardous sodium burn or explosion in contact with water.^[40,52,53]

1.2.4.2. Sodium Metal Chloride Batteries

Sodium metal chloride batteries have been invented for EV applications in 1985 by the Zeolite Battery Research Africa (ZEBRA) project.^[40,54] This battery consists of a molten sodium anode, a transition-metal chloride cathode, and a molten sodium aluminum tetrachloride (NaAlCl₄) electrolyte. Different transition-metals have been used in cathode material, but among them, only iron and nickel showed promising results. This battery has a high energy density (~90-120 Wh kg⁻¹), which is five times higher than a lead-acid battery (~30 Wh kg⁻¹). Furthermore, it is cheap compared to other technologies and safer than Na-S batteries. The ZEBRA battery performs well, while showing high robustness and a tolerance to short circuits. However, it suffers from high internal resistance. Before utilization, preheating is required in order to avoid freezing of the battery electrolyte.^[40]

1.2.5. Redox Flow Batteries

Redox flow batteries (RFBs) are similar to conventional batteries. This type of battery is able to store the electrical energy in two soluble redox couples, which are in an external electrolyte tank

(Fig. 1-5). Unlike other solid state batteries, RFBs store electrical energy within one or more electro-active species that are dissolved in liquid electrolytes. The energy density depends on the size of the electrolyte tanks, while the power is based on the design and the size of the electrochemical cell. In other words, in RFBs the energy is stored within the separated reactants, while the power is controlled via the stack. Usually different electrolytes flow through the anode and cathode compartment that are separated by a membrane.^[40,55–58]

Various types of RFBs have been developed. There are zinc-based flow batteries like zinc-bromine flow batteries (ZnBr), with different energy densities based on manufacturer ($34.4\text{--}54\text{ Wh kg}^{-1}$). These are very stable and have nearly no electrode polarization. However, they suffer from high, initial self-discharge rates, low power capabilities, and the formation of zinc dendrite during charging.

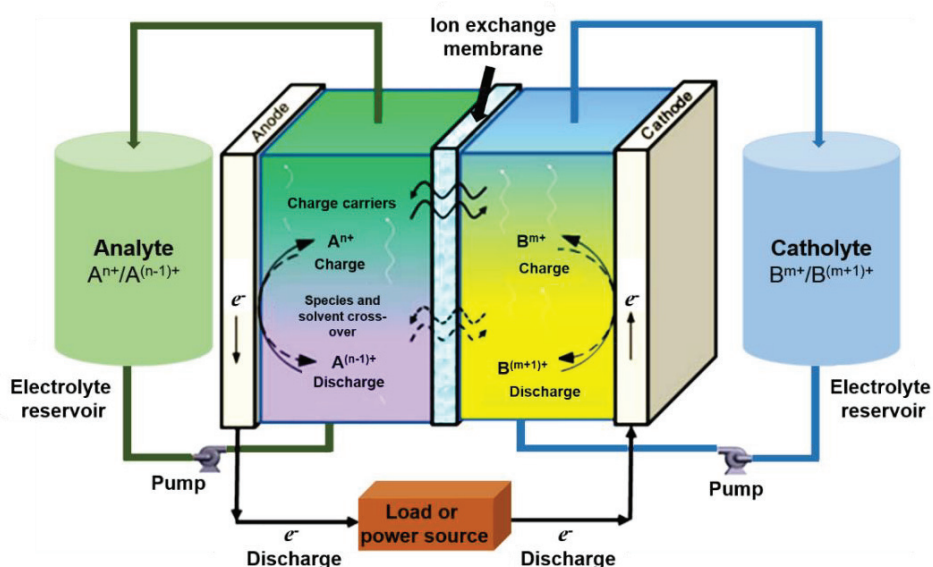


Figure 1-5. Schematic representation of a redox flow battery (adapted from [58]).

Another type of RFBs are zinc-cerium flow batteries with good charge/discharge rates and energy efficiencies. Although due to the high rate corrosion of zinc upon charging, the charge efficiency of this battery decreases and leads to gas evolution. Another promising type of RFB is the zinc-air flow battery, but due to its early development stage it has not found market application, yet.^[40,55–58]

In addition, vanadium redox flow batteries (VRBs), using sulfuric acid are a type of rechargeable RFBs based on V^{2+}/V^{3+} and V^{4+}/V^{5+} redox couples at the negative and positive electrodes, respectively. This type of battery is able to achieve a specific energy of 20 Wh kg^{-1} . The advantages of RFBs are their high flexibility regarding the design, the ability to tune and adjust power and energy independently, and they only need short time to be fully charged/discharged without any sign of aging. Their disadvantages are their low energy

densities, which are restricted by the solubility of the redox active species, high capital cost, and leakage of electrical current.

RFBs can be employed in grid-scale storage but are restricted due to the high cost of the ion-exchange membrane between positive and negative electrodes and the maintenance of the high solubility of redox molecules.^[6,10,36] For having a better overview of the aforementioned batteries, their important specifications is reported in Table 1-4.

Table 1-4. Overview of the potential batteries for utility applications.^[5,6,59-62]

Battery type	Specific energy [Wh kg ⁻¹]	Cycle life	Self-discharge per month [%]	Round-trip energy efficiency [%]
LTO/LFP	50-70	4000	2	94-99
C-LCO	155	1000	2	94-99
LMO-VO₂	75	500-3000	30	94-99
ZEBRA	95-120	3000	Negligible	75-90
Na-S	150-240	4000	Negligible	75-90
LCB	25-40	3000	-	-
VRB	10-20	5000	3-9	65-80
NCB	30-45	2000	5-20	55-70
LAB	25-40	1000	4-50	50-75

LTO/LFP = Lithium-ion batteries based on Li₄Ti₅O₂ (LTO) anode and LiFePO₄ cathode, C-LCO = Lithium-ion batteries based on carbon anode and LiCoO₂ cathode, Lithium-ion batteries based on LiMn₂O₄ (LMO) cathode and VO₂ anode, ZEBRA = Zeolite Battery Research Africa, Na-S = Sodium-sulfur batteries, LCB = Lead-carbon ultra-batteries, VRB = Vanadium redox flow batteries, NCB = Nickel-cadmium batteries, LAB = Lead-acid batteries, Round-trip energy efficiency = the ratio of energy put in during charging to energy retrieved from storage during discharging.

1.2.6. Metal-Air (Li, Na, Zn) Batteries

Metal-air batteries have become an attractive alternative to LIBs due to their high theoretical energy densities. In principle, in M-O₂ batteries, the electrochemical reduction of O₂ occurs at the cathode while electro-dissolution of the active material takes place at the anode.^[32] These batteries are facing different challenges associated with the air cathode, metal anode and electrolyte. However, after overcoming these issues they can become the next-generation EES devices for grid-scale or EVs.^[63]

1.2.6.1. Lithium-Oxygen (Li-O₂) Batteries

Lithium-oxygen (Li-O₂) batteries consist of a Li-based anode, an air cathode, and electrolyte. The electrolyte can be aprotic, aqueous, mixed aprotic-aqueous, or solid state.^[64] The Li-O₂ battery has an energy density of 3458 Wh kg⁻¹ (Li₂O₂), which is attractive for application in EVs. The specific power value is only 10% of the LIBs and the cell voltage is 2.96 V.^[11,32]

Li-O₂ batteries suffer from large overpotential, low coulombic efficiencies, poor rate performances, and fast capacity fadings. These problems are the results of the passivation of the positive electrode by Li₂O₂ films, low stability of electrode/electrolyte interface upon reduction

of O₂, and parasitic reaction of Li metal with contamination in the air and some electrolyte molecules.^[65–67]

Nowadays, lithium-air batteries are called lithium-oxygen since the air is filtered to remove the remaining CO₂, N₂, and the excess moisture. Different methods have been applied to improve the performance of this battery. These attempts employ higher-donor-number electrolyte solutions, additives in the electrolyte, or redox mediators.^[68–73] By using support electrodes made of gold^[74] or TiC^[75] instead of carbon, the lithium-oxygen battery can be cycled up to 1000 cycles. Furthermore, reversible cycling is possible by using discharge products, such as LiOH, LiO₂, and Li₂CO₃ instead of Li₂O₂ with a combination of suitable redox mediators. However, to commercialize this battery, the challenges of the electrode/electrolyte interface stability and air handling has to be solved.^[11,76–78]

1.2.6.2. Sodium-Oxygen (Na-O₂) Batteries

Sodium-oxygen batteries, with a total cell voltage of 2.3 V, contain a sodium anode, an air cathode, and a conducting organic electrolyte. Although the theoretical energy density of Na-O₂ batteries is 1108 Wh kg⁻¹ (less than 30% of Li-O₂, 3458 Wh kg⁻¹), they have remarkable advantages, such as having a lower charge overpotential (~100 mV) than Li-O₂ batteries (~1000 mV) and high coulombic efficiencies (>95%). In addition, sodium is more abundant and cheaper than lithium, as reported in Fig. 1-3 and Table 1-2. This technology is a good candidate to be applied in EVs and hybrid EVs (HEVs) because of its low polarization, but it needs further research to be ready for commercialization.^[32]

1.2.6.3. Zinc-Air Batteries

Zinc-air batteries are classified as primary and secondary (rechargeable) batteries. The commercialized primary zinc-air battery is compatible for low power electronic devices, such as hearing aids.

The electrical rechargeable type is the most developed rechargeable metal-air battery system. The production of zinc-air batteries compared to lithium-air cells is cheaper due to the higher abundance and accessibility of zinc in the earth's crust (Fig. 1-3, Table 1-2). Since this low-cost battery has a high specific energies and is environmentally friendly, it can be a promising candidate for power source and energy storage systems in the future.^[79,80]

Zinc-air batteries have four major components, which are a porous oxygen cathode with a catalyst, a porous zinc anode, alkaline electrolyte, and a separator matrix. The basic processes in this battery are the oxygen reduction reaction (ORR) during the discharge and oxygen evolution reaction (OER) during the charge. Although the theoretical potential of this battery is 1.65 V, the complete potential cannot be obtained due to dendrite formation upon recharging.^[81] The

challenges of this battery originates from the zinc electrode by formation of dendrites, leading to the short life cycle, low efficiency, rapid degradation, passivation, and self-discharge.^[80]

1.2.7. Sodium-Ion Batteries

Sodium with its similar chemical properties in comparison to lithium and high abundance in the earth's crust (Fig. 1-3, Table 1-2), has become a promising alternative to lithium. It has a low redox potential of -2.71 V vs. standard hydrogen electrode (SHE). The solvation energy of sodium ions is 30% smaller than that of lithium ions in organic solvents and therefore the charge transfer resistance is smaller and the electrode kinetics is enhanced. Recently, promising low-cost sodium-ion batteries (SIBs) have been developed and utilized in different applications, such as grid-scale energy storage, EVs, and portable electronics.^[82] In the next sections several cathode and anode materials that have been used in SIBs are reported.

1.2.7.1. Cathodes

There are different well-established open-framework materials for SIBs, such as metal-organic frameworks (MOFs), sodium super ionic conductors (natrium super ion conductor or NASICON), and Prussian blue analogs (PBAs), consisting of a covalent bond transition-metal framework with micro cavities.^[83,84]

Sodium ions have shown high ionic conductivities in NASICON with a hexagonal framework of $\text{Na}_{1+3x}\text{Zr}_2(\text{P}_{1-x}\text{Si}_x\text{O}_4)_3$. In addition, $\text{Na}_3\text{V}_2(\text{PO}_4)_3$ is a NASICON-type material with good thermal stability and a high theoretical energy density of $\sim 400 \text{ Wh kg}^{-1}$ as well as a practical energy density of 138 Wh kg^{-1} .^[85] The drawback of the NASICON-type materials is the decrease of the mobility of sodium ions due to the rotation of $\text{M}_2(\text{XO}_4)_3$ units of the framework, the derivation of the monoclinic structure, and the low electronic conductivity, which leads to poor cycle performance and low coulombic efficiency.^[86-89]

Moreover, $\text{Na}_{0.44}\text{MnO}_2$ has a unique tunnel structure and provides good cycling stability, while tolerating stress during structural changes. This material can offer a specific capacity of 140 mAh g^{-1} . The single-crystal nanowires of this material also have a high specific capacity of 128 mAh g^{-1} at a C/10 rate with good capacity retention after 1000 cycles.^[88,90,91]

From the family of transition-metal hexacyanoferrates (PBAs) with an open-framework structure, $\text{KMFe}(\text{CN})_6$ with $\text{M} = \text{Mn, Fe, Co, Ni, Cu, and Zn}$ have been synthesized by Lu et al.^[92] Among different hexacyanomethylates materials, $\text{KFe}(\text{II})\text{Fe}(\text{II})(\text{CN})_6$ has derived a reversible capacity of 100 mAh g^{-1} in an organic liquid carbonate electrolyte with a current rate of C/20 (the current rate of the cycling was determined as nC, which corresponds to a full oxidation or reduction in n^{-1} hours), even though its coulombic efficiencies were not good and have been only 60% at the initial cycle. Sodium manganese ferrocyanide

($\text{Na}_{1.32}\text{Mn}[\text{Fe}(\text{CN})_6]_{0.83} \cdot 3.5\text{H}_2\text{O}$) thin films are another PBA that have been used as a cathode material in SIBs. This material permits fast and reversible (de-)intercalation of sodium ions within the framework without any structural phase transition. The thin film sodium manganese ferrocyanide has been cycled in a propylene carbonate solution consisting of 1 M NaClO_4 , obtaining a reversible capacity of 109 mAh g^{-1} at a rate of 0.5C, a coulombic efficiency of ~95%, and an average discharge potential of 3.4 V.^[93]

An improved PBA $\text{Na}_2\text{Zn}_3[\text{Fe}(\text{CN})_6]_2 \cdot x\text{H}_2\text{O}$ (Sodium zinc hexacyanoferrate) with a well-defined structure has been utilized as a positive electrode in SIBs. The capacity provided by sodium zinc hexacyanoferrate is 56.4 mAh g^{-1} , and it holds up to its initial capacity (85.2%) after 50 cycles at a 0.18C rate in propylene carbonate (PC) based electrolytes. This structure allows the reversible diffusion of sodium ions within the framework.^[83]

Another PBA that has been used as a positive electrode in SIBs as a positive electrode is sodium manganese hexacyanomanganate ($\text{Na}_2\text{Mn}^{\text{II}}[\text{Mn}^{\text{II}}(\text{CN})_6]$) open framework. This material provides a reversible capacity of 209 mAh g^{-1} at a C/5 rate having an average potential of 2.65 V (vs. Na^0/Na^+) in PC electrolyte.^[94] You et al.^[84], in their study, introduced another PBA for SIBs, namely high-quality Prussian blue (PB) nanocrystals (HQ- NaFe , $\text{Na}_{0.61}\text{Fe}[\text{Fe}(\text{CN})_6]_{0.94}$) using $\text{Na}_4\text{Fe}(\text{CN})_6$ as an iron-source compound. This material had a lower number of zeolite water molecules and a smaller number of $[\text{Fe}(\text{CN})_6]$ vacancies in its structure, which exhibits a specific capacity of 170 mAh g^{-1} and high cycling stability after 150 cycles in an organic electrolyte (1 M NaPF_6 dissolved in ethylene carbonate (EC) and diethyl carbonate (DEC)) without any capacity loss. Although these sodium-rich compounds exhibit good performances, they usually lose their capacity in the first 10 cycles due to the phase transition from monoclinic/rhombohedral to the respective cubic structure.^[95]

1.2.7.2. Anodes

Unlike LIBs, pure graphite cannot be employed as an insertion electrode in SIBs since sodium atoms do not intercalate between carbon sheets. However, intercalation of sodium ions into other carbonaceous materials has been studied. Sodium can intercalate into soft carbon (graphitizable carbon), hard carbons (non-graphitizable carbon), and petroleum cokes, along with hydrogen-contacting carbon. Another type of anodes for SIBs can be a NASICON-type materials (low potential metal phosphates), $\text{NaTi}_2(\text{PO}_4)_3$, for both aqueous and non-aqueous cells. The capacity of this material in an aqueous electrolyte is 123 mAh g^{-1} , while the capacity is 120 mAh g^{-1} in a non-aqueous electrolyte. Moreover, amorphous TiO_2 nanotubes with an inner diameter greater than 80 nm and a wall thickness of greater than 15 nm offer a reversible (de-)intercalation of sodium ions. $\text{Na}_2\text{Ti}_3\text{O}_7$ and vanadium oxides are also candidates for low potential sodium metal oxides as anodes in SIBs. The last choice for an anode in SIBs are sodium alloy materials. The partial elements from Group IVA and VA elements, such as Sn, Sb,

and P, based on the alloying reaction mechanism, deliver high theoretical specific capacities in SIBs.^[88,96–101]

1.2.8. Aqueous Metal-Ion Batteries

Batteries in the automotive industry are required to have a fast charge/discharge time window, preferably of few seconds. On the other hand, in backup systems of large-scale energy storage for power grids, the response time can be from seconds to many hours or longer. In the last decades, among rechargeable batteries, aqueous metal-ion batteries provided lower cost, environmentally friendly, safe, and nontoxic systems, which make them a potential choice for grid-scale energy storage.^[6,102–105] In this section, different aqueous metal-ion batteries, such as aqueous LIBs (ALIBs), aqueous SIBs, aqueous aluminum batteries, and aqueous zinc-ion batteries, are discussed in detail.

The main approach is to replace the organic-based batteries that are highly flammable and toxic to overcome their safety and cost disadvantages. Water as an abundant natural electrolyte solvent is the best candidate for developing nonflammable and low-cost water-based electrolyte batteries. Aqueous electrolytes have higher ionic conductivities ($\sim 1 \text{ S cm}^{-1}$) compared to non-aqueous ones ($\sim 1\text{--}10 \text{ mS cm}^{-1}$), which allows the battery to perform with a high rate capability and fast redox reaction (excellent kinetic properties).^[106,107] The main drawback of aqueous electrolytes is their low energy densities due to their relatively narrow electrochemical stability window (1.23 V). In aqueous battery systems with voltages above 1.23 V, water electrolysis begins on the surface of the electrodes, make the system thermodynamically unstable and lead to a self-discharge and limited rate capability.^[107,108]

Several studies have focused on different aqueous metal-ion batteries. These batteries are able to provide a safe, low-cost, and environmentally friendly system compared to conventional organic LIBs for the grid-scale energy storage. They can be based on monovalent charge carriers (K^+ , Li^+ , or Na^+), multivalent charge carriers such as divalent (Mg^{2+} , Zn^{2+} , or Ca^{2+}) or trivalent (Al^{3+}) carriers, and mixed monovalent or multivalent carriers. The advantage of employing multivalent ions is their ability to provide a higher storage capacity due to multiple electron transfer.^[109,110] Since none of the commercialized secondary batteries, such as lead-acid, Ni-MH, and Ni-Cd have long cycle stabilities in aqueous electrolytes, it is important to develop a reliable safe battery with a high energy content, long life cycle, and low-cost of fabrication as a substitution for organic LIBs for large-scale energy storage systems. In the next parts of this work, a brief description of low-cost and safe aqueous metal-ion batteries is noted.^[111]

1.2.8.1. Aqueous Lithium-Ion Batteries

Due to its safety, reliability, low-cost, and green technology, aqueous LIBs (ARLBs) have received considerable interest as an alternative to organic-based LIBs. In the 1990s, Dahn et al.^[112] introduced an ARLB that incorporated LiMn_2O_4 as a cathode and VO_2 as an anode, with an average potential of 1.5 V and the specific energy of 75 Wh kg^{-1} , which is higher than lead-acid batteries, but suffered from poor cycling performance (only around 17 cycles).^[111,112] Furthermore, Ping et al.^[113] reported an ARLB in which lithium iron phosphate (LiFePO_4) was used as cathode material in a 0.5 M lithium sulfate (Li_2SO_4) aqueous solution offering a high capacity of 140 mAh g^{-1} at a 1C rate, which is 8% higher than in organic electrolytes solutions. In the work by Luo et al.^[114], LiFePO_4 was used as a cathode and a NASICON-type ($\text{LiTi}_2(\text{PO}_4)_3$) material as anode in a 0.5 M Li_2SO_4 solution. Here, the system reached 1000 cycles with good cycle stability. Moreover, Zhao et al.^[115] employed a LiFePO_4/C cathode paired with lithium trivanadate (LiV_3O_8) in 9 M LiNO_3 electrolyte and could provide high cycling performance and rate capability up to 50C.^[111]

In addition, to overcome the limitation factors of organic LIBs with a combination of the main challenge of aqueous electrolytes (i.e., the narrow stability window), researchers have proposed adjusting the alkalinity of electrolytes to suppress the hydrogen evolution reaction. However, this attempt only increased the potential of the ARLB up to 1.5 V, but caused high self-discharge rates due to the residual currents for hydrogen and oxygen evolution. Moreover, another investigation has been done by employing a highly concentrated aqueous electrolyte, namely a “water-in-salt” electrolyte. This electrolyte has a high concentration ($>20 \text{ m}$, m noted as molality) consisting of highly soluble salt, such as lithium bis(trifluoromethane sulfonyl)imide (LiTFSI). This leads to an expansion of the electrochemical stability window up to $\sim 3 \text{ V}$ due to the decomposition of salt anions on the anode before the hydrogen evolution, thus lead to the formation of a dense solid-electrolyte interphase (SEI). In the study by Suo et al.^[116,117], a full ARLB cell based on a LiMn_2O_4 cathode, Mo_6S_8 anode, and 21 m LiTFSI electrolyte has been demonstrated. The battery exhibits excellent stability at 4.5C with a capacity retention of 68% after 1000 cycles and of 78% after 100 cycles at 0.15C. At both current rates, the coulombic efficiency has been around 100%.^[116,117]

1.2.8.2. Aqueous Sodium-Ion Batteries

In addition to having low-cost raw materials and abundant sodium (Na), SIBs exhibit similar chemistry to LIBs. Therefore, SIBs have become a promising alternative to LIBs.^[11,118,119] Although organic SIBs have a high energy density and high voltage ($>3 \text{ V}$), their drawbacks such as volatility, flammability, and toxicity of organic electrolytes lead to environmental and safety concerns. Therefore, developing an alternative battery (aqueous SIB) to an organic

non-aqueous SIB for large-scale energy storage applications is a matter of importance.^[120] Since sodium-ion storage is larger (0.98 Å) than lithium-ion storage (0.69 Å), it requires a material with an acceptably large channel structure that allows the reversible (de-)intercalation of sodium ions. Since aqueous SIBs suffer from low specific energy due to their low potential, it is important to investigate new cathode materials with large reversible capacities and higher potentials.

Recently, different materials have been investigated as cathode material for aqueous SIBs. A tunnel-structured $\text{Na}_4\text{Mn}_9\text{O}_{18}$ has been introduced by Whitacre et al.^[121], but it suffers from low specific capacity, as 45 mAh g^{-1} , and a potential of 0.5 V. Chiang et al.^[122] reported on an aqueous SIB in which $\text{Na}_{0.44}\text{MnO}_2$ is used as a cathode material and $\text{NaTi}_2(\text{PO}_4)_3$ is used as an anode material. This battery had an average discharge potential of 1.1 V with an energy density of 33 Wh kg^{-1} .^[123]

Prussian blue analogues (PBAs) are other potential candidates for SIB cathodes due to their open-framework structure, electrochemical tenability, and easy synthetic procedure. Wu et al.^[123] introduced a Na-rich copper hexacyanoferrate (II) ($\text{Na}_2\text{CuFe}(\text{CN})_6$, NaCuHCF) as a cathode material for SIBs. This system was able to reach the highest discharge potential of 1.4 V obtained so far for SIBs with a specific energy of 48 Wh kg^{-1} . The coulombic efficiency of this system remained at 100% even at high current rates, thus suggests that NaCuHCF active material has a large overpotential of oxygen evolution which suppress the unfavorable oxygen evolution reaction at the charged cathode even at high rates. Accordingly, this battery exhibits a high rate and cycle capability with 88% capacity retention after 1000 cycles at a 10C rate.^[120,123] This group also reported a low-defect Prussian yellow (PY), which was cycled in 1 M Na_2SO_4 (pH = 7) and reached a capacity of 100 mAh g^{-1} at a 10C current rate and showed a good cycling stability over 500 cycles with only 20% capacity loss.^[124] As anode material, $\text{NaTi}_2(\text{PO}_4)_3$ has shown promising results in aqueous SIBs with the redox potential of -0.6 V vs. SHE.^[123]

1.2.8.3. Aqueous Aluminum-Ion Batteries

A rechargeable battery based on aluminum chemistry was developed in the early 1970s since aluminum is the most abundant metal in the earth's crust, has a higher volumetric capacity than lithium and sodium, and is characterized by a high gravimetric capacity (2980 mAh g^{-1}). Aluminum with having three charges provides higher energies than single-electron LIBs or SIBs. Furthermore, aqueous aluminum batteries are cheap and environmentally friendly. However, in this type of battery the metallic aluminum anode can undergo corrosion in the aqueous electrolyte. In addition, finding a compatible host cathode material for (de-)intercalation of trivalent aluminum ions is also a challenge.^[125–127]

Liu et al.^[128,129] were the first to introduce titanium dioxide (TiO₂) as an anode host material for reversible (de-)insertion of aluminum ion. The developed electrode of TiO₂ in 1 M AlCl₃ aqueous solution delivered a capacity of 75 mAh g⁻¹ at 4 mA cm⁻² current density. Later, they introduced an aluminum-based battery that approached 1000 cycles with a capacity retention of 54.9% at a current density of 400 mA g⁻¹.^[130] Furthermore, studies showed that one-dimensional anatase TiO₂ nanotubes can be a feasible anode material in aqueous aluminum batteries. Black anatase TiO₂ nano-leaves can deliver a high reversible capacity of 141.3 mAh g⁻¹ at a high rate of 2 A g⁻¹ in 1 M Al(NO₃)₃ and lose only 8.4% of the capacity after 300 cycles. The TiO₂ nano-leaves can facilitate aluminum-ion diffusion and electronic transport almost without any volumetric changes.^[125] In addition to TiO₂, different host materials have been proposed, such as V₂O₅ and VO₂. However, the application of vanadium oxides is limited due to their toxicity. The main challenge for aluminum batteries is choosing an appropriate host material for aluminum ions by considering their strong bonding to the host structure, which causes slow diffusion kinetics. Therefore, PBAs can be a potential group of materials for aluminum-ion (de-)intercalation. In 2014, Liu et al.^[126] reported on an aqueous aluminum battery in 0.5 M Al₂(SO₄)₃ based on CuHCF cathode material, approaching a specific capacity of 62.9 mAh g⁻¹ at a current density of 50 mA g⁻¹. However, at a high current density (400 mA g⁻¹), the capacity dropped to 46.9%. The capacity fading was explained by the shielding effect between the zeolitic water and aluminum ions in the CuHCF host lattice.

In the work by Wang et al.^[131], an aqueous zinc//aluminum battery was demonstrated. In this battery, ultrathin graphite nanosheets were used as a cathode, zinc as a negative electrode, and Al₂(SO₄)₃/Zn(CHCOO)₂ as an electrolyte. This battery delivered a high specific capacity of 60 mAh g⁻¹ at a high current density (2000 mA g⁻¹ = 33C) with excellent stability.

1.2.8.4. Aqueous Zinc-Ion Batteries

Aqueous zinc-ion batteries (ZIBs) are another cost-effective rechargeable battery for stationary grid energy. In stationary applications, high energy density is not the main focus, while the cost and availability of the materials are of primary concerns. Zinc, as a low-cost, nontoxic material with low equilibrium potential, high reversibility in aqueous solutions, and high specific energy is a potential material for aqueous batteries. Since zinc is a divalent ion, it can transfer two electrons and gives more charge capacity than monovalent ions. In addition, zinc has a low standard reduction potential (-0.76 V vs. SHE) and high volumetric capacity (5845 mAh cm⁻³), which makes it particularly attractive.^[132] Although zinc metal has high capacity (820 mAh g⁻¹), it suffers from dendritic formation in alkaline electrolytes. This can be restricted while using neutral or slightly acidic pH electrolytes.^[133] ZIBs are attractive rechargeable batteries, as zinc features higher water compatibility and stability than alkaline metals, which permit facile multivalent ion transport.^[132]

The first aqueous ZIB was introduced by Kang et al.^[134], here MnO_2 was used as cathode material in 1 M ZnSO_4 or $\text{Zn}(\text{NO}_3)_2$. After this research, polymorphous MnO_2 and PBAs were studied as potential host materials for zinc-ion intercalation.^[133] In the next parts, the cathode and anode materials used in aqueous ZIBs are described in detail.

1.2.8.4.1. Cathodes

Alpha type manganese dioxide ($\alpha\text{-MnO}_2$) is one of the promising host materials that allows the reversible (de-)intercalation of multivalent ions, such as Zn^{2+} in aqueous electrolytes. This material is currently used in commercial alkaline batteries. $\alpha\text{-MnO}_2$ structure (Fig. 1-6) enables fast kinetics and stable thermodynamics upon storing multivalent ions. Although MnO_2 is abundant, environmentally friendly, and cheap, it suffers from poor ionic and electrical conductivity as well as poor reversibility. However, Xu et al.^[135] described a ZIB based on an $\alpha\text{-MnO}_2$ cathode, ZnSO_4 aqueous electrolyte, and a zinc anode. This battery was able to deliver a specific capacity of 210 mAh g^{-1} and an energy density of 270 Wh kg^{-1} , which is higher than lead-acid or Ni-Cd batteries ($\sim 40\text{--}80 \text{ Wh kg}^{-1}$).^[134,135] In addition, Zhang et al.^[136] introduced low-cost and environmentally friendly, rod-like $\text{Na}_{0.95}\text{MnO}_2$ as cathode material for aqueous ZIBs. This material exhibits excellent cyclability up to 1000 cycles at a 4C current rate with only 8% capacity loss in 0.5 M $\text{Zn}(\text{CH}_3\text{COO})_2$ and 0.5 M CH_3COONa electrolytes. This system has achieved an energy density of up to 78 Wh kg^{-1} with an average discharge potential of 1.4 V. In 2016, Liu et al.^[137] also discussed a Zn/MnO_2 battery that offered a capacity of 285 mAh g^{-1} with only 8% capacity loss over 5000 cycles by optimizing the ZnSO_4 aqueous solution with a MnSO_4 additive.

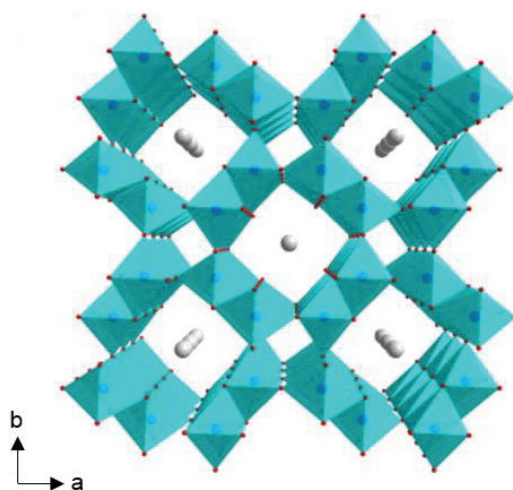


Figure 1-6. Crystal structure of $\alpha\text{-MnO}_2$ (adapted from [138]).

Layered and hydrated V_2O_5 derivatives with an open-framework crystal structure allow fast and reversible (de-)intercalation of zinc ions. As an example $\text{Zn}_{0.25}\text{V}_2\text{O}_5 \cdot n\text{H}_2\text{O}$ exhibits good

electrochemical performance with a high capacity of greater than 300 mAh g⁻¹, long life cycle with more than 1000 cycles, and good rate capability.^[109]

A layered calcium vanadium oxide bronze is another cathode material for ZIBs. Calcium-based bronze structure (CVO, Ca_{0.25}V₂O₅·nH₂O) synthesized using a one-step hydrothermal method and can provide a high capacity of 340 mAh g⁻¹ at a 0.2C rate (Fig. 1-7). The ZIB based on this cathode material can perform up to 3000 and 5000 cycles at 80C with capacity retention of 96% and 78%, respectively. The complete cell is able to deliver an energy density of 267 Wh kg⁻¹ at a power density of 53.4 W kg⁻¹.^[109] These layered and tunnel-type vanadium-based materials have shown an impressive performance as ZIB cathode materials due to their open-framework structure and multiple oxidation states of vanadium.^[133]

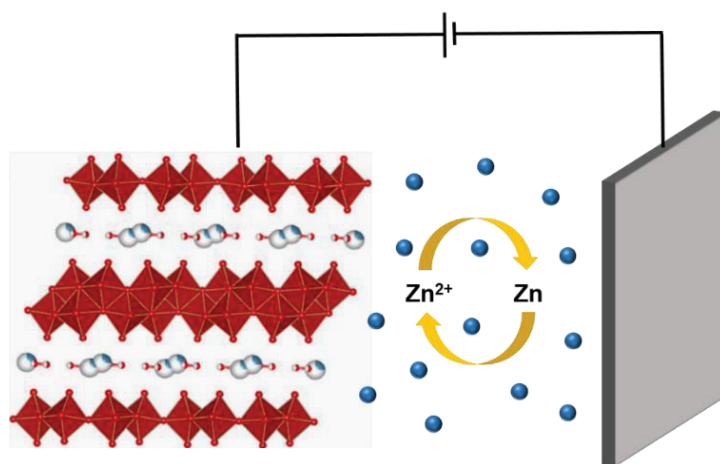


Figure 1-7. Schematic representation of a zinc-ion battery cell with CVO as the cathode, zinc metal as the anode, and a zinc containing electrolyte (adapted from [109]).

In 2016, Nazar et al.^[106] reported a pillared vanadium oxide bronze with interlayer zinc ions and water (Zn_{0.25}V₂O₅·nH₂O) as a cathode material in an aqueous ZIB.

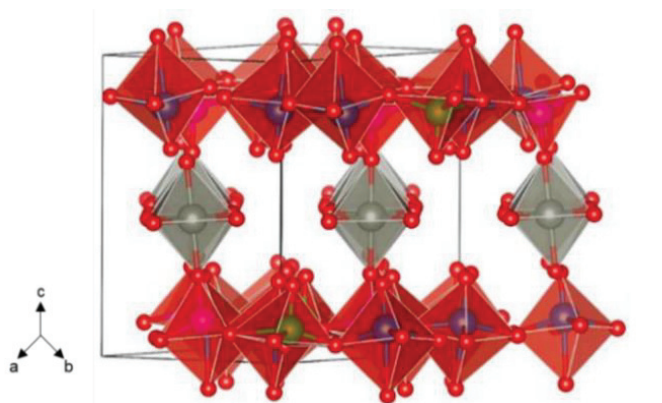


Figure 1-8. Crystal structure of Zn_{0.25}V₂O₅·nH₂O nanobelts along (110) direction (adapted from [106]).

This nanobelt material (Fig. 1-8) has been cycled in 1 M ZnSO₄ and reached a high specific energy of 250 Wh kg⁻¹. Due to the co-intercalated water molecules, this structure offered higher energy density and higher power than α-MnO₂ and zinc hexacyanoferrate (Zn₃[Fe(CN)₆]₂) and

diminished the activation energy for the charge transfer at the electrode interface. The cell offered a volumetric energy density of 450 Wh L^{-1} at a high current rate (15C) with less than 20% capacity loss over 1000 cycles.

In 2017, Xia et al.^[133] proposed ultra-long zinc pyrovanadate (ZVO, $\text{Zn}_3\text{V}_2\text{O}_7(\text{OH})_2 \cdot 2\text{H}_2\text{O}$) nanowires, which delivered a high capacity of 213 and 76 mAh g^{-1} at current densities of 50 and 3000 mA g^{-1} , respectively.

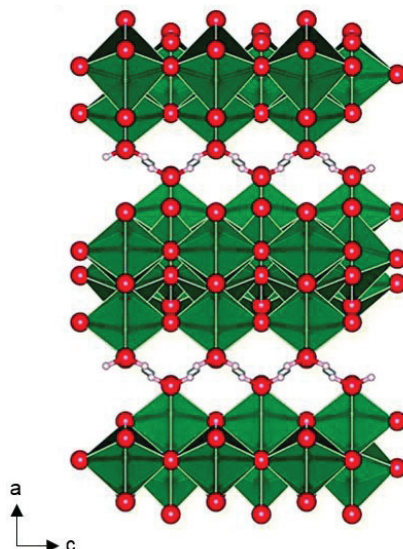


Figure 1-9. Crystal structure of layered V_3O_7 along (010) direction (adapted from [132]).

The cell of ZVO/Zn showed promising performance with stability up to 300 cycles and a coulombic efficiency of greater than 96%. It is estimated that this battery can deliver an energy density of 214 Wh kg^{-1} , which is higher than commercial LIBs. In the work by Kundu et al.^[132], a layered $\text{V}_3\text{O}_7 \cdot \text{H}_2\text{O}$ (Fig. 1-9) was introduced and delivered a high capacity of 375 mAh g^{-1} at a 1C rate in 1 M ZnSO_4 aqueous electrolyte. This structure permits reversible (de-)intercalation of zinc ions with a high rate capability and a 100% coulombic efficiency. In addition, He et al.^[139] introduced a ZIB in which $\text{H}_2\text{V}_3\text{O}_8$ nanowires were used as a cathode material, zinc as anode, and 3 M $\text{Zn}(\text{CF}_3\text{SO}_3)_2$ as aqueous electrolyte. This battery has delivered a capacity of 423.8 mAh g^{-1} at a 0.1 A g^{-1} current density with an excellent cycling stability of up to 1000 cycles at 5 A g^{-1} with only 5.7% capacity loss. This material, due to its layered structure, enables the (de-)insertion of zinc ions through its large interlayer spacing with almost no structural changes.

Environmentally friendly PBAs are promising low-cost cathode materials for ZIBs. However, they suffer from limited capacity and poor cycling stability. From this open-framework family, Zhang et al.^[140] cycled rhombohedral zinc hexacyanoferrate (ZnHCF, $\text{Zn}_3[\text{Fe}(\text{CN})_6]$) as a cathode material in ZnSO_4 , Na_2SO_4 , and K_2SO_4 aqueous electrolytes. A specific energy density of 100 Wh kg^{-1} at a power density of 1.7 kW kg^{-1} , and a capacity retention of 76% have been

obtained after 100 cycles in 1 M ZnSO₄. Furthermore, this battery had an average discharge potential of 1.7 V. This study illustrated that ZnHCF is a stable material in a ZnSO₄ electrolyte than Na₂SO₄, and K₂SO₄, and did not dissociate upon cycling in the ZnSO₄ solution. In addition, in the later work of this group,^[141] three different ZnHCF polyhedron particles (Cuboctahedron C-ZnHCF, truncated octahedron T-ZnHCF, and octahedron O-ZnHCF) were introduced as cathode materials in ZIBs (Fig. 1-10). Although the chemical composition of all three ZnHCF components are similar, they showed different electrochemical performances due to their different structures. Among all three ZnHCFs, the cuboctahedral shape showed an excellent rate capability and cyclic stability with a discharge capacity of 69.1 mAh g⁻¹ at 60 mA g⁻¹ current density. The average operating potential of a ZIB based on a C-ZnHCF cathode and a zinc anode in 3 M aqueous ZnSO₄ is 1.73 V and can deliver a specific energy density of 105 Wh kg⁻¹ with only 20% capacity loss after 200 cycles at high current density (300 mA g⁻¹).^[141]



Figure 1-10. Crystal structure of different ZnHCF polyhedrons (adapted from [141]).

Although ZnHCF has a high voltage for ZIB applications, in comparison with CuHCF, it suffers from a less stable life cycle.^[140] In 2014, Trócoli et al.^[142] noted a rechargeable aqueous ZIB based on a CuHCF cathode material with the highest reported average discharge potential so far (1.73 V vs. Zn/Zn²⁺). This battery performed in 20 mM ZnSO₄ (pH = 6) and delivered an average specific power of 52.5 W kg⁻¹ at a current density (1C) of 60 mA g⁻¹ and 477 W kg⁻¹ at a 10C current rate. Although the specific energy was 45.7 Wh kg⁻¹ at 1C with a drop to 33.8 Wh kg⁻¹ at a 10C current rate, these values are close to organic LIBs based on LTO and LFP at a 10C current rate. The capacity retention of this battery after 100 cycles was 96.3%, while in the work by Liu et al.^[140] was 76%. Trócoli et al.^[142] results have shown that this low-cost, safe, and nontoxic battery has the potential to be employed in stationary applications and to fulfill the needs of grid-scale energy storage.

1.2.8.4.2. Anodes

High-capacity zinc metal is one of the anode materials for ZIBs. Zinc is a nontoxic, abundant, and low-cost material with a high capacity of 820 mAh g⁻¹ that received great attention as an

electrode material in batteries. Zinc has a low redox potential (-0.76 V vs. SHE) and high overpotential regarding hydrogen evolution, which makes it a compatible and promising anode candidate for rechargeable aqueous metal-ion batteries. The dendrite formation of zinc and its short life cycle, due to dendrite growth upon recharging and internal short circuit, are the challenges to overcome to commercialize this ZIB. Hence, by substituting an alkaline electrolyte with a mild neutral pH or even a slightly acidic aqueous electrolyte, the dendritic zinc issues can be eliminated.^[140] In 2016, Cui et al.^[143] proposed a backside-plating configuration for a zinc anode, which prevents internal short circuiting and limits dendrite formation. A full cell battery using this anode and a nickel cathode delivered a good power rate and specific energy density of $\sim 246 \text{ Wh kg}^{-1}$ at a current density of 20 mA cm^{-1} after 800 cycles.^[107,109,143]

In addition, in 2016, Gupta et al.^[144] introduced a ZIB based on a CuHCF cathode and hyper-dendritic (HD) zinc anode in a $1 \text{ M Na}_2\text{SO}_4/0.01 \text{ M H}_2\text{SO}_4$ electrolyte. This new anode material was able to improve the life cycle of the battery having a 90% capacity retention over 300 cycles as well as hindered dendrite formation in comparison to a conventional Zn sheet. The energy efficiency of this system dropped only by 4% after 500 cycles. This performance can be obtained due to the large surface area of HD Zn, which lowers the overpotential and increases the kinetics of zinc-ion (de-)intercalation.^[107,109,144]

Furthermore, Bani Hashemi et al.^[145] improved the zinc electrodeposition efficiency of a zinc anode in an aqueous zinc-ion battery. Based on the low equilibrium electrochemical potential of metallic zinc in regard to the even lower electrochemical stability window of water, hydrogen evolution takes place. When hydrogen gas is released it suppresses the zinc electrodeposition efficiency. The electrodeposition efficiency term is defined as the ratio of the oxidation to reduction charge flow. Bani Hashemi et al.^[145] successfully increased the zinc electrodeposition efficiency to 98% by mixing the zinc powder with copper-doped Zn-Al-CO₃ layered double hydroxides (LDH) with the ratio of 1:2, as a solid-state additive for the negative electrode. They tried different ratios of zinc to LDH and studied the resulting electrochemical performances in quasi-neutral pH media (500 mM ZnSO_4). The results showed that this anode material had an excellent electrochemical performance with a maximum power density of 980 W kg^{-1} .^[145]

A challenge restricting the application of aqueous ZIBs is finding a suitable cathode material that has a stable structure and provides a high capacity during Zn²⁺ (de-)intercalation.^[145,146]

1.3. Prussian Blue and its Analogues (PB and PBAs)

To select suitable electrode materials for aqueous and non-aqueous metal-ion batteries, different criteria such as economics, abundance, safety, eco-friendliness, recyclability, and the possibility of facilitating technology should be considered. Recently, transition-metal hexacyanometallates

known as Prussian Blue Analogues (PBAs) have garnered significant interest for their wide range of applicability such as in ion exchange, humidity sensitivity, electrochemical sensing, electrocatalysis, photocatalysis, electrochromism, and electrochemical energy storage.^[147]

Prussian blue (PB) iron (II) hexacyanoferrate (II), also called ferric ferrocyanide, is an inorganic polycrystalline substance with a ~300-year history. In the eighteenth century, PB was used as a pigment for paints, printing inks, and lacquers due to its accessibility and low-cost.^[148–153] Moreover, PB and its derivatives are nontoxic and have a facile synthesis procedure with low production costs. Therefore, these characteristics make PBAs a good candidate for large-scale energy storage applications.^[147]

The chemical and crystal structure of PB was first characterized by Keggin and Miles in 1936, for use in powder diffraction patterns. PB exhibits face-centered cubic structure with a space group of $Fm\bar{3}m$ in which Fe^{2+} and Fe^{3+} ions are alternatively placed on a face-centered cubic lattice. The PB compound has two stable forms: *soluble* (alkali-rich) with a general formula of $AFe^{III}[Fe^{II}(CN)_6] \cdot xH_2O$ ($x < 10$), where A is the alkali metal cations; and *insoluble* (alkali-free) with a general formula of $Fe_4^{III}[Fe^{II}(CN)_6]_3 \cdot xH_2O$ ($10 < x < 16$) (Fig. 1-11).^[154–158] It is important to mention that the terms *soluble* and *insoluble* can be quite misleading, as both of these forms are basically insoluble in water; the term *soluble* is used for PB that is able to form a stable colloidal suspension. In addition, PB is known to be highly stable in acidic media.^[158,159]

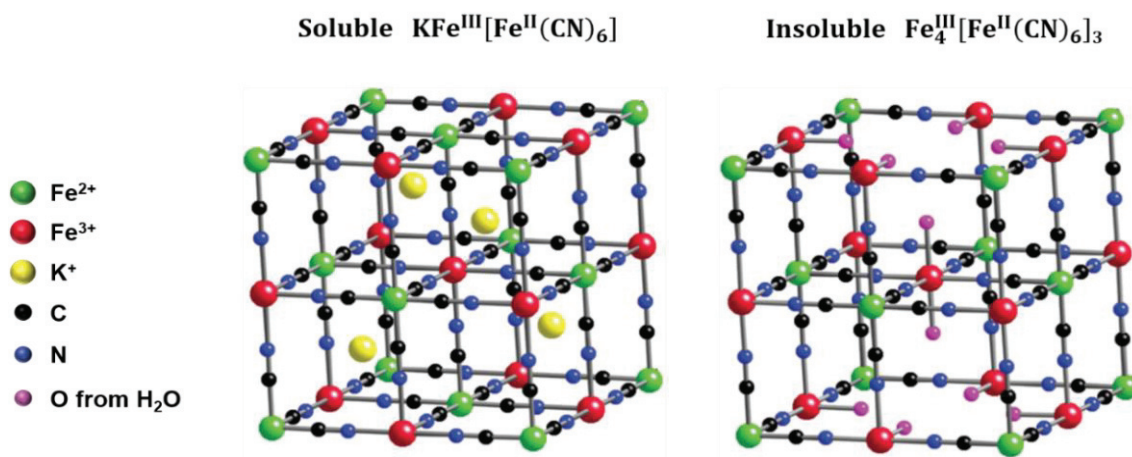
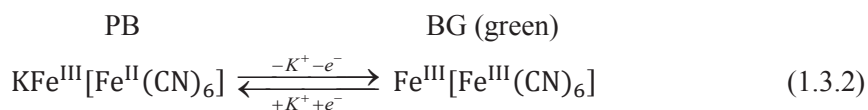
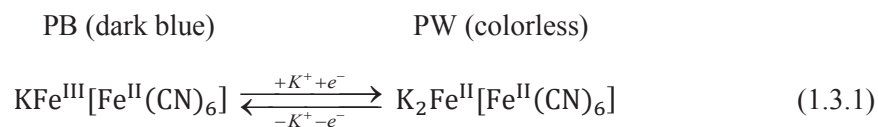


Figure 1-11. Unit cell crystal structures of soluble and insoluble PB. Water hydrogens are not shown in the insoluble structure for the sake of clarity (adapted from [158]).

Neff was the first to demonstrate PB's redox reaction. PB can form electroactive layers on the surface of an electrode after electrochemical or chemical deposition. In addition, PB allows for a stable and reversible K-insertion at room temperature in aqueous-based electrolytes.^[160] Redox reactions consist of the oxidation of low-spin iron under the formation of Berlin Green (BG) or Prussian Yellow (PY), and a reduction in high-spin iron under the formation of Prussian White (PW) or Berlin White, also known as Everitt's salt. Both compounds have cubic crystal structure similar to that of PB.^[160–163]



PBAs can be used as active material in grid-scale batteries, due to their high cycle lives and fast kinetics in aqueous electrolytes. They have face-centered cubic lattices with a nominal formula of $A_xM[M'(\text{CN})_6]_{1-y}\cdot\gamma y\cdot m\text{H}_2\text{O}$, where A is an alkaline metal cation, M and M' are transition-metal ions (e.g., M is Fe, Cu, Ni, Co, Ti, Zn, In, Ga, and Cd and M' is Fe, Ru, and Mn), γ represents a hexacyanometallate vacancy, and x , y , and m are the stoichiometric numbers. In addition, PBA lattices have large interstitial sites called 'A sites' with a diameter of 4.6 Å, and spacious channels with a diameter of 3.2 Å in the direction of (100). Owing to these sites and channels, the PBA structure has a high diffusion coefficient of 10^{-9} to 10^{-8} $\text{cm}^2 \text{s}^{-1}$ and higher ionic conductivity than other cathode materials.

PBAs, in addition to guest alkali cation, consist of water molecules in the interstitial sites of the framework. The unit cell dimension is 10.2 Å. In their structure, the high-spin (hs) Fe^{3+} ions and low-spin (ls) Fe^{2+} are coordinated with the nitrogen and carbon of the cyano-ligand, respectively. PBAs can be synthesized using different metal elements as starting reagents with various stoichiometric ratios, and contain different transition-metal ions.

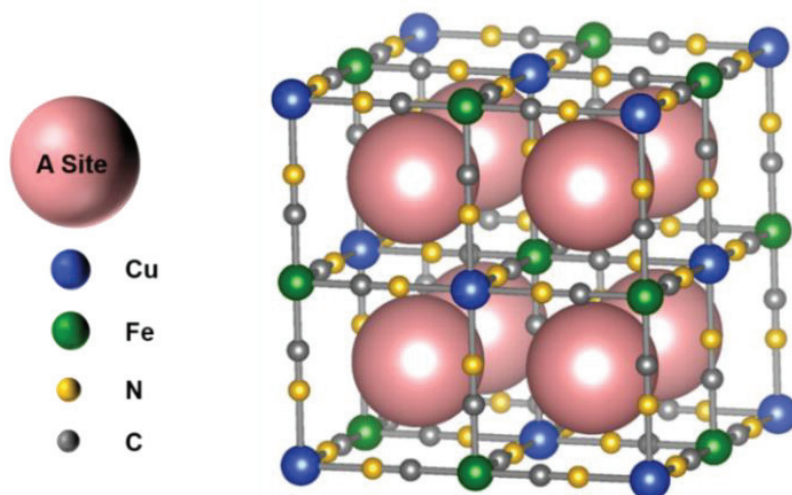


Figure 1-12. Framework of copper hexacyanoferrate (CuHCF).

Copper hexacyanoferrate (CuHCF), cobalt hexacyanoferrate (CoHCF), zinc hexacyanoferrate (dimorphic ZnHCF, cubic and rhombohedral), and nickel hexacyanoferrate (NiHCF) are some examples of nano-sized PBAs. PB/PBAs with nano-sized particles have a high surface area to

volume ratio that facilitates rapid electron and ion transfer to/from the material and leads to systems with high power densities. Fig. 1-12 shows the structure of CuHCF, as an example of the PBA family. In the CuHCF structure, Cu^{2+} is coordinated with the nitrogen and high-spin Fe^{3+} is coordinated with the carbon, since the ionic radii of Cu^{2+} (87 pm) is larger than Fe^{3+} (78.5 pm).^[164]

PBAs allow for the fast and facile reversible (de-)intercalation of monovalent (Li^+ , Na^+ , and K^+) and multivalent (Mg^{2+} , Ca^{2+} , Zn^{2+} , and Al^{3+}) ions to their open-channel structure.^[84,120,147,162,165] The rigid open framework (or zeolitic structure) of PBAs with large interstitial sites also allows for the fast and reversible (de-)intercalation of ions within the lattice structure. The diffused ions must be smaller than the pore size of the framework; this leads to an easy (de-)insertion within the structure and maintains lattice electroneutrality.^[84,147,162]

In PB/PBAs, octahedral transition-metal ions are linked through cyanide (CN) ligands. Each unit cell has eight subunits (interstitial sites/sub cells) that can accommodate neutral molecules and ions that have been charge-balanced by the transition ions. Within the PBA framework, two kinds of water molecules can be found: the zeolitic type that is situated in the octahedral center of the sub-cells and the coordinated type, which is chemically coordinated with the M ions. Zeolitic water can shield the charge of an inserted ion to facilitate its insertion while reducing the electrostatic forces between the host material and ion, as well as enhance the diffusion kinetics. In addition, thermogravimetric studies have illustrated that the water content depends on the temperature and humidity during synthesis.^[126,165,166]

Although PB and PBAs are used in electrochemical energy storage systems, they suffer from limited capacity, low coulombic efficiency, and poor cycle stability. These problems are the result of $[\text{Fe}(\text{CN})_6]$ vacancies and the interstitial water in the PBA structure. Large $[\text{Fe}(\text{CN})_6]$ vacancies can decrease the electronic conductivity of PBAs and cause lattice distortion upon cycling, leading to poor electrochemical performance. Furthermore, coordinated water molecules in the crystal structure can be decomposed or constrain ion (de-)insertion through the structure and cause PB structure collapse. Thus, the aforementioned reasons can lead to bad PBA performance.^[84,147]

As a metal hexacyanoferrate material, CuHCF is a low-toxicity, low-cost, and chemically stable compound with a wide range of pH values and different applications such as precursors for hydroxide films, electrochemical removal of cesium from aqueous radioactive wastes, sensors for heavy metals, and use as an active material in aqueous metal-ion batteries. This substance has the ability to present reversible redox reactions in different electrolytes.^[162,167–171]

Different studies have reported the (de-)intercalation of monovalent and multivalent ions in PB and PBAs. Cui et al.^[172,173] investigated the intercalation of divalent ions such as Mg^{2+} , Ca^{2+} , Sr^{2+} , and Ba^{2+} into a NiHCF framework. By inserting the aforementioned divalent ions, the cell

provided a reversible discharge capacity of 50 mAh g⁻¹ after 2000 cycles. Moreover, these researchers studied the insertion of trivalent ions (Y³⁺, Nd³⁺, Ce³⁺, La³⁺, and Sm³⁺) into CuHCF. The results imply that [Fe(CN)₆] vacancies, as well as coordinated waters, have a substantial effect on the insertion kinetics of multivalent ions. Another investigation was conducted on the insertion of sodium and potassium cations into a low-strain NiHCF. Energy efficiencies of 90% and 83% were obtained during potassium and sodium cycling, respectively, at a 41.7C current rate. Although almost no capacity was lost during the electrochemical cycling of the sodium for over 5000 cycles at a low current rate (8.3C), in potassium, the capacity was stable only for 1000 cycles and afterwards dropped 1.75% per 1000 cycles each.^[174]

In another study by this group, an aqueous battery in a solution of 1 M KNO₃ and 0.01 M HNO₃ (pH = 2) and employing copper hexacyanoferrate as a cathode material was introduced. This system showed an excellent cyclability at a high rate (17C) with capacity retentions of 94.6% and 83% after 10000 and 40000 cycles, respectively.^[175] In 2012, this group investigated the (de-)intercalation of monovalent cations (Na⁺, K⁺, Li⁺, and NH₄⁺) in CuHCF and NiHCF structures in different acidic aqueous solutions of 1 M LiNO₃, 1 M NaNO₃, 1 M KNO₃, and 0.5 M (NH₄)₂SO₄. The capacity retention levels of CuHCF in NH₄⁺, Na⁺, and Li⁺ ions after 500 cycles at an 8.3C rate were 91%, 77%, and 35%, respectively. Conversely, the cycled CuHCF in K⁺ reached a higher capacity retention of 99% after the same number of cycles. In the NiHCF case, no evidence of capacity loss in Na⁺ and K⁺ was reported, though in NH₄⁺, 12% of the capacity was lost, and a drastic loss occurred in Li⁺. This research demonstrates that CuHCF and NiHCF are both electrochemically active and serve as stable cathode material upon being cycled in sodium and potassium solutions, and they both perform with rapid kinetics and long cycle lives.^[176]

Later, an aqueous battery based on a CuHCF cathode and an activated carbon/polypyrrole (AC/PPy) hybrid anode was proposed. The electrochemical performance of this battery was examined upon (de-)intercalation of the potassium ions. This cell, with a voltage of 1.1 V, provided an energy efficiency of 79% at 50C and almost no capacity loss after 1000 cycles at a 10C rate with a 99.9% coulombic efficiency.^[177] Since studies have shown that CuHCF and NiHCF can offer excellent stability and cyclability at high current rates and long cycle lives with low capacity losses, a cathode material based on copper-nickel alloy hexacyanoferrate nanoparticles (CuNiHCF) was introduced. This new material permitted the reversible insertion of monovalent ions such as sodium and potassium. In 1 M KNO₃ and at a 500 mA g⁻¹ current density, CuNiHCF with a Cu/Ni ratio of 0.56:0.44 lost only 9% of its capacity over 2000 cycles, while in 1 M NaNO₃, no evidence of capacity loss was seen after the same number of cycles.^[178] The research by Mizuno et al.^[179] studied the (de-)intercalation of Mg²⁺ in CuHCF in a 1 M Mg(NO₃)₂ aqueous electrolyte. Hydrated Mg²⁺, due to its fast transport, showed a high rate

capability with a reversible specific capacity of 60 mAh g⁻¹. Table 1-5 includes an overview of some of the studied aqueous batteries based on PBAs and their average potentials.

Table 1-5. Overview of certain aqueous batteries based on PBAs (adapted from [108,140,142,174,175,180–184]).

Cathode	Anode	Average potential [V]	Electrolyte	Electrolyte pH
CuHCF	PB	0.5	0.05 M K ₂ SO ₄	4
CuHCF	CuHCF/PB	0.9	1 M KNO ₃	2
CuHCF	AC/PPy	1.1	1 M K ₂ PO ₄	1
CuHCF	Zn	1.73	0.02 M ZnSO ₄	6
NiHCF	NiHCF	0.59	1 M NaNO ₃	2
		0.69	1 M KNO ₃	
NiHCRu	NiHCF	0.5	0.1 M NaClO ₄	3
Na ₂ NiFe(CN) ₆	NaTi ₂ (PO ₄) ₃	1.27	1 M Na ₂ SO ₄	7
			0.5 M Na ₂ SO ₄	
ZnHCF	Zn	1.5	0.5 M K ₂ SO ₄	2
			1 M ZnSO ₄	
PB	PB	0.68	0.1 M K ₂ SO ₄	1

1.4. Aim of the Work

As already pointed out in the introduction, the main worldwide goal is reducing fossil-fuel consumption, CO₂ emission, and as a result preventing global warming. Renewable energy sources have the highest potential to provide the worldwide energy demand. However, it is important to develop new technologies to integrate them (wind, water, and solar power) into the grid-scale energy storage. Accordingly, a low-cost and scalable EES that provides long life cycle, high energy as well as power should be developed. As already mentioned in the previous sections, batteries among EESs have received a great attention as reliable energy storage systems for stationary applications. Aqueous metal-ion batteries among rechargeable batteries became a potential choice for grid-scale energy storage in the last decades.^[6,102–105]

Due to the promising results of Trócoli et al.^[142], in this Ph.D. work the focus was on studying and improving their proposed system in detail. They introduced a low-cost, environmentally friendly, nontoxic, aqueous zinc-ion battery based on PB derivatives. Copper hexacyanoferrate (CuHCF) was used as a cathode, zinc foil as an anode, and 20 mM ZnSO₄ as an aqueous electrolyte. It has been shown that standard CuHCF has reached 96.3% of its specific charge after 100 cycles with an average discharge potential of 1.73 V at a current rate of 1C.^[142] Although the system offered a consistent cyclability and rate capability, the standard CuHCF active material degraded upon cycling. Therefore, the main goals in this work are to understand the origin of the degradation of the proposed cathode material and to develop a strategy to prevent or postpone the aging of standard CuHCF active material.

For this purpose, one should study the properties and the effects of each battery compartment on the final battery performance. In order to do so, detailed investigations have been done regarding the cathode material, the electrolyte, and their respective impact on the electrochemical performance. The correlation between the electrochemical properties of standard CuHCF and the nature of the electrolyte as well as the applied current rates was also studied. Since in the work of Trócoli et al.^[142] it was shown that CuHCF undergoes a degradation upon cycling, it is necessary to focus on the nature of this phenomenon and to study whether this degradation mechanism leads to any structural or morphological changes within the CuHCF. This aim has been accomplished with the help of various analytical techniques, such as galvanostatic cycling with potential limitation (GCPL), X-ray diffraction (XRD), scanning electron microscopy (SEM), and energy dispersive X-ray spectroscopy (EDX). Finally, in order to solve the capacity and energy losses upon cycling and to achieve a battery with a long life cycle, new cathode materials have been developed. Optimization of the synthesis conditions enabled the development of new materials for rechargeable ZIBs for stationary applications.

2. Experimental

2.1. Materials and Instruments

Table 2-1. List of the materials and chemicals used in this thesis.

Materials / Chemicals	Supplier	Assay
1-Methyl-2-pyrrolidinone (NMP, C₅H₉NO)	Sigma-Aldrich	99.5%
Apiezon Wax W and Etch Resist	Apiezon	-
Bipolar plate	SGL Group	FR 10 with the thickness of 1.5 mm, PV15 with the thickness of 0.6 mm
Carbon black (C65)	Timcal	-
Carbon cloth	Fuel cell earth	-
Copper (II) nitrate trihydrate (Cu(NO₃)₂·3H₂O)	Sigma-Aldrich	98-103%
Deionized water	VWR Chemicals	GPR RECTAPUR [®] , Conductivity = Max. 1.5 μS cm ⁻¹
Graphite (SFG6)	Timcal	-
Manganese (II) chloride (MnCl₂)	Sigma-Aldrich	≥99%
Foam rubber (Moosgummi-Platten Sortiment)	VBS	Thickness: 1 mm
Nitric acid (HNO₃)	Sigma-Aldrich	≥65%
Polyvinylidene fluoride (PVDF)	Solvay	Solef S5130
Potassium hexacyanoferrate (II) trihydrate (K₄Fe(CN)₆·3H₂O)	Sigma-Aldrich	98.5-102%
Potassium hexacyanoferrate (III) (K₃Fe(CN)₆)	Sigma-Aldrich	≥99%
Potassium nitrate (KNO₃)	Sigma-Aldrich	≥99%
Polyoxymethylene plate (POM)	Friedrich Benien GmbH & Co. KG	Thickness: 2 mm
Separator	Whatman [®] GE Health Care	GF/A Glass microfiber filter
Sodium ferrocyanide decahydrate (Na₄Fe(CN)₆·10H₂O)	Sigma-Aldrich	≥99%
Toluene	VWR Chemicals	99.9%
Ultrapure water	Sartorius	Type 1, Conductivity = 0.055 μS cm ⁻¹
Zinc chloride (ZnCl₂)	Sigma-Aldrich	≥98%
Zinc fluoride (ZnF₂)	Sigma-Aldrich	99%
Zinc nitrate hexahydrate (Zn(NO₃)₂·6H₂O)	Sigma-Aldrich	≥99%
Zinc oxide (ZnO)	Honeywell Fluka	≥99%
Zinc perchlorate hexahydrate (Zn(ClO₄)₂·6H₂O)	Alfa Aesar	≥99.997%
Zinc powder	Sigma-Aldrich	-
Zinc sheet	Goodfellow	99.95%, Thickness: 0.125 mm
Zinc sulfate monohydrate (ZnSO₄·H₂O)	Sigma-Aldrich	≥99.9%

Table 2-2. List of devices used in this thesis.

Device	Supplier	Model
Balance	Sartorius	MSE224S-100-DI
Centrifuge	Hettich	Universal 320 R
Electronic contact thermometers	IKA	ETS-D5
Energy dispersive X-ray spectroscopy (EDX)	ThermoFisher Scientific	FEI Helios NanoLab TM 600 DualBeam TM
Inductively coupled plasma mass spectrometry (ICP-MS)	Wessling Laboratorien GmbH Analysis according to ISO 17294-2 ^A standard	
Magnet stirrer	IKA	RH digital
Optical stereo microscope	Zeiss	Stereomicroscope Stemi 508
Oven	ThermoFisher Scientific	Heratherm OMH 60
Peristaltic pump	Cole-Parmer	Ecoline VC MS/CA II
Potentiostat	Biologic	VMP3
Scanning electron microscopy (SEM)	ThermoFisher Scientific	FEI Helios NanoLab TM 600 DualBeam TM
Sonication bath	Elma-ultrasonic	Elmasonic P
Ultra-Turrax disperser	IKA	T 10 basic
X-ray diffractometer (XRD)	Rigaku	MiniFlex600

2.2. Synthesis of Materials

In this thesis, the aim is to optimize the structure of active material (CuHCF) to prolong the life cycle of ZIBs and gain a stable system with high energy and power. As mentioned, most of the PB/PBA structures are inherently disordered,^[165] which has a huge effect on the performance of a battery. Hence, it is important to obtain an active material with less defects in the lattice. For this purpose, one can act on the synthesis route and conditions.

2.2.1. Synthesis of Standard Copper Hexacyanoferrate (CuHCF)

The standard CuHCF has been synthesized by means of a co-precipitation method. Thus, 120 mL of 100 mM nitrate solution containing the copper transition-metal ($\text{Cu}(\text{NO}_3)_2 \cdot 3\text{H}_2\text{O}$) and 120 mL of 50 mM of $\text{K}_3\text{Fe}(\text{CN})_6$ were simultaneously added dropwise to 60 mL H_2O under vigorous stirring using a peristaltic pump at room temperature. The tubes that were used for dropping had an internal diameter of 0.64 mm, while a flow rate of 0.1 mL min^{-1} was used. The dropping time was controlled by the speed setting on the device (dropping speed = 10, 2h dropping). After finishing pumping the two solutions, the resulting suspension was stirred for 30 more minutes, followed by sonicating for 30 minutes. Afterwards, the suspension rested overnight. Thereafter, the precipitate was centrifuged and washed with a solution containing 1 M KNO_3 and 10 mM HNO_3 , followed by distilled water, and was dried at 60°C overnight. Finally, the fine powder was ground with a mortar and pestle.

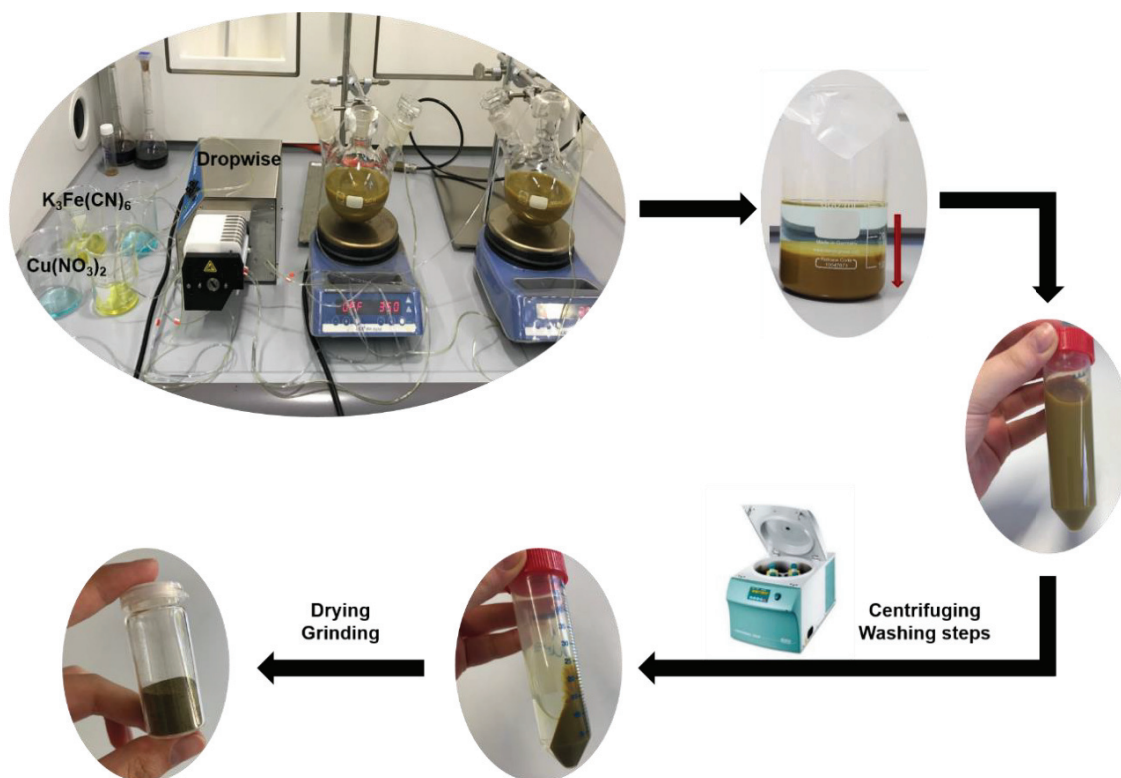


Figure 2-1. Standard CuHCF synthesis procedure.

2.2.2. Synthesis of Copper Zinc Hexacyanoferrate Mixtures (CuZnHCF)

For preparing copper zinc hexacyanoferrate mixtures, a mixture of $\text{Cu}(\text{NO}_3)_2 \cdot 3\text{H}_2\text{O}$ and $\text{Zn}(\text{NO}_3)_2 \cdot 6\text{H}_2\text{O}$ (120 mL) with the desired Cu:Zn ratio (85:15, 90:10, 93:7, 95:5, and 98:2) was prepared. The respective mixture and 50 mM of $\text{K}_3\text{Fe}(\text{CN})_6$ (120 mL) were simultaneously added dropwise to 60 mL H_2O under vigorous stirring at room temperature. The rest of the synthesis procedure was followed as in the previous section.

2.2.3. Synthesis of Copper Hexacyanoferrate Based on different Dropping Speeds

For these syntheses, all the parameters were kept the same, as explained in Section 2.2.1. Only the dropping speed was different: using fast speed (2 mL min^{-1} , dropping speed = 20, 1h dropping) and slow speed (0.5 mL min^{-1} , dropping speed = 5, 4h dropping).

2.2.4. Synthesis of Copper Hexacyanoferrate Based on different Temperatures

For these syntheses, all the parameters were kept the same as in Section 2.2.1, but the temperature was controlled ($2\text{-}3^\circ\text{C}$ or 70°C) during the whole synthesis time. In particular, for low temperature synthesis, the flask was placed in a bath of ice ($2\text{-}3^\circ\text{C}$) and for high

temperature, the flask was placed in a hot bath of water (70°C). Furthermore, the temperature was also controlled during the sonicating step.

2.2.5. Synthesis of Copper Hexacyanoferrate Based on different Atmospheres and Temperatures

As reported, the standard CuHCF synthesis was done at room temperature in air atmosphere. Moreover, different syntheses were done by controlling the oxygen (performed under argon or in air) combined with different temperatures. In particular, argon gas was purged for 30 minutes in 60 mL H₂O having a sealed round bottom three-neck flask at different temperatures (room temperature, 2-3°C, and 70°C). After 30 minutes, solutions of Cu(NO₃)₂·3H₂O and K₃Fe(CN)₆ were simultaneously added dropwise to the water under vigorous stirring, and the argon line was fixed above the suspension level. After finishing the process, the suspension was stirred for a further 30 minutes. The temperature of the suspension was controlled during the entire synthesis. Afterwards, the suspension was transferred in a beaker and sealed by parafilm. Argon was purged for 10 more minutes into the beaker. After that, the suspension was sonicated in an ultrasonic bath. The temperature of the sonication bath was also controlled based on the dropping temperature (room temperature, 2-3°C, or 70°C). The suspension was allowed to sit overnight, and the precipitate was centrifuged and washed with a solution containing 1 M KNO₃ and 10 mM HNO₃, followed by distilled water, and was dried at 60°C.

2.2.6. Synthesis of ZnHCF

The ZnHCF synthesis was conducted via the co-precipitation method. Thus, 100 mL of 20 mM ZnCl₂ and 100 mL of 20 mM K₃Fe(CN)₆ were simultaneously added in a dropwise fashion to 200 mL H₂O under vigorous stirring and using a peristaltic pump at reaction temperature of 100°C. The dropping time was controlled by the speed setting on the device (dropping speed = 10, 2h dropping). After finishing pumping the two solutions, the resulting suspension was stirred for 30 more minutes, followed by sonication for 30 minutes, and then was allowed to sit overnight. Thereafter, the precipitate was centrifuged and washed with distilled water, and dried at 60°C overnight. Finally, a fine powder was ground with a mortar and pestle. An X-ray diffraction pattern was taken of this powder, while the diffraction reflections were similar to those reported in Joint Committee on Powder Diffraction Standards (JCPDS 33-1061) and in reference ^[185].

2.3. Electrode Fabrication

To prepare electrodes for electrochemical tests, a slurry containing 80 wt% active material, 2 wt% graphite (SFG6) for increasing the conductivity within the layers, 9 wt% amorphous

carbon (C65) as a conductive additive to decrease the intra-particle resistance, and 9 wt% polyvinylidene fluoride (PVDF) binder solution in N-methylpyrrolidone (NMP, 25 mg mL⁻¹) was mixed via an Ultra-Turrax disperser. The slurry was stirred for 30 min (10 min stirring followed by 10 min resting) at 4000 rpm. The polymeric binder was used to improve the mechanical stability of the electrode.^[161] Afterwards, the slurry was painted on a carbon cloth current collector with a mass loading of at least 10 mg per cm².

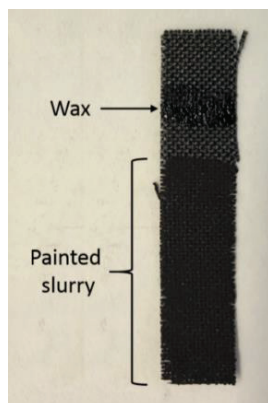


Figure 2-2. Coated carbon cloth current collector with active material.

The coated electrodes were dried in the oven at 60°C. Upon drying, the NMP evaporated from the electrodes and only the C65 conductive layer, SFG6, and PVDF remained. The evaporation leads to a decrease in contact resistance between the current collector and the active material. Thereafter, the capillarity of the carbon cloth was blocked by painting wax (dissolved in Toluene) above the active material paste. Finally, the electrodes were dried at 60°C.

In order to perform a power test a zinc counter electrode was fabricated. To prepare zinc electrodes, a slurry containing 70 wt% of active material, 20 wt% amorphous carbon (C65), and 10 wt% polyvinylidene fluoride (PVDF) binder solution in N-methylpyrrolidone (NMP, 25 mg mL⁻¹) was mixed via an Ultra-Turrax disperser. The slurry was stirred for 30 min (10 min stirring followed by 10 min resting) at 4000 rpm. Afterwards, the slurry was painted on a carbon cloth current collector with an area of 1.13 cm². The coated electrodes were dried in the oven at 60°C.

2.4. Electrochemical Cells

The electrochemical measurements were performed in a flooded three-electrode cell (Fig. 2-3a). In this conical cell, the desired synthesized copper hexacyanoferrate was used as working electrode (WE), zinc foil as counter electrode (CE), Ag/AgCl (in 3 M KCl) as reference electrode (RE), and a selected zinc-salt solution as an aqueous electrolyte.

For the power test measurements, the experiments were done in a modified version of a differential electrochemical mass spectrometry-electrochemical impedance spectroscopy

(DEMS-EIS) cell^[186] (Fig. 2-3b). The experiment was done in a three-electrode cell configuration while zinc electrodes were used as RE and CE, and synthesized CuZnHCF mixture with a Cu:Zn ratio of 93:7 as WE.

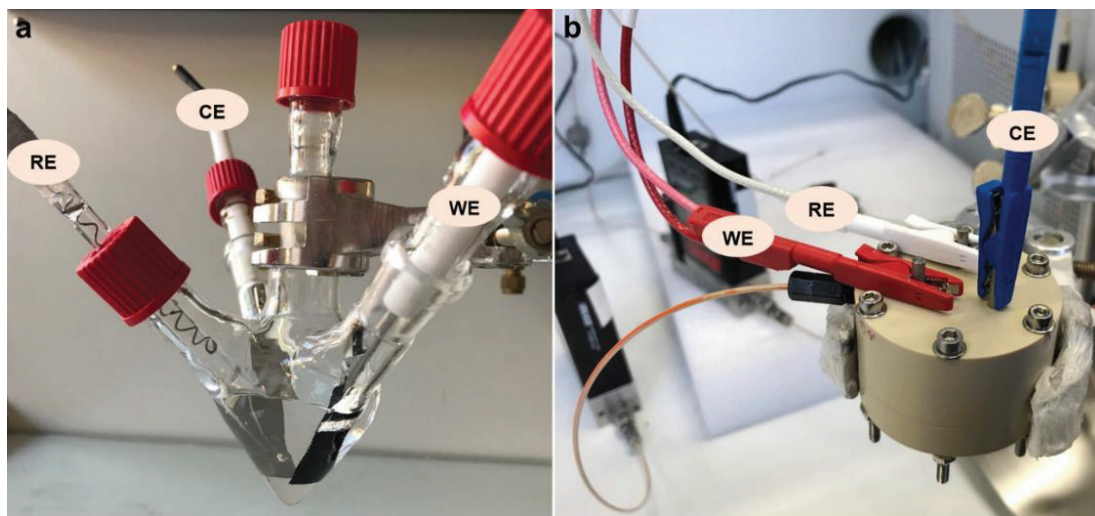


Figure 2-3. (a) Flooded three-electrode cell and (b) DEMS-EIS cell utilized for electrochemical measurements.

2.5. Characterization Techniques

In this work, different techniques are employed to study the performance of a ZIB. With the help of these techniques, information about the active material, electrodes, and electrolytes can be obtained.

2.5.1. Galvanostatic Cycling with Potential Limitation

The galvanostatic cycling with potential limitation (GCPL) technique is a method to characterize the electrochemical systems. In this technique, a constant current is applied while the change in potential is monitored within a given potential range. With the help of this technique, parameters such as specific capacity, thermodynamic equilibrium potential, kinetic overpotential, coulombic and energy efficiency, and power after cycling an electrochemical system, can be obtained. All of the electrochemical measurements in this study are performed using a BioLogic VMP3 instrument.

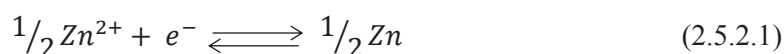
2.5.2. Thermodynamic and Kinetic Analysis

In order to understand the performance of a rechargeable battery, it is important to study the electrochemical reactions of the system from both the thermodynamic and kinetic perspectives. The mechanism of a battery is based on the conversion of chemical and electrical energies. The main electrochemical reactions are oxidation and the reduction reaction between each electrode and ion-conductive electrolyte. While discharging, the reduction and oxidation reactions occur

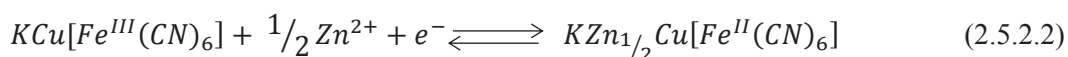
at the positive and negative electrodes, respectively. Upon charging (oxidation), electrons flow from the cathode to the anode side through an external circuit while converting the electrical energy to chemical energy. Due to this reaction, the charge passes through an electrolyte/separator/membrane toward the cathode electrode. The opposite process occurs upon discharge.^[187,188]

The schematic configuration of the studied aqueous ZIB in this thesis is illustrated in Fig. 2-4, and the reactions at the positive and negative electrodes, as well as the total reaction, are as follows:

At the negative electrode:



At the positive electrode:



Total reaction:

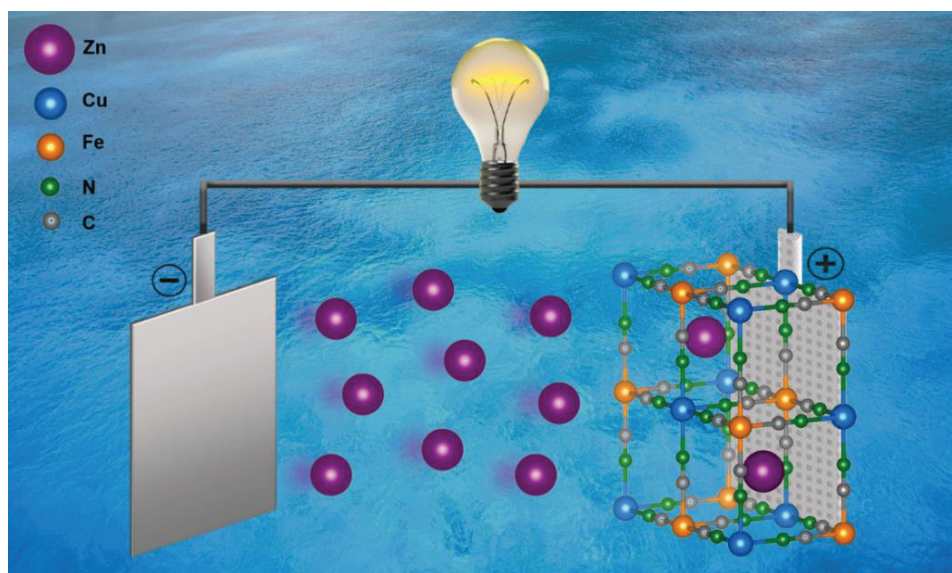
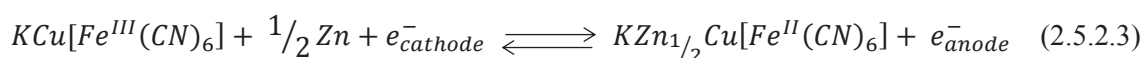


Figure 2-4. Schematic illustration of an aqueous ZIB in a zinc-based electrolyte (standard CuHCF as the positive electrode and zinc foil as the negative electrode).

The electrochemical reaction is a process in which the electrons transfer in an electron ion conductor and charged species through an ion conductor. When the zinc ions

completely/partially lose their solvation shell and move from the bulk solution towards the electrode/electrolyte interface, negatively charged species accumulate on the other side of the interface and lead to form an electrical double layer (EDL). Upon an electrochemical reaction, the redox species pass through the EDL and the interfacial potential becomes the limiting parameter, controlling the direction as well as the rate of the charge transfer. In the other words, the rate of the electron transfer at the interface depends on the potential. This is called a faradaic process. Conversely, at some potential range no charge transfer reaction happens because conditions are thermodynamically and kinetically unfavorable. In this case, specific interactions such as adsorption and desorption can take place; these are called non-faradaic processes.^[187,188] The total cell voltage is composed of two half-reactions (Eqs. 2.5.2.4 and 2.5.2.5) and is equal to the difference between the potentials at the positive and negative electrodes.

$$\Delta E = E_{cathode} - E_{anode} \quad (2.5.2.4)$$

To determine the cell potential, one can study the electrochemical thermodynamics under equilibrium conditions in a reversible system. In a galvanic cell, the Gibbs free energy (i.e., the total energy available from a reaction) is associated with the maximum electrical energy and is equal to:

$$\Delta G = -nF\Delta E_{eq} \quad (2.5.2.5)$$

where n is the number of transferred electrons per mole of reactants, F is the Faraday constant ($F = 96485 \text{ C mol}^{-1}$), and ΔE_{eq} is the equilibrium voltage (open-circuit voltage, zero current). Additionally, there is a relationship between the standard electrode voltage and standard free Gibbs energy.

$$\Delta G^\circ = -nF\Delta E_{eq}^\circ = -nF(E_{eq,cathode}^\circ - E_{eq,anode}^\circ) \quad (2.5.2.6)$$

where ΔE_{eq}° is the standard equilibrium voltage, G° is the standard free Gibbs energy, and E_{eq}° is the standard electrode potential at equilibrium. From these equations one can derive the Nernst equation, which illustrates the relationship between the equilibrium electrode voltage, standard electrode voltage, and bulk concentration of the species. The Nernst equation for the studied ZIB, based on Equation 2.5.2.3, can be written as follows:

$$\Delta E_{eq} = \Delta E^\circ - \frac{RT}{F} \ln \left(\frac{a_{KZn_{1/2}Cu[Fe^{II}(CN)_6]}}{a_{KCu[Fe^{III}(CN)_6]}} \right) \quad (2.5.2.7)$$

where a is the activity, R is the gas constant ($R = 8.314 \text{ J K}^{-1} \text{ mol}^{-1}$), and T is absolute temperature (K). However, a real electrochemical system never stays in equilibrium conditions; the potential deviates from the equilibrium value. This behavior is called polarization and causes an overpotential in the system. The overvoltage, a loss due to current flow, can be calculated as the difference between the equilibrium voltage and cell voltage.

$$\eta = \Delta E - \Delta E_{eq} \quad (2.5.2.8)$$

This phenomenon can be generated from different electrochemical steps such as electron or ion transfers at the interface and mass transportation between the bulk of the electrolytes and the electrode's surface. The step with the slowest rate is the rate-determining step; it controls the kinetics of the reaction. The total overvoltage of the system can be written as the contribution of the following overpotentials:

$$\eta = \eta_o + \eta_{ct} + \eta_{mt} + \eta_{nu} + \eta_{bu} + \eta_{cr} \quad (2.5.2.9)$$

where η_o is the ohmic overpotential, η_{ct} is the charge transfer overpotential, η_{mt} is the mass transport overpotential, η_{nu} is the nucleation overpotential, η_{bu} is the bubble overpotential, and η_{cr} is the crystallization overpotential. The ohmic overpotential depends on the resistances of the different components of the cell such as electrodes, electrolytes, separators, current collectors, and cable contacts. The ohmic overpotential relationship is as follows. Here, i is the applied current and R is the ohmic internal resistance.^[187,188]

$$\eta_o = iR_{int} \quad (2.5.2.10)$$

In addition, during an electrochemical reaction, charged species (either electrons or ions) are transferred through the interface. The electrochemical reaction follows the activated complex theory or transition state theory, which explains that the reaction proceeds through a transition state that has higher energy than either the reactants or products. The kinetics of an electrochemical reaction can be explained by the Butler-Volmer equation, which determines the relationship between the current and charge transfer overpotential. In Equation 2.5.2.11, i_0 is the exchange current density, α is the charge transfer coefficient (i.e., the measure of the symmetry of the energy barrier), F is the Faraday constant ($F = 96485 \text{ C mol}^{-1}$), R is the gas constant ($R = 8.314 \text{ J K}^{-1} \text{ mol}^{-1}$), and T is absolute temperature (K).^[187,188]

$$i = i_0 \left[\exp\left(\frac{(1-\alpha)F}{RT} \eta_{ct}\right) - \exp\left(-\frac{\alpha F}{RT} \eta_{ct}\right) \right] \quad (2.5.2.11)$$

Mass transport overpotential or concentration overpotential (η_{mt}) occurs due to the concentration gradient between the reactants or products at the surface and the bulk of the electrolyte. Mass transport can happen in different forms such as diffusion, migration, and convection.

Since this research studied the effects of the different concentrations of zinc solutions on the stability of a battery, it is important to understand the relationship between ionic conductivity and the nature of the electrolyte. The molar conductivity of a solution (Λ_m) depends on the number of ions present in the solution and can be calculated by the following equation, where ν_+ and ν_- are the number of cations and anions per formula, respectively, and λ_+ and λ_- are the molar conductivities for the cations and anions, respectively.^[187,189]

$$\Lambda_m = \nu_+ \lambda_+ + \nu_- \lambda_- \quad (2.5.2.12)$$

Table 2-3. Molar conductivities of certain employed ions at 25°C in this study.^[189]

Ion	λ $10^{-4} [\text{m}^2 \text{S mol}^{-1}]$
Li^+	38.66
$\frac{1}{2} \text{Zn}^{2+}$	52.8
$\frac{1}{2} \text{SO}_4^{2-}$	80

Based on Equation 2.5.2.12 and Table 2-3, the ionic conductivity for an aqueous ZnSO_4 solution is:

$$\Lambda_{m,\text{ZnSO}_4} = (2 \times 52.8)10^{-4} + (2 \times 80)10^{-4} = 0.0266 \text{ m}^2\text{S mol}^{-1}$$

Based on this value, the ionic conductivities for 20 mM and 100 mM ZnSO_4 are 0.532 S m^{-1} and 2.66 S m^{-1} , respectively. It is interesting as well to calculate and compare the ionic conductivity of an aqueous Li_2SO_4 solution with ZnSO_4 , since the LIBs attracted great attention during last decades. The ionic conductivity for an aqueous Li_2SO_4 is:

$$\Lambda_{m,\text{Li}_2\text{SO}_4} = (2 \times 38.66)10^{-4} + (2 \times 80)10^{-4} = 0.0237 \text{ m}^2\text{S mol}^{-1}$$

The transport number is the fraction of the current that has been transferred by each species present in the solution^[187] and it is equal to:

$$t_i = \frac{I_i}{I_{total}} = \frac{\lambda_i \nu_i}{\Lambda_m} \quad (2.5.2.13)$$

Based on Eq. 2.5.2.13, the transport numbers of zinc and lithium ions are as following:

$$t_{Zn^{2+}} = \frac{\nu_{Zn^{2+}} \lambda_{Zn^{2+}}}{\Lambda_m} = \frac{105.6 \times 10^{-4}}{0.0266} = 0.3969$$

$$t_{Li^+} = \frac{\nu_{Li^+} \lambda_{Li^+}}{\Lambda_m} = \frac{2 \times 38.66 \times 10^{-4}}{0.0237} = 0.3262$$

In a solution, the sum of the transport numbers is always equal to 1.^[190]

$$\sum t_+ + \sum t_- = 1 \quad (2.5.2.14)$$

One can also calculate the ionic mobility of an ion with the following equation:

$$u_i = \frac{\lambda_i}{(z_i F)^2} \quad (2.5.2.15)$$

where u_i is the mobility defined as the velocity attained of an ion in a unit's electric field strength, λ_i is the ionic molar conductivity, z_i is the ionic charge, and F is the Faraday constant ($F = 96485 \text{ C mol}^{-1}$). From Eq. 2.5.2.15, the ionic mobility for zinc and lithium ions can be calculated as following:

$$u_{Zn^{2+}} = \frac{\lambda_{Zn^{2+}}}{(z_{Zn^{2+}} F)^2} = \frac{(2 \times 52.8)10^{-4}}{(2 \times 96485)^2} = 2.8358 \times 10^{-13} \text{ m}^2 \text{ mol s}^{-1} \text{ V}^{-1} \text{ c}^{-1}$$

$$u_{Li^+} = \frac{\lambda_{Li^+}}{(z_{Li^+} F)^2} = \frac{38.66 \times 10^{-4}}{(96485)^2} = 4.1528 \times 10^{-13} \text{ m}^2 \text{ mol s}^{-1} \text{ V}^{-1} \text{ c}^{-1}$$

Based on the calculated values it can be mentioned that although the transport number of zinc ion is higher than of lithium, its mobility is lower. As it is reported in Table 2-4, the hydrated ionic radii of zinc ion is bigger than lithium ion. It is also known that the mobility has an inverse relation with the size of the hydrated ion. From the above calculations this fact was confirmed. From these information it can be noted that lithium ions in an aqueous sulfate solution move faster than zinc ions, while the fraction of the total current carried by lithium ion is smaller than zinc ions. Therefore, the conductivity of the zinc ions in $ZnSO_4$ is higher than lithium ions in Li_2SO_4 . It is worth mentioning that for the intercalation mechanism, the potential of the intercalation and electrochemical performance of the guest ion to the host structure depend on

the ionic radius of the inserted ion, its charge number, the solvation degree, and the concentration of the electrolyte. The cations with higher ionic radii intercalate at higher potentials and lead to higher energy densities.^[120] Monovalent cations (de-)intercalate into the PBA structure without complete dehydration. They offer a fast insertion with high charge/discharge rate capabilities. Due to their partial hydration, the interfacial ions transfer and the ionic diffusion accelerates.^[179] Moreover, small monovalent cations intercalate more easily than those that are multivalent. Since multivalent cations are strong Lewis acids, they need larger levels of desolvation energy (i.e., the energy required to detach the cation from its solvent solvation shell) at the interface of the electrode. Due to their strong coulombic repulsion, they show slow diffusive transport.^[110,191,192] However, most of the divalent cations have a smaller size and higher charge than those that are monovalent. The desolvation energy of these cations increases with the charge density of the metal cation, slows down the diffusion of the ions, and lowers the insertion potential.^[132] It is important to note that the intercalation potential for each cation depends on its ionic radii (the higher the ionic radii, the more energy is needed for the intercalation process, leading to a potential shift to higher values).

In ZIBs, since the ‘A sites’ of PBAs (or host material) are larger than the (de-)inserted ions, a small lattice strain occurs upon cycling.^[94] Zinc ions with higher hydrated ionic radii have higher charge densities and degrees of solvation. When the ratio of the charge to the radius of the ion is higher, the coordination of the water molecules to that ion is stronger. Table 2-4 compares the ionic radii, hydrated ionic radii, and standard electrode potentials of important intercalated cations.

Table 2-4. Comparison of standard redox potentials, densities, ionic and hydrated ionic radii for monovalent and multivalent cations.^[120]

Cation	Ionic radius [Å]	Hydrated ionic radius [Å]	Density [g cm⁻³]	Standard electrode potential [V vs. SHE]
Li⁺	0.76	3.82	0.534	-3.05
Na⁺	1.02	3.58	0.968	-2.71
K⁺	1.38	3.31	0.862	-2.93
Mg²⁺	0.72	4.28	1.74	-2.36
Ca²⁺	0.99	4.12	1.54	-2.87
Zn²⁺	0.74	4.30	7.14	-0.76

Different parameters must be calculated to analyze the performance of a battery. The first is the capacity, which is the amount of charge a battery can deliver. This value depends on the mass of the active material in the system. The theoretical capacity (C_t) of an electrochemical cell is the amount of electric charge stored in the cell; it is expressed by Equation 2.5.2.16, where n is the number of reactive electrons per formula unit, F is the Faraday constant, and $M.W.$ is the molar weight of the material:

$$C_t = \frac{nF}{3.6 \times M.W.} \quad (2.5.2.16)$$

As an example, the theoretical capacity of CuHCF in a ZIB with a molar mass of $310.316 \text{ g mol}^{-1}$ is equal to 86.38 mAh g^{-1} . The theoretical capacity of a hexacyanoferrate cathode is always higher than the practical capacity. This deviation is due to the synthesis method (co-precipitation), which delivers a powder with 30% vacancy. The presence of the zeolitic water contents can also vary with the temperature and humidity at the time of synthesis. In addition, only the C-coordinated ions are electrochemically active; therefore, only half of the ‘A sites’ are available to contribute to the total capacity.^[94] When a battery is cycled, the capacity retention (or cycle aging) of the battery can be calculated as:

$$\frac{\text{discharge capacity of the last cycle}}{\text{maximum discharge capacity}} \quad (2.5.2.17)$$

The calendar aging of a battery is the irreversible proportion of capacity loss during storage. Another factor is the coulombic efficiency of the system. Coulombic efficiency is defined as a ratio of the total charges put into the battery at the discharge to the charge at oxidation. Energy density in a battery is the amount of energy stored in the system by volume or the weight of active material (Wh L^{-1} or Wh kg^{-1}). This value can be obtained from the potential profiles by calculating the integral of the discharge curves (i.e., the intercalation of the ions). The energy retention can be also calculated similar to the capacity retention in which instead of capacity the value obtained as energy is placed. The life cycle of a battery is the ability of an electrochemical cell to deliver a capacity higher than a certain limit (80% of the nominal capacity).

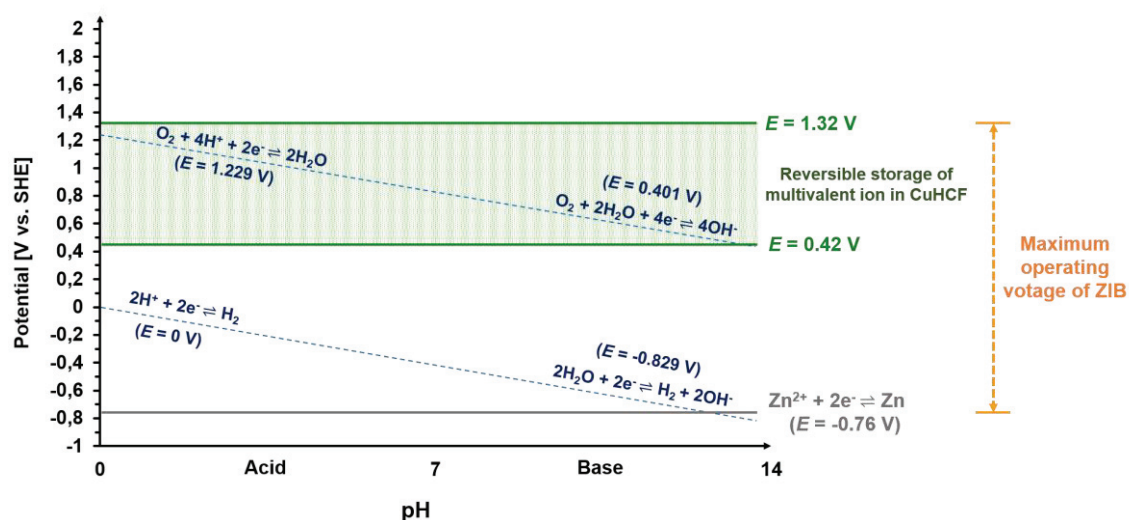


Figure 2-5. The potential range of a ZIB based on standard CuHCF cathode and Zn anode vs. SHE by considering thermodynamic stability window of water.

Fig. 2-5 shows the potential range of cathodic and anodic reactions in a ZIB based on a standard CuHCF cathode and zinc anode. From the standard reduction potentials table^[189], zinc ions have a standard reduction potential of -0.76 V vs. SHE. Standard CuHCF is usually cycled in an aqueous zinc solution between 0.2 and 1.1 V and Ag/AgCl (3 M KCl); therefore, its potential range vs. SHE is 0.42 to 1.32 V. Since this battery is aqueous-based, it is also important to consider the stability window of water.

2.5.3. X-Ray Diffraction

Information about the crystal structure of the materials and thin films, determining the orientation of a single crystal or grain, the chemical composition, and their physical properties can be obtained with the X-ray diffraction (XRD) analytical technique. In this technique, an X-ray beam is generated towards the sample and cleavage faces of the crystals reflect the X-ray beams at certain angles of incidence (θ). This relation can be determined with Bragg's law ($n\lambda = 2d \sin\theta$), where d is the distance between the atomic layers in a crystal, λ is the wavelength of the incident X-ray beam, and n is an integer.^[193] The XRD patterns that are shown in this study were recorded on a Rigaku MiniFlex 600 X-ray diffractometer with a step width of 0.02° , using Cu $K\alpha$ radiation ($\lambda = 1.5406 \text{ \AA}$). The intensity of all of the XRD data have been normalized between 0 and 1 with the following algorithm based on OriginLab 2015 graphing and analysis software. The normalized value (Y') is equal to $\frac{Y - Y_{min}}{Y_{max} - Y_{min}}$. It is important to note that interpreting XRD data with Rietveld refinement is a well-known technique in crystallography. With this technique, it is possible to analyze the whole diffraction pattern and to obtain information about the ratio of crystalline to amorphous phases, lattice parameters, space group, atomic positions, atomic site occupancies, and unit cell dimensions. To employ this technique, a well-known crystal structure (i.e., a structure model from the database) and chemical composition is needed. Unfortunately, it was not possible in the current research to find an exact model compatible with the synthesized samples. Although close models have been used, the fittings were not satisfying since there are several phases with nearly identical crystal structure but different chemical compositions. Furthermore, for identifying the new phase(s) no compatible JCPDS data have been found. Another issue was the presence of an amorphous carbon cloth current collector. The amorphous part of carbon hides major reflections of the new phase and only the minor reflections have been visible. Hence, identification of new phase(s) was more difficult or even not possible.

2.5.4. Scanning Electron Microscopy and Energy Dispersive X-Ray Spectroscopy

The scanning electron microscopy (SEM) was used to study the microstructure morphology of the synthesized active materials and their particle size. In principle, a focused beam of high energy electrons is used to generate signals at the surface of the specimens. From the interaction between the specimen and electrons, an image containing the information about the sample morphology, chemical composition, and crystal structure is obtained. Additionally, SEM enables the analysis of selected point locations on the sample. With this approach, the chemical composition (coupled with Energy Dispersive X-Ray Spectroscopy (EDX)) of the sample can be determined. In this study, several samples were characterized with this technique after cycling. All the SEM images were taken with a FEI Helios NanoLab™ 600 DualBeam™ apparatus.^[194]

2.5.5. Inductively Coupled Plasma Mass Spectrometry

In this thesis, an inductive coupled plasma mass spectrometry (ICP-MS) as an analytical technique has been utilized. ICP-MS is a powerful method for qualitative and quantitative trace element detection. With this technique, one can detect the concentration of metals and some non-metals even in small amounts. In this work the concentration of the released ions in the electrolyte after cycling was determined with the help of this technique. For this purpose, the selected electrolytes have been collected after cycling and tested with ICP-MS. Wessling Laboratorien GmbH has analyzed the desired samples.

3. Investigation of the Effects of the Electrolyte and Current Rate on the Aging of Standard CuHCF

In 2015, Trócoli and La Mantia proposed an environmentally friendly and nontoxic, aqueous zinc-ion battery based on a CuHCF cathode and a zinc foil anode in 20 mM ZnSO₄ (pH = 6) electrolyte. This battery offered a capacity retention of 96.3% after 100 cycles at a 1C current rate with an average discharge potential of 1.73 V. In addition, the power delivered by this system was comparable to an organic LIBs based on Li₄Ti₅O₁₂ and LiFePO₄. Although this system provided good cyclability and rate capabilities after 100 cycles (as shown in Fig. 3-1), the active material tended to degrade and the shapes of the potential profiles changed according to the number of cycles.^[142]

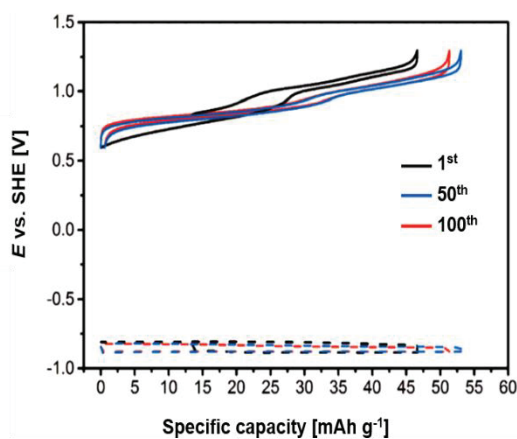


Figure 3-1. Potential profiles of CuHCF (solid line) and a Zn film (dashed line) at a rate of 1C in 20 mM ZnSO₄ (extracted from [142]).

Due to its high rate capabilities, this system has the potential to be employed in grid-scale energy storage. Since the main goal of this research was to develop an ideal reversible aqueous zinc-ion battery that is reliable, affordable, safe, and efficient in terms of both energy and power, the focus of this work was on further investigation of the system (i.e., the cathode material) introduced by Trócoli and La Mantia.^[142]

Several important aspects of aqueous zinc-ion batteries based on standard CuHCF were examined. In this chapter, the results which have been published in 2016^[195] and 2018^[196] are explained. The effects of the nature and concentration of the electrolyte as well as the current rate on the performance of the standard CuHCF were analyzed. As the standard CuHCF degrades upon cycling, further investigations on the reasons of aging were studied. Furthermore, with the help of GCPL and XRD techniques, an attempt was made to study whether the degradation mechanism leads to phase changes. At last based on the obtained results, a phase transformation mechanism was proposed to explain the nature of the new formed phase(s).

3.1. Effects of the Nature of the Electrolyte

Here, the effects of the nature of the electrolyte on the performance of standard CuHCF are described. For this research, standard CuHCF was cycled at a 1C current rate in 20 mM of different zinc salt solutions, such as ZnSO₄, Zn(ClO₄)₂, ZnF₂, and Zn(NO₃)₂.

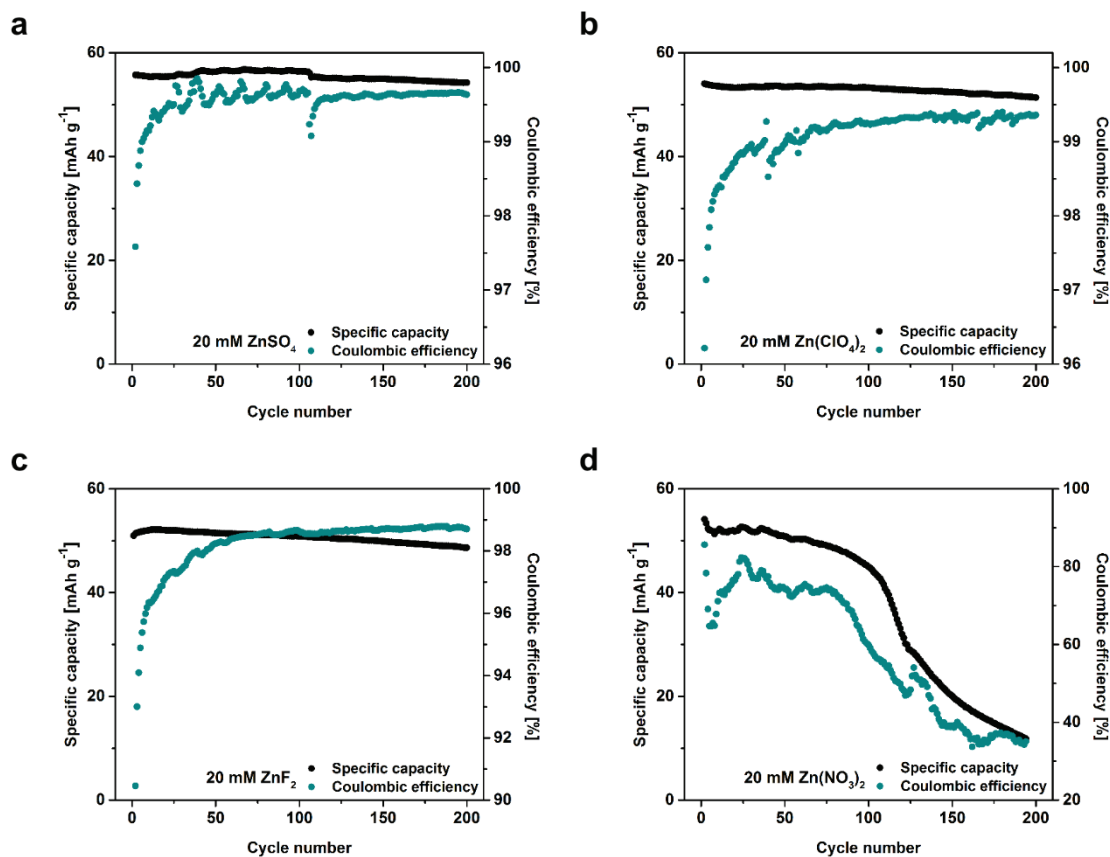


Figure 3-2. Long-term cycling of standard CuHCF at a rate of 1C in 20 mM of (a) ZnSO₄, (b) Zn(ClO₄)₂, (c) ZnF₂, and (d) Zn(NO₃)₂ aqueous solutions.

The capacity retention and coulombic efficiency of each solution after 200 cycles was extracted from Fig. 3-2 and reported in Table 3-1. As it is clear from Fig. 3-2 and Table 3-1, standard CuHCF loses capacity upon cycling, but the capacity loss depends on the electrolyte's nature (i.e., the different anion).

Table 3-1. The percentages of capacity retentions and coulombic efficiencies of standard CuHCF after 200 cycles in various 20 mM zinc salt solutions.

At 200 th cycle	Solutions			
	20 mM ZnSO ₄	20 mM Zn(ClO ₄) ₂	20 mM ZnF ₂	20 mM Zn(NO ₃) ₂
Capacity retention	95.52%	95.07%	93.3%	21.89%
Coulombic efficiency	99.64%	99.36%	98.7%	35.05%

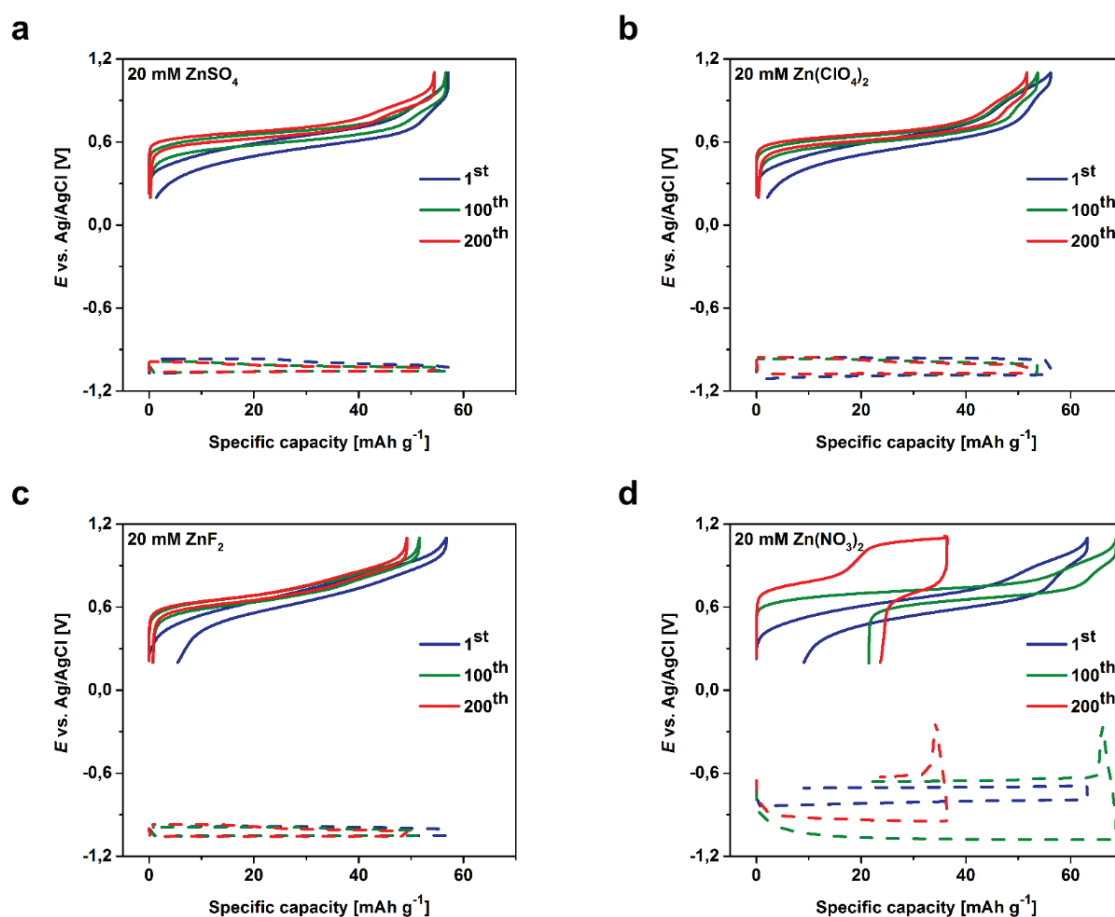


Figure 3-3. Potential profiles of standard CuHCF (solid line) and Zn foil (dashed line) at a rate of 1C in 20 mM of (a) ZnSO_4 , (b) $\text{Zn}(\text{ClO}_4)_2$, (c) ZnF_2 , and (d) $\text{Zn}(\text{NO}_3)_2$ aqueous solutions.

Fig. 3-3 shows the potential profiles of standard CuHCF (solid lines) and zinc foil (dashed lines) at the 1st, 100th, and 200th cycles for each electrolyte. GCPL was performed in the potential range of 0.2 to 1.1 V vs. Ag/AgCl (3 M KCl) to avoid any hydrogen or oxygen evolution reactions interfering with the capacity and performance of the system. Upon discharge, zinc ions were intercalated through the standard CuHCF structure (A sites) and low-spin Fe^{3+} was converted to low-spin Fe^{2+} (Equation 2.5.2.2).

As it is clear from Fig. 3-3, the shapes of the potential profiles for all of the solutions were almost the same, except for $\text{Zn}(\text{NO}_3)_2$. The mid-composition reaction potential (i.e., the potential at which the intercalation of Zn^{2+} takes place) for all of the electrolytes at the first cycle was approximately 0.6 V vs. Ag/AgCl (3M KCl), and upon cycling was raised to higher values. This shift in the $\text{Zn}(\text{NO}_3)_2$ was greater than in the other solutions and led to a higher overpotential. The weak performance of standard CuHCF in $\text{Zn}(\text{NO}_3)_2$ can be explained by the NO_3^- ion. The nitrate ion is the most oxidized form of nitrogen in the environment; it destroys zinc anodes due to an oxidation reaction and possibly the formation of dendritic zinc, followed by hydrogen evolution, formation of ZnO or $\text{Zn}(\text{OH})_2$, and an increase in the local pH.

In addition, it was observed that the overpotential of the zinc anode in $\text{Zn}(\text{ClO}_4)_2$ was higher than in ZnSO_4 and ZnF_2 , while the ClO_4^- ion was also an oxidizing agent but not as strong as the nitrates. Therefore, due to the contact between the zinc anode and ClO_4^- ion, it is possible that a thin layer of ZnO formed which led to a slowdown in the reaction rate. In the other solutions, after the cycling attributable to the zinc deposition, a compact layer formed on the zinc anode as was mentioned in references [134,142].

Zhang et al.^[140] studied the cycling of ZnHCF in three different solutions (Na_2SO_4 , K_2SO_4 , and ZnSO_4). These researchers discovered that the ZnHCF was dissociated in Na_2SO_4 and K_2SO_4 electrolytes, while in ZnSO_4 it was stable. Therefore, it was important to check for the existence of cyanide complexes in the cycled solutions. For this purpose, each cycled solution was tested with FeCl_3 ; no evidence of precipitation was detected. In addition, to investigate the dissolution of standard CuHCF, a sample from each solution after cycling was extracted and the concentration of copper and iron were analyzed by ICP-MS. Based on the obtained data, the variations in the concentrations of copper (ΔC_{Cu}) and iron (ΔC_{Fe}) before and after cycling were calculated. These values were normalized by the mass of the active material and reported in Table 3-2.

Table 3-2. Variation of concentration of iron (ΔC_{Fe}), copper (ΔC_{Cu}), and specific charge fading (ΔQ) after 200 cycles in 20 mM of different electrolytes, as calculated by ICP-MS analysis.

Elements	Solutions			
	20 mM ZnSO_4	20 mM $\text{Zn}(\text{ClO}_4)_2$	20 mM ZnF_2	20 mM $\text{Zn}(\text{NO}_3)_2$
ΔC_{Fe} ($\mu\text{mol g}^{-1}$)	4.6	~0	2.0	1.5
ΔC_{Cu} ($\mu\text{mol g}^{-1}$)	2.7	1.0	0.9	0.3
ΔQ (mAh g^{-1})	0.20	0.02	0.08	0.05

From the ΔC_{Cu} and ΔC_{Fe} values, it is possible to calculate the specific charge fading for ΔQ ($\Delta Q = \frac{(\Delta C_{\text{Cu}} + \Delta C_{\text{Fe}})F}{3600}$, where F is the Faraday constant = 96485 C mol^{-1}). From this information, it can be concluded that the reversible specific charge fading was not due to the dissolution of standard CuHCF, but rather can be attributed to the degradation mechanism. However, since the ΔQ values were below the actual charge fading, the aging mechanism could not exclusively be due to the removal of copper or iron from the standard CuHCF. In Section 3.4 a mechanism for the degradation of standard CuHCF upon cycling is proposed.

3.2. Effects of the Electrolyte Concentration

Since the main goal of this work was to develop an ideal aqueous zinc-ion battery with high power efficiency that is compatible with stationary applications, a higher concentration of electrolyte was needed. When the concentration is higher, the conductivity of the solution will

increase. The conductivity of a solution depends on the number of charge carriers (concentration of zinc ions), the mobility of the charge carriers and their charge. Accordingly, based on the Butler-Volmer equation (Eq. 2.5.2.11), by increasing the electrolyte concentration the reaction rate increases. In addition, the diffusion of zinc ions gets faster. Therefore, in this section the effects of the electrolyte concentration on the performance of the standard CuHCF are described. Among four different zinc salt solutions used in the previous section, only ZnSO_4 and $\text{Zn}(\text{ClO}_4)_2$ were chosen for further experiments. The reason for this was the low solubility of the ZnF_2 (86 mM) and instability of $\text{Zn}(\text{NO}_3)_2$. Fig. 3-4 shows the long-term cycling and coulombic efficiencies of standard CuHCF in 100 mM of ZnSO_4 and 100 mM of $\text{Zn}(\text{ClO}_4)_2$.

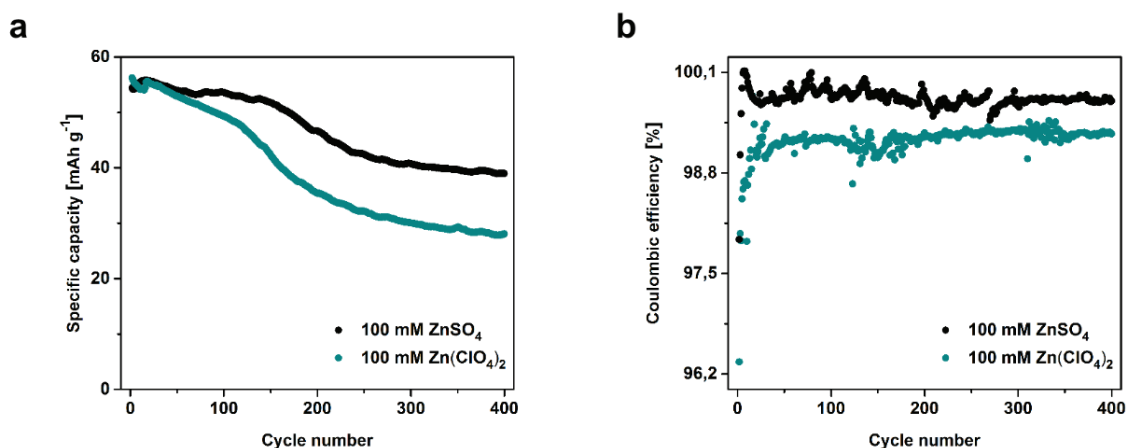


Figure 3-4. (a) Long-term cycling and (b) coulombic efficiencies of standard CuHCF at a rate of 1C in 100 mM ZnSO_4 and 100 mM $\text{Zn}(\text{ClO}_4)_2$, respectively.

Table 3-3. The percentages of capacity retentions and coulombic efficiencies of standard CuHCF after 400 cycles in 100 mM ZnSO_4 and 100 mM $\text{Zn}(\text{ClO}_4)_2$.

At 400 th cycle	Solutions	
	100 mM ZnSO_4	100 mM $\text{Zn}(\text{ClO}_4)_2$
Capacity retention	69.86%	49.95%
Coulombic efficiency	99.73%	99.30%

Table 3-3 notes the capacity retentions and coulombic efficiencies of standard CuHCF in each solution after 400 cycles. From these data, two important pieces of information were obtained. First, the capacity fading upon cycling at higher concentrations was strongly affected by the nature of the anion. In other words, the capacity loss in the presence of ClO_4^- was higher than for SO_4^{2-} . Second, by comparing the capacity fading levels at the 200th cycle in 100 mM ZnSO_4 (83.6%) and 100 mM $\text{Zn}(\text{ClO}_4)_2$ (62.96%) with the data reported in Table 3-1, it is clear that the higher concentration had a negative effect on standard CuHCF stability, and the aging of the active material occurred at a faster rate. In addition, from the potential profiles in both solutions (Figs. 3-5 (a-b)), it is clear that the shapes of the profiles changed due to cycling and the mid-composition potential for the (de-)intercalation processing increased.

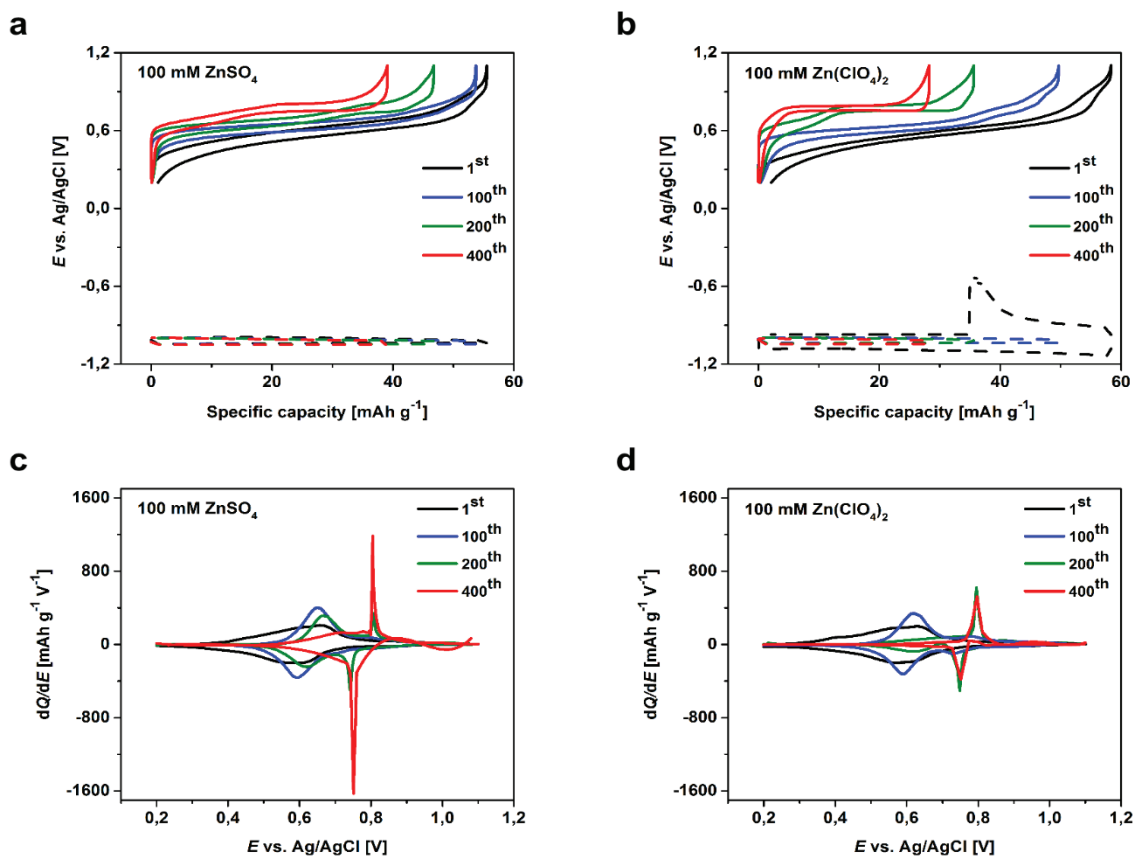


Figure 3-5. (a,b) Potential profiles of standard CuHCF (solid line) and Zn foil (dashed line) at a rate of 1C in 100 mM ZnSO₄ and Zn(ClO₄)₂, respectively. (c,d) Differential specific charge profiles at different numbers of cycles for standard CuHCF measured at a rate of 1C in 100 mM ZnSO₄ and Zn(ClO₄)₂, respectively.

In all cycling measurements, there is always a potential hysteresis between the charge and discharge curves. As expected based on the second law of thermodynamics, it was observed that the charge potential was always higher than the discharge potential. This hysteresis could have been due to the polarization arising from the resistance of the electrode materials. When the polarization occurred, the discharge potential shifted down to lower values than the open circuit voltage. In order to compensate that, it raised the charge potential. Another reason for the higher charge potential at charging rather than discharging was the internal resistance drop (i.e., the resistance of the electrolyte, electrode materials, and connectors), which is called the IR drop. When an IR drop occurs, more energy is consumed. This leads to a loss of battery efficiency. The driving force for the electrochemical phase transformation during the insertion of ions into the electrodes is known as overpotential. It is worth mentioning that since the system was not at the ideal state, the charge and discharge curves are not symmetrical and the corresponding energy changes in the discharge curve are different from those in the charging step. When the electrode (standard CuHCF) charges, more energy is consumed to promote the ions and electrons to lower energy states, but while discharging the ions are intercalated into the structure

of the material, which is followed by a decrease in energy. This difference in energy explains the potential gap between the charge and discharge curves in all of the potential profiles.^[197–199]

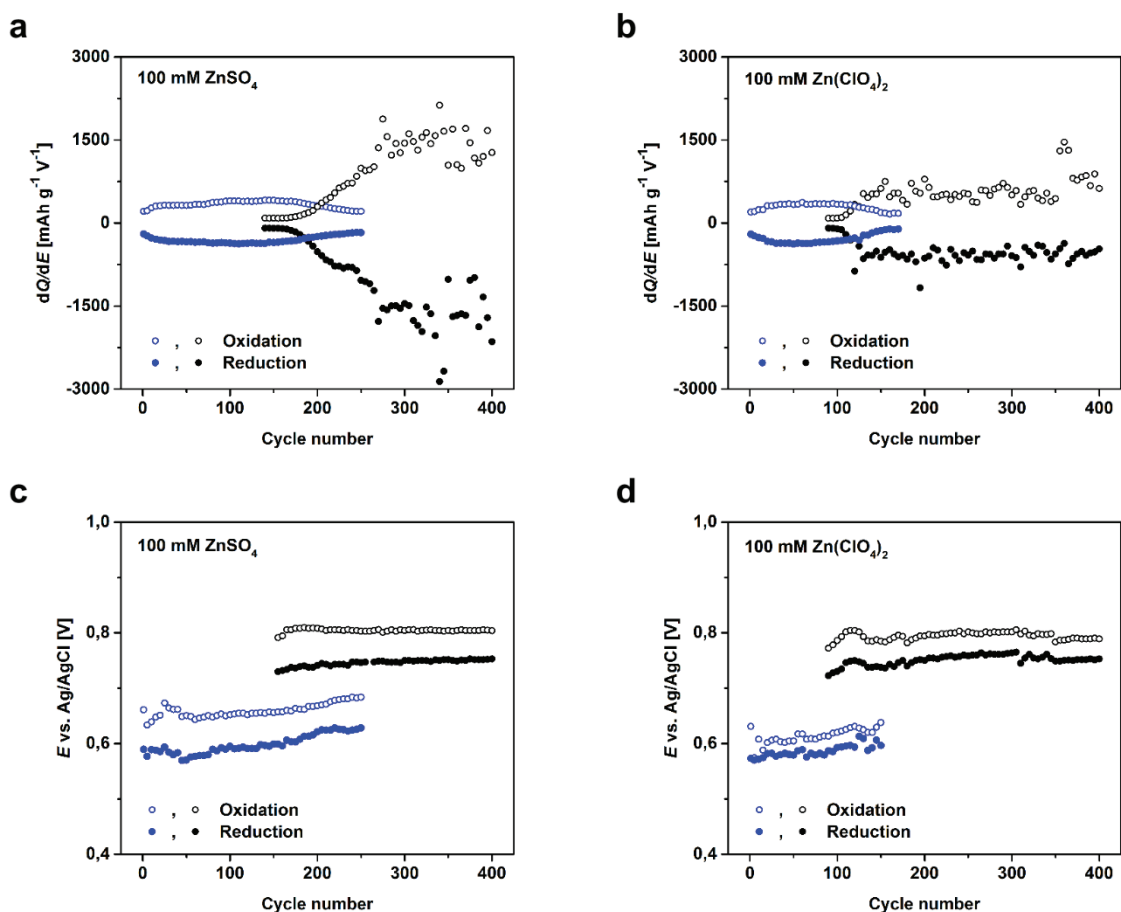


Figure 3-6. The intensities and potential locations of the cathodic and anodic peaks of the differential specific charge profiles of standard CuHCF in (a,c) 100 mM ZnSO₄ and (b,d) 100 mM Zn(ClO₄)₂, respectively. The blue circles indicate the first redox couple and the black circles show the second one.

From the shapes of the potential profiles, one can determine the phase reaction (i.e., single or two-phase^[200]). The original CuHCF is (de-)intercalate zinc ions through a single-phase mechanism. However, Figs. 3-5 (a-b) show a two-step plateau, along with an increase in the average cell voltage at higher number of cycles. For better insight into the (de-)intercalation process, Figs. 3-5 (c-d) illustrate the differential specific charge profiles (dQ/dE vs. E) for both electrolytes at different numbers of cycles. In both solutions, the shapes of the differential charge profiles changed upon cycling. At each cycle stage, two oxidation and two reduction peaks were observed. The first set of redox peaks were broad, typical for single-phase insertion, and the intensity tended to decrease during cycling. These redox peaks were located around 0.62 V vs. Ag/AgCl (3 M KCl). The second set of redox peaks were sharp, which is typical for two-phase insertion, and the intensity rose with the number of cycles. The location of the second set of redox peaks was around 0.75 V vs. Ag/AgCl (3 M KCl).^[200] In order to study the thermodynamic and kinetic aspects of the system in each solution, the anodic and cathodic peak

intensity locations, as well as the potential locations, have been plotted separately vs. the number of cycles (Fig. 3-6).

From the graphs, it is clear that in 100 mM ZnSO₄, the second set of redox peaks appeared around the 180th cycle and in 100 mM Zn(ClO₄)₂ the second set appeared earlier, around the 100th cycle. These results agree with the change in potential profile shape at the same number of cycles (Figs. 3-5 (a-b)). It is worth mentioning that this phase transformation was not observed in 20 mM solutions up to 200 cycles (Fig. 3-3).

Furthermore, from Figs. 3-6 (a-b) it can be concluded that the intensity of the second set of redox peaks depended on the nature of the anion, and upon cycling, it tended towards a constant value. This value for the 100 mM ZnSO₄ was around 1400 mAh g⁻¹ V⁻¹ and for 100 mM Zn(ClO₄)₂, it was around 500 mAh g⁻¹ V⁻¹. For the first set of redox peaks, the peak intensities for both solutions began at the same value (200 mAh g⁻¹ V⁻¹), but upon cycling disappeared. The potential locations for both set of redox peaks in both solutions did not change significantly upon cycling.

To investigate the thermodynamic and kinetic effects of the (de-)intercalation process on the peak potential location, the thermodynamic equilibrium potential (E_t) and kinetic overpotential (η) were calculated and plotted vs. the number of cycles, as was done in Madej et al.^[201] work. These values were obtained as follows:

$$E_t = \frac{E_a + E_c}{2} \quad (3.2.1)$$

$$\eta = \frac{E_a - E_c}{2} \quad (3.2.2)$$

where E_a and E_c are the anodic and cathodic potentials, respectively.

As shown in Figs. 3-7 (a-b), the value for E_t for the second set of redox peaks was almost constant and independent from the nature of the anion, but this value for the first set of redox peaks drifted towards the anodic potentials upon cycling. From Figs. 3-7 (c-d), it can be seen that η in the presence of sulfates was around 22 to 40 mV and changed slightly upon cycling in both redox reactions, while in the presence of perchlorates the range was 10 to 22 mV. The first set of redox reactions showed lower values than the second. From these parameters, it can be concluded that the two redox processes were inversely related to one another. In other words, the appearance and an increase in the intensity of the second redox peaks occurred in parallel with the decrease and disappearance of the first redox couple. This behavior, as well as the increase in potential in both experiments (Fig. 3-5), can be explained by the standard CuHCF structural change, changes in the chemical composition of the CuHCF, and electrostatic repulsion^[108] within the CuHCF structure upon cycling.

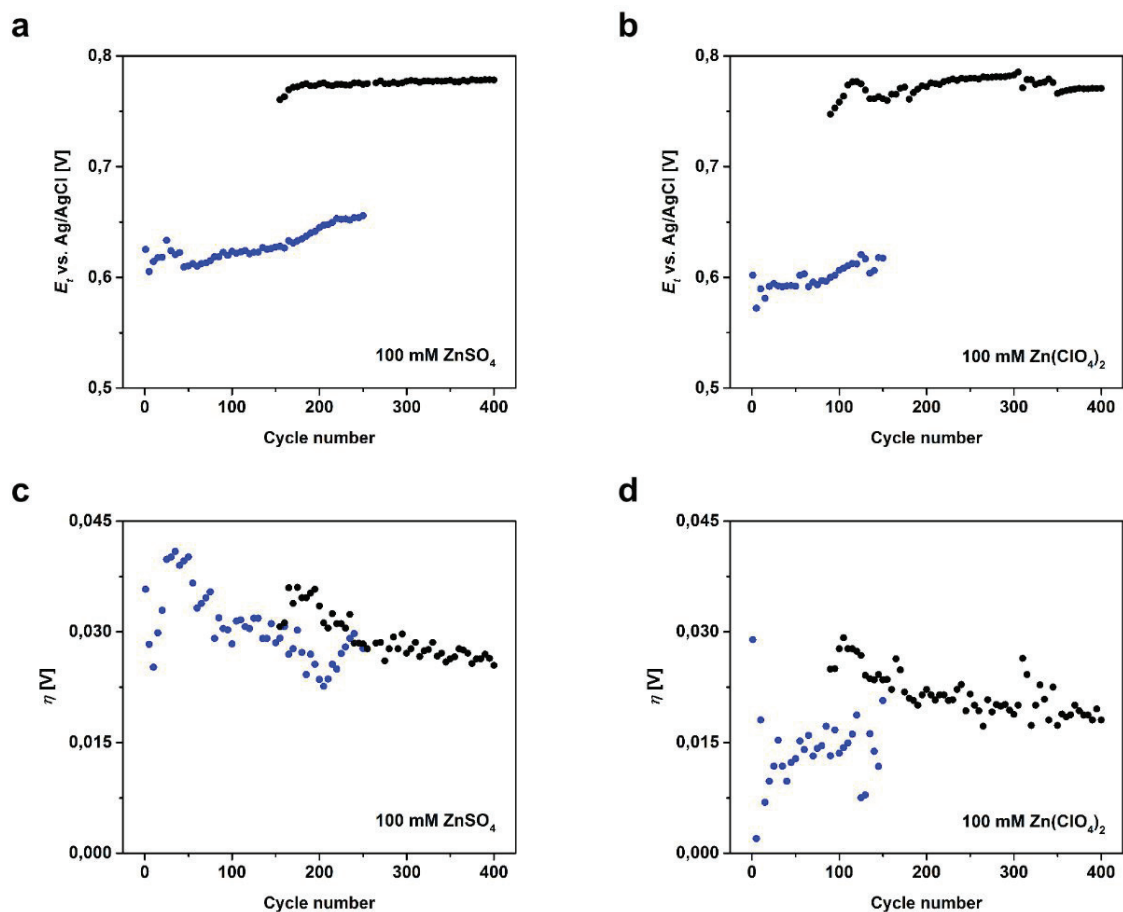


Figure 3-7. (a,b) Thermodynamic and (c,d) kinetic effects observed for standard CuHCF in 100 mM ZnSO₄ and 100 mM Zn(ClO₄)₂, respectively. The blue circles indicate the first redox couple and the black circles identify the second one.

In addition to the obtained results, to determine the formation of the second phase, an XRD measurement for the samples cycled in 20 mM and 100 mM of Zn(ClO₄)₂ was carried out after 500 cycles. In Fig. 3-8, the XRD pattern for the standard CuHCF electrode without cycling is shown in green. The XRD patterns for the cycled standard CuHCF electrodes are shown in black and blue, and the XRD pattern for the as-prepared ZnHCF electrode based on the synthesis procedure and explained in the experiment section (Section 2.2.6) is shown in orange. The detailed information about the as-synthesized standard CuHCF and its crystal structure is discussed in Chapter 4.

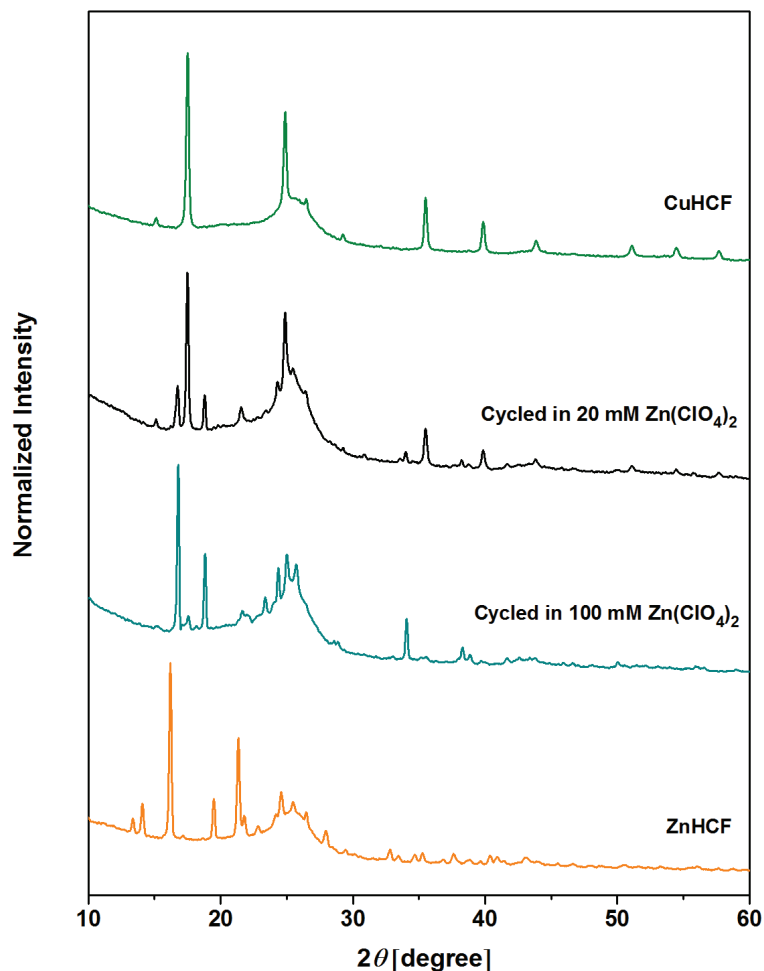


Figure 3-8. X-ray diffraction patterns of uncycled standard CuHCF electrode, cycled standard CuHCF electrodes in 20 mM and 100 mM Zn(ClO₄)₂, and uncycled as-prepared ZnHCF electrode.

At the first glance, an amorphous hump around 25° 2θ is evident for all of the samples. To clarify the origin of the amorphous phase, XRD measurements were run for carbon black (i.e., C65 added during electrode fabrication; Section 2.3) and a carbon cloth current collector. By comparing Figs. 3-8 and 3-9, it is clear that the amorphous humps around 25° and 44° 2θ corresponds with the presence of the C65 and carbon cloth. The reflection at around 32° 2θ which is clearer in Fig. 3-9 is due to the silicon wafer substrate which has been placed on the sample holder.

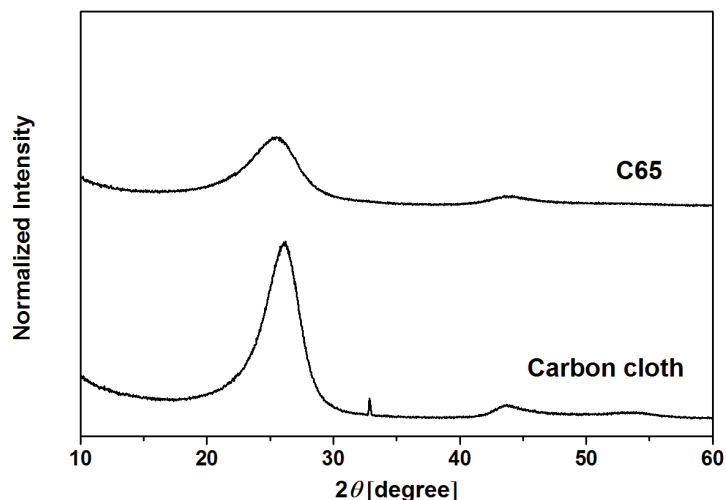


Figure 3-9. X-ray diffraction patterns for the conductive additive carbon black (C65) and carbon cloth current collector.

In comparison to the uncycled CuHCF, new reflections were found in the XRD patterns of the cycled one. These newly observed reflections can be attributed to the formation of additional phase(s). However, the pattern of the sample cycled in 20 mM $\text{Zn}(\text{ClO}_4)_2$ is close to the uncycled standard CuHCF (in green). This result agrees with its potential profile (Fig. 3-10).

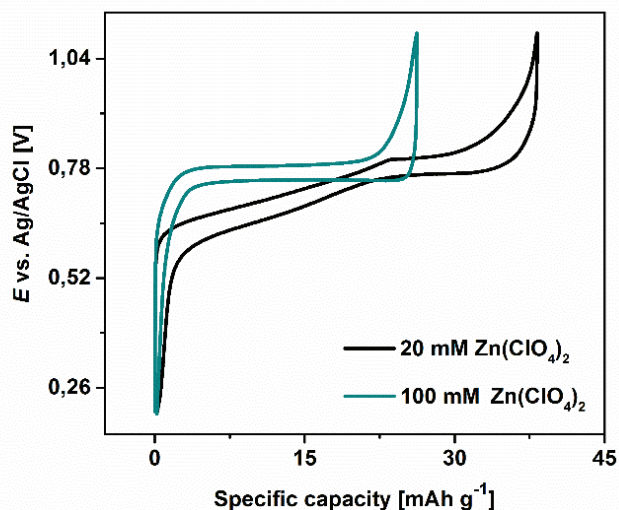


Figure 3-10. Potential profiles of standard CuHCF in 20 mM and 100 mM $\text{Zn}(\text{ClO}_4)_2$ at the 500th cycle.

From Fig. 3-10, two-step plateaus were observed for the sample cycled in 20 mM $\text{Zn}(\text{ClO}_4)_2$; the one occurring at approximately half charge can be attributed to the original material (i.e., standard CuHCF) and the latter corresponds with the second redox reaction. Conversely, the potential profile for the sample cycled in 100 mM $\text{Zn}(\text{ClO}_4)_2$ only showed a flat plateau at a higher potential, suggesting that upon cycling standard CuHCF has been converted and new phase or phases formed. This was confirmed by the XRD pattern (in blue). The XRD results of this sample in addition to some of the main standard CuHCF reflections revealed new

reflections. These new reflections are matching with some of ZnHCF reflections, although the whole pattern did not match completely. Therefore, it can be suggested that the conversion of standard CuHCF to ZnHCF happened partially. In Section 3.4, a probable mechanism of the phase transformation, the appearance of new reflections in the XRD diffractograms of the cycled samples, and the effects of the phase transformation on the aging of the standard CuHCF are discussed in detail.

3.3. Effects of the Current Rate

Since in stationary applications the fast and efficient response to fluctuations in renewable energy sources is a matter of importance, it is critical to have batteries with a high rate capability. Therefore, in this section the influence of the current rate on the performance of standard CuHCF is described. Standard CuHCF was cycled at 5C (full oxidation/reduction in 12 minutes) and 10C (full oxidation/reduction in 6 minutes) current rates in a 100 mM ZnSO₄ solution. Fig. 3-11 indicates the long-term cycling and coulombic efficiencies of the standard CuHCF for 1000 cycles at both current rates.

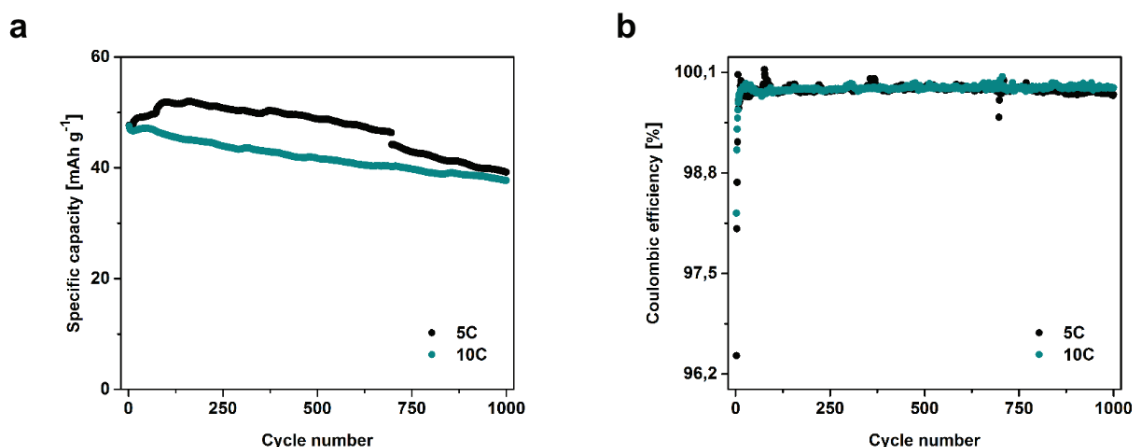


Figure 3-11. (a) Long-term cycling and (b) coulombic efficiencies of standard CuHCF at 5C and 10C current rates in 100 mM ZnSO₄.

Table 3-4 indicates the extracted capacity retentions and coulombic efficiencies of standard CuHCF after 1000 cycles at each current rate. Although the coulombic efficiency levels changed slightly, the degradation of the standard CuHCF occurred faster at a lower current rate (5C).

Table 3-4. The percentages of capacity retentions and coulombic efficiencies of standard CuHCF after 1000 cycles in 100 mM ZnSO₄, at the 5C and 10C current rates.

Current rate	Capacity retention	Coulombic efficiency
5C	75.42%	99.81%
10C	79.36%	99.9%

Fig. 3-12 illustrates the potential profiles of standard CuHCF cycled at 5C and 10C, as well as their differential specific charge profiles. The phase change was observed around the 600th cycle at the 5C current rate and weakly after the 800th cycle at 10C, while at a 1C current rate this phenomenon occurred around the 200th cycle (Figs. 3-5 (a,c)) in the same solution. These results suggest that the phase transformation could happen when the active material is in a determined state of charge, or it could have a completely chemical nature. Furthermore, when the current rate was higher the capacity loss was less than the lower rate and the standard CuHCF could be cycled for a longer period of time.

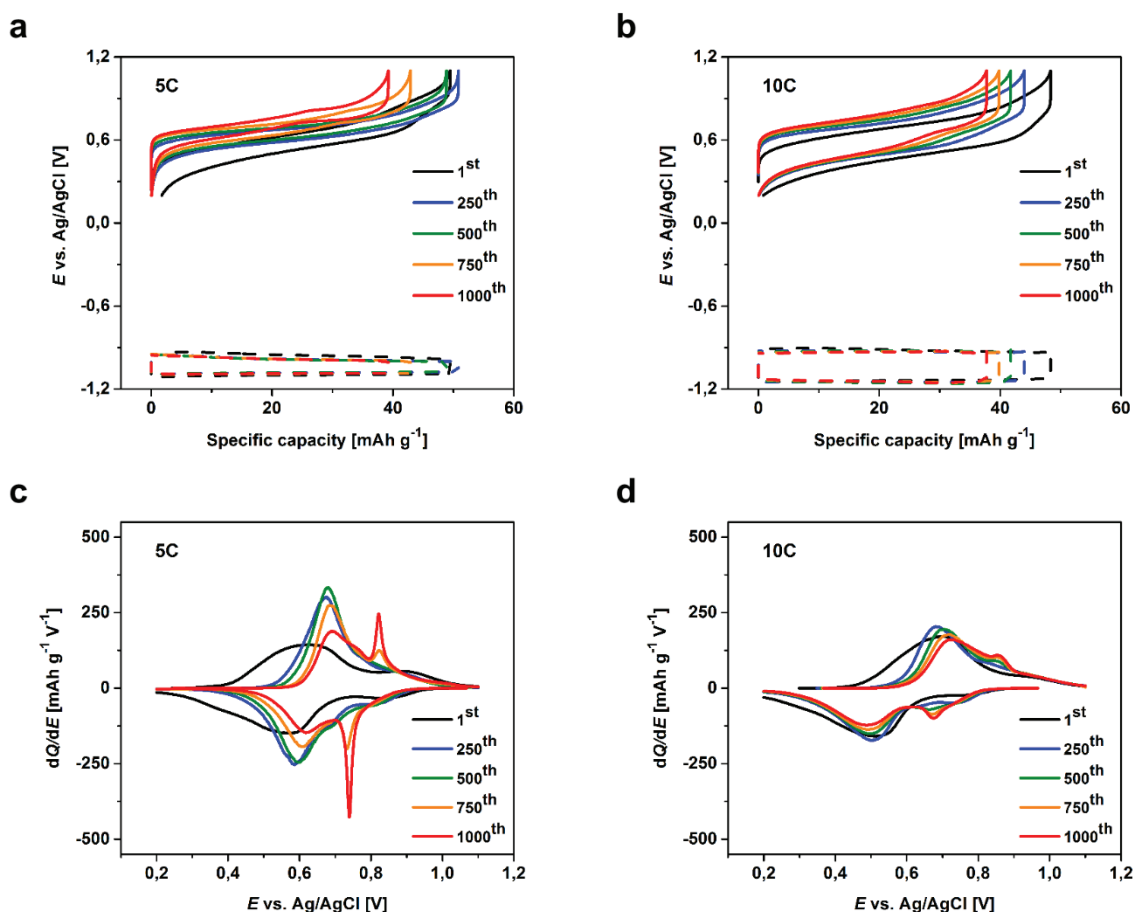


Figure 3-12. (a,b) Potential profiles of standard CuHCF (solid line) and Zn foil (dashed line) at 5C and 10C current rates in 100 mM ZnSO₄, respectively. (c,d) Differential specific charge profiles at different numbers of cycles for standard CuHCF measured at 5C and 10C current rates in 100 mM ZnSO₄, respectively.

An increase in intensity and sharpening of the second set of redox peaks at a 5C current rate upon cycling was determined from the differential specific charge profiles (Figs. 3-12 (c-d)). These results clarified that the formation of the second phase at a lower current rate was more favorable, while at a higher current rate the phase transformation was postponed to a higher number of cycles. Also, at a higher current rate the redox peaks were broader; this was a consequence of the higher overpotential. The thermodynamic potential (E_i) and kinetic overpotential (η) were calculated to investigate the thermodynamic and kinetic behaviors of

standard CuHCF at different current densities, as it was discussed in the previous section; each has been plotted against the number of cycles (Fig. 3-13).

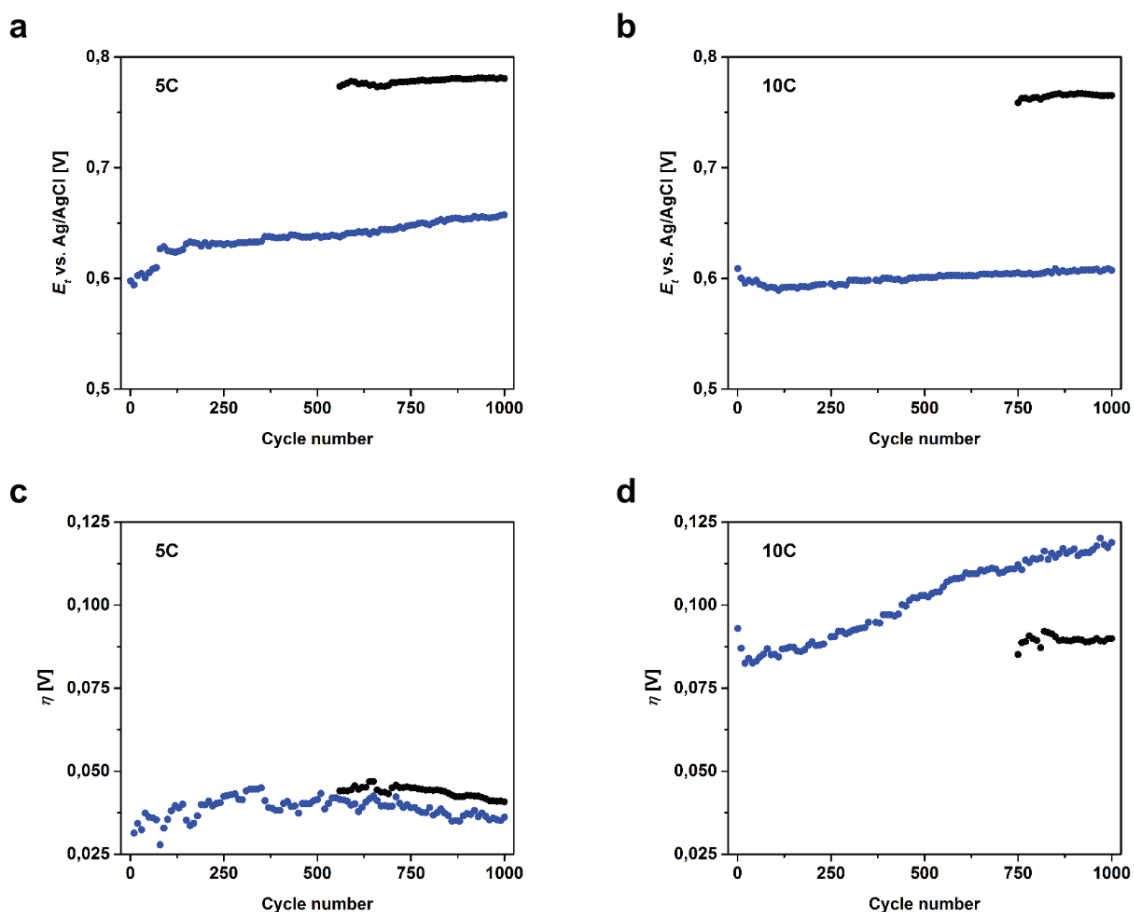


Figure 3-13. (a,b) Thermodynamic and (c,d) kinetic effects observed for the standard CuHCF in 100 mM ZnSO₄ at 5C and 10C currents, respectively. The blue circles indicate the first redox couple and the black circles represent the second one.

These results indicate that the thermodynamic potentials for both redox couples were nearly independent of the current rate. However, the overpotentials increased when the current rate was higher as expected.

So far the results showed that the occurrence of the phase transformation is depending on different parameters and has a negative effect on the degradation of CuHCF active material. These factors are namely the nature and the concentration of the electrolyte as well as the current rate which have been discussed in detail in the previous parts. Therefore, it is of primary importance to study the nature of this phenomenon.

Recently, Trócoli et al.^[196] studied the phase transformation of CuHCF upon cycling in 0.1 M Zn(ClO₄)₂ solution and a mixture of 0.1 M Zn(ClO₄)₂ + 2 M NaClO₄. Their results showed that the cycle stability of CuHCF not only was dependent on the anion but also on the co-cation. They observed a similar trend to this Ph.D. work, while the new formed phase(s) had higher insertion potential. In addition, their results suggested that the intercalation of sodium

ions is thermodynamically more favorable than zinc ions. The appearance of the second plateau at high potentials for the sample cycled in 0.1 M $\text{Zn}(\text{ClO}_4)_2 + 2 \text{ M NaClO}_4$ mixture was postponed to higher numbers of cycle. The capacity retention for CuHCF cycled after 500 cycles in the mixture mentioned above was higher (73.3%) than the sample cycled in 0.1 M $\text{Zn}(\text{ClO}_4)_2$ without the presence of sodium (58.1%). Another promising outcome was the high energy retention of 81.9% after 500 cycles for CuHCF cycled in 0.1 M $\text{Zn}(\text{ClO}_4)_2 + 2 \text{ M NaClO}_4$ mixture while in 0.1 M $\text{Zn}(\text{ClO}_4)_2$ only 68% were achieved. Furthermore, they also suggested that zinc ions could substitute copper ions from the CuHCF lattice and convert CuHCF to an unknown Zn-based distorted phase. Additionally, the Fe(II)/Fe(III) can be partially substituted by either zinc or copper ions.^[196] Based on the mentioned study and the discussed results in the previous sections, in the next part a mechanism for the phase transformation of CuHCF upon cycling in zinc-based solutions is proposed.

3.4. Phase Transformation Mechanism

Since in stationary applications long-term cycling is of critical importance, it is crucial to develop a mechanism for explaining the origins of the phase transformation (i.e., the appearance of the new phase) and the structural changes that occur during standard CuHCF cycling, and attempt to overcome the major capacity decay and aging that results.

Several studies have examined the structural changes and electrochemical performances of different forms of PB. In the work of Dostal et al.^[202], the electrochemical behavior of PB that was mechanically attached to a graphite electrode was studied in a potassium and cadmium solution containing aqueous electrolytes while performing cyclic voltammetry (CV). The results showed that the ion-exchange process could occur not only at the interstitial sites but also at the lattice sites. In the presence of cadmium cations, PB can convert into cadmium hexacyanoferrate ($\text{K}_2\text{Cd}[\text{Fe}(\text{CN})_6]$) as a newly formed phase.^[202,203] Zakharchuk et al.^[204] also investigated the insertion of cadmium (II) ions at PB interstitials, leading to distortions in the lattice.

Widmann et al.^[205] studied the electrochemical formation and mechanochemical properties (i.e., the effects of milling time) for potassium copper (II)/zinc (II) hexacyanocobaltate (III)/hexacyanoferrate (III) ($\text{KCu}_x\text{Zn}_{1-x}[\text{hcc}]_x[\text{hcf}]_{1-x}$) upon the mechanical mixing of KCuHCC and KZnHCF cycled in 0.1 M KNO_3 . Reddy et al.^[206] and Schwudke et al.^[207] also studied the electrochemical behaviors of other mixed hexacyanoferrates, such as nickel-iron hexacyanoferrate and iron-copper hexacyanoferrate.

Based on the information obtained from the above-mentioned research and considering the results from previous sections, it is possible to propose a probable mechanism for the phase

transformation in standard CuHCF. Fig. 3-14a illustrates the hypothetical aging mechanism for standard CuHCF during the intercalation of zinc ions.

As it was mentioned in Section 1.3, standard CuHCF has a 3D open-framework structure that allows for facile insertion and extraction of guest zinc ions through its ‘A sites’ upon electrochemical reduction and oxidation of carbon- or nitrogen-coordinated metal ions. When critical amounts of intercalated zinc were reached in the lattice, the zinc ions were able to occupy $[\text{Fe}(\text{CN})_6]$ vacancies (indicated as V is the mechanism), leading to lattice distortion and poor electrochemical performance.

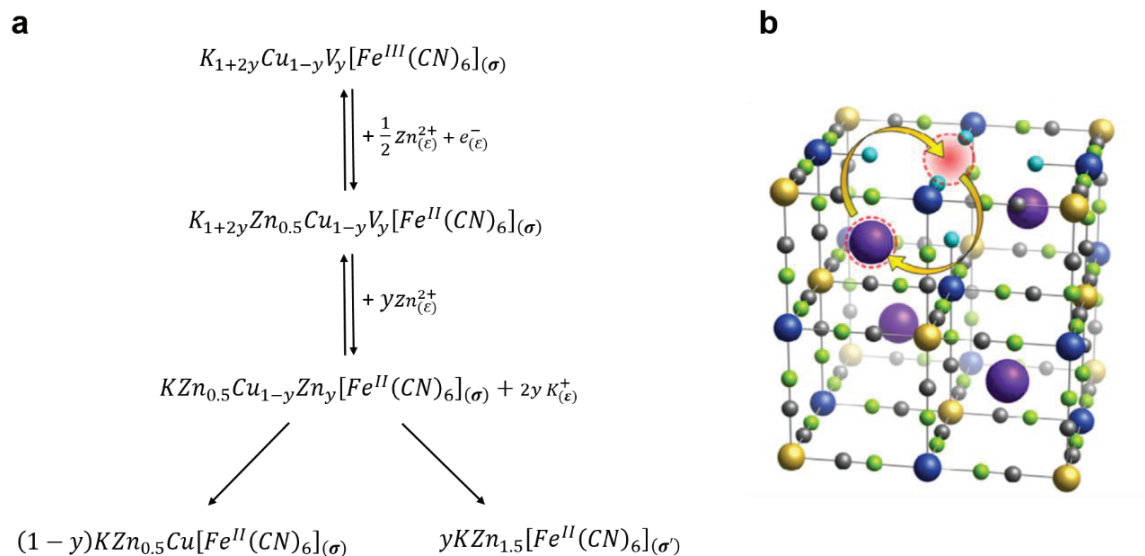


Figure 3-14. (a) Hypothetical aging mechanism for standard CuHCF during the intercalation of zinc ions. σ , σ' represent the active material phases, ε is the electrolyte solution phase, V indicates the vacancies in the lattice. (b) A schematic model of CuHCF illustrating the reversible zinc ion hopping between 8c and 4a crystallographic sites in the cavity and $[\text{Fe}(\text{CN})_6]$ voids. Color coding: Zn-purple, Fe-yellow, Cu-blue, N-green, C-grey, and H_2O -light blue (extracted from [108]).

This occupancy was followed by the formation of a CuZnHCF mixture and/or nucleating ZnHCF while the zinc ions replaced the copper’s position. It is important to stress that this hypothetical mechanism does not omit the original phase of standard CuHCF while formation of the new phase/or phases, since the completion of this formation depends on different parameters such as the cycling number, the concentration of the electrolyte and the nature of the electrolyte. Accordingly, it was determined that the phase transformation occurred during the charging/discharging reactions and could lead to a change in the standard CuHCF composition as well as crystallography in zinc salt solutions. Therefore, the capacity loss and aging of the standard CuHCF upon cycling, the potential shift regarding the ion-exchange reaction, and the two-step voltage plateau can be explained by the proposed mechanism and the electrostatic repulsion within the standard CuHCF framework. It is important to note that from the results described in the previous sections, it is clear that the nature of the anions in the electrolyte plays a fundamental role in the formation of the new phase(s), although they were not included in the

proposed phase transformation mechanism. From the results of previous sections, it can be seen that the phase transformation likely occurred at higher concentrations of electrolyte and lower current densities.

Relatedly, in the work of Renman et al.^[108] the (de-)intercalation of zinc ions into standard CuHCF was studied via an advanced *in operando* synchrotron XRD. Their results were in agreement with the above proposed mechanism. Their results were determined that the zinc ions not only occupied $[\text{Fe}(\text{CN})_6]$ vacant sites and tunnels (A sites), but also could reversibly hop/swap from the cavities to the vacant Fe sites as more and more zinc ions were inserted electrochemically into the structure, leading to a non-linear change in the standard CuHCF unit-cell parameter (Fig. 3-14b). It is worth mentioning that the phase transformation during zinc (de-)intercalation also depends on the thermodynamics and kinetics of the system, and plays an important role regarding the calendar and cycle aging of the battery.

4. Optimizing the Standard CuHCF Structure by Adding a Co-Ion

As mentioned before, the main goal in grid-scale energy storage is developing a battery with a long lifetime, high power density, and more efficient energy storage. From the previous chapter, it is clear that the degradation of the standard CuHCF was initiated upon cycling, and its impact on the life cycle and cycle aging of the system were thoroughly discussed. Therefore, after considering the information already collected, it is reasonable to further consider ways of overcoming these problems.

After considering the XRD results illustrated in Fig. 3-8, the explanations for the appearance of new reflections during cycling in concentrated zinc salt solutions, and the phase transformation mechanism, it is of primary importance to postpone or eliminate the aging of standard CuHCF by optimizing its crystal structure. To accomplish this goal, in this chapter the attempts to modify the standard CuHCF structure by acting on the synthesis route is described, in order to achieve the goal of a more stable system with a long life cycle.

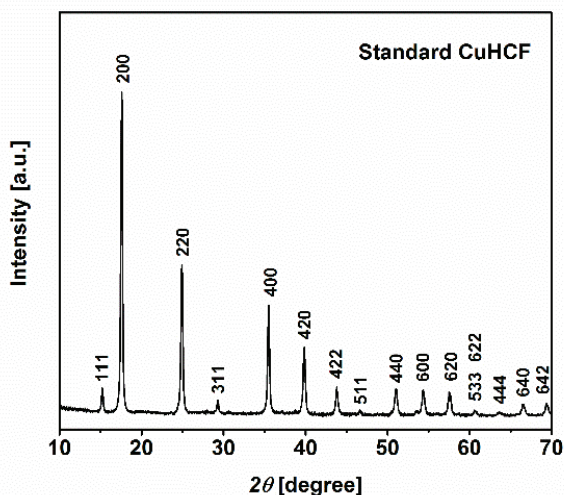


Figure 4-1. X-ray diffraction pattern of the standard CuHCF powder.

Fig. 4-1 shows the XRD pattern of the standard as-prepared CuHCF (Section 2.2.1). All of the reflections are indexed and in agreement with the well-known structure reported in the literature, with the space group of $Fm\bar{3}m$.^[175,208]

Since upon phase transformation, zinc ions not only occupy the interstitial sites but also the regular crystal sites, it is a good option to substitute zinc ions during synthesis into the standard CuHCF lattice. For this purpose, different mixtures of CuZnHCF were synthesized (Section 2.2.2) in which copper was partially substituted with zinc, namely with Cu:Zn at the following ratios: 85:15, 90:10, 93:7, 95:5, and 98:2. In order to determine if the phase and the crystallinity for each mixture powder changed compared to standard CuHCF, XRD

measurements were run for each powder. Since the Cu:Zn ratio at each sample is different, it is interesting to investigate whether there is a peak shift in the XRD pattern for each sample or not. Although all of the parameters for each XRD test were set the same, in order to prevent any errors due to sample preparation or displacement, each sample was mechanically ground with commercial zinc oxide (ZnO) powder as a reference material. Furthermore, the XRD measurements have run at the 0% SOC (pristine powder, 0% intercalated zinc) for all of the samples in order to eliminate the effect of the SOC on the lattice parameters changes. This idea is related to the work of Pasta et al.^[177] which showed that the lattice parameter of standard CuHCF or any other PBAs is decreasing upon discharging and a shift of XRD reflections to higher 2θ angles is observed. Moreover, Wessells et al.^[175] studied the crystal structure of the standard CuHCF at different state of charge. They also observed that upon de-intercalation of potassium ions from standard CuHCF structure (100% SOC), the lattice parameters were increased of 0.9%. In doing so, the diffraction signals shifted to lower 2θ angles. This happens due to the increase of the $[\text{Fe}(\text{CN})_6]^{4-}$ radius upon oxidizing, as the length of iron-carbon bond increases. Although the lattice parameters changed, no evidence of new reflections have been observed which is suggesting that only a single-phase reaction occurred, which is typical for (de-)insertion of monovalent cations. It is also important to mention the results from Renman et al.^[108] study in which a similar two-step voltage plateau have been observed in their potential profiles of standard CuHCF upon (de-)intercalation of zinc ions. It has been investigated that the change in unit-cell parameter of standard CuHCF is associated with a two-electron transfer mechanism. In other words, the electrochemical oxidation of iron (II) to iron (III) and de-insertion of zinc ions lead to a non-linear change of the standard CuHCF unit-cell parameter. The de-intercalation of zinc ions occurs in two distinct steps, attributed to the two-step plateau. Bases on this information and utilizing a reference material any error due to the sample preparation or displacement should be excluded. It is important to note that ZnO have been selected as a reference material since it is crystalline, its crystal structure is known, and its XRD reflections at lower 2θ angles do not match with the XRD reflections of the samples that need analysis. Furthermore, it is stable under X-ray beam and do not react chemically with the samples. For each measurement the amount of employed ZnO was one seventh of the respective powder. Fig. 4-2a shows the XRD patterns of commercial ZnO, and its mixtures with standard CuHCF and the CuZnHCF variations. The XRD pattern of commercial ZnO was compatible with those published in references ^[209,210]. In order to exclude any shift due to the sample preparation, each respective XRD pattern has been shifted in a way that the ZnO reflections of each pattern matches the ones of ZnO pristine pattern. After this modification, the comparison between the XRD patterns of standard CuHCF and CuZnHCF mixtures is reliable.

From Fig. 4-2a, it can observe that the XRD patterns of standard CuHCF and the mixtures look similar and contain sharp reflections, which indicate high crystallinity.

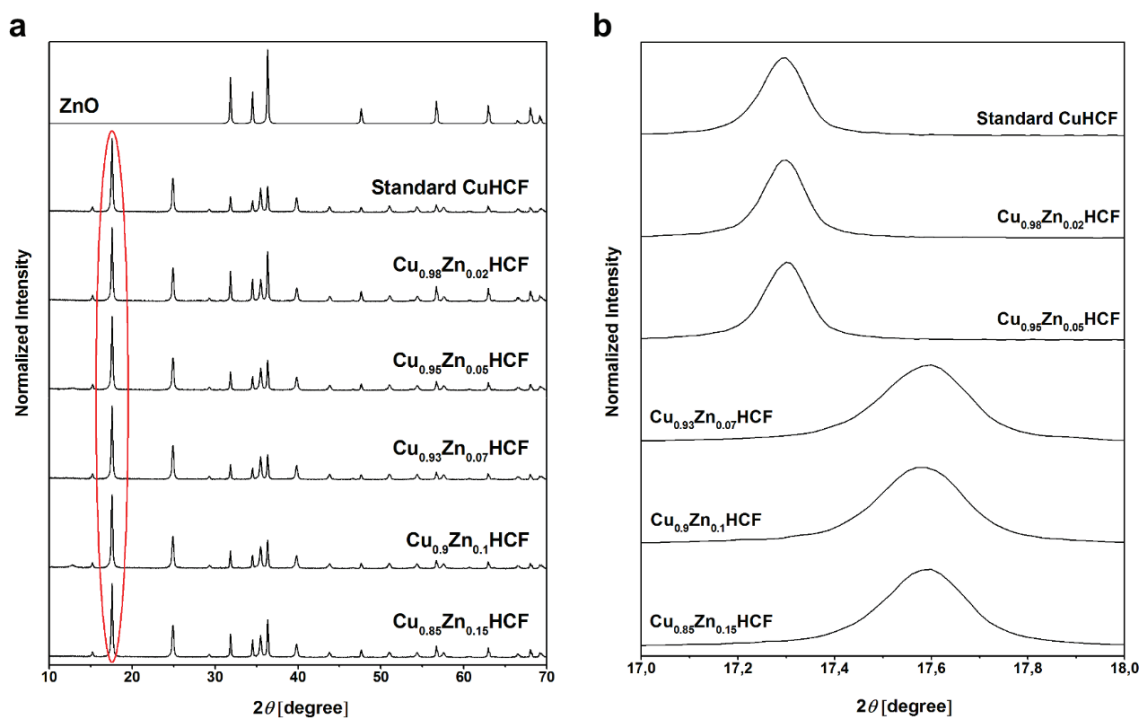


Figure 4-2. X-ray diffraction patterns of (a) pristine ZnO and mixture of ZnO with standard CuHCF powder and other CuZnHCF mixtures. (b) A zoom-in of X-ray diffraction patterns for mixture of ZnO with standard CuHCF powder and CuZnHCF mixtures, between 17° and 18° 2θ .

To better understand the relationship between the ratios of substituted zinc in CuHCF structure and the resulting lattice parameters changes, Fig. 4-2b illustrates a zoom-in on the position of the (200) reflection. From these results, it can be concluded that the unit cell volumes of the standard CuHCF and mixtures with Cu:Zn ratios of 98:2 and 95:5 were the same, since the position of the (200) reflection in all of them is almost identical. However, by increasing the amount of zinc in the lattice, the position of the (200) reflection shifted to higher 2θ angles. In other words, the lattice parameters for mixtures with Cu:Zn ratios of 93:7, 90:10, and 85:15 decreased. From these results, it can be argued that after adding a critical amount of zinc during synthesis, the size of unit cell changed and caused a shift in the reflections position and did not follow the Vegard's law. It is important to note that different parameters can affect the position of the reflections in XRD. Although the effects of the SOC and the errors due to the sample preparation or displacements have been omitted before the XRD measurements, any change in the crystal lattice can be depend on the amount of substituted ions as well as their crystal ionic radii.^[164] Although in this case the ionic radii of zinc and copper ions are almost the same ($\text{Zn}^{2+} = 88 \text{ pm}$, $\text{Cu}^{2+} = 87 \text{ pm}$), this hypothesis cannot be completely true and when the amount of substituted zinc is very low, no evidence of any change in the XRD patterns is visible.

However, the presence of potassium and water molecules in the structure might influence the crystal structure.

In addition, to investigate the spatial distribution of elements and determine the number of present phases in each sample, an elemental mapping via an EDX measurement was performed for all of the synthesized powders. A few milligram of each powder were placed on the sample holder and a thin layer of Pt:Pd (80:20) was sputtered on top to prevent occurring charging effects. Since a carbon patch was used to fixate the powder, the elemental mapping of carbon is not included in the images below. However, a cyanide ligand is presented in each sample; by showing only nitrogen mapping, it can be assumed that at the same positions the carbon atoms are also present.

Fig. 4-3 illustrates the elemental mapping of standard CuHCF and the SEM image of the investigated area. It is clearly visible that the distributions of iron, copper, and nitrogen are homogenous, which indicates the actual CuHCF phase. Although oxygen and potassium atoms were also distributed all over the sample (overlapping with other elements), at some points their intensities were higher (brighter contrast). Therefore, it can be concluded that an oxide form of potassium was present. One possibility could be the formation of potassium hydrogen carbonate (KHCO_3) or potassium carbonate (K_2CO_3), which was initiated from the mixture of potassium nitrate and nitric acid during the washing step or from the $\text{K}_3\text{Fe}(\text{CN})_6$ reaction reagent (Section 2.2.1).

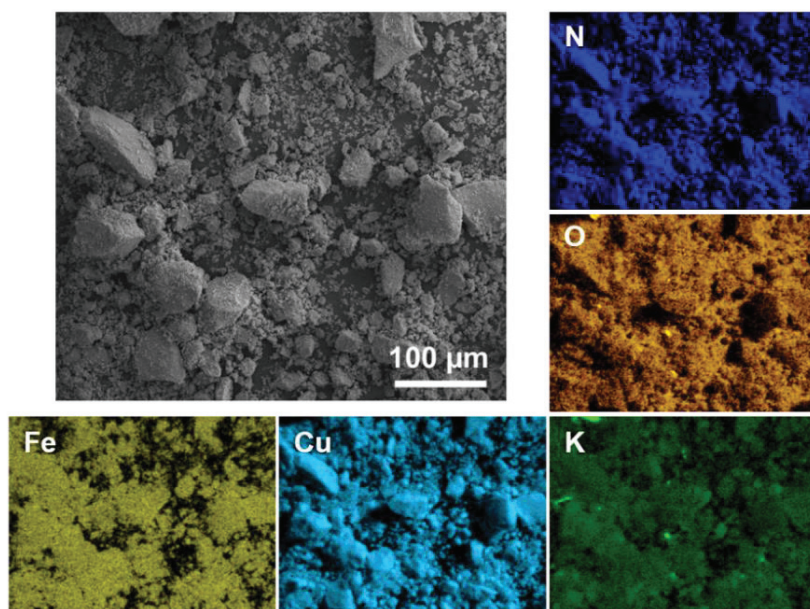


Figure 4-3. SEM and EDX elemental mapping (nitrogen, oxygen, potassium, copper, and iron) of standard CuHCF powder.

Fig. 4-4 depicts the elemental mapping and SEM image of the $\text{Cu}_{0.98}\text{Zn}_{0.02}\text{HCF}$ powder. The results suggest that all of the elements were homogeneously distributed over the sample; there was no evidence of any extra phase.

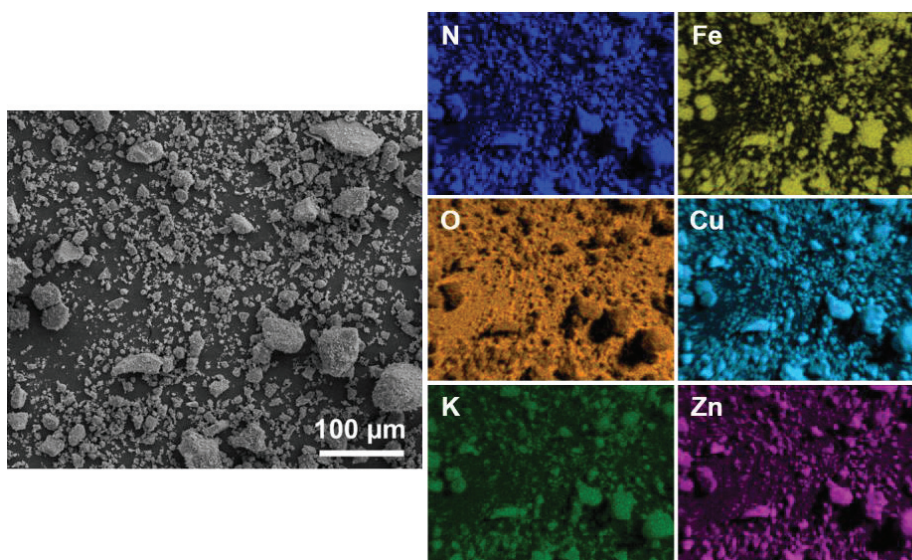


Figure 4-4. SEM and EDX elemental mapping (nitrogen, oxygen, potassium, copper, iron, and zinc) of the $\text{Cu}_{0.98}\text{Zn}_{0.02}\text{HCF}$ mixture powder.

The same results as shown in Fig. 4-4 can be observed in Fig. 4-5 for the $\text{Cu}_{0.95}\text{Zn}_{0.05}\text{HCF}$ synthesized powder; only one single phase existed in this mixture.

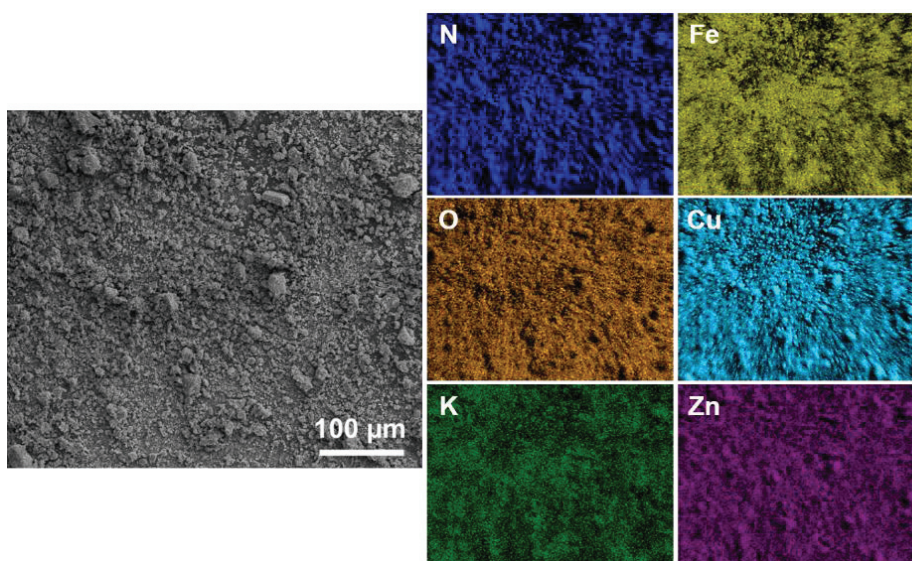


Figure 4-5. SEM and EDX elemental mapping (nitrogen, oxygen, potassium, copper, iron, and zinc) of the $\text{Cu}_{0.95}\text{Zn}_{0.05}\text{HCF}$ mixture powder.

Fig. 4-6 includes the elemental mapping and SEM image of the $\text{Cu}_{0.93}\text{Zn}_{0.07}\text{HCF}$ powder. It is worth noting that, although the sample conductivity was increased, still some of the mapping images were appearing blurry due to specimen drift under the electron beam. From Fig. 4-6, it can be seen that the distribution of all the elements except potassium and oxygen was homogenous. In this sample, contrary to standard CuHCF (Fig. 4-3), the oxygen did not overlap

with all of the potassium-rich points. Therefore, in addition to the initial phase ($\text{Cu}_{0.93}\text{Zn}_{0.07}\text{HCF}$) and the potassium carbonate another potassium-rich phase was found.

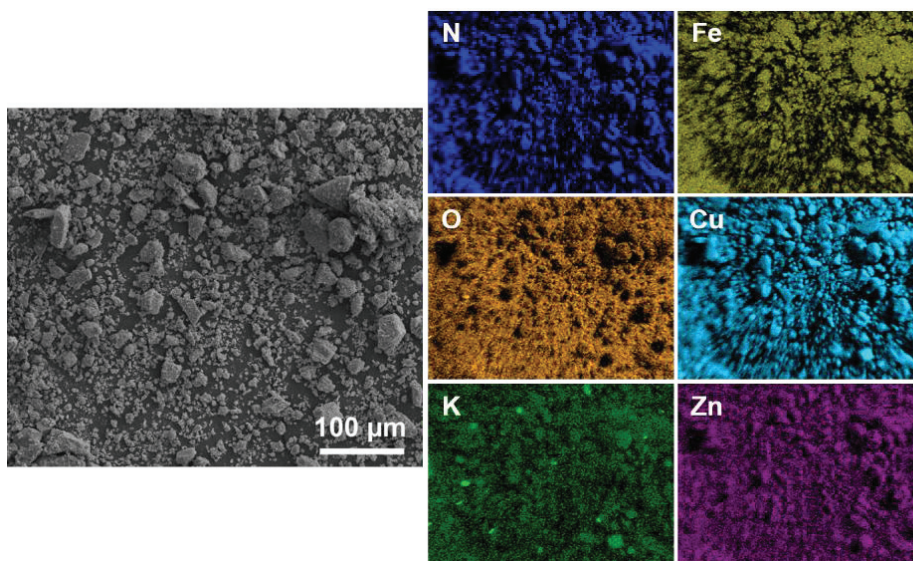


Figure 4-6. SEM and EDX elemental mapping (nitrogen, oxygen, potassium, copper, iron, and zinc) of the $\text{Cu}_{0.93}\text{Zn}_{0.07}\text{HCF}$ mixture powder.

By observing the elemental mapping of the $\text{Cu}_{0.90}\text{Zn}_{0.10}\text{HCF}$ synthesized powder (Fig. 4-7), the same results and explanations as described for $\text{Cu}_{0.93}\text{Zn}_{0.07}\text{HCF}$ (Fig. 4-6) were validated.

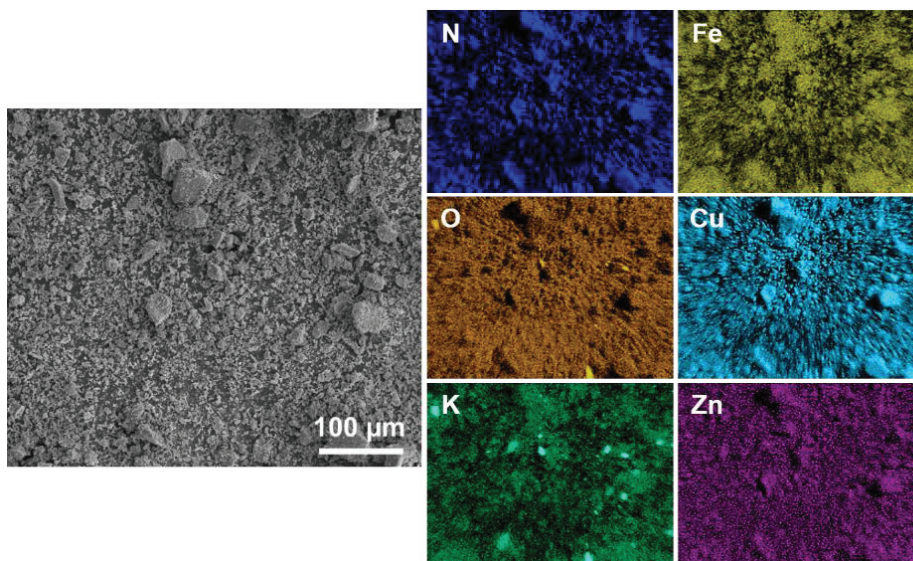


Figure 4-7. SEM and EDX elemental mapping (nitrogen, oxygen, potassium, copper, iron, and zinc) of the $\text{Cu}_{0.9}\text{Zn}_{0.1}\text{HCF}$ mixture powder.

Finally, the elemental mapping for the $\text{Cu}_{0.85}\text{Zn}_{0.15}\text{HCF}$ powder is shown in Fig. 4-8. As can be seen therein, all of the elements were homogeneously distributed over the complete sample; only one point with a high potassium intensity is visible. Although at this point none of the elements had high intensities, iron and oxygen overlapped in this area. Therefore, in addition to the

original phase, a phase containing potassium, iron, and oxygen was determined, however, it remained unidentified.

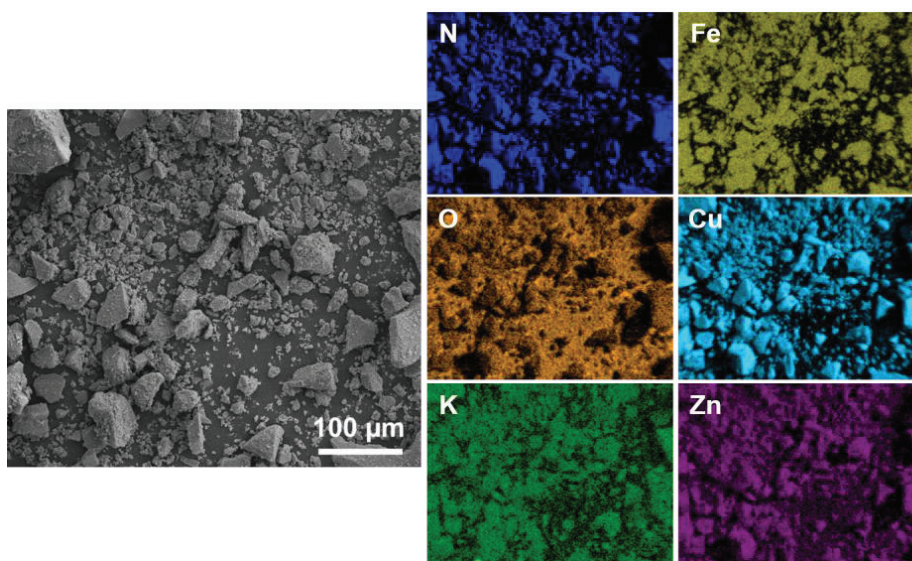


Figure 4-8. SEM and EDX elemental mapping (nitrogen, oxygen, potassium, copper, iron, and zinc) of the $Cu_{0.85}Zn_{0.15}HCF$ mixture powder.

In addition to the SEM images and EDX elemental mappings at an exemplary area for each sample, images with higher magnifications were taken.

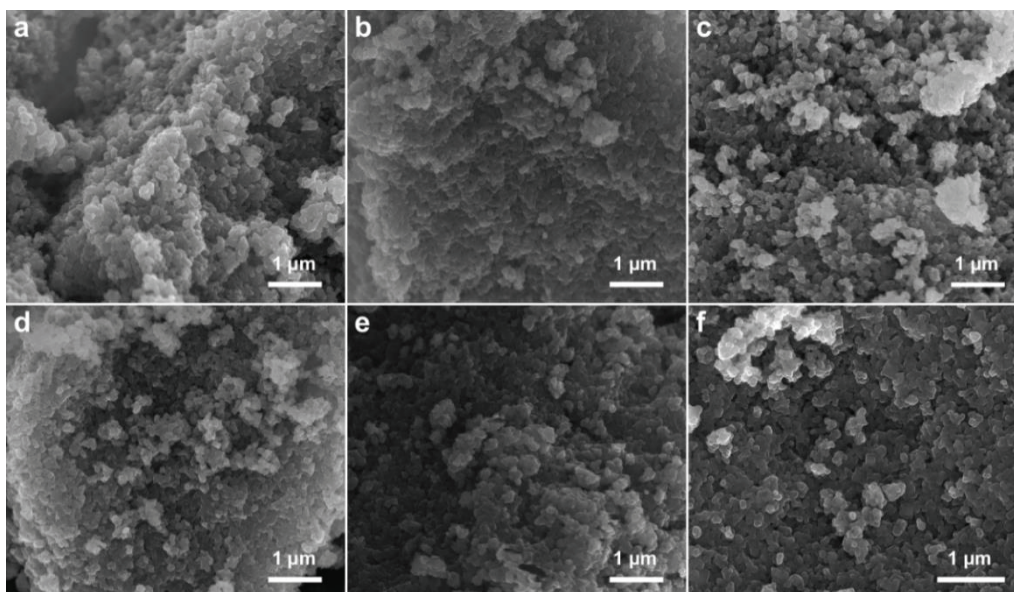


Figure 4-9. SEM images of (a) standard CuHCF powder, CuZnHCF mixture powders with Cu:Zn ratio of (b) 98:2, (c) 95:5, (d) 93:7, (e) 90:10, and (f) 85:15, scale bar 1 µm.

These images (Fig. 4-9) illustrate the particle sizes and morphologies for each synthesized powder. Since the morphologies of all powders seem similar, it is likely that the sample morphologies are independent from the composition of each powder. Each powder consisted of agglomerated polydisperse spherical particles with an average size of 80 to 90 nm. The particles aggregated to reveal a highly porous assembly. The nano-sized CuHCF and CuZnHCF

particles, due to their high surface area to volume ratio, facilitated a rapid and short ion transport throughout the material (i.e., increased the diffusion rate).

Thus far, all of the CuZnHCF mixtures and standard CuHCF were evaluated via crystallography and from a morphological perspective. In the following the performance of each sample, based on its electrochemical behavior will be discussed. Fig. 4-10 indicates the long-term cycling of all of the samples cycled at a current rate of 1C in 20 mM and 100 mM ZnSO₄.

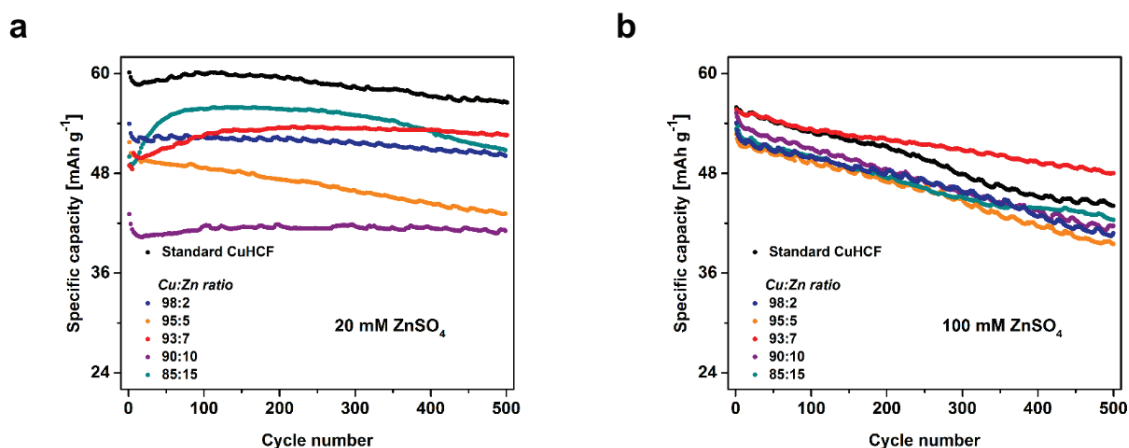


Figure 4-10. Long-term cycling of standard CuHCF and different CuZnHCF mixtures at a 1C current rate in (a) 20 mM and (b) 100 mM ZnSO₄ after 500 cycles.

Based on the data extracted from Figs. 4-10, 4-13 and 4-16, the capacity retention as well as the energy retention for each sample after 500 cycles in both concentrations with respect to their maximum value is calculated and reported in Table 4-1.

Table 4-1. Percentages of energy and charge retention for standard CuHCF and CuZnHCF mixtures at a 1C rate after 500 cycles in 20 mM and 100 mM of ZnSO₄.

		Solutions			
		20 mM ZnSO ₄		100 mM ZnSO ₄	
		Energy	Charge	Energy	Charge
Synthesized CuZnHCF with certain Cu:Zn ratios	Standard CuHCF	103.9%	94%	85.26%	78.84%
	98:2	105.6%	92.83%	83.66%	75.49%
	95:5	90.3%	83.43%	82.56%	74.89%
	93:7	123.1%	98.12%	92.52%	86.26%
	90:10	110.7%	95.32%	81.46%	75.39%
	85:15	125.4%	90.78%	85.93%	78.96%

Based on these results, it can be seen that in 20 mM ZnSO₄, all of the samples degraded upon cycling, but among them only the Cu_{0.93}Zn_{0.07}HCF mixture showed a low capacity loss (~1.9%) after 500 cycles.

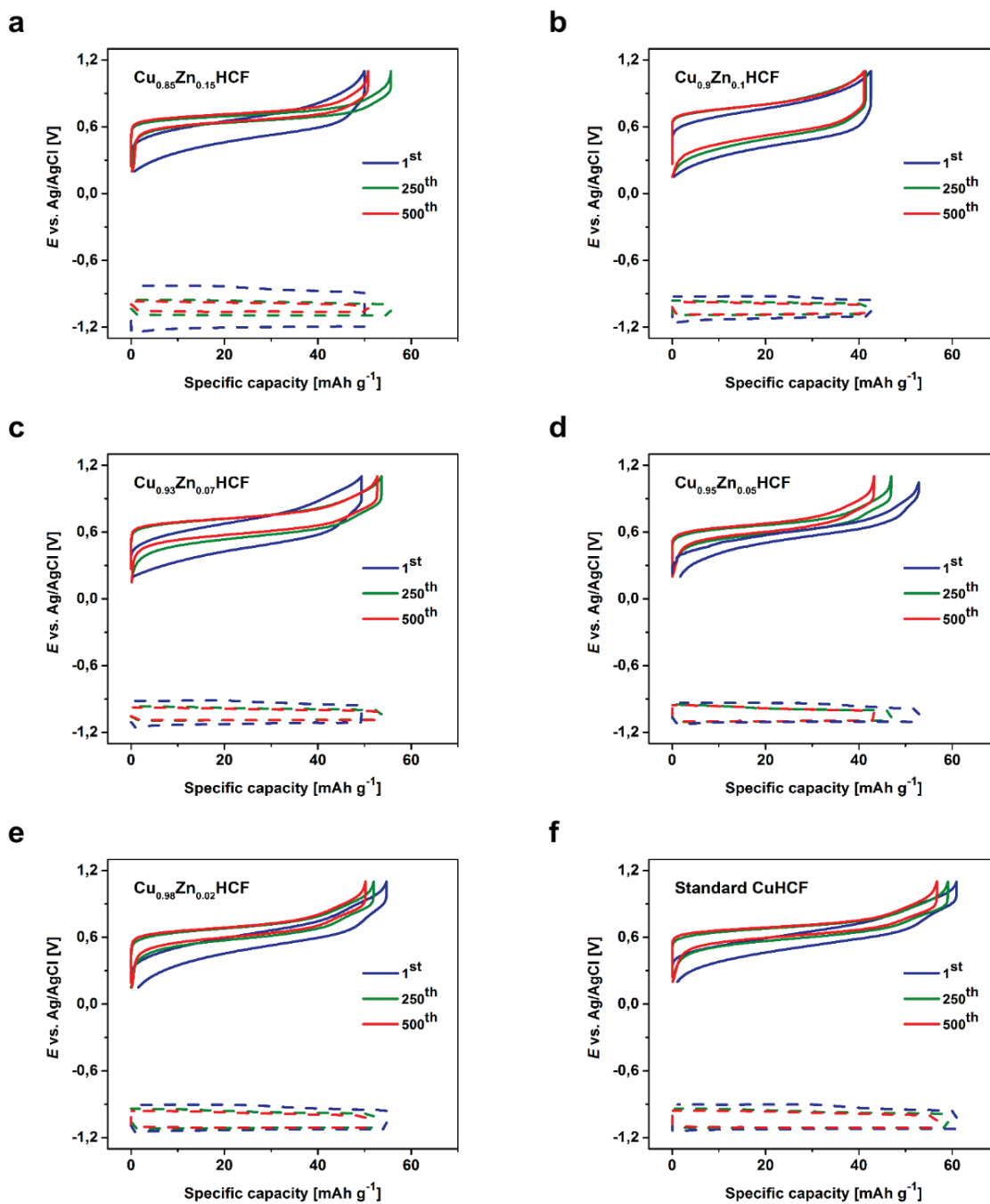


Figure 4-11. Potential profiles of CuZnHCF mixtures with Cu:Zn ratio of (a) 85:15, (b) 90:10, (c) 93:7, (d) 95:5, (e) 98:2, (f) standard CuHCF (solid line) and Zn foil (dashed line) at a rate of 1C in 20 mM ZnSO₄, respectively.

The potential profiles, differential charge profiles, and changes in specific energy, charge, and average potential provided by each sample at different numbers of cycles in 20 mM ZnSO₄ are reported in Figs. 4-11, 4-12 and 4-13, respectively. Changes were visible in the shapes of the potential profiles during cycling for the samples containing higher copper percentages (Fig. 4-11).

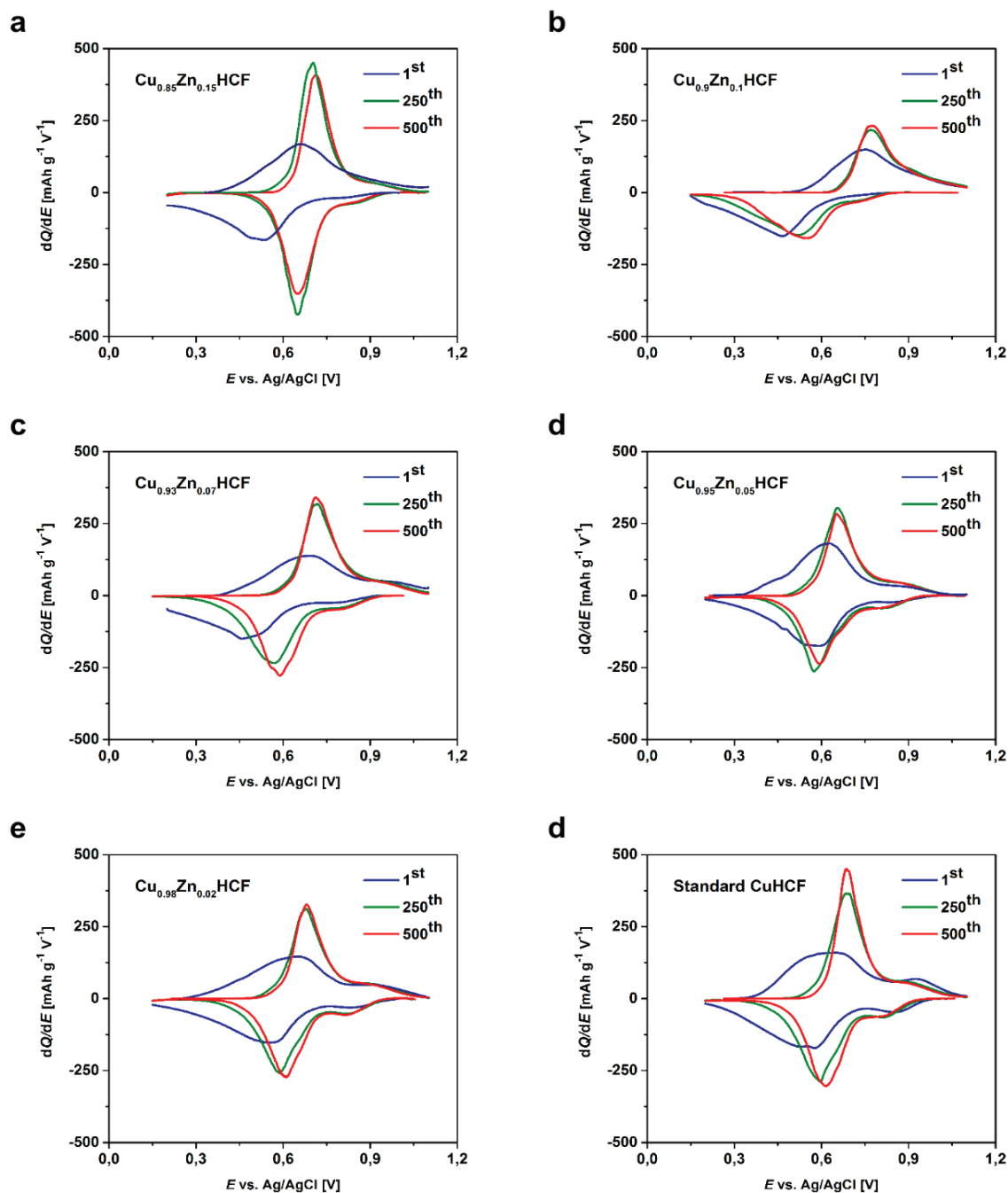


Figure 4-12. Differential specific charge profiles at different number of cycles of CuZnHCF mixtures with Cu:Zn ratio of (a) 85:15, (b) 90:10, (c) 93:7, (d) 95:5, (e) 98:2, and (f) standard CuHCF measured at 1C current rate in 20 mM ZnSO_4 , respectively.

The differential plots (Fig. 4-12) of all the samples demonstrate that upon cycling, the intensity of the first set of redox peaks increased. The appearance of the second redox peaks in the samples with high percentages of copper were revealed at lower number of cycles in comparison with those with low copper percentages. For all of the samples, the reduction reaction potential (i.e., the zinc ion insertion) upon cycling shifted to higher values. The intercalation process required more energy, leading to a higher total cell voltage ($E_{WE}-E_{CE}$).

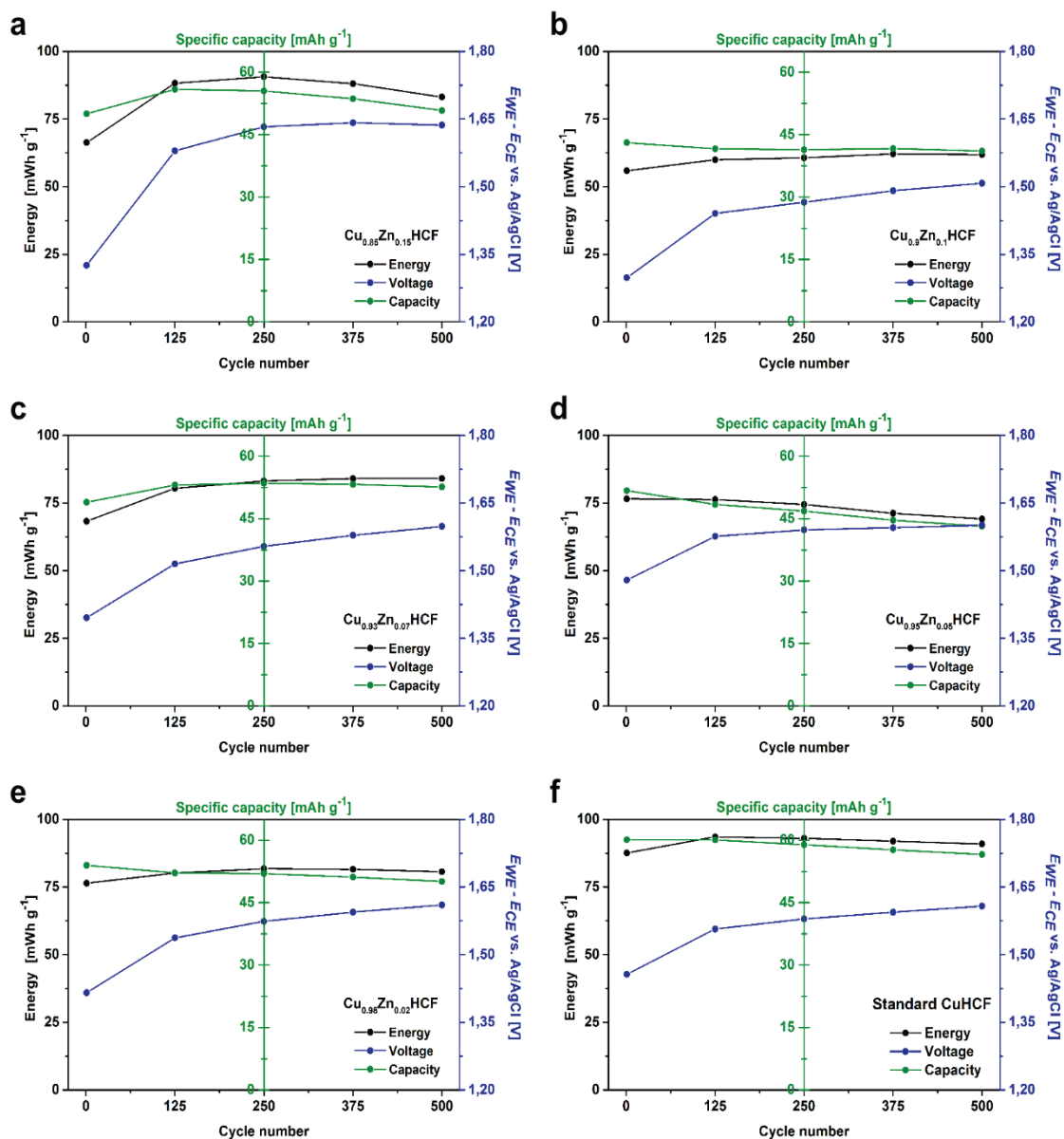


Figure 4-13. Specific energy, charge, and average potential provided by CuZnHCF mixtures with Cu:Zn ratio of (a) 85:15, (b) 90:10, (c) 93:7, (d) 95:5, (e) 98:2, and (f) standard CuHCF at 1C current rate in 20 mM ZnSO₄ at different number of cycles, respectively.

From Fig. 4-13, it can also be observed that the energy increased during cycling in all of the samples except for the Cu_{0.95}Zn_{0.05}HCF mixture. This can be the reason for the energy retention values reported in Table 4-1 that are greater than 100%. As discussed in Section 3.2, at higher concentrations degradation of the active material is faster. The results obtained after cycling in 100 mM ZnSO₄ were in agreement with the previous results.

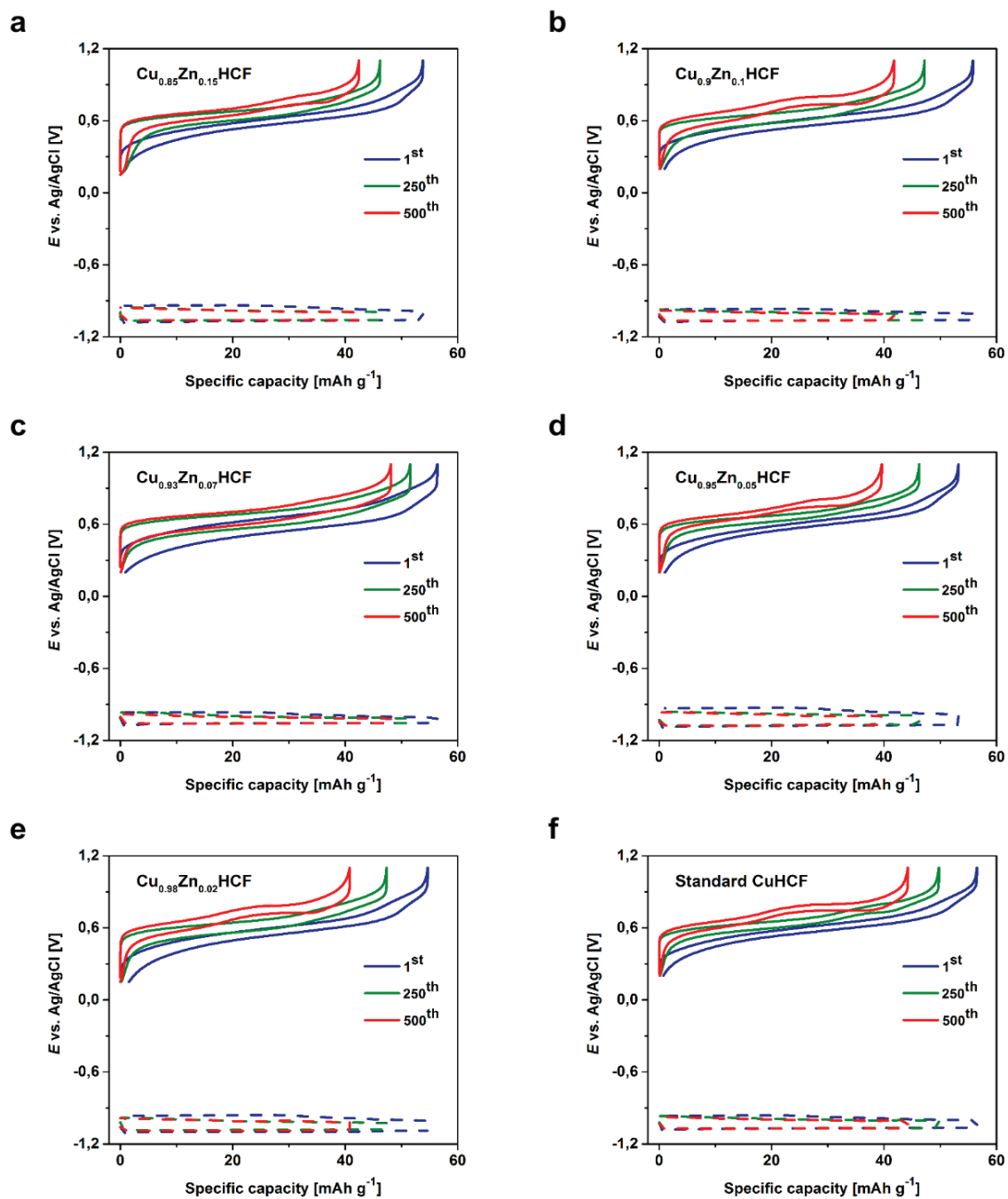


Figure 4-14. Potential profiles of CuZnHCF mixtures with Cu:Zn ratio of (a) 85:15, (b) 90:10, (c) 93:7, (d) 95:5, (e) 98:2, (f) standard CuHCF (solid line) and Zn foil (dashed line) at a rate of 1C in 100 mM ZnSO₄, respectively.

Among all mixtures like in 20 mM ZnSO₄, the Cu_{0.93}Zn_{0.07}HCF mixture showed the best electrochemical performance only minor capacity fading. The potential profiles, differential charge profiles, and changes in specific energy, charge, and average potential provided by each sample at different numbers of cycles in 100 mM ZnSO₄ are reported in Figs. 4-14, 4-15 and 4-16, respectively.

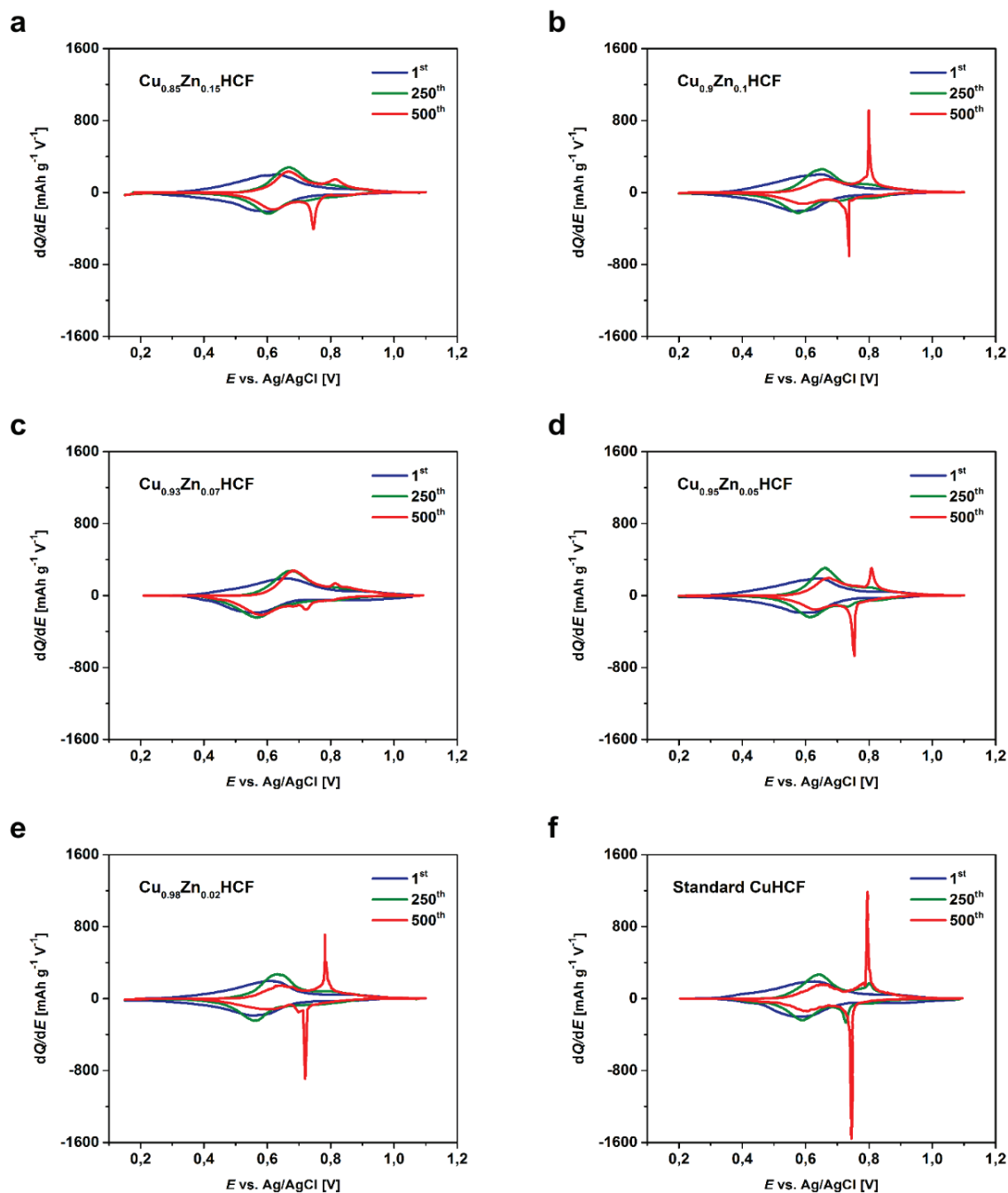


Figure 4-15. Differential specific charge profiles at different number of cycles of CuZnHCF mixtures with Cu:Zn ratio of (a) 85:15, (b) 90:10, (c) 93:7, (d) 95:5, (e) 98:2, and (f) standard CuHCF measured at 1C current rate in 100 mM ZnSO_4 , respectively.

From Fig. 4-14, it is clear that the mid-composition potential for all of the samples from the 1st to 500th cycle shifted to higher values, leading to an increase in the total cell voltage upon cycling (Fig. 4-16). The change in shape of the potential profiles (i.e., two-step plateau) for all of the samples cycled in 100 mM ZnSO_4 except the $\text{Cu}_{0.93}\text{Zn}_{0.07}\text{HCF}$ mixture was more dominant than in 20 mM. This was followed by the appearance of the second redox peaks in the

differential specific charge profiles (Fig. 4-15); the intensities of the peaks tended towards higher values, although the first set of redox peaks suppressed lower values.

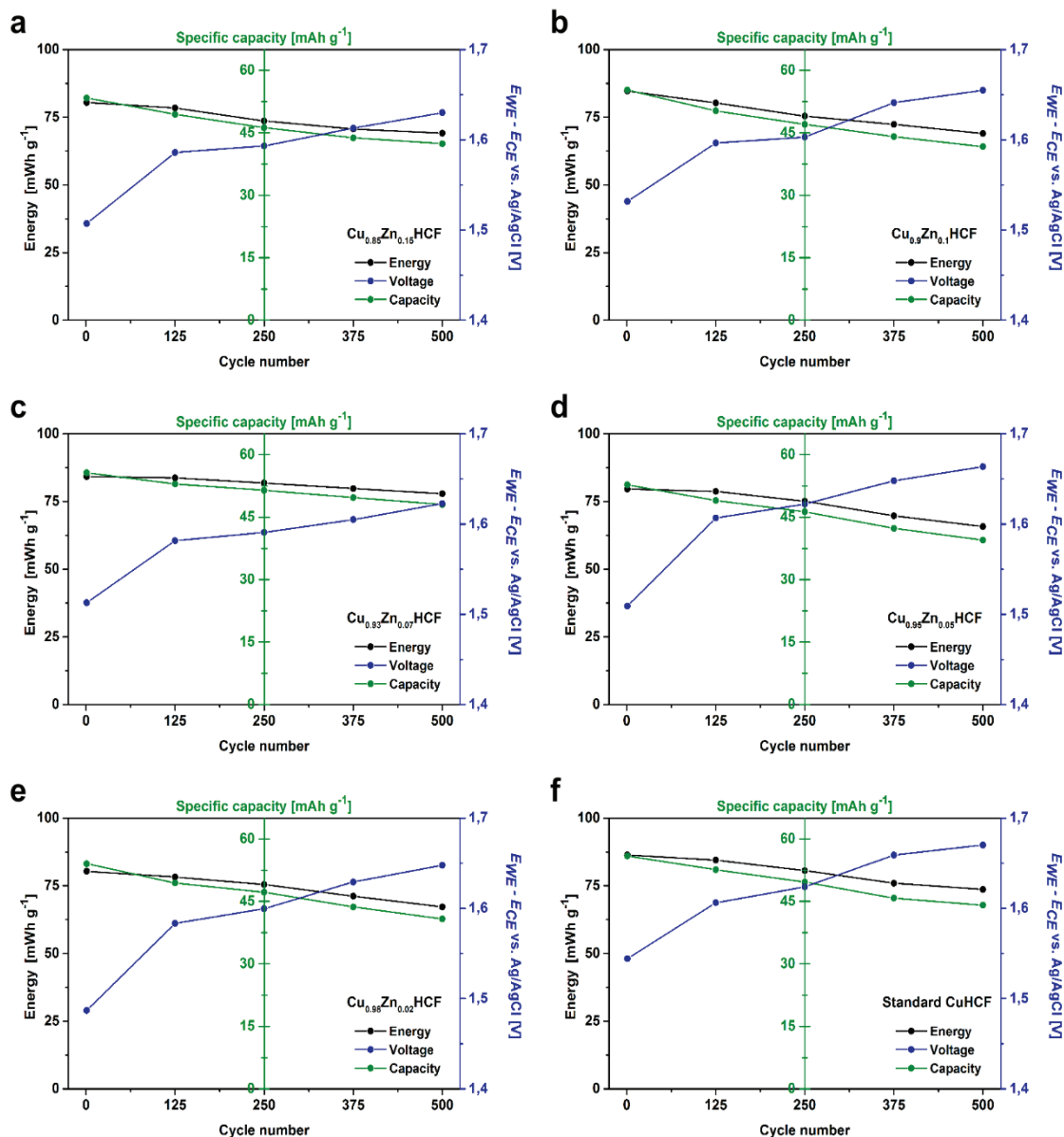


Figure 4-16. Specific energy, charge, and average potential provided by CuZnHCF mixtures with Cu:Zn ratio of (a) 85:15, (b) 90:10, (c) 93:7, (d) 95:5, (e) 98:2, and (f) standard CuHCF at 1C current rate in 100 mM ZnSO₄ at different number of cycles, respectively.

It is worth mentioning that in the Cu_{0.93}Zn_{0.07}HCF mixture, the second set of redox peaks had lower intensities than those of the other samples. In other words, the phase transformation mechanism in this mixture was less favorable during cycling and postponed to higher numbers of cycles. Since at higher concentrations more zinc was present in the electrolyte, the reaction was expected to occur easier and faster.

Therefore, as it is also clear from Fig. 4-14, the overpotential (η , the reaction-driving force) of the cycled samples in 100 mM ZnSO₄ was smaller than in the 20 mM ZnSO₄. In other words, at

low concentrations, it is probable that the amount of zinc ions in the electrolyte is not enough to (de-)intercalate into the structure. Even through applying high currents the overpotential was not decreased and the polarization will become significant. Another explanation may be the mass of the active material. If the loading mass is high, at low electrolyte concentrations the (de-)intercalation will be difficult, finally leading to high polarization. In addition, in all samples cycled in 100 mM ZnSO₄, the energy dropped upon cycling, whereas the Cu_{0.93}Zn_{0.07}HCF mixture delivered the highest value with an energy retention of 92.52%.

Since among all samples, a CuZnHCF mixture with a Cu:Zn ratio of 93:7 showed the best performance in both 20 mM and 100 mM ZnSO₄ electrolytes, for further analysis and investigation a comparison between this particular mixture and the standard CuHCF is described in the next chapter.

5. Electrochemical and Crystallographic Performances of Standard CuHCF and the Cu_{0.93}Zn_{0.07}HCF Mixture in Different Electrolytes

As discussed in the previous chapter, the Cu_{0.93}Zn_{0.07}HCF mixture in ZnSO₄ solutions showed the best electrochemical performance with the highest capacity and energy retention of all the CuZnHCF mixtures and standard CuHCF. This chapter describes the electrochemical performance and crystallographic characterization of the Cu_{0.93}Zn_{0.07}HCF mixture and standard CuHCF before and after long-term cycling (i.e., 1000 cycles) in 20 mM and 100 mM ZnSO₄.

5.1. Electrochemical Characterization of Standard CuHCF and the Cu_{0.93}Zn_{0.07}HCF Mixture in 20 mM ZnSO₄

Fig. 5-1 shows the long-term cycling and coulombic efficiency for standard CuHCF and the Cu_{0.93}Zn_{0.07}HCF mixture at a 1C current rate in 20 mM ZnSO₄ (pH = 4.8) for 1000 cycles. The information from these graphs is summarized in Table 5-1.

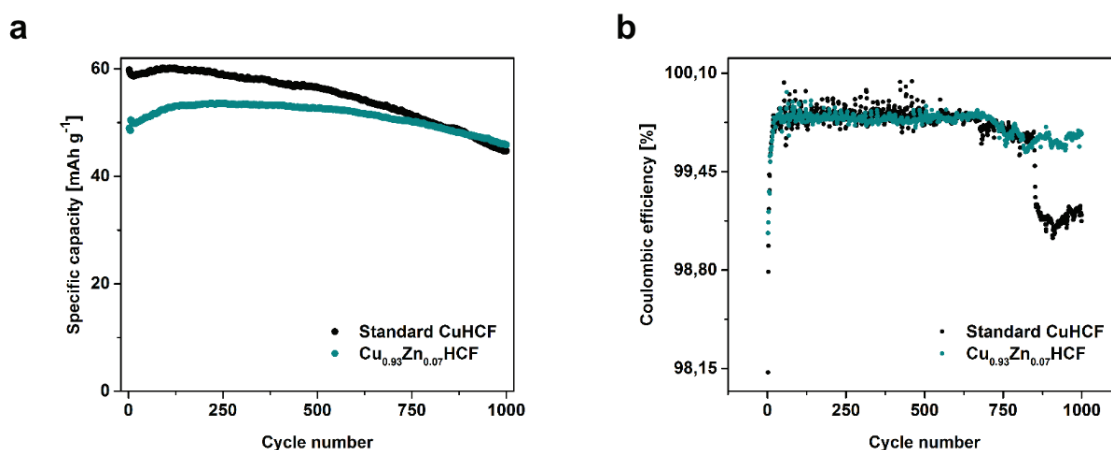


Figure 5-1. (a) Long-term cycling and (b) coulombic efficiencies of standard CuHCF and the Cu_{0.93}Zn_{0.07}HCF mixture at a 1C current rate in 20 mM ZnSO₄.

Table 5-1. Percentages of energy and charge retention and the coulombic efficiency values for the standard CuHCF and Cu_{0.93}Zn_{0.07}HCF mixture at a 1C rate after 500 and 1000 cycles in 20 mM ZnSO₄.

	20 mM ZnSO ₄ Solution					
	After 500 cycles			After 1000 cycles		
	Energy	Charge	Coulombic efficiency	Energy	Charge	Coulombic efficiency
Standard CuHCF	103.83%	94%	99.76%	80.88%	74.35%	99.16%
Cu _{0.93} Zn _{0.07} HCF	123.11%	98.12%	99.8%	87.74%	85.54%	99.7%

Although the initial specific capacity of the Cu_{0.93}Zn_{0.07}HCF mixture was lower than the standard CuHCF (59.8 mAh g⁻¹), it exhibited a better performance after 1000 cycles with a

capacity loss of ~11% only (as compared to standard CuHCF). Standard CuHCF was only able to deliver ~74% of its initial capacity upon cycling and based on the battery life cycle definition it was basically a spent battery. Moreover, the coulombic efficiency for the standard CuHCF dropped to ~99% after 750 cycles. However, this value stayed stable at around 99.7% for the Cu_{0.93}Zn_{0.07}HCF mixture. After the cycling, the pH of the electrolyte was also measured for both samples. The pH value of the 20 mM ZnSO₄ solutions after 1000 cycles for the standard CuHCF was 5.98 and for the Cu_{0.93}Zn_{0.07}HCF was 6.6. This suggests that upon cycling, the pH value of the 20 mM ZnSO₄ stays close to the neutral value which is a positive factor for employing this environmentally friendly system in a stationary application.

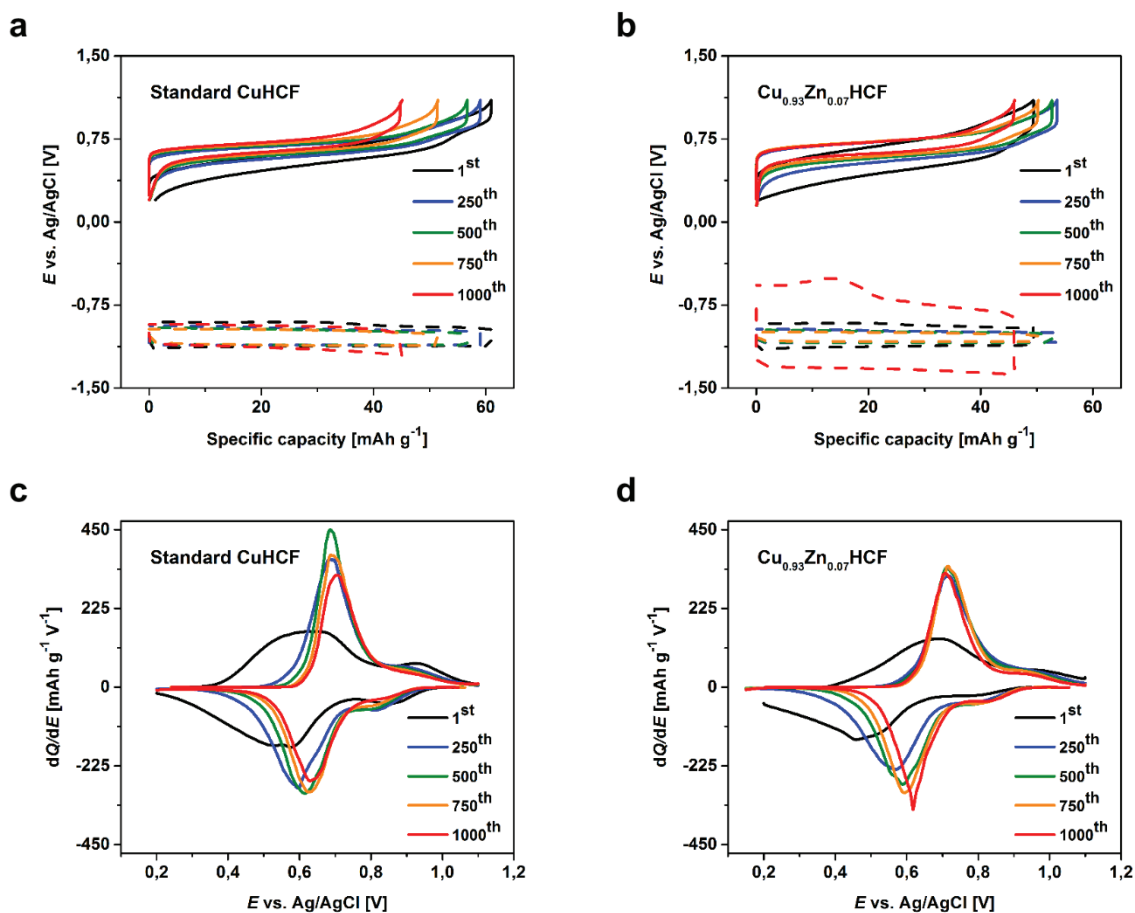


Figure 5-2. Potential profiles of (a) standard CuHCF (solid line) and (b) Cu_{0.93}Zn_{0.07}HCF mixture (solid line) at a 1C current rate in 20 mM ZnSO₄, potential profiles of the Zn foil counter electrode is shown with dashed line in both graphs. (c,d) Differential specific charge profiles at different numbers of cycles for standard CuHCF and the Cu_{0.93}Zn_{0.07}HCF mixture measured at a 1C current rate in 20 mM ZnSO₄, respectively.

Since the Cu_{0.93}Zn_{0.07}HCF mixture presented remarkable stability, it is important to understand how different its potential profiles and differential specific charge profiles were from the standard CuHCF. Fig. 5-2 indicates the potential profiles and differential specific charge profiles for the Cu_{0.93}Zn_{0.07}HCF mixture and standard CuHCF. By comparing Figs. 5-2a and

5-2b, it is clear that the mid-composition reaction potential in both cases increased during cycling, although no particular change in the curve shape was observed. In the differential profiles for both cases, two oxidation and reduction peaks were visible. However, the intensity of the second set of redox peaks was much smaller than the first and did not raise significantly during cycling. The intensities of the first set of redox peaks for both samples did increase, but after 500 cycles the standard CuHCF shifted more towards the lower values than the mixture did. These results suggest that upon cycling, a new phase(s) formed. Fig. 5-3 illustrates the changes in specific energy, charge, and average potential for the standard CuHCF and Cu_{0.93}Zn_{0.07}HCF mixture at different numbers of cycles.

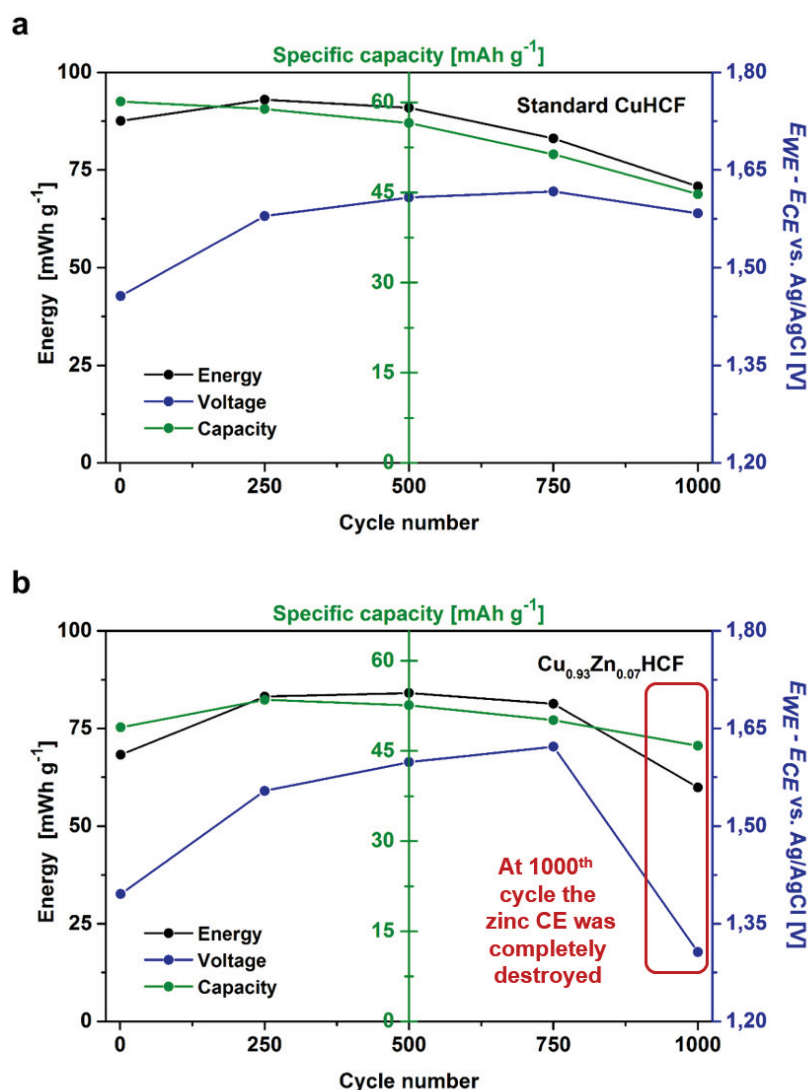


Figure 5-3. Specific energy, charge, and average potential provided by (a) the standard CuHCF and (b) the Cu_{0.93}Zn_{0.07}HCF mixture, at 1C current rate in 20 mM ZnSO₄ at different numbers of cycles.

From these graphs, it was possible to extract the energy retention for each sample after 1000 cycles (Table 5-1). For both samples, an increase in specific energy during cycling was

observed followed by a subsequent decrease. Although the standard CuHCF reached a higher energy density at around the 250th cycle than the Cu_{0.93}Zn_{0.07}HCF mixture, after 1000 cycles it delivered less specific energy (~80%). The reason that the total cell potential for the Cu_{0.93}Zn_{0.07}HCF mixture is low can be due to the high overpotential at the zinc negative electrode (Fig. 5-2b). The high overpotential is attributed to the zinc foil counter electrode which upon cycling got destroyed. Therefore, a decline for all three parameters (capacity, energy, and total cell voltage) in Fig. 5-3b was visible. Hence, the results for the Cu_{0.93}Zn_{0.07}HCF mixture after the 750th cycle are not representative.

In a modified DEMS-EIS cell (Section 2.4, Fig. 2-3b), a power test was conducted with the Cu_{0.93}Zn_{0.07}HCF mixture as an active material and a zinc counter electrode. Due to the cell configuration (i.e., a compact cell), it was supposed that the electrolyte resistance would decrease, and that the kinetic behavior would improve.

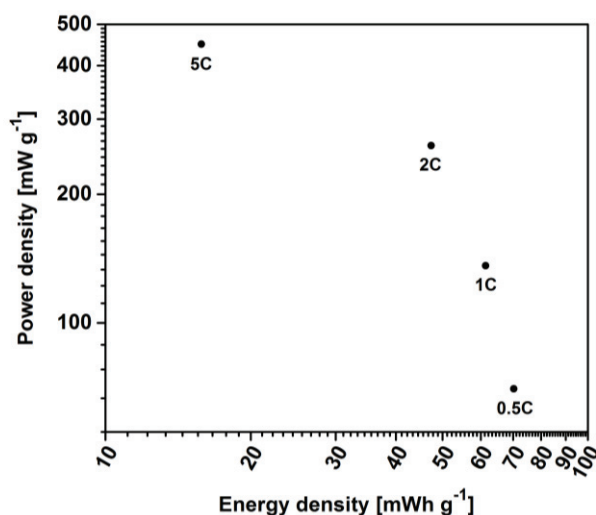


Figure 5-4. Ragone plot of the Cu_{0.93}Zn_{0.07}HCF/ZnSO₄/Zn battery. The power and energy densities were calculated based on the mass of the CuZnHCF active material.

Fig. 5-4 depicts the evolution of the power and energy densities with changes in current density. The maximum specific power density of 449 W kg⁻¹ was achieved at a 5C current rate. Hereby, the power density was higher than the one from the flooded geometric cell reported by Trócoli et al.^[142]. The specific energy density of the cell reported herein decreased from 70.2 Wh kg⁻¹ at 42 mA g⁻¹ (0.5C) to 15.8 Wh kg⁻¹ at 425 mA g⁻¹ (5C). It should be noted that by performing the measurement in a compact cell, the energy and power densities at high cycling rates improved in comparison with those of the flooded geometric cell.

In order to obtain a better understanding of the location of the ZIB introduced in relation to other EES systems, this battery is illustrated in the Ragone plot below. Since real energy storage devices contain passive elements, the values obtained from Fig. 5-4 were multiplied by a factor equal to 0.66 and were located in Fig. 5-5 (yellow area). Although this battery has a lower

specific power and energy compared to LIBs, it delivers an impressive performance, which is better than VRBs, and close to lead-acid batteries.

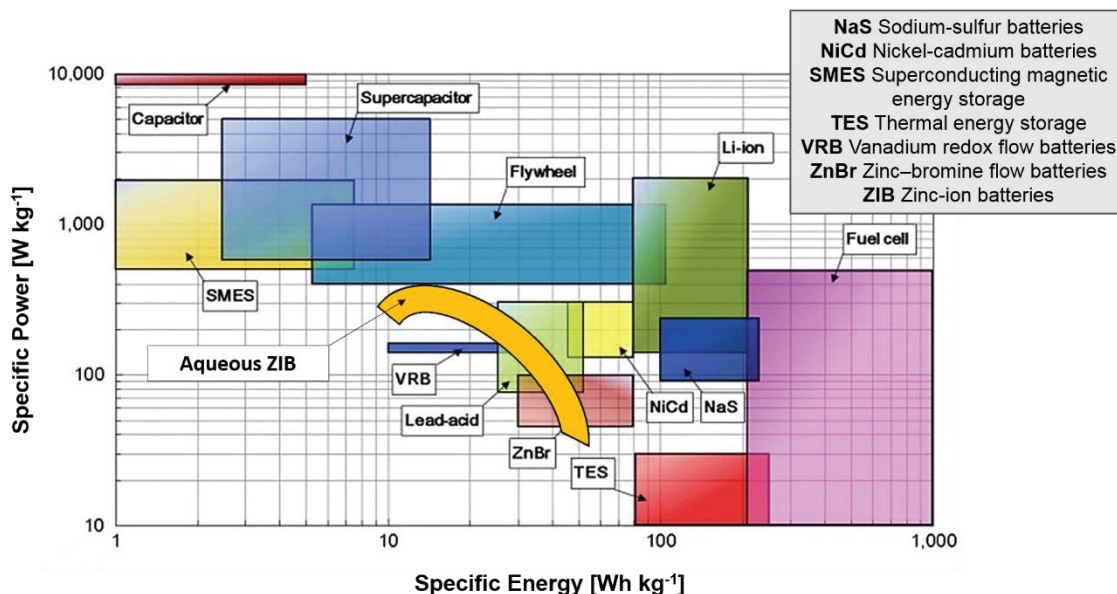


Figure 5-5. Comparison of specific powers and energies of different energy storage devices and the introduced aqueous zinc-ion battery based on $\text{Cu}_{0.93}\text{Zn}_{0.07}\text{HCF}$ (adapted from ^[211]).

To gather additional insight into the performance of standard CuHCF and the $\text{Cu}_{0.93}\text{Zn}_{0.07}\text{HCF}$ mixture, it was necessary to combine the electrochemical analysis with crystallographic techniques such as XRD, SEM, and EDX. Therefore, in the next section the crystallographic characterizations for both samples before and after 1000 cycles in 20 mM ZnSO_4 are discussed.

5.2. Crystallographic Characterization of Standard CuHCF and $\text{Cu}_{0.93}\text{Zn}_{0.07}\text{HCF}$ Mixture Before and After Cycling in 20 mM ZnSO_4

First, XRD analyses for the standard CuHCF and $\text{Cu}_{0.93}\text{Zn}_{0.07}\text{HCF}$ electrodes were conducted before and after cycling in 20 mM ZnSO_4 . Fig. 5-6 includes the XRD patterns for both samples. As it was already mentioned in Section 3.2, the amorphous humps around 25° and 44° 2θ can be attributed to the presence of C65 and the used carbon cloth (Fig. 3-9). After cycling, new reflections were visible for both. The new reflections in the $\text{Cu}_{0.93}\text{Zn}_{0.07}\text{HCF}$ were sharper and had higher intensities, which suggests that amount of the secondary phase(s) after cycling was higher than that of the standard CuHCF. However, for both samples the appearance of new reflections corresponded to a phase transformation. It is important to mention that in the potential profiles of both samples (Figs. 5-2a and 5-2b), no evidence of a clear two-step plateau was found. Additionally, the intensities of the second redox peaks in the differential specific charge profiles changed slightly during cycling. Although the second set of redox peaks did not

get sharper (which is typical for a two-phase reaction), the appearance of new reflections from the XRD data implies that an extra phase in addition to the original one formed in both samples during cycling.

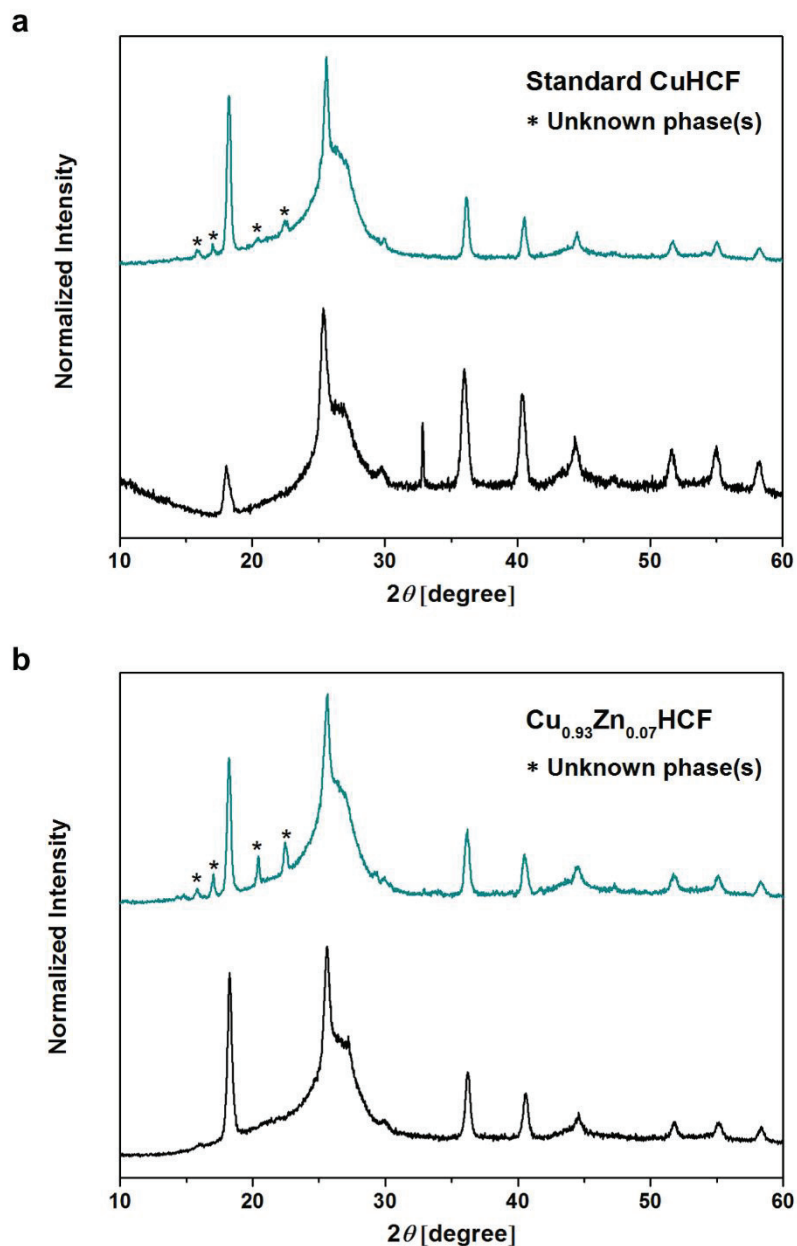


Figure 5-6. X-ray diffraction patterns of the (a) standard CuHCF electrode and (b) $\text{Cu}_{0.93}\text{Zn}_{0.07}\text{HCF}$ electrode before cycling (black) and after 1000 cycles (blue) at a 1C rate in 20 mM ZnSO_4 .

Therefore, it was necessary to employ another technique to obtain information about the samples before and after cycling. For this purpose, SEM-EDX studies were performed in order to obtain quantitative evaluation of the sample compositions. The SEM-EDX measurements of the samples have been done at fully discharged state. Before cycling, both samples consisted of

nanoparticles and big chunks (Fig. 5-7). The size of the nanoparticles ranged from 80 to 90 nm. The big chunks, however, consisted of hard agglomerations of spherical particles.

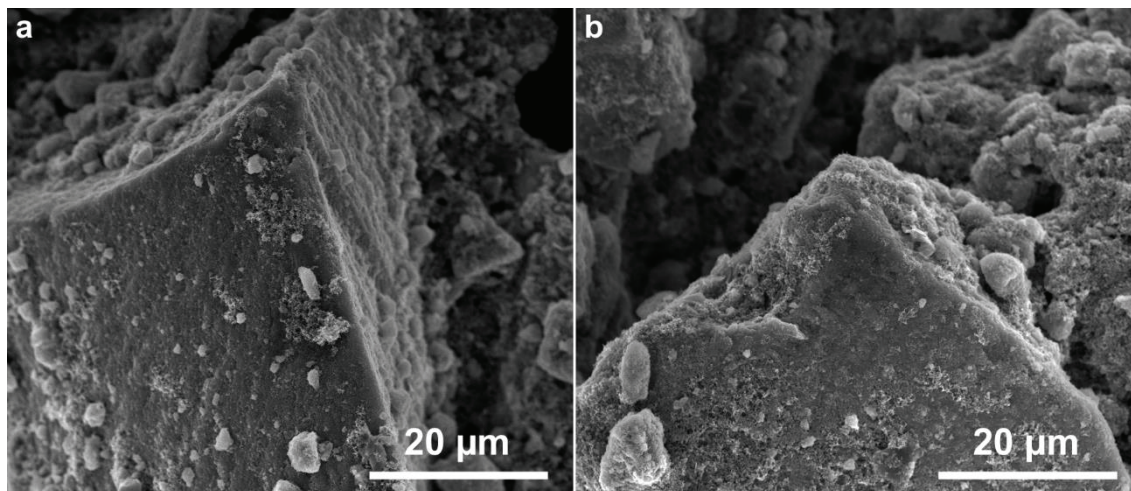


Figure 5-7. SEM images of the (a) standard CuHCF electrode and (b) $\text{Cu}_{0.93}\text{Zn}_{0.07}\text{HCF}$ electrode before cycling, with a scale bar of 20 μm .

After cycling, different morphologies were observed for both electrodes. Since the actual compositions were hard to determine the present morphologies will be named: phase 1, phase 2, and nanoparticles. As the initial samples (standard CuHCF and $\text{Cu}_{0.93}\text{Zn}_{0.07}\text{HCF}$) consisted of nanoparticles, detailed investigations were only conducted for the phase 1 and phase 2 morphologies. It should be noted that several EDX point measurements at different positions were analyzed for each morphology, but only the average values of similar compositions are reported in this work. Additionally, since the peaks given off as electrons return from the K electron shell of copper and zinc are overlapping, the following EDX representation data considered the peaks given off as electrons returning to the L electron shells for both atoms. SEM images are shown for each sample containing all of the explored compositions with similar morphologies.

First, the results of the cycled standard CuHCF electrode in 20 mM ZnSO_4 are presented. The first obtained morphology was named phase 1 and had a cubic shape. The cubes had an edge length of 3 to 15 μm . Based on this cubic morphology, two different compositions were revealed. Fig. 5-8a shows a SEM image containing exemplary EDX point measurements for two different compositions with the same morphology. Figs. 5-8b and 5-8c exhibit the EDX spectra; green crosses correspond with calculated average composition of phase 1-1 and orange crosses with calculated average composition of phase 1-2. As it is clear from these results, the cubic morphology consisted of iron- and zinc-rich compositions.

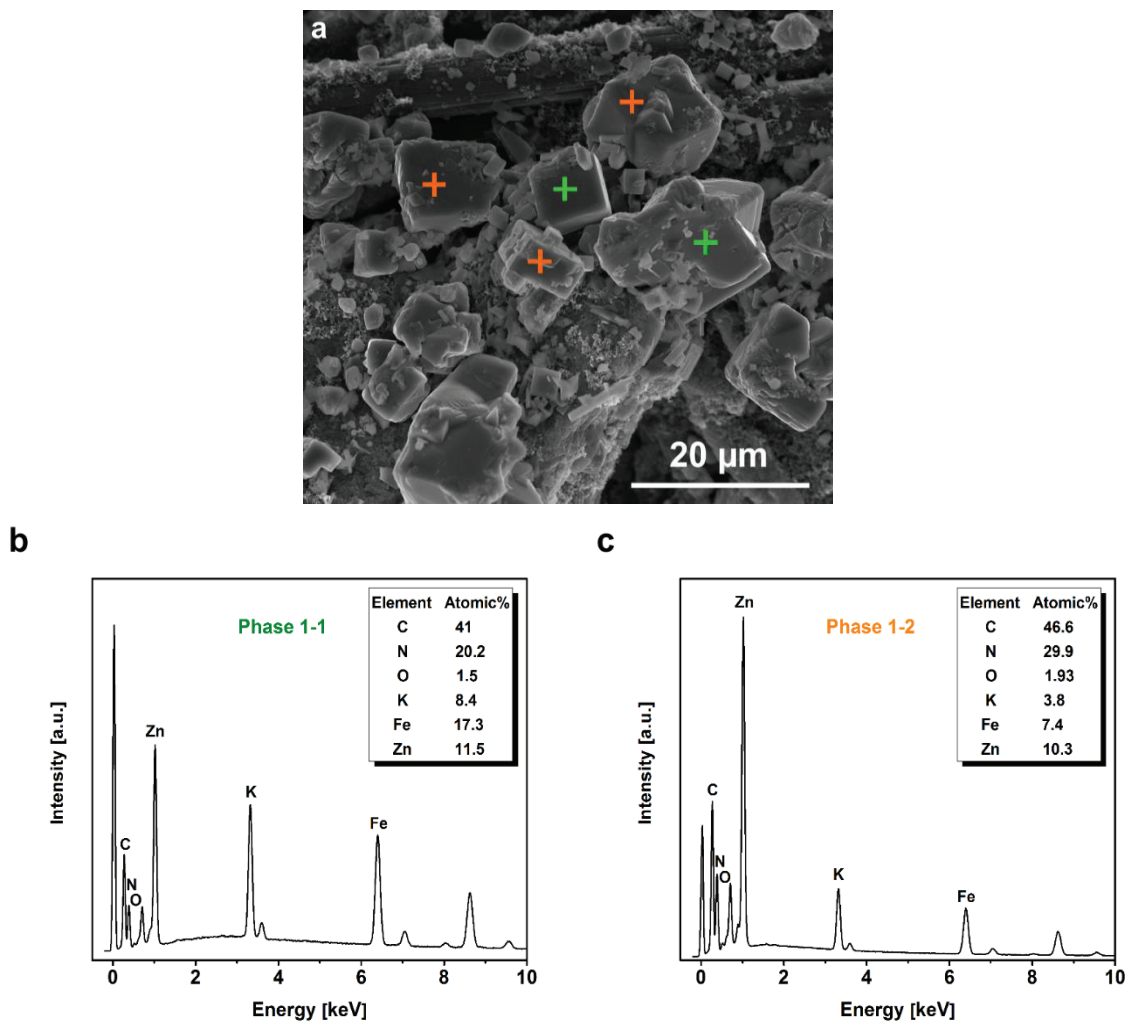


Figure 5-8. (a) SEM image of standard CuHCF electrode after 1000 cycles at a 1C rate in 20 mM ZnSO₄ with exemplary EDX point measurements, (b) exemplary EDX spectrum of the cubic morphology (green crosses) with calculated average composition (phase 1-1), and (c) exemplary EDX spectrum of the cubic morphology (orange crosses) with calculated average composition (phase 1-2).

An interesting point is that no evidence of copper was observed in either composition. This suggests that new phases formed upon cycling, which is in agreement with the XRD data. Based on the normalized values on iron phase 1-2 had almost double the amount of zinc and potassium compared to phase 1-1. By cancelling out the carbon, nitrogen, and oxygen, it is possible to calculate the ratios of potassium to iron and zinc for each composition. These ratios are reported in Table 5-2.

Table 5-2. Ratios of potassium to iron and zinc at each composition with a cubic morphology for cycled standard CuHCF electrode in 20 mM ZnSO₄.

Phase	K : Fe : Zn ratio
Phase 1-1	0.5 : 1 : 0.7
Phase 1-2	0.96 : 1 : 1.5

From these results, it can be concluded that the formation of new phases upon cycling took place based on the phase transformation mechanism (Fig. 3-14a). These new phases were either composed by KZnHCF or a mixture of iron-substituted zinc hexacyanoferrate (KZnFeHCF).

Fig. 5-9 includes a SEM image and the respective EDX spectra for phase 2. Figs. 5-9b to 5-9d show the EDX spectra with the calculated average compositions shown by blue crosses (phase 2-1), green crosses (phase 2-2), and orange crosses (phase 2-3).

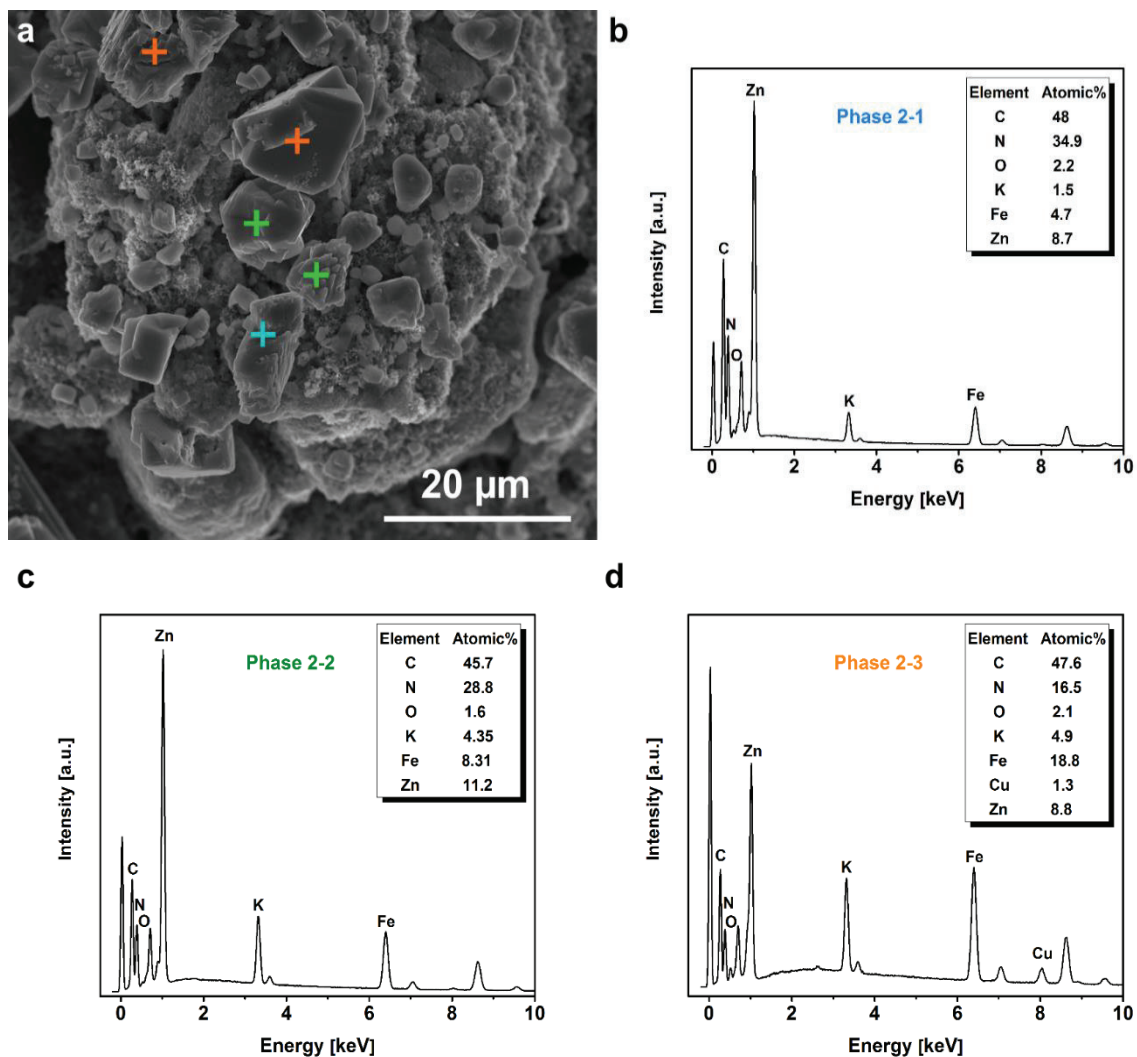


Figure 5-9. (a) SEM image of standard CuHCF electrode after 1000 cycles at a 1C rate in 20 mM ZnSO₄ with exemplary EDX point measurements, (b) exemplary EDX spectrum of the non-cubic morphology (blue cross) with calculated average composition (phase 2-1), (c) exemplary EDX spectrum of the non-cubic morphology (green crosses) with calculated average composition (phase 2-2), and (d) exemplary EDX spectrum of the non-cubic morphology (orange crosses) with calculated average composition (phase 2-3).

Phase 2 was another morphology observed in the standard CuHCF electrode after cycling. As it is clear from the SEM image, this non-cubic shaped phase consisted of big flakes not fully grown and with no regular shape. Here, the flakes had an edge length of 3 to 10 μm.

From the EDX data, three different compositions were found. Two compositions included higher amounts of zinc and no presence of copper, while the other one was an iron-rich phase with copper. The difference between phases 2-1 and 2-2 was the amount of potassium and zinc. In particular, based on the normalized values on iron the amount of potassium was almost 1.5 times higher and zinc ~1.4 times lower in phase 2-2 than in phase 2-1.

By extracting data from the EDX spectra, the ratio of potassium to iron, copper, and zinc in each composition with the same morphology could be summarized (Table 5-3). These results suggest that the newly formed phases were KZnHCF, KZnFeHCF, and KCuZnHCF.

Table 5-3. The ratio of potassium to iron, copper, and zinc at each composition with a non-cubic morphology for cycled standard CuHCF electrode in 20 mM ZnSO₄.

Phase	K : Fe : Cu : Zn ratio
Phase 2-1	0.35 : 1 : 0 : 1.88
Phase 2-2	0.53 : 1 : 0 : 1.35
Phase 2-3	0.26 : 1 : 0.08 : 0.5

Similar experiments were conducted for a Cu_{0.93}Zn_{0.07}HCF electrode after 1000 cycles. Two different morphologies were detected, phase 1 and phase 2, in which phase 1 had a cubic morphology and phase 2 was non-cubic. Fig. 5-10 consists of the SEM image and EDX spectra for phase 1. The EDX spectra with the calculated average composition are shown by green crosses (phase 1-1); the other is illustrated with orange crosses also with calculated average composition (phase 1-2) (Figs. 5-10b and 5-10c, respectively). Both phases were zinc-rich and similar to those obtained from standard CuHCF (Fig. 5-8); they did not contain any copper. One of the differences between the cubes after cycling in Cu_{0.93}Zn_{0.07}HCF and standard CuHCF were their shape and form. In particular, in the case of the Cu_{0.93}Zn_{0.07}HCF, the cubes were well-shaped and fully grown upon cycling, with an edge length of 2 to 12 μm.

The EDX data were used to determine the ratio of potassium to iron and zinc for each composition with a cubic morphology for the cycled Cu_{0.93}Zn_{0.07}HCF electrode (Table 5-4).

Table 5-4. The ratio of potassium to iron and zinc at each composition with a cubic morphology for the cycled Cu_{0.93}Zn_{0.07}HCF electrode in 20 mM ZnSO₄.

Phase	K : Fe : Zn ratio
Phase 1-1	0.4 : 1 : 1.9
Phase 1-2	0.4 : 1 : 1

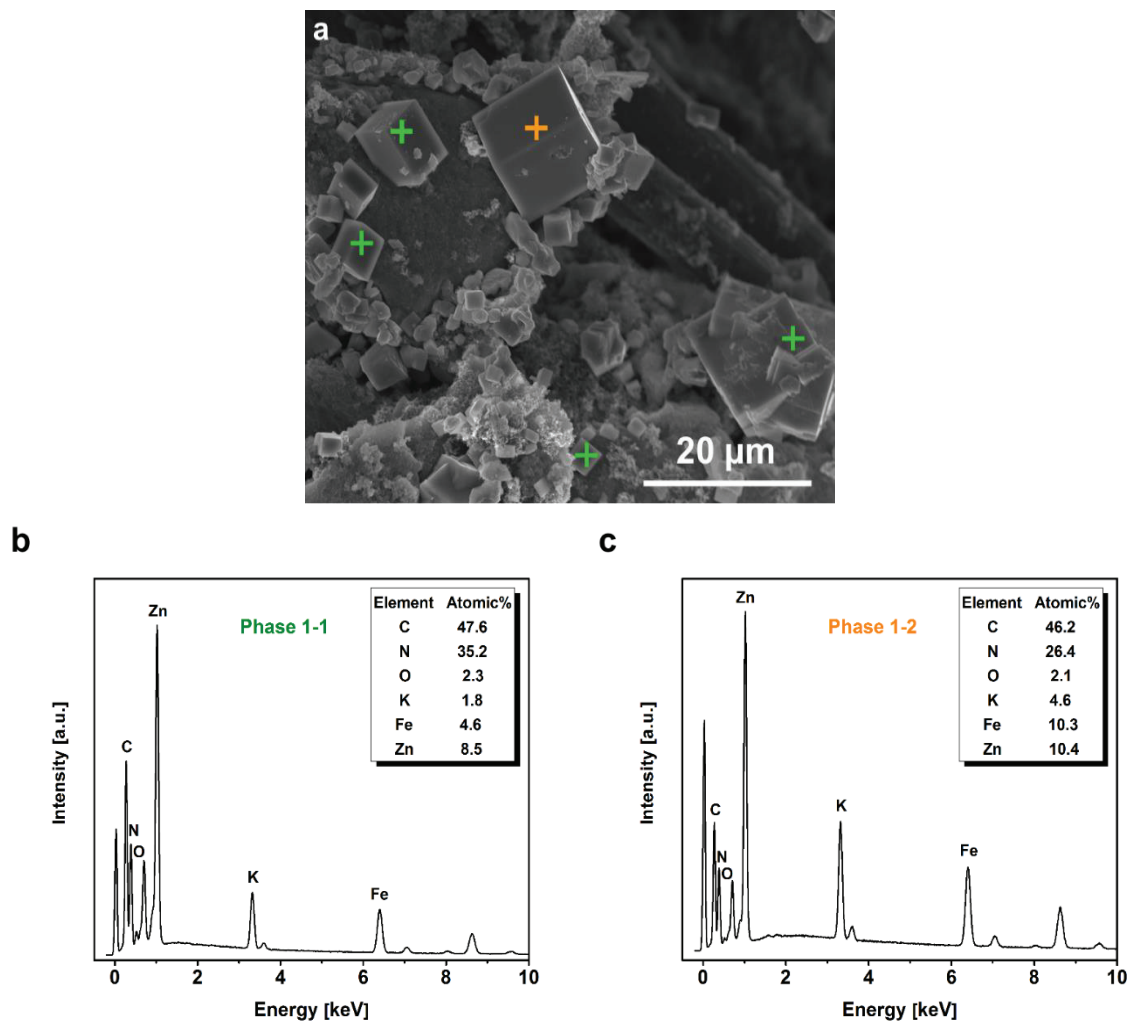


Figure 5-10. (a) SEM image of $\text{Cu}_{0.93}\text{Zn}_{0.07}\text{HCF}$ electrode after 1000 cycles at a 1C rate in 20 mM ZnSO_4 with exemplary EDX point measurements, (b) exemplary EDX spectrum of the cubic morphology (green crosses) with calculated average composition (phase 1-1), and (c) exemplary EDX spectrum of the cubic morphology (orange crosses) with calculated average composition (phase 1-2).

By comparing these data with Table 5-2, it can be concluded that though the morphologies of both samples were the same, based on the normalized values on iron the compositions were quite different. In the case of pure CuHCF, not only did the potassium increase, but also the zinc (in phase 1-2, as compared to phase 1-1). Conversely, in $\text{Cu}_{0.93}\text{Zn}_{0.07}\text{HCF}$, the amount of zinc in one composition was double that of the other. Therefore, the newly formed phases can be considered derivatives of KZnHCF or a mixture of KZnFeHCF.

Finally, SEM and EDX analyses were conducted for the second morphology observed in the cycled $\text{Cu}_{0.93}\text{Zn}_{0.07}\text{HCF}$ electrode. The edge length range for these particles was 5 to 14 μm . This morphology consisted of only two compositions, one iron-rich and the other zinc-rich. The EDX spectra with calculated average composition indicated by orange crosses (phase 2-1) and the EDX spectra with calculated average composition represented by green crosses (phase 2-2)

are shown in Figs. 5-11b and 5-11c, respectively. From the EDX data, the ratios of potassium to iron, copper, and zinc for each composition with a non-cubic morphology are reported in Table 5-5.

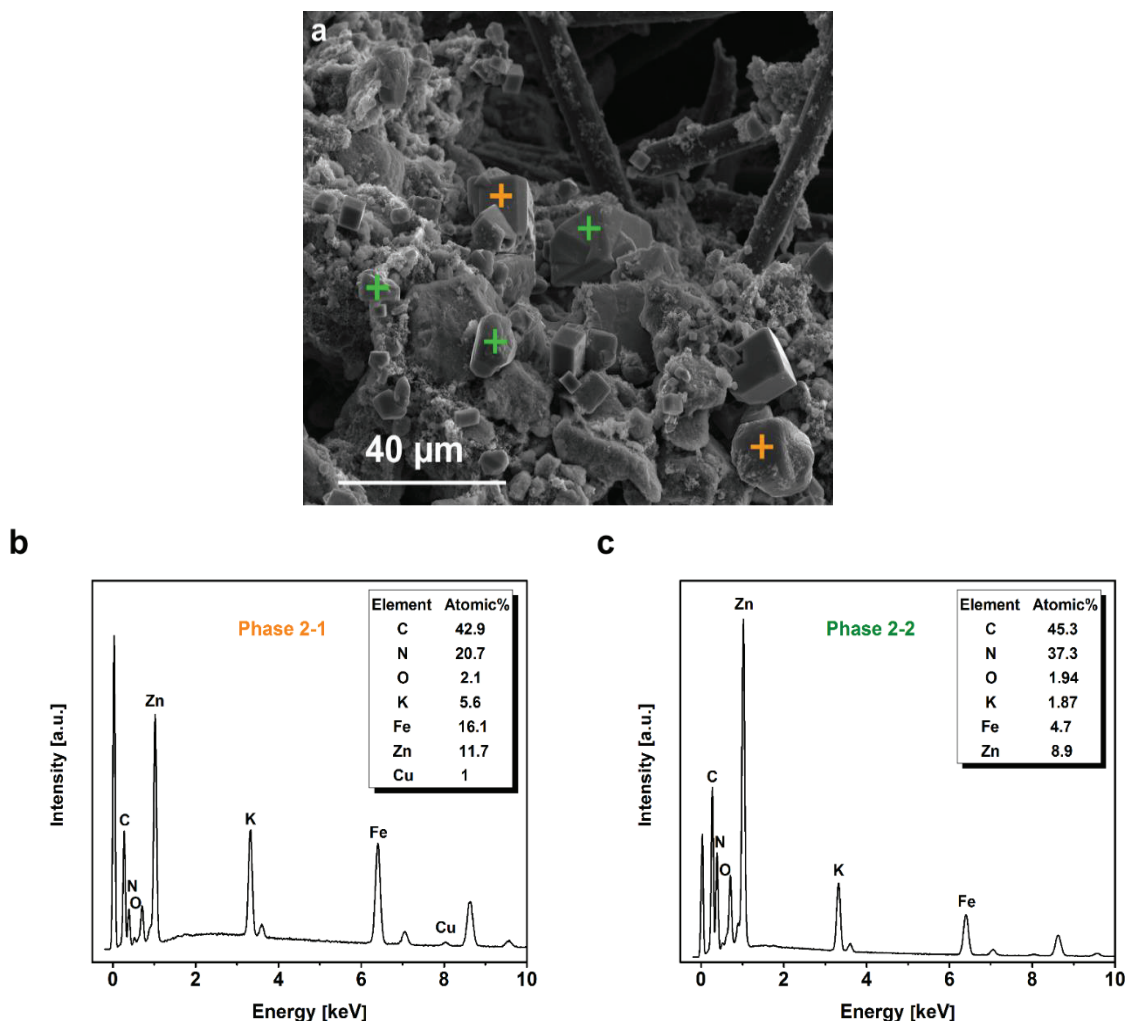


Figure 5-11. (a) SEM image of $\text{Cu}_{0.93}\text{Zn}_{0.07}\text{HCF}$ electrode after 1000 cycles at a 1C rate in 20 mM ZnSO_4 with exemplary EDX point measurements, (b) exemplary EDX spectrum of the non-cubic morphology (orange crosses) with calculated average composition (phase 2-1), and (c) exemplary EDX spectrum of the non-cubic morphology (green crosses) with calculated average composition (phase 2-2).

Table 5-5. Ratios of potassium to iron, copper, and zinc at each composition with a non-cubic morphology for the cycled $\text{Cu}_{0.93}\text{Zn}_{0.07}\text{HCF}$ electrode in 20 mM ZnSO_4 .

Phase	K : Fe : Cu : Zn ratio
Phase 2-1	0.34 : 1 : 0.07 : 0.79
Phase 2-2	0.4 : 1 : 0 : 1.9

It is clear that in both compositions, based on the normalized values on iron the amounts of potassium and iron were almost the same, but the zinc in phase 2-2 was ~2.4 times higher than in phase 2-1. Another difference was the presence of copper in phase 2-1, which suggests that not only was KZnHCF formed upon cycling, but also a mixture of KCuZnHCF or

KCuZnFeHCF evolved. It is worth mentioning that the ratio of potassium to iron, copper, and zinc in phase 2-1 and phase 2-2 of cycled $\text{Cu}_{0.93}\text{Zn}_{0.07}\text{HCF}$ electrode is similar to phase 2-3 and phase 2-1 of the cycled standard CuHCF electrode, respectively; i.e. almost the same compositions at the same morphology have been derived for both samples upon cycling in 20 mM ZnSO_4 .

To conclude, it should be mentioned that the $\text{Cu}_{0.93}\text{Zn}_{0.07}\text{HCF}$ showed excellent electrochemical performance compared to the standard CuHCF. This mixture delivered 85.54% capacity retention and 87.74% energy retention after 1000 cycles in 20 mM ZnSO_4 . The maximum specific power density of 449 W kg^{-1} at a 5C current rate was achieved in the compact cell; this value was higher than what was reported in the literature [142]. With the help of crystallographic techniques, it was possible to confirm the occurrence of the phase transformation mechanism for both the standard CuHCF and $\text{Cu}_{0.93}\text{Zn}_{0.07}\text{HCF}$ mixture samples. However, with the GCPL technique, no clear change in the shapes of the potential profiles or increase in the second set of redox peaks upon cycling was observed. In fact, phase transformation was responsible for the increase in (de-)intercalation potential; it contributed to the energy retention. In both cases, energy retention with respect to capacity retention was higher. This was due to an increase in the total cell voltage. As the (de-)intercalation potential shifted to higher values, it allowed the material to reach superior energy levels. From the SEM-EDX measurements of both samples after 1000 cycles, it was determined that adding to the original phase (nanoparticles), two other morphologies were present: a cubic morphology (phase 1) and a non-cubic morphology (phase 2). Each morphology consisted of at least two different compositions. All of the achieved compositions were either iron-rich or zinc-rich. However, in some compositions a small amount of copper was also present. In particular, in the cubic morphology (phase 1) of both samples, no copper was observed, and the possible compositions could have been either KZnHCF or KZnFeHCF. For the non-cubic morphology (phase 2), compositions with and without copper were obtained, which plausibly could have been KZnHCF, KZnFeHCF, KZnCuFeHCF, or KCuZnHCF.

In sum, substituting zinc in the standard CuHCF structure with a Cu:Zn ratio of 93:7 enabled the battery to be cycled more than 1000 times with high stability, even when the phase transformation mechanism occurred. The structure of the standard CuHCF improved and the degradation of the active material was postponed.

Since achieving a system with high power, high concentration electrolytes is necessary, in the next parts the electrochemical and crystallographic characterizations of standard CuHCF and $\text{Cu}_{0.93}\text{Zn}_{0.07}\text{HCF}$ in 100 mM ZnSO_4 are described.

5.3. Electrochemical Characterization of Standard CuHCF and the Cu_{0.93}Zn_{0.07}HCF Mixture in 100 mM ZnSO₄

Fig. 5-12 shows the long-term cycling and coulombic efficiency for standard CuHCF and the Cu_{0.93}Zn_{0.07}HCF mixture at a 1C current rate in 100 mM ZnSO₄. The capacity retention values and coulombic efficiencies after 1000 cycles for both samples are reported in Table 5-6.

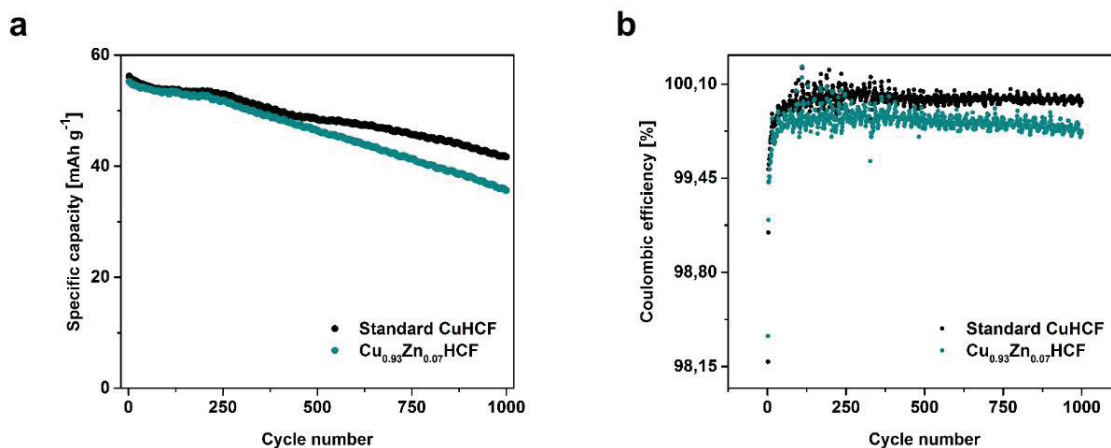


Figure 5-12. (a) Long-term cycling and (b) coulombic efficiencies of standard CuHCF and the Cu_{0.93}Zn_{0.07}HCF mixture at a 1C current rate in 100 mM ZnSO₄.

Unfortunately, the performance of the Cu_{0.93}Zn_{0.07}HCF was not as good as in 20 mM ZnSO₄. However, it should be remembered that higher electrolyte concentrations are boosting the aging of the active material and cause faster degradation, as it was shown in Chapter 3. From the potential profiles, the two-step plateau and increase in the average cell voltage and number of cycles can be observed for both samples. The differential specific charge profiles also showed the appearance of the second redox peaks, owing to the phase transformation mechanism; their intensities increased with the number of cycles.

Table 5-6. Percentages of energy and charge retention for the standard CuHCF and Cu_{0.93}Zn_{0.07}HCF mixture at a 1C rate after 500 and 1000 cycles in 100 mM ZnSO₄.

	100 mM ZnSO ₄ Solution					
	After 500 cycles			After 1000 cycles		
	Energy	Charge	Coulombic efficiency	Energy	Charge	Coulombic efficiency
Standard CuHCF	94.4%	85.40%	99.98%	82.57%	73.53%	99.97%
Cu _{0.93} Zn _{0.07} HCF	90.96%	83.62%	99.82%	70.89%	64.1%	99.78%

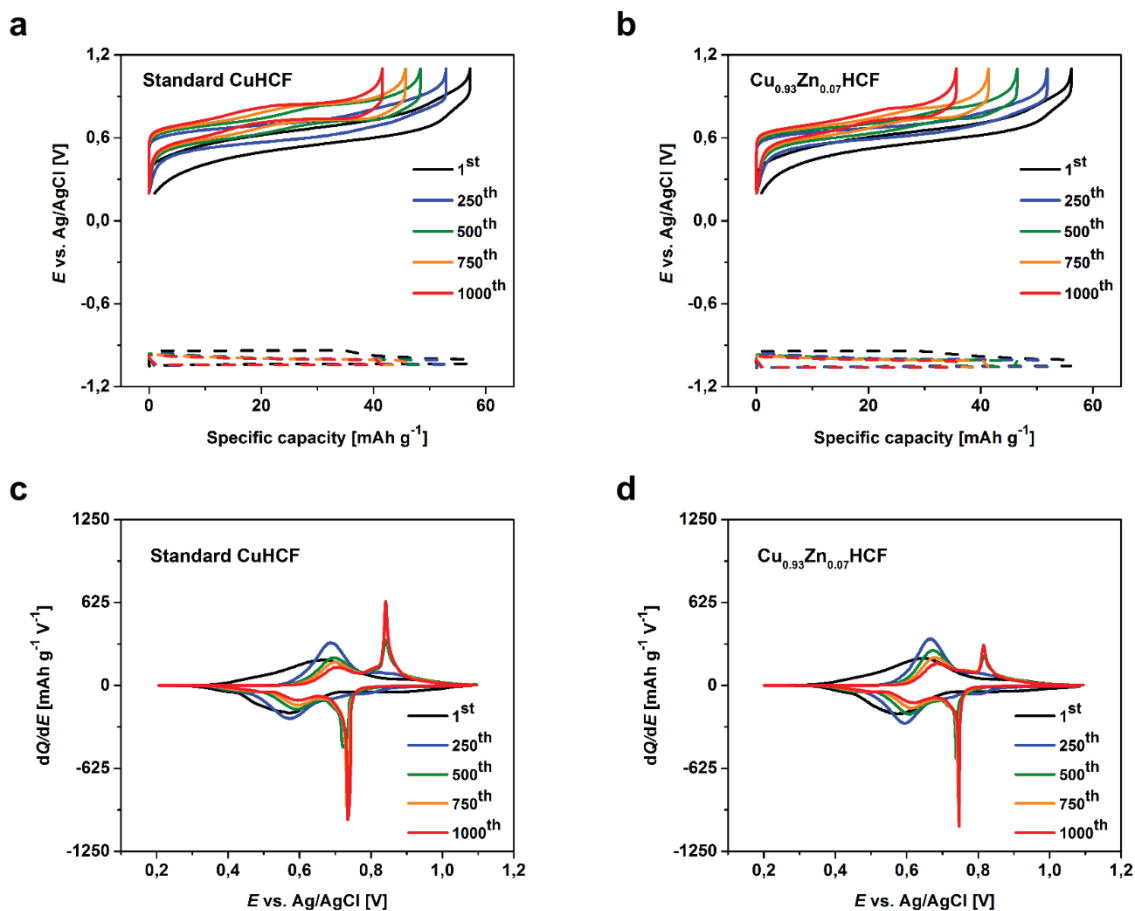


Figure 5-13. (a,b) Potential profiles of the (a) standard CuHCF (solid line), (b) Cu_{0.93}Zn_{0.07}HCF mixture (solid line) at a 1C current rate in 100 mM ZnSO₄, potential profiles of the Zn foil counter electrode is shown with dashed line in both graphs. (c,d) Differential specific charge profiles at different numbers of cycles for the standard CuHCF and Cu_{0.93}Zn_{0.07}HCF mixture measured at a 1C current rate in 100 mM ZnSO₄, respectively.

It is also worth mentioning that the Cu_{0.93}Zn_{0.07}HCF had a smaller overpotential compared to the standard CuHCF, but the amount of charge and energy delivered after even 500 cycles were both lower. Although after 500 cycles the capacity faded in both samples, continued cycling up to 1000 cycles was attempted because at times the material can stabilize upon cycling. However, this did not happen here. As a result of the two-step plateau and an increase in the (de-)intercalation potential, the total cell voltage increased upon cycling (Fig. 5-14).

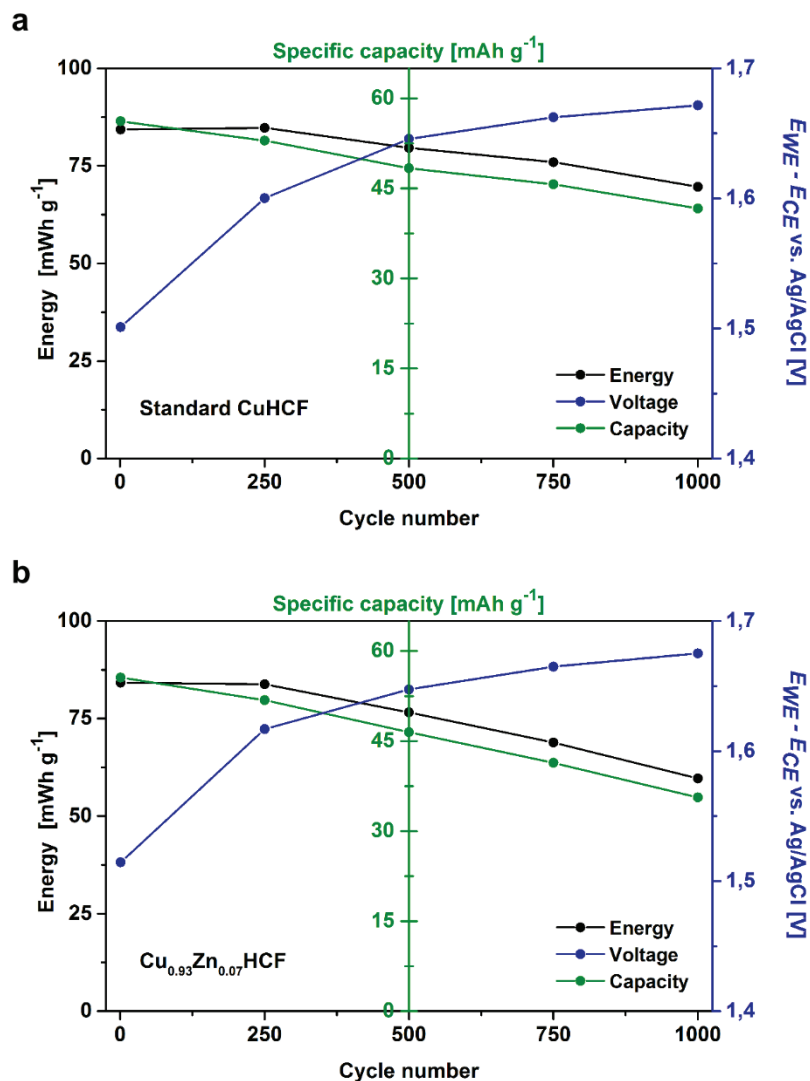


Figure 5-14. Specific energy, charge, and average potential provided by the (a) standard CuHCF and (b) Cu_{0.93}Zn_{0.07}HCF mixture at a 1C current rate in 100 mM ZnSO₄ at different numbers of cycles.

From these results, it was determined that the electrochemical performance of Cu_{0.93}Zn_{0.07}HCF upon cycling in 100 mM ZnSO₄ was worse than in 20 mM ZnSO₄. Therefore, to investigate the effects of phase transformation, XRD, SEM, and EDX analyses were conducted for standard CuHCF and Cu_{0.93}Zn_{0.07}HCF electrodes after cycling.

5.4. Crystallographic Characterization of Standard CuHCF and Cu_{0.93}Zn_{0.07}HCF Mixture Before and After Cycling in 100 mM ZnSO₄

XRD measurements have been done for standard CuHCF and Cu_{0.93}Zn_{0.07}HCF electrodes before and after cycling in 100 mM ZnSO₄ (Fig. 5-15).

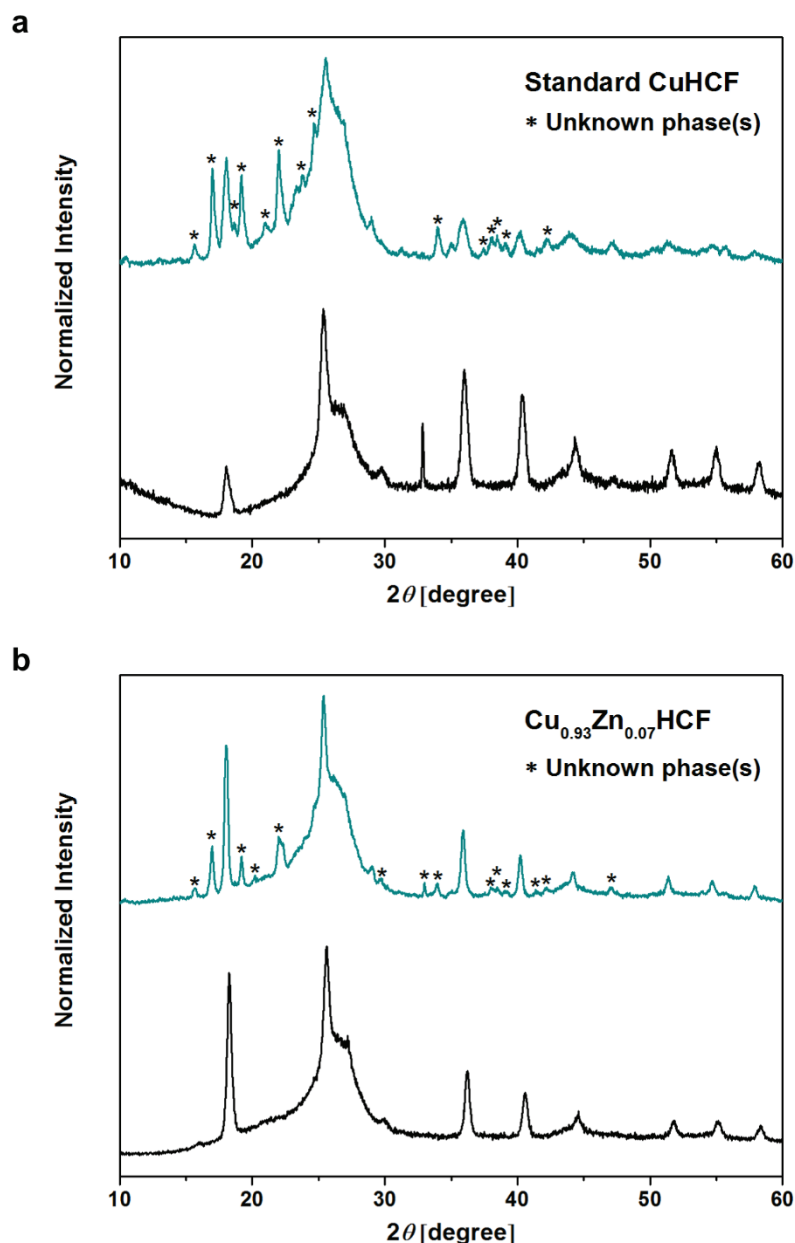


Figure 5-15. X-ray diffraction patterns of (a) standard CuHCF electrode and (b) Cu_{0.93}Zn_{0.07}HCF electrode before cycling (black) and after 1000 cycles (blue) at 1C rate in 100 mM ZnSO₄.

Both electrodes have been cycled till fully oxidized state, while afterwards XRD tests have been run. As described before the amorphous humps around 25° and 44° 2θ are attributed to the presence of C65 and carbon cloth, respectively (Fig. 3-9). XRD patterns of both samples have

shown the presence of additional new reflections after cycling. In the XRD pattern of standard CuHCF after cycling, the new reflections (new phases) have higher intensities than in Cu_{0.93}Zn_{0.07}HCF that can suggest that the amount of the secondary phase(s) in this sample is higher than in the mixture. In addition to the original CuHCF phase, extra phase(s) have been formed upon cycling. Some of these new formed reflections are matching with the ones for the sample cycled in 20 mM ZnSO₄ (Fig. 5-6), while others are still unknown. The appearances of the new reflections in 100 mM ZnSO₄ are also in agreement with the electrochemical analysis.

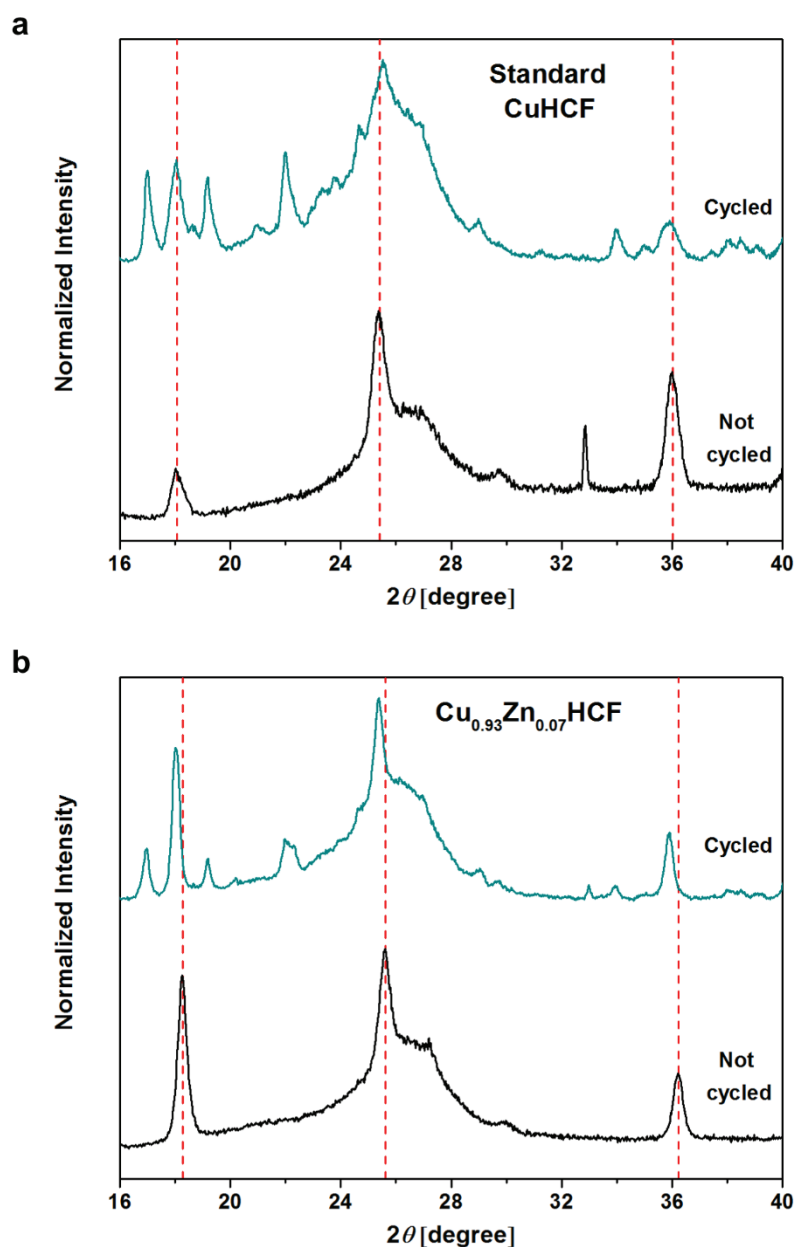


Figure 5-16. X-ray diffraction patterns of (a) standard CuHCF electrode and (b) Cu_{0.93}Zn_{0.07}HCF electrode before cycling (black) and after 1000 cycles (blue) at 1C rate in 100 mM ZnSO₄ between 16° and 40° 2θ angle.

It is interesting that in 20 mM ZnSO₄ the appearance of the new phase(s) has a negative effect on the electrochemical performance of standard CuHCF and lead to earlier degradation of the active material. On the contrary, it seems like the formation of new phase(s) in 100 mM ZnSO₄ does not have a negative effect as much as in 20 mM ZnSO₄. This suggests that the appeared new phases (unidentified ones) in standard CuHCF sample cycled in 100 mM ZnSO₄ can have different nature and compositions compared to the ones in 20 mM ZnSO₄. It is possible that the formed new phases at 100 mM ZnSO₄ for Cu_{0.93}Zn_{0.07}HCF sample are electrochemically inactive, which suggests that in the new formed phases no vacancy/empty sites remain in the lattice for (de-)intercalation of zinc ions. To investigate the effect of cycling on the lattice parameters, a zoom in of the XRD patterns of standard CuHCF and Cu_{0.93}Zn_{0.07}HCF samples after cycling between 16° and 40° 2θ angle is shown in Fig. 5-16. In this figure, a shift of the (200), (220), and (400) reflections can be observed. In the case of standard CuHCF, the position of these reflections before and after cycling did not drastically change, while in the case of Cu_{0.93}Zn_{0.07}HCF, the reflections shifted to lower 2θ angles. A shift to lower 2θ angle can be either attribute to an increase of lattice parameter upon cycling, which is accompanied by volume expansion of the unit-cell for the initial phase (Cu_{0.93}Zn_{0.07}HCF) or due to sample offset since no reference material was used.

Since the results of these samples, which were cycled in 100 mM, are different from ones in 20 mM ZnSO₄, it is important to investigate the composition of the new formed phases in each sample after cycling in order to explain the poor electrochemical performance especially in the case of Cu_{0.93}Zn_{0.07}HCF. Therefore, a quantitative evaluation of the composition of the present phases was performed via SEM-EDX. For both electrodes, four different morphologies have been found. For the cycled standard CuHCF these morphologies are namely phase 1, phase 3, phase 4, and nanoparticles and for the cycled Cu_{0.93}Zn_{0.07}HCF are phase 1, phase 3, phase 5, and nanoparticles. In this section only the detailed investigations for phase 1, phase 3, phase 4 and phase 5 morphologies are noted. Here, the EDX measurements were done similar to Section 5.2. First, the results of the cycled standard CuHCF electrode after 1000 cycles in 100 mM ZnSO₄ is shown. Fig. 5-17a, represents the morphology of phase 1 which had a cubic shape. The cubes had an edge length of 2 to 10 μm. Based on this cubic morphology, three different compositions could be revealed. Fig. 5-17a shows a SEM image containing exemplary EDX point measurements for three different compositions with the same morphology. Figs. 5-17b to 5-17d exhibit the EDX spectra including the orange crosses correspond with calculated average composition of phase 1-1, green crosses with calculated average composition of phase 1-2, and blue crosses with calculated average composition of phase 1-3.

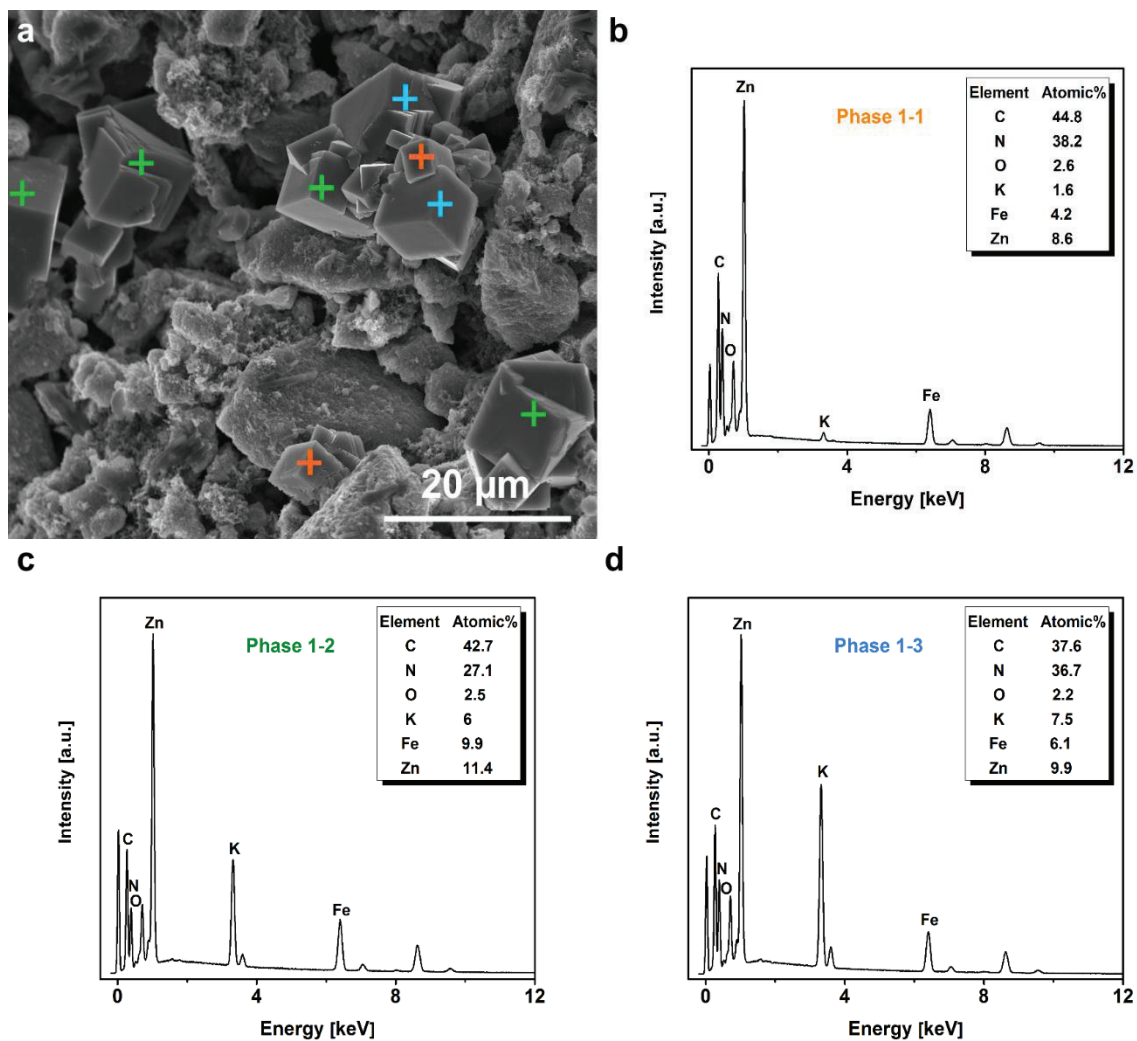


Figure 5-17. (a) SEM image of standard CuHCF electrode after 1000 cycles at a 1C rate in 100 mM ZnSO₄ with exemplary EDX point measurements, (b) exemplary EDX spectrum of the cubic morphology (orange crosses) with calculated average composition (phase 1-1), (c) exemplary EDX spectrum of the cubic morphology (green crosses) with calculated average composition (phase 1-2), and (d) exemplary EDX spectrum of the cubic morphology (blue crosses) with calculated average composition (phase 1-3).

These results suggest that the cubic morphologies only include zinc-rich compositions while no copper is present in any of the compositions. In compositions phase 1-1 and 1-2, after zinc the amount of iron was higher than potassium ($Zn > Fe > K$), while in phase 1-3 the potassium value was higher than iron ($Zn > K > Fe$). By cancelling out the carbon, nitrogen, and oxygen, it is possible to calculate the ratios of potassium to iron and zinc for each composition. These ratios are reported in Table 5-7.

Table 5-7. The ratio of potassium to iron and zinc for each composition with a cubic morphology for cycled standard CuHCF electrode in 100 mM ZnSO₄.

Phase	K : Fe : Zn ratio
Phase 1-1	0.36 : 1 : 2.1
Phase 1-2	0.58 : 1 : 1.25
Phase 1-3	1.25 : 1 : 1.72

Based on these results, it can be noted that the formation of new phases upon cycling took place based on the phase transformation mechanism (Section 3.4). These new phases were either composed by KZnHCF or a mixture of iron-substituted zinc hexacyanoferrate (KZnFeHCF).

In Fig. 5-18, the SEM image and the respective EDX spectra for phase 3 is reported. The phase had a needle shaped morphology with an edge length of 2 to 18 μm.

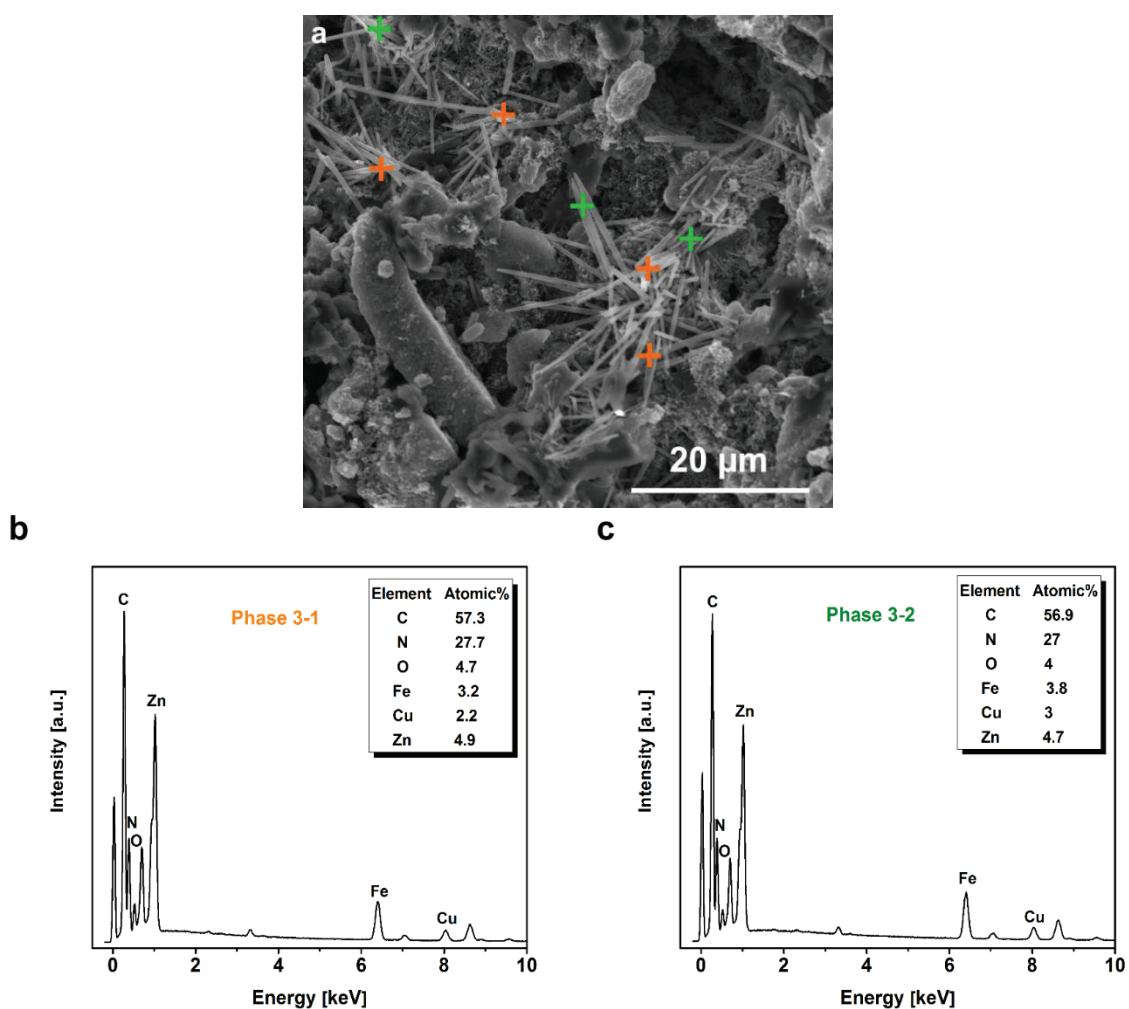


Figure 5-18. (a) SEM image of standard CuHCF electrode after 1000 cycles at a 1C rate in 100 mM ZnSO₄ with exemplary EDX point measurements, (b) exemplary EDX spectrum of the needle shaped morphology (orange crosses) with calculated average composition (phase 3-1), and (c) exemplary EDX spectrum of the needle shaped morphology (green crosses) with calculated average composition (phase 3-2).

Table 5-8. The ratio of iron to copper, and zinc for each composition with needle shaped morphology for cycled standard CuHCF electrode in 100 mM ZnSO₄.

Phase	Fe : Cu : Zn ratio
Phase 3-1	1 : 0.72 : 1.54
Phase 3-2	1 : 0.64 : 1.12

Based on the EDX results, phase 3 consisted of two different compositions (Table 5-8). Although both compositions are zinc-rich (Zn>Fe>Cu), based on the normalized values on iron the amount of copper and zinc in phase 3-1 were around 1.2 times higher than in phase 3-2. Regarding this morphology no evidence of potassium was observed. Based on these results, the possible composition for the needle shaped morphology can be CuZnHCF with different ratio of copper to zinc.

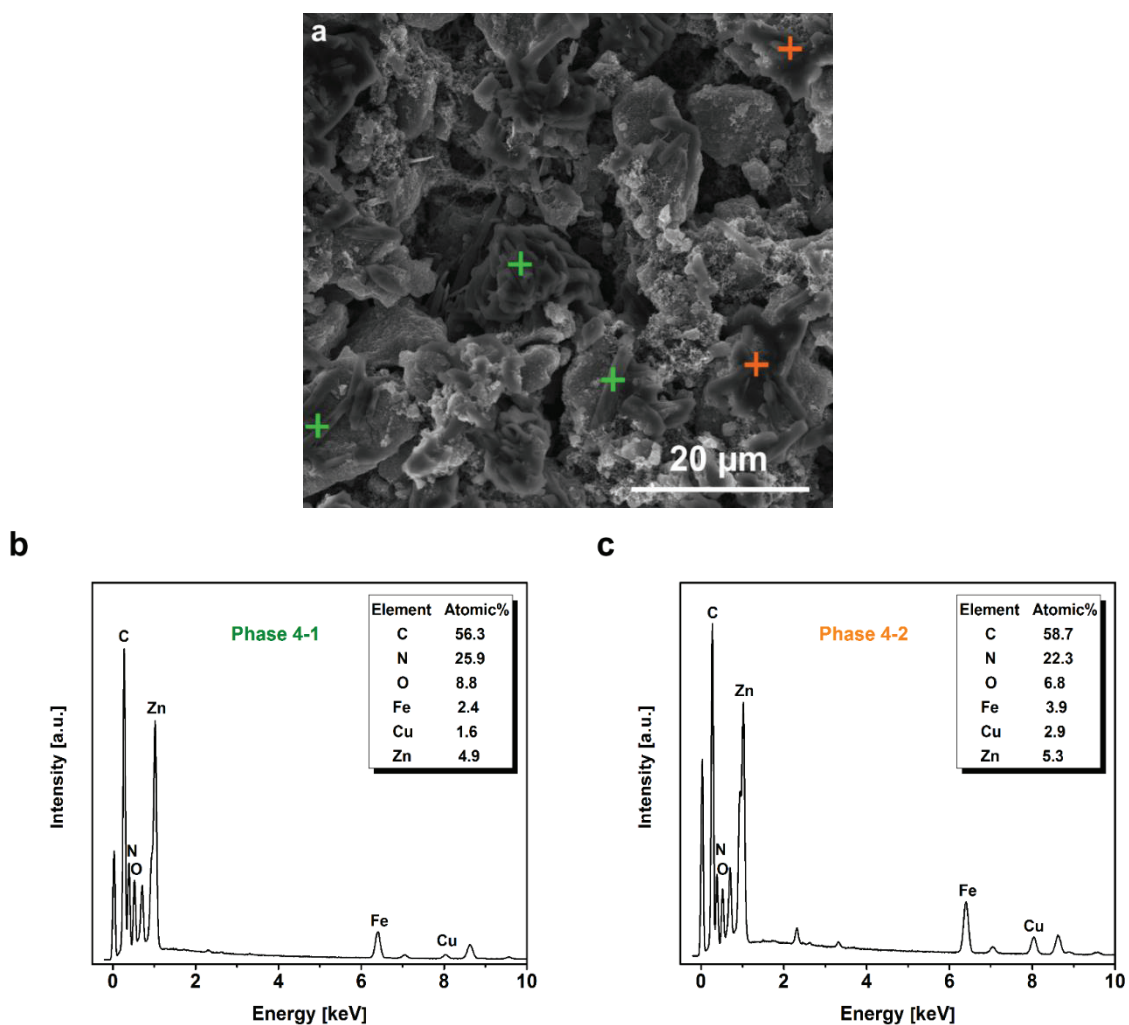


Figure 5-19. (a) SEM image of standard CuHCF electrode after 1000 cycles at a 1C rate in 100 mM ZnSO₄ with exemplary EDX point measurements, (b) exemplary EDX spectrum of plate shaped morphology (green crosses) with calculated average composition (phase 4-1), and (c) exemplary EDX spectrum of plate shaped morphology (orange crosses) with calculated average composition (phase 4-2).

At last the SEM image and the respective EDX spectra for phase 4 are illustrated in Fig. 5-19. Phase 4 was another morphology discovered in the standard CuHCF electrode after cycling. Figs. 5-19b and 5-19c show the EDX spectra with the calculated average compositions shown by green crosses (phase 4-1) and orange crosses (phase 4-2). As it is clear from the SEM image, this plate shaped phase had edge length of 2 to 12 μm and was not observed neither in cycled standard CuHCF nor $\text{Cu}_{0.93}\text{Zn}_{0.07}\text{HCF}$ electrodes in 20 mM ZnSO_4 . This morphology as well as the phase 3, was not observed in standard CuHCF and $\text{Cu}_{0.93}\text{Zn}_{0.07}\text{HCF}$ electrodes cycled in 20 mM ZnSO_4 .

From the EDX data, two different compositions were found. The two phases included a zinc-rich phase without any potassium. The difference between phases 4-1 and 4-2 was the amount of zinc and copper. In particular, based on the normalized values on iron the amount of zinc in phase 4-1 was almost 1.4 times higher and copper ~ 1.2 times lower than in phase 4-2. By extracting data from the EDX spectra, the ratio of iron to copper, and zinc in each composition with the same morphology was summarized (Table 5-9). These results suggest that the newly formed phases can be CuZnHCF.

Table 5-9. The ratio of iron to copper and zinc for each composition with a plate shaped morphology for cycled standard CuHCF electrode in 100 mM ZnSO_4 .

Phase	Fe : Cu : Zn ratio
Phase 4-1	1 : 0.68 : 2
Phase 4-2	1 : 0.8 : 1.4

Similar experiments were conducted for a $\text{Cu}_{0.93}\text{Zn}_{0.07}\text{HCF}$ electrode cycled in 100 mM ZnSO_4 after 1000 cycles. In addition to the $\text{Cu}_{0.93}\text{Zn}_{0.07}\text{HCF}$ nanoparticles three other morphologies were detected (phase 1, phase 3 and phase 5). Phase 1 had a cubic morphology, phase 3 had a needle shaped morphology, and phase 5 had spike structure.

Fig. 5-20 consists of the SEM image and EDX spectra for phase 1. For this morphology three different compositions were found. The EDX spectrum with the respective calculated average composition indicated by orange crosses (phase 1-1), the EDX spectrum with calculated average composition represented by green crosses (phase 1-2), and the EDX spectrum with calculated average composition represented by blue crosses (phase 1-3) are shown in Figs. 5-20b to 5-20d. Except for the phase 1-3 composition ($\text{Zn} > \text{Fe} > \text{K}$), all other compositions are iron-rich ($\text{Fe} > \text{K} > \text{Zn}$). There is no evidence of copper in this phase. Similar to the $\text{Cu}_{0.93}\text{Zn}_{0.07}\text{HCF}$ electrode cycled in 20 mM ZnSO_4 the cubes are well-shaped, while the edge length of them after cycling in 100 mM ZnSO_4 are bigger (3 to 21 μm) than in 20 mM ZnSO_4 .

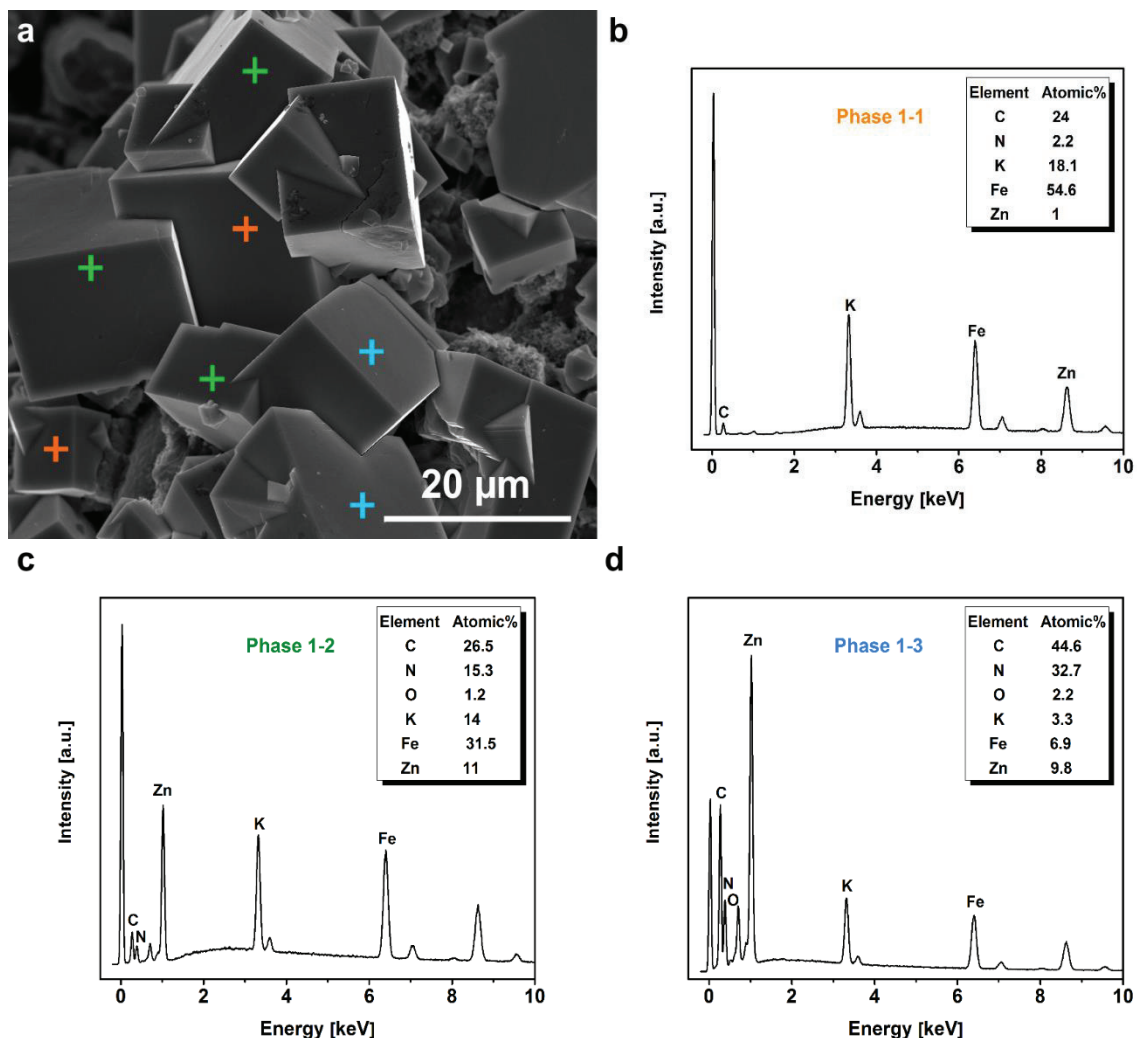


Figure 5-20. (a) SEM image of $\text{Cu}_{0.93}\text{Zn}_{0.07}\text{HCF}$ electrode after 1000 cycles at a 1C rate in 100 mM ZnSO_4 with exemplary EDX point measurements, (b) exemplary EDX spectrum of the cubic morphology (orange crosses) with calculated average composition (phase 1-1), (c) exemplary EDX spectrum of the cubic morphology (green crosses) with calculated average composition (phase 1-2), and (d) exemplary EDX spectrum of the cubic morphology (blue crosses) with calculated average composition (phase 1-3).

By extracting the EDX data for the cubic morphology, the respective ratios of potassium, iron and zinc for the cycled $\text{Cu}_{0.93}\text{Zn}_{0.07}\text{HCF}$ electrode (Table 5-10) were determined.

Table 5-10. The ratio of potassium to iron and zinc at each composition with a cubic morphology for cycled $\text{Cu}_{0.93}\text{Zn}_{0.07}\text{HCF}$ electrode in 100 mM ZnSO_4 .

Phase	K : Fe : Zn ratio
Phase 1-1	0.3 : 1 : 0.01
Phase 1-2	0.4 : 1 : 0.4
Phase 1-3	0.5 : 1 : 1.5

Based on the results shown in Table 5-10, the probable new formed phase can be considered as derivatives of KZnHCF or a mixture of KZnFeHCF . Here, phase 1-3 had a similar composition

to the one obtained at the cycled standard CuHCF electrode having cubic morphology as well. However, the compositions of phase 1-1 and phase 1-2 were not observed in cycled standard CuHCF electrode.

In Fig. 5-21, the SEM image and the respective EDX spectra for phase 3 are reported. The phase had a needle shaped morphology similar to phase 3 of the cycled standard CuHCF with a edge length of 1 to 5 μm . The length of this phase is shorter than in cycled standard CuHCF electrode. Based on the EDX results, phase 3 consists of three different compositions (Table 5-11).

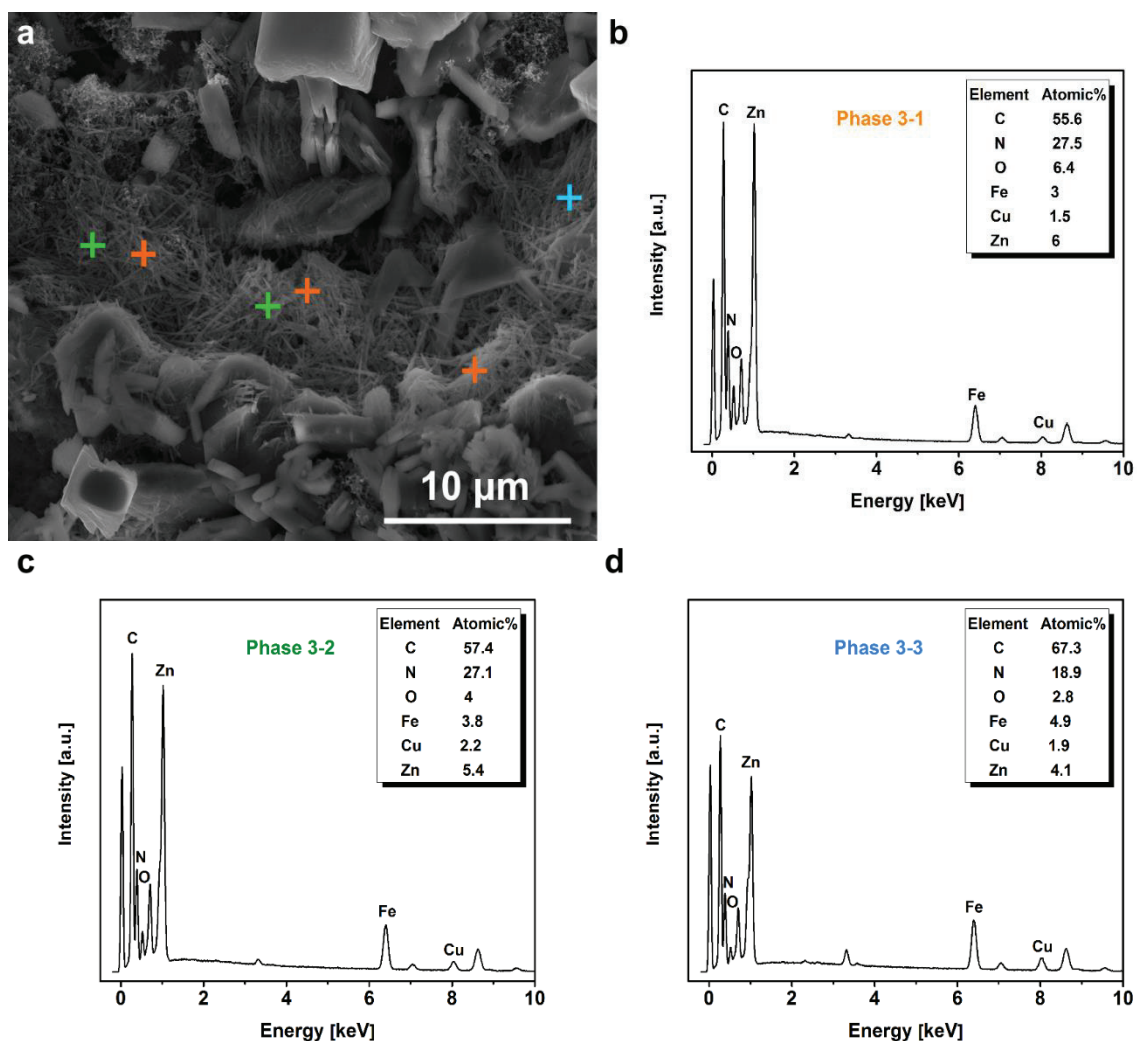


Figure 5-21. (a) SEM image of $\text{Cu}_{0.93}\text{Zn}_{0.07}\text{HCF}$ electrode after 1000 cycles at a 1C rate in 100 mM ZnSO_4 with exemplary EDX point measurements, (b) exemplary EDX spectrum of needle shaped morphology (orange crosses) with calculated average composition (phase 3-1), (c) exemplary EDX spectrum of needle shaped morphology (green crosses) with calculated average composition (phase 3-2), and (d) exemplary EDX spectrum of needle shaped morphology (blue crosses) with calculated average composition (phase 3-3).

Table 5-11. The ratio of iron to copper and zinc at each composition with a needle shaped morphology for cycled $\text{Cu}_{0.93}\text{Zn}_{0.07}\text{HCF}$ electrode in 100 mM ZnSO_4 .

Phase	Fe : Cu : Zn ratio
Phase 3-1	1 : 0.5 : 1.9
Phase 3-2	1 : 0.6 : 1.4
Phase 3-3	1 : 0.4 : 0.9

Two compositions are zinc-rich ($\text{Zn} > \text{Fe} > \text{Cu}$) and the other one (phase 3-3) is iron-rich. The main difference between all three compositions is the ratio of zinc to the other elements. In this morphology similar to phase 3 of the standard CuHCF cycled in 100 mM ZnSO_4 , no potassium was observed. However, an extra composition (phase 3-3) in addition to the other two has been revealed in the cycled $\text{Cu}_{0.93}\text{Zn}_{0.07}\text{HCF}$ electrode. Based on these results, the possible compositions for the needle shaped morphology can be CuZnHCF or CuFeZnHCF.

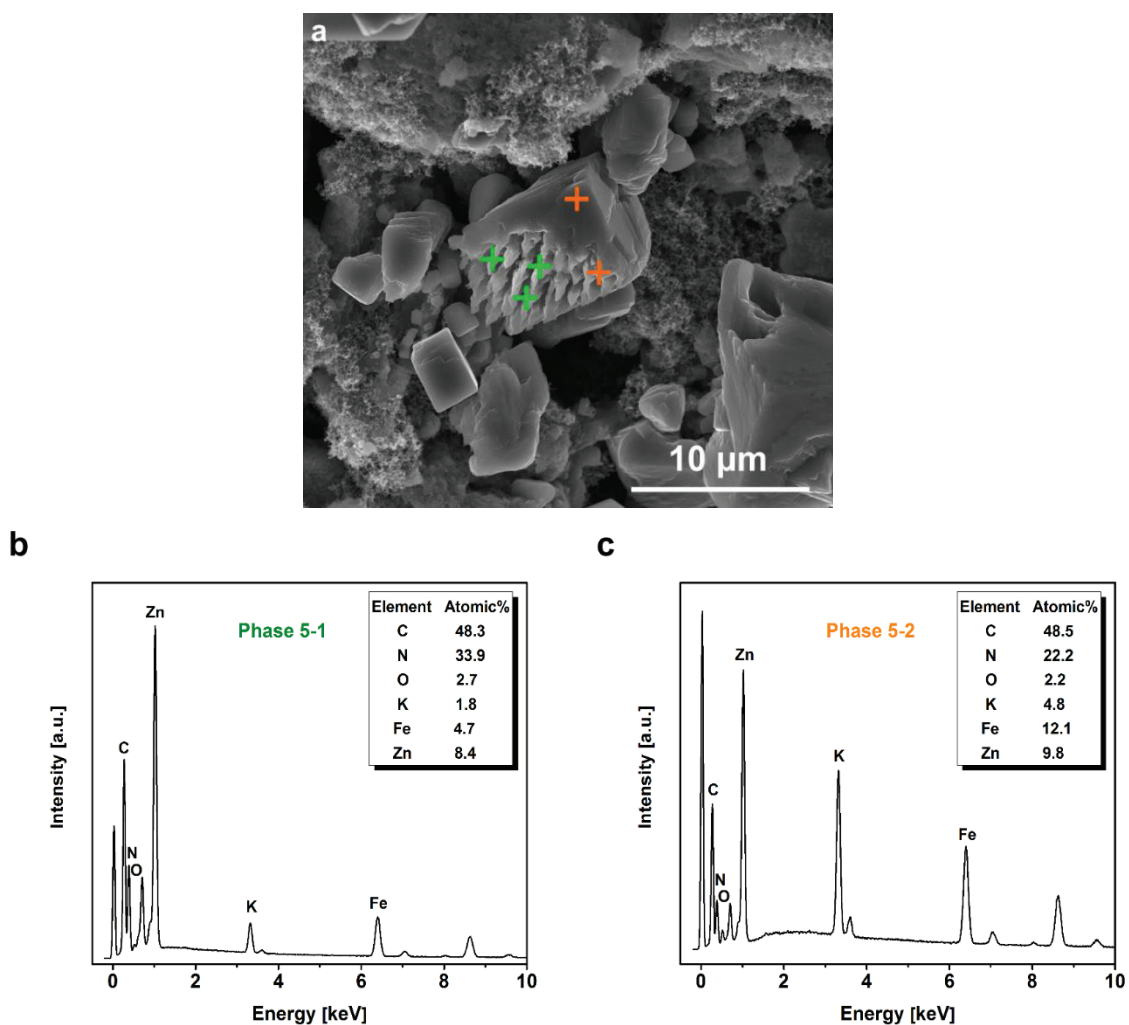


Figure 5-22. (a) SEM image of $\text{Cu}_{0.93}\text{Zn}_{0.07}\text{HCF}$ electrode after 1000 cycles at a 1C rate in 100 mM ZnSO_4 with exemplary EDX point measurements, (b) exemplary EDX spectrum of spike shaped morphology (green crosses) with calculated average composition (phase 5-1), and (c) exemplary EDX spectrum of spike shaped morphology (orange crosses) with calculated average composition (phase 5-2).

At last, the SEM image and the EDX spectra with the calculated average compositions regarding phase 5 is illustrated in Fig. 5-22. Here, phase 5 has a spike shaped morphology. Fig. 5-22a suggests that the spike shaped structure is grown on some sides of the cubic morphology (phase 1) after cycling in 100 mM ZnSO₄, although this specific morphology (phase 5) has not been observed for the standard CuHCF electrode cycled in the same solution. Phase 5 has two different compositions, iron- and zinc-rich. Similar to the cubic morphology no copper has been traced in the phase 5 compositions. The edge length determination for this morphology is difficult since each spike is connected into the cubic morphology and they are not separated. This morphology (phase 5) as well as the phase 3, was not observed in the Cu_{0.93}Zn_{0.07}HCF electrode cycled in 20 mM ZnSO₄.

From the EDX data, the ratios of potassium to iron, and zinc at each composition having spike shaped morphology are reported in Table 5-12. The differences between phase 5-1 and phase 5-2 are not only due to the zinc-rich or iron-rich compositions, but also based on the normalized values on iron, the amount of potassium in phase 5-1 is almost 2.25 times higher than in phase 5-2. Based on these results, the probable composition can be considered as derivatives of KZnHCF or a mixture of KZnFeHCF.

Table 5-12. The ratio of potassium to iron and zinc at each composition with spike shaped morphology for cycled Cu_{0.93}Zn_{0.07}HCF electrode in 100 mM ZnSO₄.

Phase	K : Fe : Zn ratio
Phase 5-1	0.4 : 1 : 1.8
Phase 5-2	0.39 : 1 : 0.8

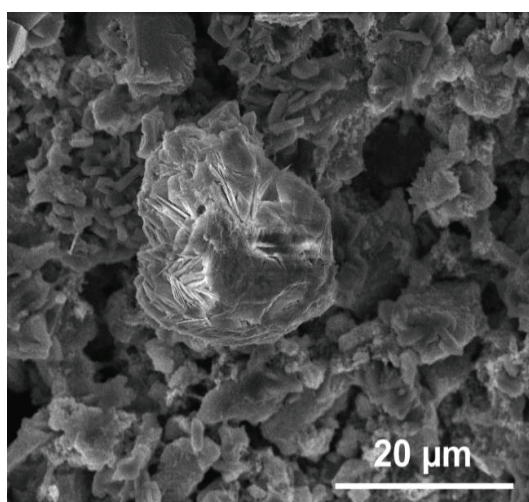


Figure 5-23. SEM image of the ZnSO₄ parasitic phase appeared in standard CuHCF and Cu_{0.93}Zn_{0.07}HCF electrodes after 1000 cycles at a 1C rate in 100 mM ZnSO₄.

In addition to the aforementioned morphologies (phase 1, phase 3, phase 4, phase 5, and nanoparticles) determined in both standard CuHCF and Cu_{0.93}Zn_{0.07}HCF electrodes after 1000

cycles in 100 mM ZnSO₄, ZnSO₄ as a parasitic phase has also been detected. This suggests that after long immersing time in this solution, zinc sulfate precipitated, while it did not take part in any of the occurring electrochemical reactions. The appearance of this inactive phase can also be attributed to the poor electrochemical performance, since less available zinc ions were present in the electrolyte for (de-)intercalating into the host material. As it is clear in Fig. 5-23, there are some parts with high brightness. This is due to the charging effect in the SEM. This artefact effect is taking place whenever a specimen or portion of it behaves as an insulator.

To sum up, the results of the electrochemical part it was shown that the Cu_{0.93}Zn_{0.07}HCF performed worse than standard CuHCF in 100 mM ZnSO₄ which in lower concentration the results were vice versa. Although in both samples upon cycling the phase transformation occurred, the standard CuHCF after cycling in 100 mM ZnSO₄ up to 1000 cycles delivered 12% higher energy and around 9.4% charge than Cu_{0.93}Zn_{0.07}HCF. The appearance of new reflections in XRD results confirmed the formation of the new phases at both samples upon cycling. The SEM-EDX measurements of both samples determined that in addition to the original phase (nanoparticles), three other morphologies were present: a cubic morphology (phase 1), a needle morphology (phase 3), and plate or spike shaped morphology (phase 4 or 5). Each morphology consisted of at least two different compositions. All of the achieved compositions were either iron-rich or zinc-rich. However, in some compositions a small amount of copper was also present. In particular, in the cubic morphology (phase 1) of both samples, no copper was observed, and the possible compositions could have been either KZnHCF or KZnFeHCF. The needle morphologies (phase 3) were achieved in both samples without any presence of potassium and the plausible compositions can be either CuZnHCF or CuZnFeHCF. For the plate morphology (phase 4) at cycled standard CuHCF electrode, compositions with copper and no potassium were obtained, which plausibly could have been CuZnHCF with different ratios of copper to zinc. At last, the spike shaped morphology (phase 5) at the cycled Cu_{0.93}Zn_{0.07}HCF electrode consisted of iron-rich and zinc-rich compositions without any copper but with potassium in their structures. Based on these results, it can be mention that the morphology of each sample had been changed electrochemically upon cycling and there is a strong relationship between the electrochemical performances and the crystallographic forms. The main evident difference between cycled standard CuHCF and Cu_{0.93}Zn_{0.07}HCF electrode is the appearance of plate and spike shaped morphologies. This can be the reason of the poor electrochemical performance of Cu_{0.93}Zn_{0.07}HCF in 100 mM ZnSO₄. In particular the spike morphology at cycled the Cu_{0.93}Zn_{0.07}HCF electrode contained potassium, while in the plate shaped morphology no potassium was involved. Furthermore, in the plate morphology at the cycled standard CuHCF, the traces of copper have been revealed which suggests that the phase

formation was not fully accomplished in this sample and this new phase is electrochemically active even after 1000 cycles. Therefore, the formation of the new phases in standard CuHCF cycled in 100 mM ZnSO₄ did not slow down the electrochemical reaction.

As an overview, two schematic representations for CuHCF and Cu_{0.93}Zn_{0.07}HCF samples cycled in both 20 mM and 100 mM ZnSO₄ have been shown in Figs. 5-24 and 5-25. In these schematics, the main focus is on the illustration of the morphological changes upon cycling and the resulting different phases with different compositions. Different colors for each morphology indicate different identified compositions.

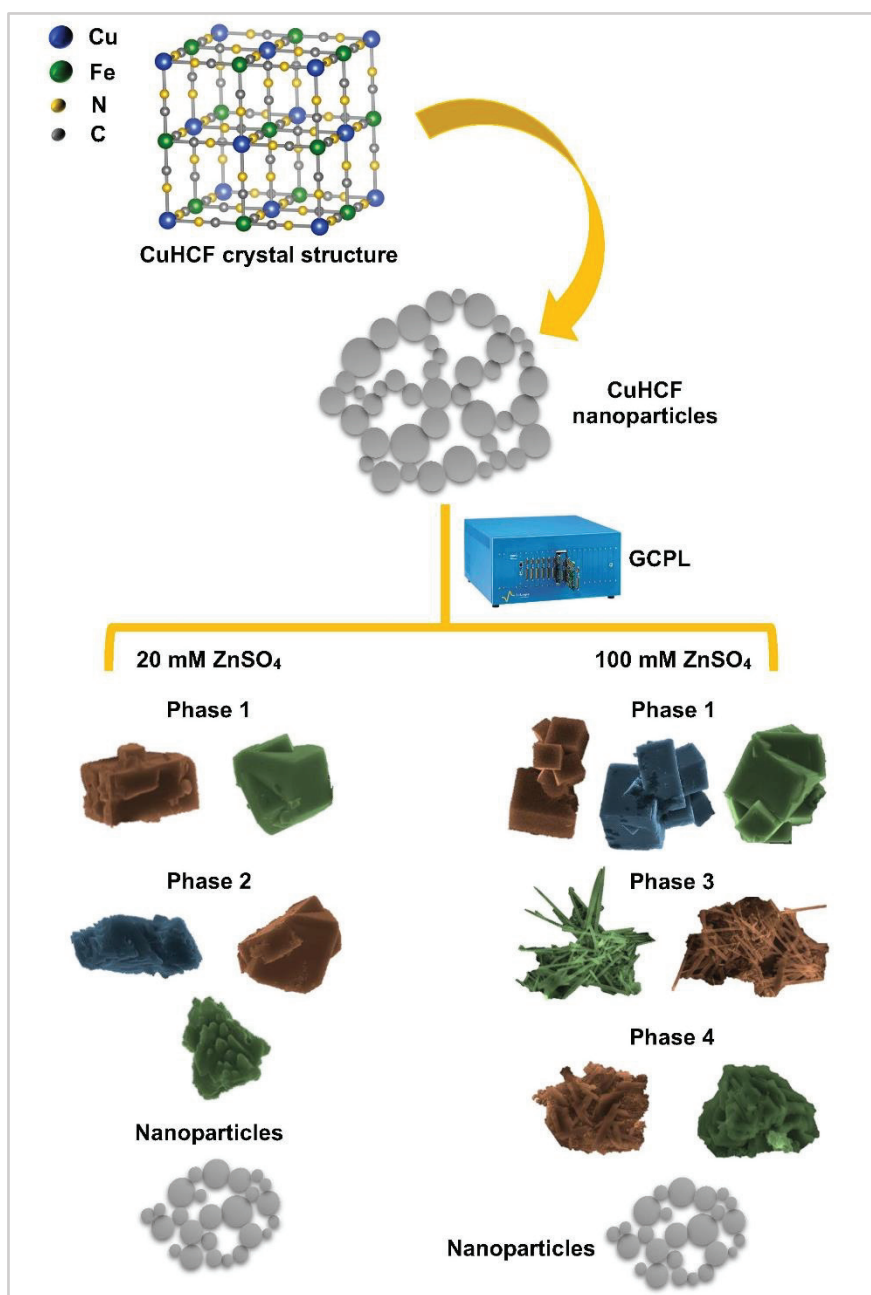


Figure 5-24. Schematic presentation of standard CuHCF morphology before and after cycling in ZnSO₄ solutions.

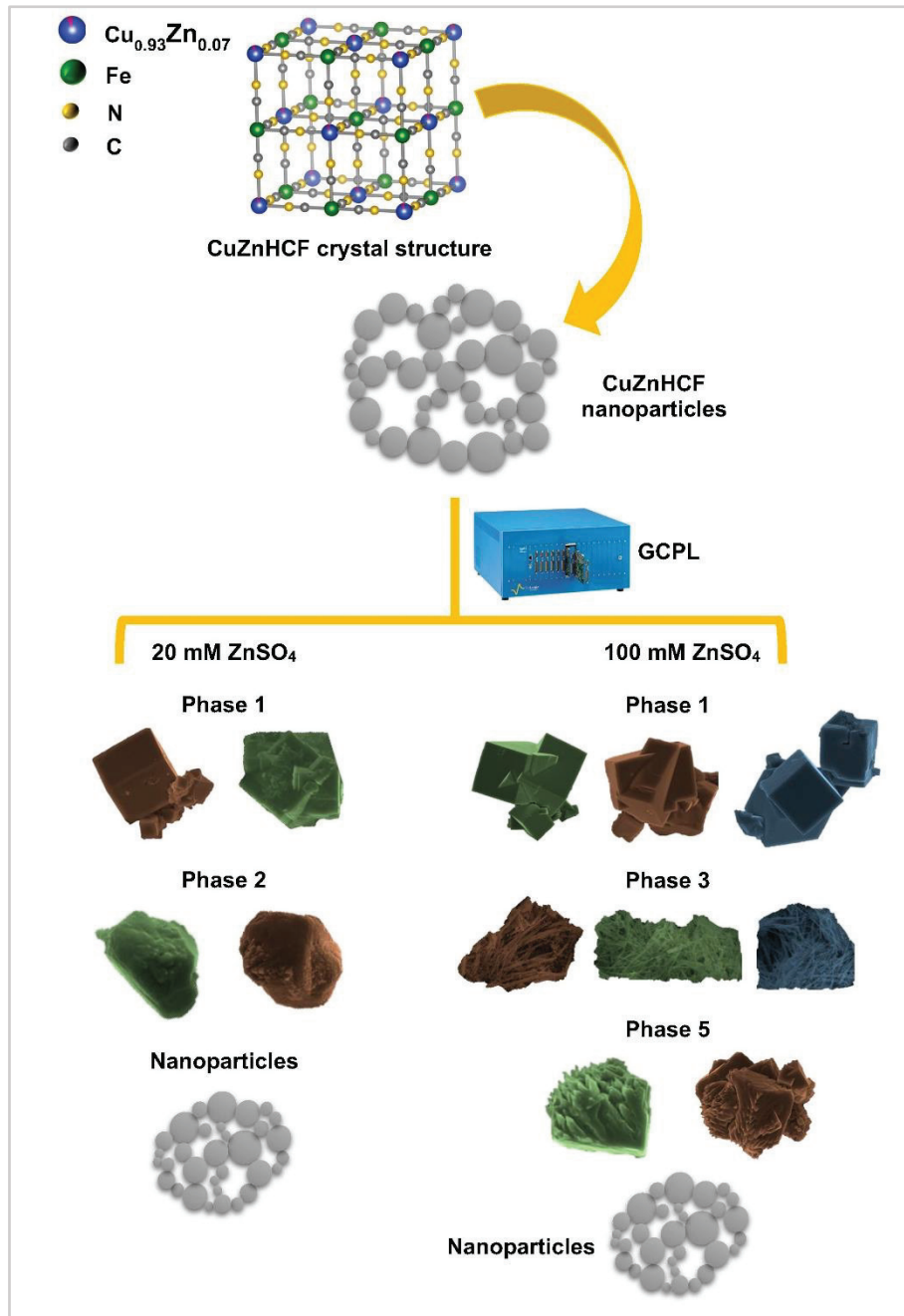


Figure 5-25. Schematic presentation of $\text{Cu}_{0.93}\text{Zn}_{0.07}\text{HCF}$ morphology before and after cycling in ZnSO_4 solutions.

6. Controlling Synthesis Parameters

In Chapters 3, the effect of electrolyte (nature and concentration), current rate and the phase transformation on the aging of standard CuHCF have been discussed. The study has been continued in Chapter 4 with the aim of optimizing standard CuHCF structure with the help of a co-ion. For this purpose, different CuZnHCF mixtures have been synthesized and characterized. Among them, the mixture with Cu:Zn ratio of 93:7 has shown a better performance than standard CuHCF in 20 mM ZnSO₄. But this material could not deliver high capacity and energy in 100 mM ZnSO₄ due to the formation of new unfavorable phases (Chapter 5). As mentioned before, a suitable energy storage system should fulfill the needs of stationary applications (high power density, fast response and long life cycle). Therefore, optimizing the structure of active material is of primary importance. This can be done by controlling the thermodynamic driving force of the reaction, which can be done by adjusting the synthesis routes and conditions. In the following the effect of the pumping speed, temperature, and atmosphere during synthesis on the electrochemical performance of standard CuHCF is studied.

6.1. Effect of Dropping Speed

As explained in Section 2.2.3, different CuHCFs with slow (0.5 mL min⁻¹) and fast (2 mL min⁻¹) precipitation speeds have been synthesized. In Fig. 6-1, the XRD patterns of standard CuHCF synthesized with original recipe (Section 2.2.1), and the ones synthesized with slow and fast dropping speed is shown. Based on the XRD data and the Scherrer equation^[212] the crystal sizes for each powder have been calculated and are reported in the Fig. 6-1. Scherrer equation is as following:

$$\tau = \frac{K\lambda}{\beta \cos\theta} \quad (6.1)$$

where τ is the average crystalline size, K is the shape factor (equal to 0.9), λ is the X-ray wavelength (equal to 1.540598 Å), β is the full width at half maximum (FWHM), and θ is the Bragg angle.^[212] By comparing the respective grain size for each sample, it can be mentioned that at slower precipitation speed the crystal size is bigger than the faster precipitation rate. This is in agreement as it was expected. When the dropping speed increases, less time is available for formation of the material and smaller crystals would have grown. From the XRD patterns no clear shifts in the reflection positions have been observed for both samples compared to the standard CuHCF patterns. Since the crystal size of these materials are almost the same and the

XRD patterns looks similar, it can be concluded that the crystallinity of all the samples are similar to the standard CuHCF.

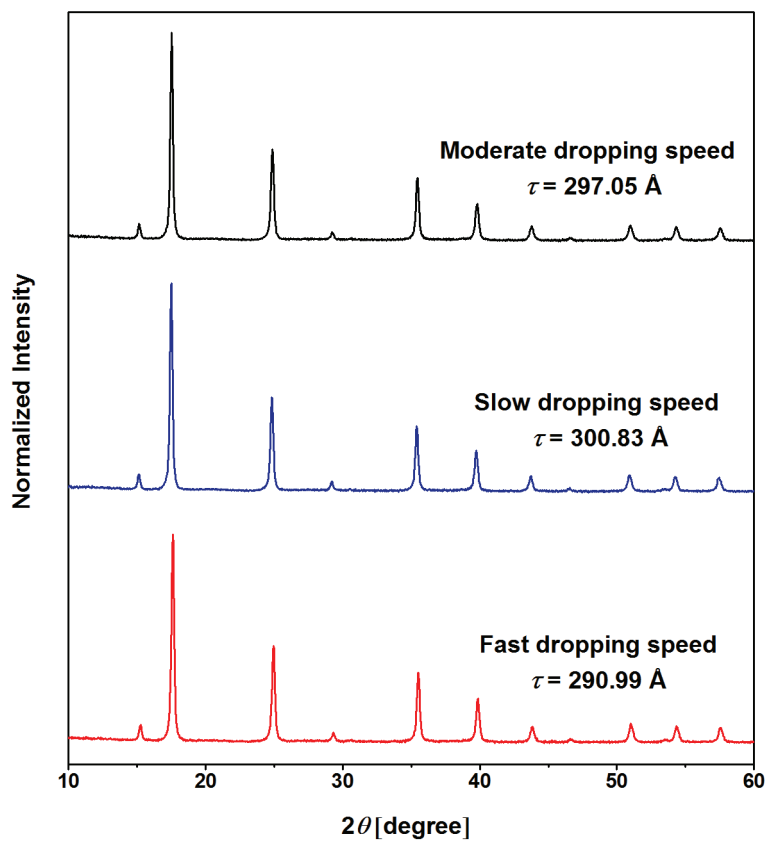


Figure 6-1. X-ray diffraction patterns of CuHCF powder synthesized with moderate dropping speed (black line), slow dropping speed (blue line), and fast dropping speed (red line).

In Fig. 6-2, the potential profiles of these new materials in 100 mM ZnSO₄ at 1C is presented.

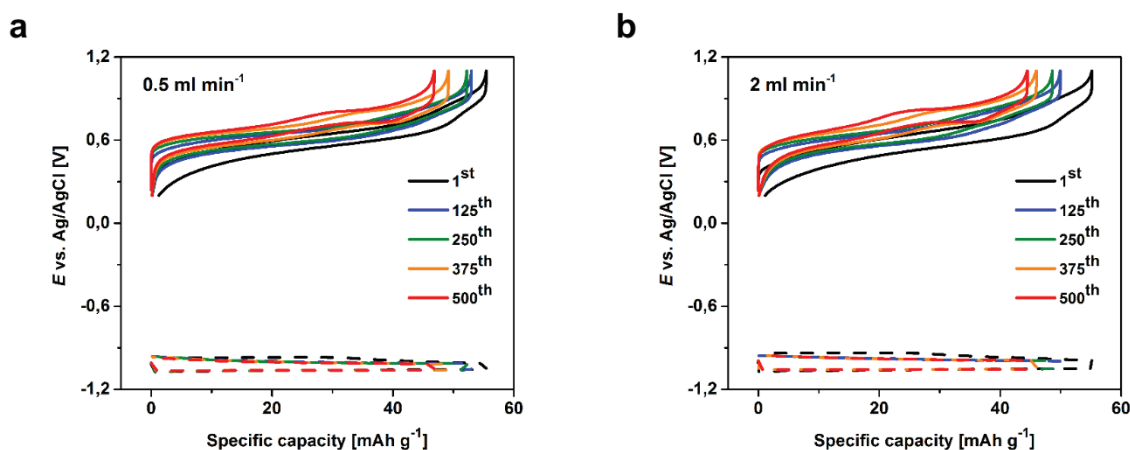


Figure 6-2. Potential profiles of CuHCF (solid line) and zinc foil (dashed line) synthesized with (a) 0.5 mL min⁻¹ and (b) 2 mL min⁻¹ pumping speed at 1C current rate in 100 mM ZnSO₄, respectively.

The capacity retention as well as the energy retention for both materials after 500 cycles is summarized in Table 6-1. These values are extracted from the graphs shown in the Fig. 6-3.

Table 6-1. Percentage of energy and charge retention for CuHCF synthesized with different pumping speed at 1C rate in 100 mM ZnSO₄.

After 500 cycles		
Pumping speed	Energy	Charge
0.5 mL min ⁻¹	93.06%	85.25%
2 mL min ⁻¹	89.6%	81.27%

By comparing the potential profiles of these new materials (Fig. 6-2) with standard CuHCF (Fig. 5-13a), it can be mentioned that the shape of the profiles with the number of cycling changed and a two-step plateau has been observed similar to standard CuHCF.

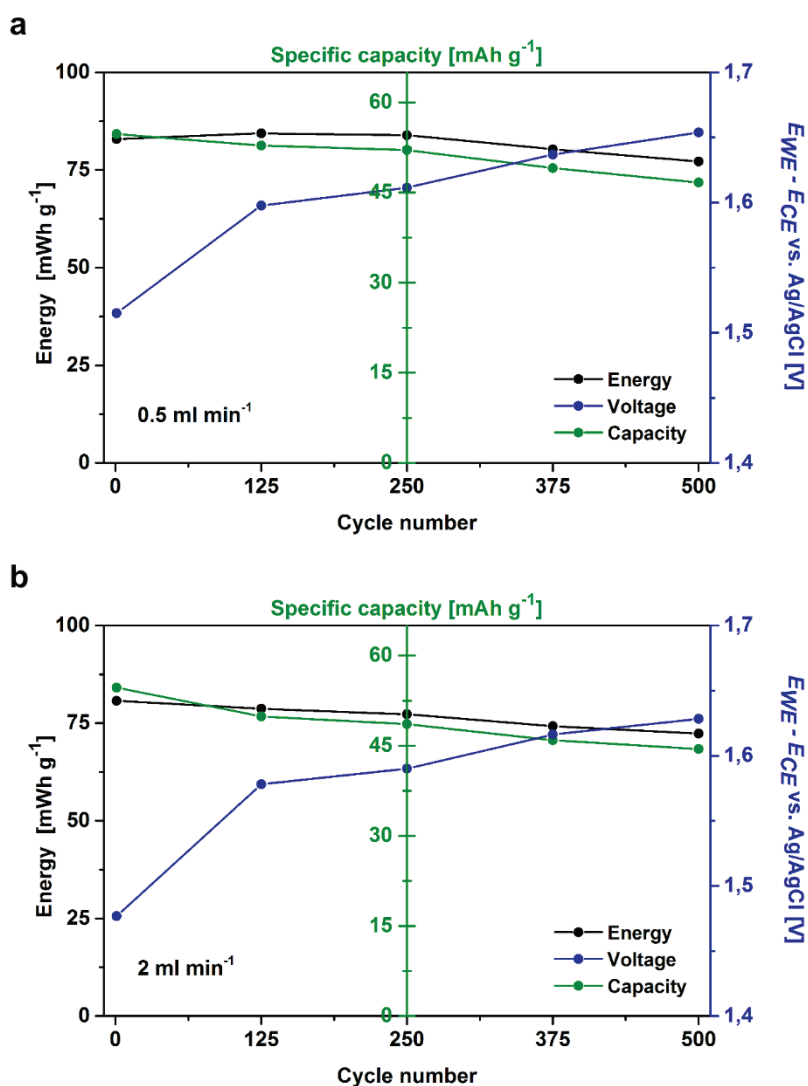


Figure 6-3. Specific energy, charge, and average potential provided by CuHCF synthesized with (a) slow pumping speed and (b) fast dropping speed, in 100 mM ZnSO₄ at different number of cycles, respectively.

In other words, the phase transformation mechanism in these samples also occurred upon cycling. It was also observed that the mid-composition potential with the number of cycles was shifted to the higher values. Higher overpotential at both cathode and anode side for the material

synthesized with fast dropping speed, can also lead to the poor performance of the active material. From the values reported in Table 6-1, it can be obtained that fast dropping speed has a negative effect on the performance, while the capacity dropped to 81.27% after 500 cycles. Although this value for the material synthesized with slow dropping speed (85.25%) is close to the charge retention of standard CuHCF (85.4%, Table 5-6) after 500 cycles. In addition, with the slow precipitation speed, the energy obtained in the system was higher than in the rapid case. Therefore, it can be concluded that the faster the precipitation during synthesis, the more unstable the active material is. It is also important to mention that, although with XRD no remarkable changes in the new synthesized materials have been observed, electrochemically the pumping speed had an impact on the overall performance.

6.2. Effect of Temperature

Another parameter which generally has a strong influence on the synthesis and the performance of the obtained product is temperature. In this section, the effect of the synthesis temperature on the life cycle of the battery is investigated. The temperature has been adjusted once at 70°C and another time at 2-3°C. The synthesis procedures have been explained in Section 2.2.4.

Hereby, the work of Yang et al.^[213] in which different PBs while having different solution temperatures have been synthesized, is worth mentioning. Four different temperatures namely 0°C, 20°C, 60°C, and 80°C have been selected. From their XRD patterns, no significant changes have been observed, however the calculated d-spacing for the sample synthesized at 0°C was 10.22 Å and upon raising the temperature to 80°C this value increased up to 10.38 Å.^[213]

In Fig. 6-4, the XRD patterns of the synthesized standard CuHCF and the new CuHCFs synthesized at high and low temperatures are shown. As it was expected at low temperatures the crystal size of active material got smaller, the calculated crystalline size followed this hypothesis. Since the crystal size of new CuHCFs did not change drastically and no clear shift in XRD reflections was observed, it can be mentioned that the temperature has no effect on any phase change in this specific PB. In addition, from the electrochemical results shown by Yang et al.^[213] it was indicated that the material synthesized at low temperature had better cyclability and rate capability compared to the other ones. However, the results obtained in this thesis suggest that the materials obtained at room or high temperature (70°C) have better electrochemical performance than low temperature ones (2-3°C). It is important to stress that in this thesis the temperature of the precipitation has been controlled, while in the work of Yang et al.^[213] the temperatures of the precursor's solutions have been controlled.

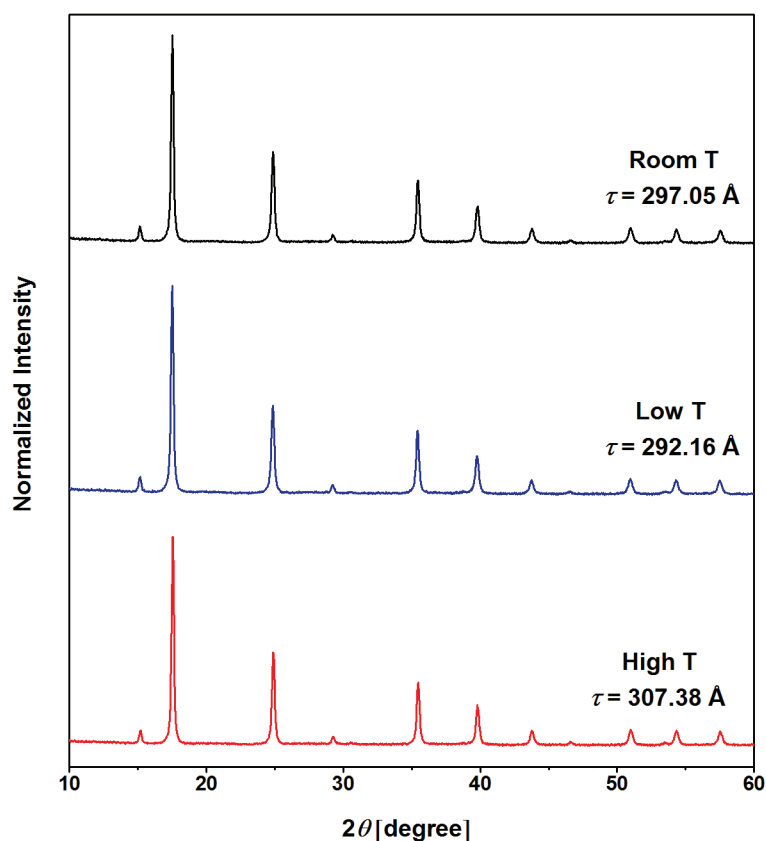


Figure 6-4. X-ray diffraction patterns of CuHCF powder synthesized at room temperature (black line), low temperature (blue line), and high temperature (red line).

Furthermore, in the study of Inoue et al.^[214] with the help of ^{57}Fe Mössbauer spectroscopy they tried to discover the thermal decomposition of PB in vacuum. The results suggest that no change in the coordination environment of PB can be observed when the heat-treatment process was done at lower temperatures than 200°C . However, at temperatures above 250°C the cyano ligands would flip.^[214]

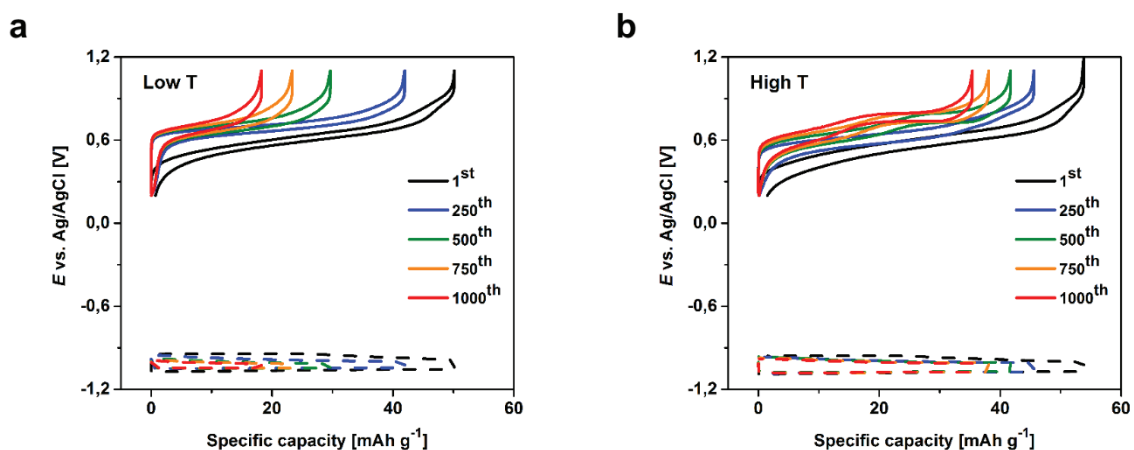


Figure 6-5. Potential profiles of CuHCF (solid line) and zinc foil (dashed line) synthesized at (a) low temperature and (b) high temperature at 1C current rate in 100 mM ZnSO_4 , respectively.

In Fig. 6-5, the potential profiles of materials synthesized at high and low temperatures cycled in 100 mM ZnSO₄ at 1C are illustrated. From the potential profiles the shift of the reduction reaction potential to higher values is clear. The profiles for the sample synthesized at high temperature undergo a two-step plateau during cycling, while this did not happen in the other sample. In other words, the phase transformation phenomenon favorably occurred at the sample synthesized at high temperature. The summary of the capacity retention and the energy retention (extracted from Fig. 6-6) after 500 and 1000 cycles is noted in Table 6-2.

Table 6-2. Percentage of energy and charge retention for CuHCF synthesized at different temperatures at 1C rate in 100 mM ZnSO₄.

Synthesis temperature	After 500 cycles		After 1000 cycles	
	Energy	Charge	Energy	Charge
Low T	64.5%	59.87%	39.6%	35.6%
High T	85.69%	78.16%	74.14%	66.3%

Based on these results and the mentioned studies, it can be suggested that the temperature during synthesis process has an important effect on the electrochemical performance of the material, while the heat-treatment of the active material with less than 200°C would not change anything in the active material structure. It is clear that changing the temperature did not have a positive effect on the performances of the system. It is probable that the synthesized materials have more defects than standard CuHCF, or the amount of zeolitic water in the structure as well as the vacancies have been changed and did not reach the optimal value.

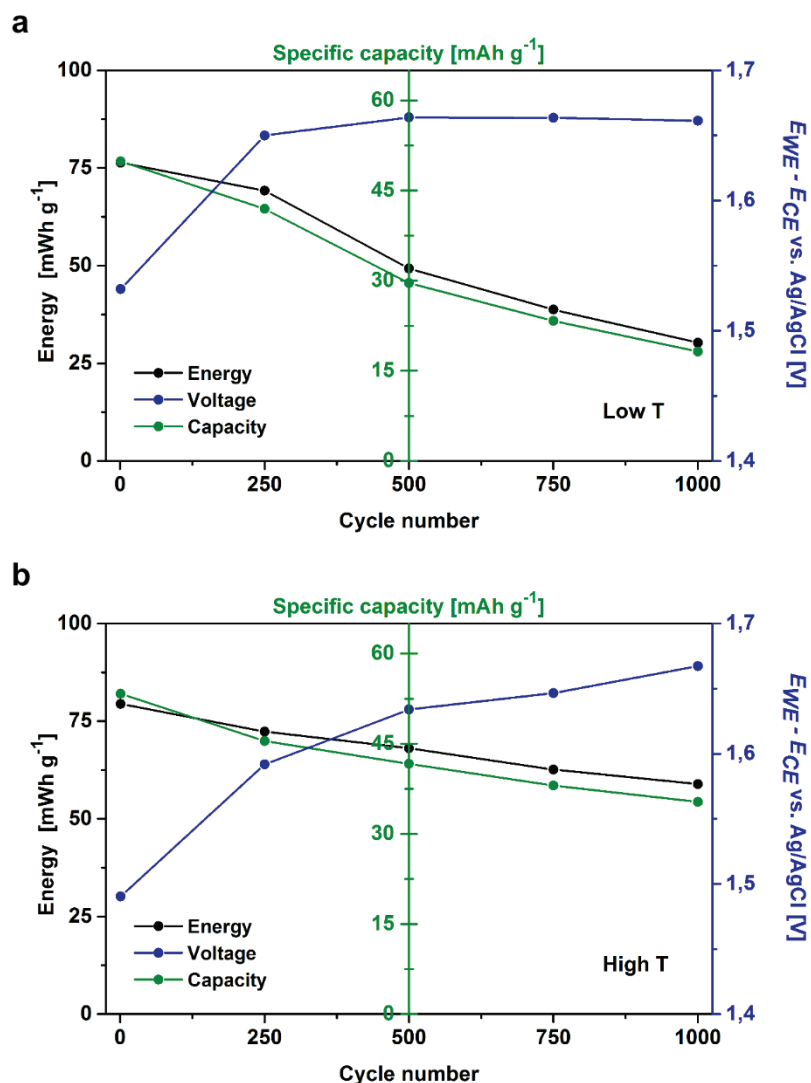


Figure 6-6. Specific energy, charge, and average potential provided by CuHCF synthesized at (a) low temperature and (b) high temperature, in 100 mM ZnSO_4 at different number of cycles, respectively.

6.3. Effect of Argon and Temperature

In this section, in addition of controlling temperature during synthesis, the atmospheres during the precipitation and sonication have been controlled (Section 2.2.5). Three different powders under argon atmosphere at three different temperatures have been synthesized. The XRD patterns of each powder are shown in Fig. 6-7. The crystalline size of each powder revealed a linear relationship between the temperature and the grain size. In other words, by increasing the synthesis temperature, the crystal size got bigger. From the XRD patterns no clear shifts have been observed. All of the reflections were sharp and did not show any extra reflections (no new phase). Therefore, the crystal structures of the new synthesized powders are similar to the standard CuHCF. In other words, the presence of argon as well as temperature had no clear

impact on the crystal structure of the new synthesized powders, although a slight change in crystal size was observed.

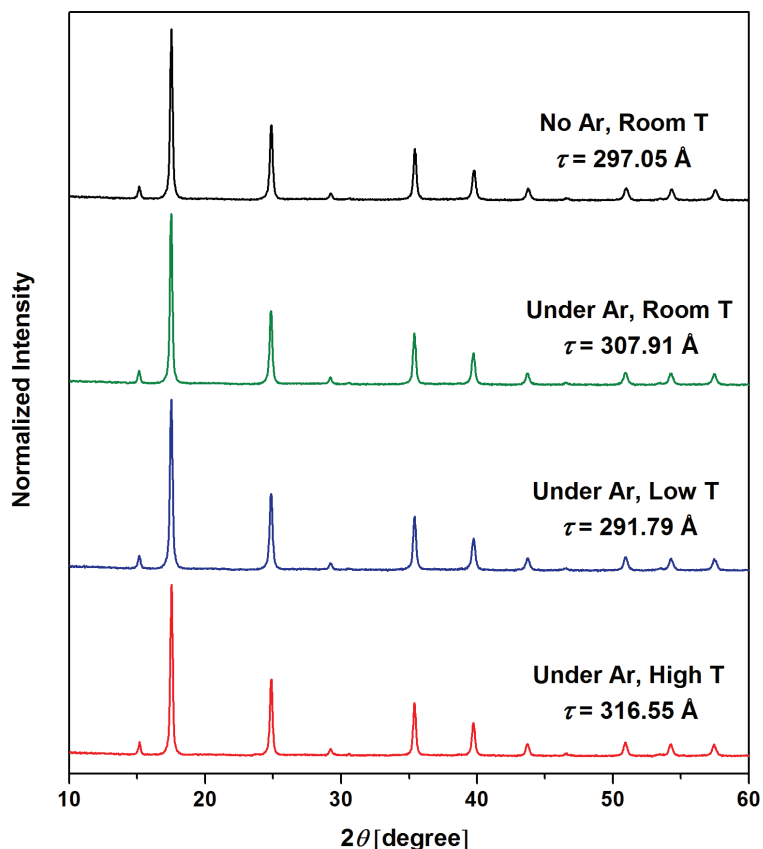


Figure 6-7. X-ray diffraction patterns of CuHCF powder synthesized under air atmosphere at room temperature (black line), under argon at room temperature (green line), under argon at low temperature (blue line), and under argon at high temperature (red line).

It is worth mentioning the work from Aparicio et al.^[215], in which the thermal decomposition of PB under argon has been studied. XRD and ⁵⁷Fe Mössbauer spectroscopy have been performed to identify the phases before and after heat-treatment. It discovered that the decomposition reaction is depending on the release of cyanide ligands from the PB structure. The thermal decomposition of PB had three stages dehydration, crystal structure change, and decomposition. It also suggested that the PB decomposition under air atmosphere followed by an exo-thermic effect and release of (CN)₂ or HCN gases and formation of iron oxide as decomposition product.^[215] Although the results of this mentioned study are quite important since in this thesis the temperature did not rise more than 70°C, the decomposition of the active material did not happen. Besides, there is a difference between the heat-treatment process and controlling the temperature while precipitation time. It is believed^[215] that the change of temperature and atmosphere would not lead to any change of the composition but rather the rate of particle growths, the zeolitic water between channels of the framework, and the vacancies.

In order to check if the electrochemical performances of new synthesized materials are similar to standard CuHCF, GCPL have been run for each material.

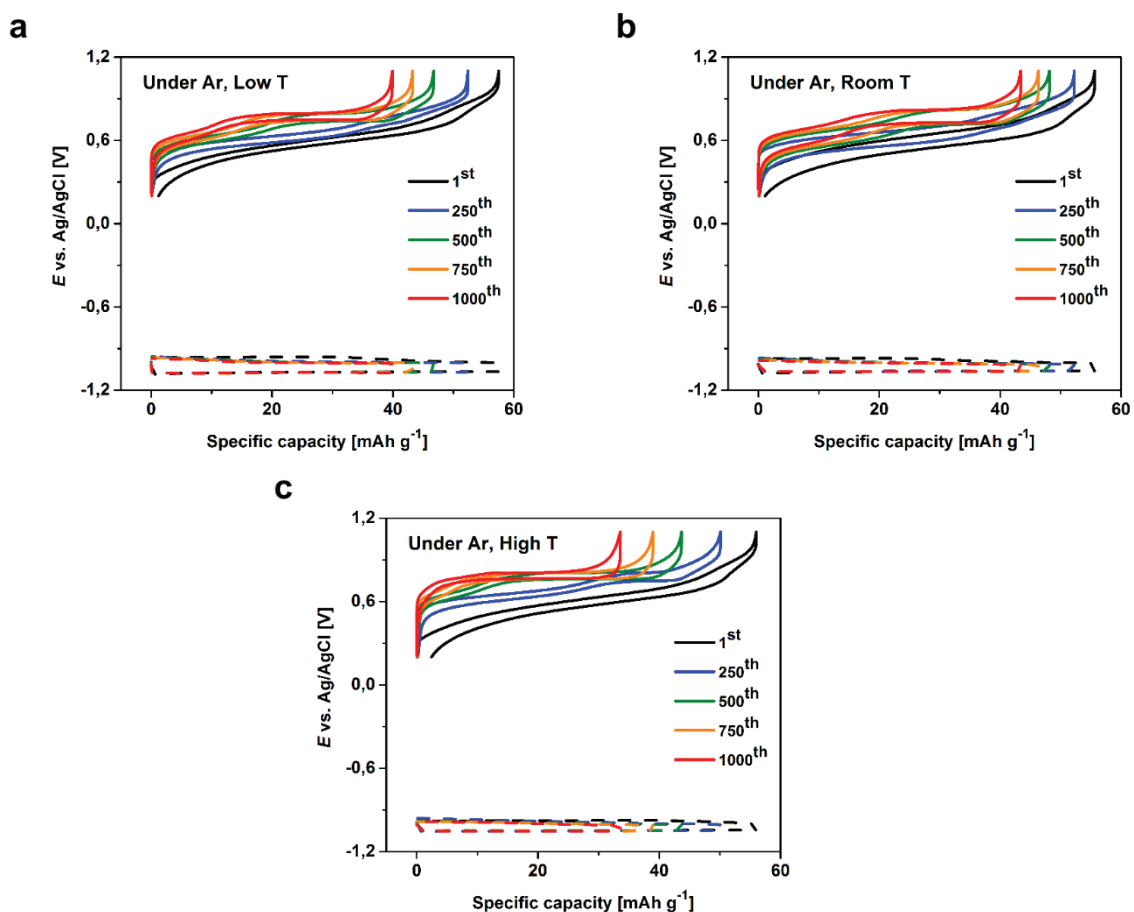


Figure 6-8. Potential profiles of CuHCF (solid line) and zinc foil (dashed line) synthesized (a) under argon at low temperature, (b) under argon at room temperature, and (c) under argon at high temperature, respectively.

Fig. 6-8 illustrates the potential profiles of each material cycled up to 1000 cycles in 100 mM ZnSO₄. It is clear that upon cycling the shape of the charge-discharge curves have been changed and the mid-composition potential shifted to higher values. A clear two-step plateau was appeared for all three samples that suggest the occurrence of phase transformation. It is interesting to mention that the first plateau for the samples synthesized under argon at low and room temperatures did not vanish upon cycling. This implies that upon cycling the intensity of the first redox peaks at the differential specific charge profiles decreased and even at 1000th cycle this phase is present in addition to the second one. However, in the other sample (synthesized under argon at 70°C) upon cycling the first redox peaks disappeared and only the second one remained. Based on these results and Fig. 6-9 in which the specific energy, charge, and average potential evolution are provided for each sample, the capacity retention and the energy retention after 500 and 1000 cycles is calculated and reported in Table 6-3.

Table 6-3. Percentage of energy and charge retention for CuHCF synthesized under argon at different temperatures at 1C rate in 100 mM ZnSO₄.

Synthesis temperature	After 500 cycles		After 1000 cycles	
	Energy	Charge	Energy	Charge
Under Ar, Low T	88.94%	82.81%	77.3%	70.1%
Under Ar, Room T	94.96%	87.33%	87.1%	78.7%
Under Ar, High T	90.19%	78.73%	70.3%	60.5%

By comparing these results with the performance of standard CuHCF, it can be mentioned that the specific charge after 1000 cycles provided by the sample synthesized under argon at room temperature is ~7% higher than standard CuHCF and for the energy this value increased up to ~5.5%.

These results suggest that the argon atmosphere has a huge impact on the CuHCF performance and it increased the energy retention after 1000 cycles from 82% to 87%. This can mean that the battery could be stable up to 1500 cycles, thus reaching the performances of a classic high power lithium-ion battery. Although the role of argon on the synthesis of CuHCF is not fully clear yet, more investigations with the help of other techniques is needed. The material synthesized under argon atmosphere at room temperature showed remarkable electrochemical results, although no phase changes were observed. Nevertheless, it was helpful to perform an elemental mapping of the as-prepared powder.

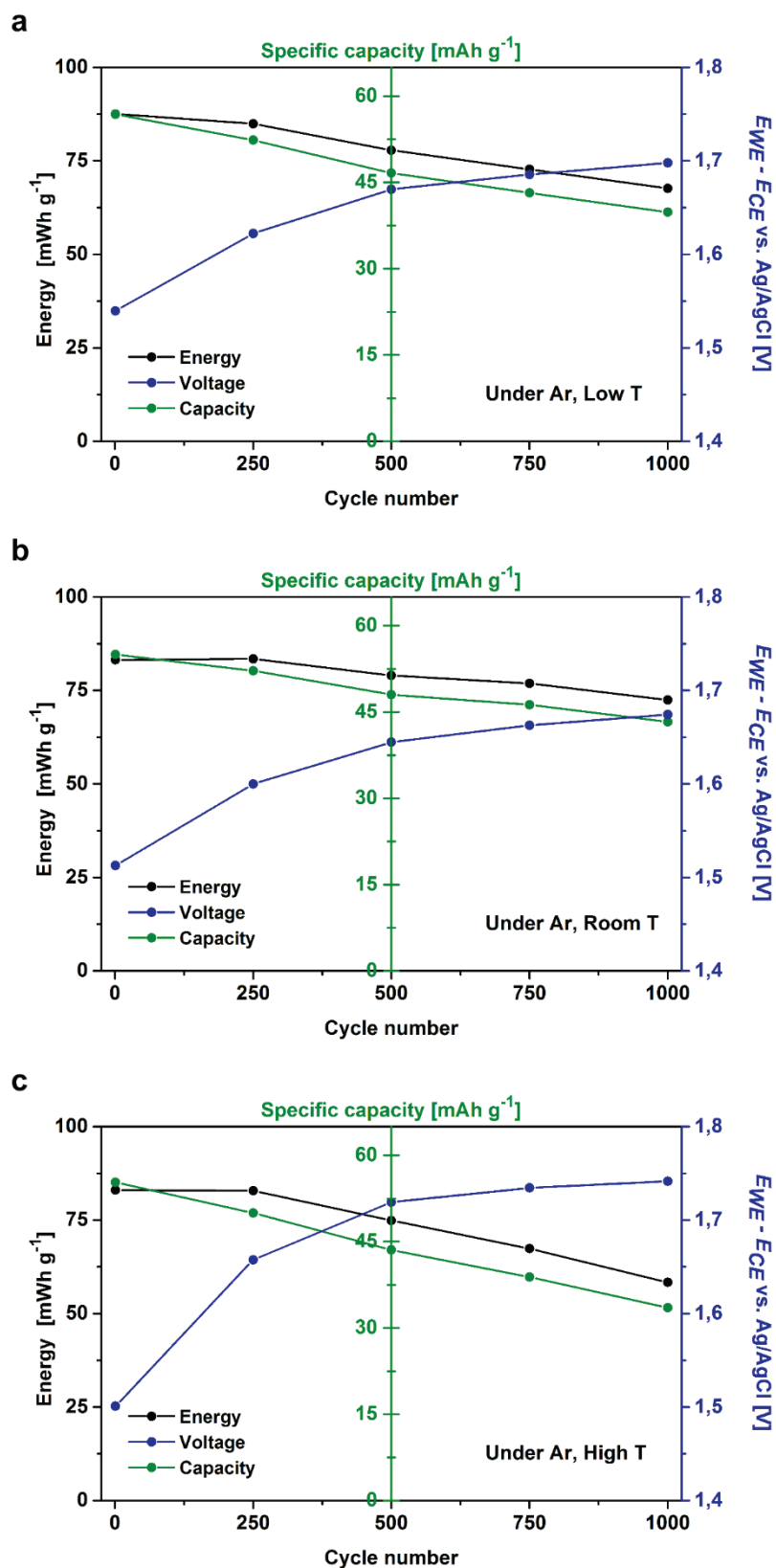


Figure 6-9. Specific energy, charge, and average potential provided by CuHCF synthesized at (a) under argon at low temperature, (b) under argon at room temperature, and (c) under argon at high temperature, in 100 mM ZnSO₄ at different number of cycles, respectively.

In Fig. 6-10 the SEM image of the CuHCF powder synthesized under argon as well as the elemental mapping is shown. From the SEM image it is clear that the powder consists of agglomerated polydisperse spherical particles (less than 100 nm) and that they aggregate to reveal a highly porous assembly. From the elemental mapping, it is clear that all of the elements are distributed homogeneously all over the sample and that there is no evidence of any extra phase.

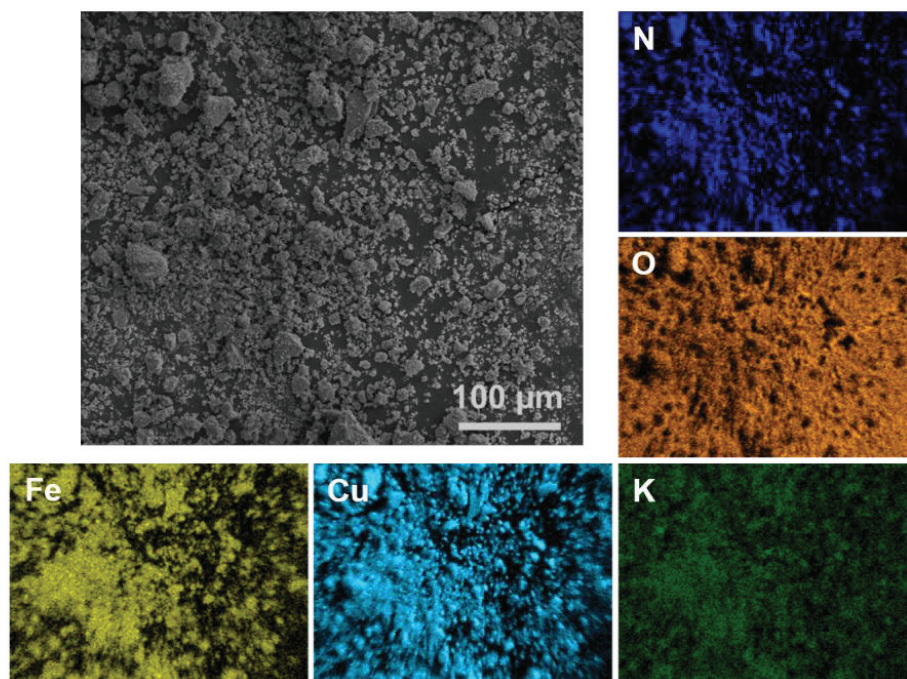


Figure 6-10. SEM and EDX elemental mapping (nitrogen, oxygen, potassium, copper, and iron) of new CuHCF powder synthesized under argon at room temperature.

To conclude it can be mentioned that this new synthesis condition provides a new perspective to develop materials for rechargeable zinc-ion batteries for stationary applications and for short-time storage of the solar and wind power with higher energy.

7. Discussion and Results Comparison

Based on the ‘International Energy Outlook’^[216] the world energy consumption is increasing yearly and it affects the international energy markets. In 2015, the total world energy consumption was reported to be 575 quadrillion BTU and it is expected to reach 736 quadrillion BTU till 2040.^[216] Therefore, it is critical to exploit energy from other resources than fossil fuels. As renewable resources are the fastest growing energy source, it is critical to develop compatible energy storage systems such as batteries to integrate them effectively into electricity systems. Since aqueous batteries, due to their remarkable advantages, attract great attention during the last decades among other rechargeable batteries, investigating and developing a system based on this type of batteries is very important. Accordingly, the main purpose of this study was developing a low-cost and environmentally friendly aqueous zinc-ion battery based on CuHCF and its derivatives. This chapter provides a global discussion of the experimental results presented in the previous chapters, in order to give an overview of the major achievements.

In 2015, Trócoli and La Mantia^[142] proposed an aqueous zinc-ion battery based on a CuHCF cathode from Prussian blue family and zinc foil anode in 20 mM ZnSO₄ (pH = 6) electrolyte. CuHCF has an open framework structure and allows for fast and facile (de-)intercalation of monovalent and multivalent ions. The battery that La Mantia^[142] et al. introduced was able to provide a capacity retention of 96.3% after 100 cycles at a 1C current rate with an average discharge potential of 1.73 V. Although the system offered a good cyclability and rate capability, the used standard CuHCF active material degraded upon cycling. Therefore, it is interesting to investigate the effect of different parameters on the electrochemical performance of this battery and to try to improve the system for long-term cycling to make it compatible for grid-scale energy storage.

First, the effects of the nature of the electrolyte on the standard CuHCF have been examined. For this purpose, standard CuHCF was cycled in 20 mM of different zinc salt solutions, such as ZnSO₄, Zn(ClO₄)₂, ZnF₂, and Zn(NO₃)₂, at a 1C current rate. The electrochemical performances showed that the nature of the electrolyte has a huge impact on the capacity loss. The capacity retention of standard CuHCF after 200 cycles in 20 mM of ZnSO₄, Zn(ClO₄)₂, ZnF₂, and Zn(NO₃)₂ is 95.52%, 95.07%, 93.3%, and 21.89%, respectively. The poor performance of standard CuHCF in Zn(NO₃)₂ has been discussed. Based on NO₃⁻ ions being a strong oxidizing agent the zinc foil anode was destroyed. The perchlorate anion also is known as a slow oxidizing agent which affects the zinc anode negatively and decreases the kinetic of the reaction. The results of the ICP-MS illustrated that the specific charge fading upon cycling was not exclusively attributed to the dissolution of copper or iron from the standard CuHCF active

material. The aging of standard CuHCF is associated with the degradation mechanism (Section 3.4).

For achieving an energy storage system with high power, a high concentrated electrolyte is needed. Here, standard CuHCF has been cycled in 100 mM ZnSO₄ and Zn(ClO₄)₂ aqueous electrolytes. Due to the fact that ZnF₂ has low solubility and nitrates are highly unstable, these two solutions were omitted for further studies. After cycling standard CuHCF in 100 mM ZnSO₄ and Zn(ClO₄)₂ separately, the values for the capacity retention at each solution suggested that aging of standard CuHCF is not only depending on the nature of the electrolyte but also on the concentration of it. In particular, the capacity retention of standard CuHCF in 100 mM ZnSO₄ was 69.86% while in Zn(ClO₄)₂ it was 49.95% after 400 cycles. The electrochemical performances depicted that when the concentration of electrolyte was higher, the degradation of standard CuHCF occurred faster. From their potential profiles and the differential specific charge profiles, it can be obtained that in addition to the single-phase reaction, a two-phase reaction was taking place. Upon cycling the first reaction (first redox peaks) tended to decrease while the second one took the lead. XRD results of cycled standard CuHCF in 20 mM and 100 mM Zn(ClO₄)₂ illustrated the appearance of new reflections (new phases) after 500 cycles. Regarding the sample cycled in 20 mM Zn(ClO₄)₂ in addition to the new reflections, the main reflections of standard CuHCF remained and were dominant. Although the reflections for the sample cycled in 100 mM Zn(ClO₄)₂ consisted of some of the main standard CuHCF reflections and ZnHCF reflection, its XRD pattern did not match completely with the ZnHCF pattern. Therefore, the conversion of CuHCF to ZnHCF occurred partially for this sample. Based on these results a probable mechanism for phase transformation in standard CuHCF was suggested. This mechanism indicated that upon cycling zinc ions intercalate through the CuHCF structure and occupy the 'A sites'. When critical amounts of intercalated zinc were reached in the lattice, the zinc ions occupy [Fe(CN)₆] vacancies and lead to lattice distortion and poor electrochemical performance. This occupancy was followed by nucleating CuZnHCF mixture and/or ZnHCF. This phase transformation can change the composition and crystallography of standard CuHCF in zinc salt solutions. The degradation of standard CuHCF upon cycling, the potential shifts and the two-step voltage plateau in the potential profiles can all be explained by the proposed mechanism and the electrostatic repulsion within the CuHCF framework. In addition to the effects of the nature of the electrolyte and its concentration, the effect of the current rate on the electrochemical performance of standard CuHCF had been investigated. For this reason, standard CuHCF was cycled at 5C and 10C current rates in 100 mM ZnSO₄ for 1000 cycles. The specific capacity retention at 5C and 10C was equal to 75.42% and 79.36%, respectively. It was obtained that the degradation of the standard CuHCF occurred faster at a lower current rate (5C). The electrochemical results

clarified that the formation of the second phase at a lower current rate was more favorable, while at a higher current rate the phase transition was postponed to a higher number of cycles. All these results depict that the performance of the system is strongly dependent on the current rate, cycling number, concentration of the electrolyte and, the nature of the electrolyte solution. In order to prevent or postpone the degradation of the standard CuHCF several attempts have been done to modify the standard CuHCF structure by acting on the synthesis route. As the zinc ions not only occupy the interstitial sites but also the regular crystal sites of CuHCF upon cycling, an attempt was made to substitute zinc ions during synthesis into the CuHCF lattice. Different mixtures of CuZnHCF were synthesized in which copper was partially substituted with zinc, in particular Cu:Zn ratios were 85:15, 90:10, 93:7, 95:5, and 98:2. The XRD patterns of standard CuHCF and the CuZnHCF mixtures contain sharp reflections and indicated high crystallinity. From the XRD patterns it was obtained that after adding a critical amount of zinc during synthesis, the size of unit cell at each CuZnHCF mixture changed and caused a shift in the reflection position. Therefore, substituting zinc in CuHCF lattice lead to change of lattice parameters. Furthermore, the SEM images of each synthesized powder consisted of agglomerated polydisperse spherical particles with an average size of 80 to 90 nm. The particles aggregated to reveal a highly porous assembly. The nano-sized CuHCF and CuZnHCF particles have high surface area to volume ratio that facilitated a rapid and short ion transport throughout the material. The results also illustrated that the morphologies at each sample is independent from the composition. To investigate the spatial distribution of elements and to determine the number of present phases in each sample, an elemental mapping via an EDX measurement was performed for all of the synthesized powders. For all powders the distribution of the elements was homogeneous but only for a few of them an extra parasitic phase such as oxide form of potassium (KHCO_3 or K_2CO_3) was present. Thereafter, long-term cycling for each sample at a current rate of 1C in 20 mM and 100 mM ZnSO_4 has been performed. The electrochemical results showed that all of the samples degraded upon cycling, but among them only the $\text{Cu}_{0.93}\text{Zn}_{0.07}\text{HCF}$ mixture had high specific charge retention of 98.12% and 86.26% as well as high energy in 20 mM and 100 mM ZnSO_4 after 500 cycles, respectively. The results in 100 mM were also in agreement with the first statement, that at higher electrolyte concentration the degradation of active material occurred faster. Changes in the shapes of the potential profiles and the differential plots during cycling for all the CuZnHCF mixtures in both solutions were visible. The reduction reaction potential upon cycling shifted to higher values and lead to an increase in the total cell voltage upon cycling. The phase transformation in $\text{Cu}_{0.93}\text{Zn}_{0.07}\text{HCF}$ mixture was less favorable during cycling and was postponed to higher number of cycles. Since among all samples, a $\text{Cu}_{0.93}\text{Zn}_{0.07}\text{HCF}$ mixture had the best performance in both 20 mM and 100 mM ZnSO_4 electrolytes, the electrochemical and crystallographic

characterization of this particular mixture and the standard CuHCF in 20 mM and 100 mM ZnSO₄ after 1000 cycles have been studied in detail. Cu_{0.93}Zn_{0.07}HCF has shown a good rate capability and cyclability in 20 mM ZnSO₄ in comparison with standard CuHCF. The obtained energy after 1000 cycles regarding this sample is 6.86% higher than in standard CuHCF. On the contrary, this sample was not able to deliver as high energy in 100 mM than in 20 mM ZnSO₄ after 1000 cycles. For understanding the effect of the phase transformation on the crystallography, morphology and composition of each sample after cycling, XRD measurements and SEM-EDX were performed. Both techniques suggested the formation of new phase(s). SEM-EDX illustrated different morphologies at each cycled sample. For the samples cycled in 20 mM ZnSO₄ three morphologies have been detected (nanoparticles, phase 1, and phase 2). Since the nanoparticles have the original CuHCF or Cu_{0.93}Zn_{0.07}HCF composition, more focus was on the other phases. Phase 1 had cubic morphology with two different compositions at each sample. No evidence of copper was observed. In particular the compositions of the new formed phases with cubic morphology could be KZnHCF and KZnFeHCF with different stoichiometric ratios. Phase 2 was based on non-cubic morphology which consisted of at least two different compositions. At standard CuHCF these compositions could be KZnHCF, KZnFeHCF, and KCuZnHCF, while in Cu_{0.93}Zn_{0.07}HCF they were likely to be KZnHCF and a mixture of KCuZnHCF or KCuZnFeHCF. In Table 7-1, a summary of the detected morphologies and their possible compositions in 20 mM ZnSO₄ is noted.

Table 7-1. An overview of the determined morphologies and their probable compositions by SEM-EDX for standard CuHCF and Cu_{0.93}Zn_{0.07}HCF electrodes after 1000 cycles in 20 mM ZnSO₄.

	20 mM ZnSO ₄			
	Phase 1		Phase 2	
Standard CuHCF	cubic	KZnHCF KZnFeHCF	non-cubic	KZnHCF KCuZnHCF KZnFeHCF
Cu_{0.93}Zn_{0.07}HCF	cubic	KZnHCF KZnFeHCF	non-cubic	KZnHCF KCuZnHCF KCuZnFeHCF

For the samples cycled in 100 mM ZnSO₄ five different morphologies have been detected (nanoparticles, phase 1, phase 3, phase 4, and phase 5). Standard CuHCF consisted of CuHCF nanoparticles, cubic morphology (phase 1) with compositions of KZnHCF and KZnFeHCF, needle shaped morphology (phase 3) with composition of CuZnHCF, and plate shaped morphology (phase 4) with composition of CuZnHCF. Phase 3 and phase 4 did not have any potassium in their structure, while phase 1 did not contain any copper. Cycled Cu_{0.93}Zn_{0.07}HCF consisted of Cu_{0.93}Zn_{0.07}HCF nanoparticles, cubic morphology (phase 1) with compositions of KZnHCF and KZnFeHCF (similar to phase 1 of standard CuHCF), needle shaped morphology (phase 3) with compositions of CuZnHCF and CuZnFeHCF, and spike shaped morphology

(phase 5) with compositions of KZnHCF and KZnFeHCF. These results can suggest that the cubic and needle shaped morphologies at both cycled samples in 100 mM ZnSO₄ had almost similar compositions. The major difference was between phase 4 and 5, which not only its morphology was different in each sample but also its composition. In table below, a summary of the detected morphologies and their possible compositions in 100 mM ZnSO₄ is noted.

Table 7-2. An overview of the determined morphologies and their probable compositions by SEM-EDX for standard CuHCF and Cu_{0.93}Zn_{0.07}HCF electrodes after 1000 cycles in 100 mM ZnSO₄.

		100 mM ZnSO ₄				
		Phase 1		Phase 3		Phase 4
Standard CuHCF	cubic	KZnHCF KZnFeHCF	needle	CuZnHCF	Plate	CuZnHCF
Cu_{0.93}Zn_{0.07}HCF	cubic	KZnHCF KZnFeHCF	needle	CuZnHCF CuZnFeHCF	spike	Phase 5 KZnHCF KZnFeHCF

By considering all the electrochemical and crystallographic results of standard CuHCF and Cu_{0.93}Zn_{0.07}HCF electrodes cycled in 20 mM and 100 mM ZnSO₄, it can be concluded that optimizing standard CuHCF by substituting zinc in CuHCF structure during synthesis successfully postponed the phase transformation mechanism, although at high concentration the Cu_{0.93}Zn_{0.07}HCF mixture did not perform as well as in 20 mM ZnSO₄. This can be explained by the formation of new phases, which had different compositions in comparison with the ones at standard CuHCF. It is possible that the new formed phases are inactive that leads to poor electrochemical performance. In other words, changes of morphology can lead to capacity losses upon cycling. To accomplish the main goal of this study and to obtain an active material with high power density and long life cycle different synthesis conditions were examined. The effects of the pumping speed, temperature, and atmosphere during synthesis on the electrochemical performance of the final product cycled in 100 mM ZnSO₄ were investigated. Table 7-3 shows a summary of the electrochemical performances of different powders cycled at 1C rate in 100 mM ZnSO₄.

Table 7-3. Summary of the percentages of energy and charge retention for different active materials cycled at 1C rate in 100 mM ZnSO₄.

Synthesized CuHCF	After 500 cycles		After 1000 cycles	
	Energy	Charge	Energy	Charge
Standard	94.41%	85.38%	81.39%	73.53%
0.5 mL min⁻¹	93.06%	85.25%	-	-
2 mL min⁻¹	89.6%	81.27%	-	-
Low T	64.5%	59.87%	39.6%	36.5%
High T	85.69%	78.16%	74.14%	66.3%
Under Ar, Low T	88.94%	82.81%	77.3%	70.1%
Under Ar, Room T	94.96%	87.33%	87.1%	78.2%
Under Ar, High T	90.19%	78.73%	70.3%	60.5%

By comparing all data, it can be mentioned that the argon atmosphere had a huge impact on the performances of the CuHCF, increasing the energy retention after 1000 cycles from 81% to 87%. That means that the battery could be stable up to 1500 cycles, thus reaching the performances of a classic high power LIB. The role of argon on the synthesis of CuHCF is not yet clear and was unpredictable. However, it is obvious that argon atmosphere has an enormous effect and among the attempted strategies was the one with higher success. This new synthesis condition provides a new perspective to develop materials for rechargeable zinc-ion batteries for stationary applications and for short-time storage of the solar and wind power with higher energy. During this Ph.D. work, the finally delivered energy and the lifetime of an aqueous zinc-ion battery was enhanced up to 1000 cycles due to the development of a new active material. Among the active materials as cathode in aqueous zinc-ion batteries, CuHCF and its derivatives from the Prussian blue family showed a promising result. Since aqueous batteries became an attractive energy storage system for grid-scale due to their remarkable advantages despite having a low cell operating voltage, it is possible to connect several cells of it in series to reach the overall operating voltage. Finally, it is interesting to compare the developed battery from this work with the most common batteries which are nowadays utilized in grid-scale energy storage systems. Therefore, in Table 7-4 the technical characteristics of certain electrical energy storage technologies are reported. Although LIBs are the most widely used battery technology for grid-scale energy storage, they are not the cost-effective choice for long-term storages. Accordingly, other EESs such as the ones mentioned in Table 7-4 are competing with them with regard to cost and energy efficiency despite their advantages and challenges. As the main goal of energy storage development is to select a battery, which is affordable and reliable with high efficiency, aqueous zinc-ion batteries based on modified CuHCF offer a noticeable opportunity for further developments.

Table 7-4. Merit of certain electrical energy storage systems.^[211]

Battery type	Suitable storage duration	Cycle life [cycles]	Specific energy [Wh kg ⁻¹]	Specific power [W kg ⁻¹]
Aqueous ZIB based on modified CuHCF cathode material	Hours-months	Up to 1500	10-47	46-297
Lead-acid	Minutes-days ^[22] Short-to-medium term	500-1000 ^[22] 200-1800 ^[217]	30-50 ^[22] 25-50 ^[218]	75-300 ^[22] 250 ^[219] 180 ^[220]
Li-ion	Minutes-days ^[22] Short-to-medium term	1000-10000 ^[22] Up to 20000 ^[221]	75-200 ^[22] 90 ^[219] 120-200 ^[222]	150-315 ^[22] 300 ^[219] 500-2000 ^[220]
Na-S	Long-term ^[223]	2500 ^[22] 3000 ^[224] 2500-4500 ^[13]	150-240 ^[22] 100 ^[107] 174 ^[225]	150-230 ^[22] 90-230 ^[221] 115 ^[217]

Battery type	Suitable storage duration	Cycle life [cycles]	Specific energy [Wh kg ⁻¹]	Specific power [W kg ⁻¹]
Ni-Cd	Minutes-days ^[22]	2000-2500 ^[22]	50-75 ^[22]	150-300 ^[22]
	Short and long-term	3500 ^[226]	5 ^[219]	160 ^[217]
PSB	Hours-months ^[22]	-	~15-30 ^[229]	-
	Long-term ^[228]			
VRB	Hours-months ^[22]	12000+ ^[22]	10-30 ^[22]	166 ^[231]
	Long-term ^[228]	13342 ^[230]		
ZnBr	Hours-months ^[22]	2000+ ^[22]	30-50 ^[22]	100 ^[232]
	Long-term ^[228]	1500 ^[230]	80 ^[232]	45 ^[233]
				75 ^[233]

Na-S = Sodium-sulfur battery, Ni-Cd = Nickel-cadmium battery, VRB = Vanadium redox flow battery, ZnBr = Zinc bromine flow battery, PSB = Polysulfide bromine flow battery.

Fig. 7-1 represents some storage technologies based on their anticipated level of research, development, and demonstration (RD&D) against time. Although the proposed aqueous ZIB of this work is far from the maturity level, due its impressive characteristics further investigations are required. The topic of energy storage is wide enough and everyday it needs further attention due to the world energy demand. Therefore, researches and energy storage developers not only should focus on the technical aspects of an energy storage system but also on economic and environmental aspects.

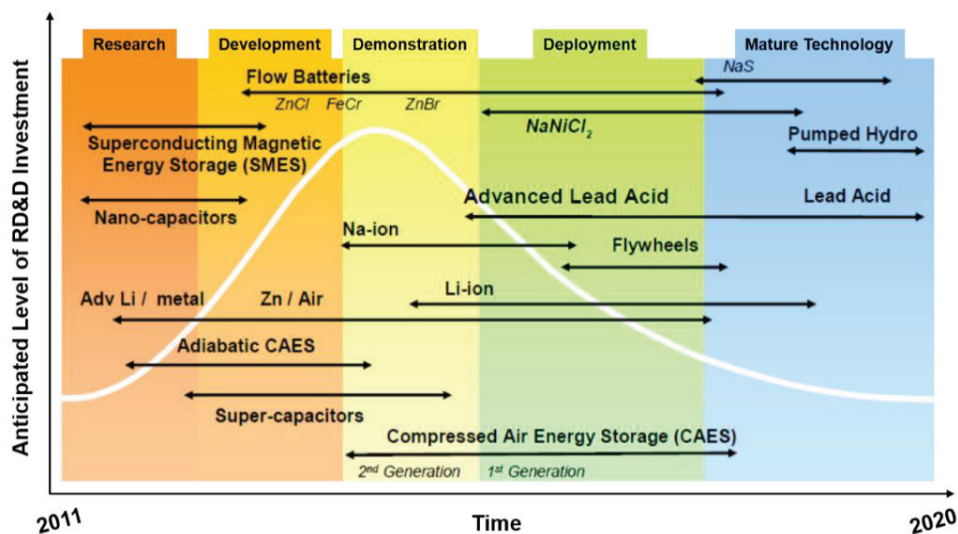


Figure 7-1. The level of technological maturity against the anticipated RD&D investment for variety of energy storage technologies (adapted from ^[234]).

8. Construction of 1 Wh Zinc-Ion Battery Based on PBAs

In this chapter, the results of the Bachelor student's project from WISE 2016/2017 and WISE 2017/2018 are described. During this project, we tried to construct an aqueous zinc-ion full cell battery based on PBAs with an energy of 1 Wh. In this battery standard CuHCF was used as cathode material, zinc foil as anode, glass microfiber filter as separator, and 100 mM ZnSO₄ as electrolyte. Fig. 8-1 shows the schematic design of the cell which has been used for the first test.

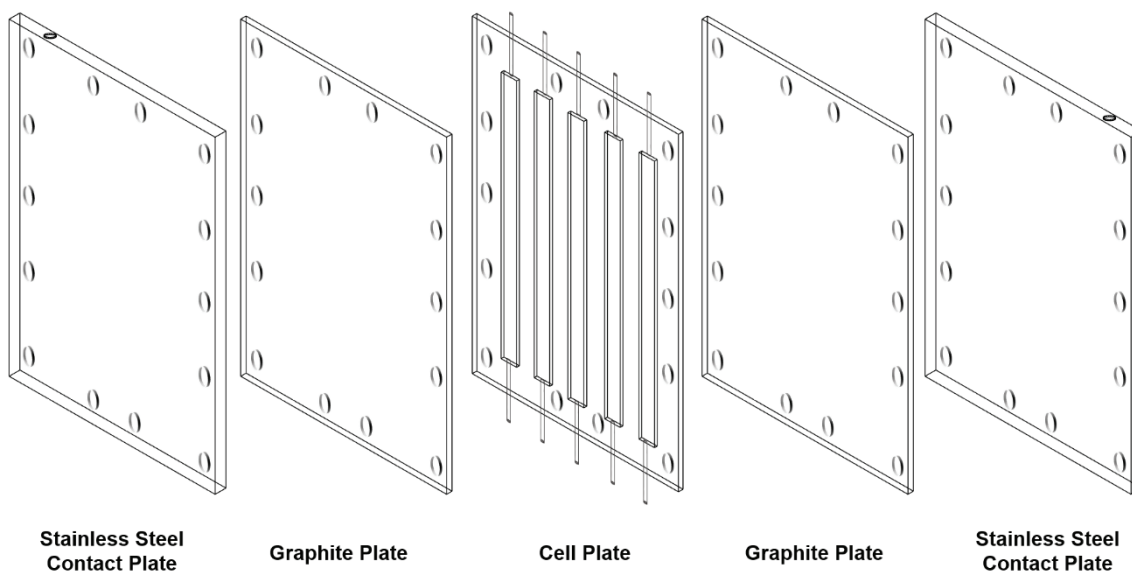


Figure 8-1. Schematic design of the first full cell battery.

The cell consisted of five parts. A plate made of stainless steel was used in each side of the cell, in order to protect the next layers as well as the whole cell from any damage and also to hold the cell sealed tightly. The graphite plates (bipolar plates with the thickness of 1.5 mm) were placed after stainless-steel plates. This type of plates is usually utilized in flow batteries and allows assembling individual cells to large-scale stacks. Bipolar plates with high porosity, large surface area, and well electrical properties have received great attention. Their good electrical conductivity (via the plate and along the plate) as well as chemical resistance can be mentioned as outstanding properties. These plates are able to facilitate an efficient charge exchange during charging and discharging. The last compartment of the cell was the cell plate in which the cathode, separators, and anode was placed. The cell plate had five chambers (1 × 10 cm). In this design, the cell plate was made of Plexiglas and was covered by Teflon tape to prevent any leakage. At the top and bottom part of this plate, metallic connectors with an inner diameter of 0.58 mm and outer diameter of 0.9 mm were placed into its frame. The electrolyte will be

flowed through these connectors into each chamber. Since the main goal of this chapter is obtaining an aqueous zinc-ion battery with energy of 1 Wh, four layers of the cell plate had been used between each pair of bipolar plates. Around 13 g of standard CuHCF had been synthesized (3.25 g per each cell plate, 650 mg per each chamber). The electrochemical performance of the active material had been tested with the help of GCPL in advance. During painting the slurry on the carbon cloth current collector, the active material was distributed as homogeneously as possible at each chamber. At each chamber three painted carbon cloths with standard CuHCF slurry, two separators, and one zinc foil were placed. The reason for using three carbon cloths in each chamber was the limited available area, which could have been painted since each carbon cloth stripe could only hold a maximum ~200 mg of active material. After assembling the cell, the potential between each layer had been checked in order to make sure that no short circuit exists. For pumping the electrolyte through the cell, the peristaltic pump had been used. At first the electrolyte had been pumped by a tube that could flow 0.1 mL min^{-1} electrolyte to the inlet of the first cell plate. Thereafter, the outlet of the first layer was connected to the inlet of the second cell plate and this sequence continued till the last layer. At the end the tube that came out from the outlet of the last cell plate was put into an empty beaker. Pumping electrolyte had been done for around 30 min in order to distribute electrolyte in all of the chambers and to remove any extra oxygen or over pressure at each chamber. For better understanding an image of the set-up is shown in Fig. 8-2.

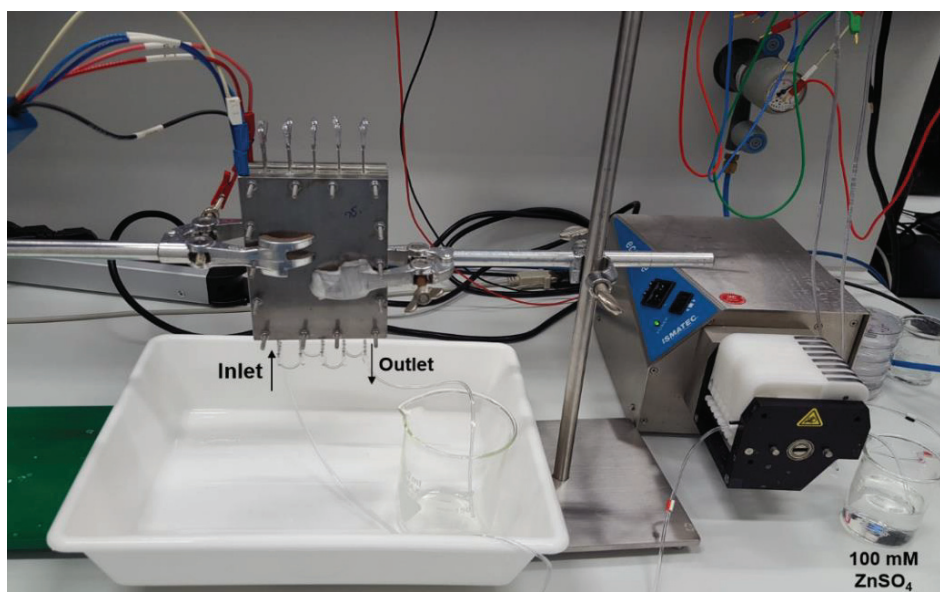


Figure 8-2. The aqueous zinc-ion full cell battery based on the first design.

After making sure that each layer was filled with electrolyte, open circuit voltage (OCV) had been measured. Here, an OCV in the range of 5 to 6 V vs. Zn/Zn^{2+} was obtained. Since the cell plates were connected in series with each other, the potential range for running galvanostatic cycling should have been multiplied by four (number of layers) and the applied current should

have been divided by four. Therefore, the cycling was done between 4.72 to 8.32 V vs. Zn/Zn²⁺ at the constant current of 0.233 mA (at 1C). To prevent destroying the active material the measurement started with a low current rate (C/2). As it is clear in the potential profile (Fig. 8-3), after reaching 8.32 V the reduction step started but did not recover any charge and was followed by the next oxidation step. This means that no zinc ions intercalated through the system. A huge overpotential had been also observed upon cycling.

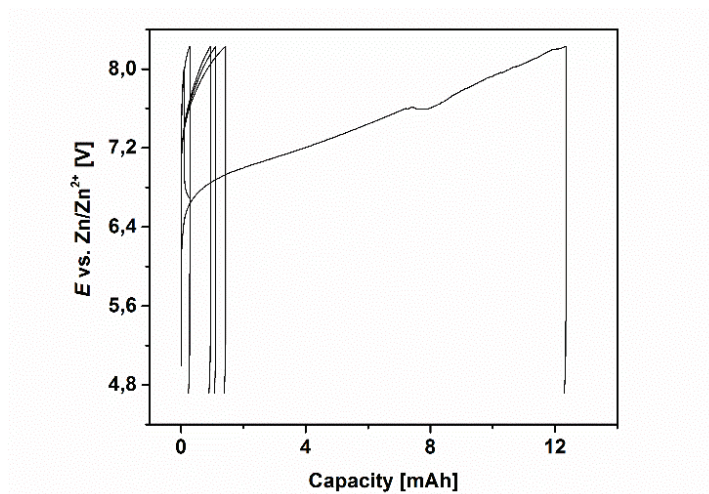


Figure 8-3. The potential profile of the aqueous zinc-ion full cell battery performed in the first designed cell.

After running the experiment several drawbacks for the cell had been clear. In the following some of these problems are mentioned.

1. The electrolyte had been leaking during pumping where the metallic connectors were glued to the Plexiglas frame. Also, there was a leakage from each layer of cell plate during the whole experiment. This issue was caused by the tightness of the cell and degradation of the glue in the humid atmosphere.
2. Since metallic screws were used to tighten the cell, it was difficult to avoid any short circuit even though the screws have been covered by an insulator plastic layer.
3. Several internal short circuits occurred due to the electrolyte leakage from one chamber to the other. The cell plate with this problem was completely destroyed and could not be cycled again. When this problem was noticed, we tried to remove that specific layer and to cycle the other three layers, but unfortunately the oxidation did not happen. After disassembling the cell and removing the unusable layer, it was observed that all of the working electrodes (standard CuHCF) at this layer have been destroyed.
4. Although we tried to distribute the slurry equally at each chamber, it was difficult to be sure that at each carbon cloth stripe the same amount of active material was painted. Therefore, the calculated applied current based on the total mass of the active material had slight errors.

5. As it was observed from the potential profile, a huge overpotential upon cycling occurred. This can be caused due to internal short circuits between layers or at each layer itself. Additionally, if any contact problem exists in the cell, a big polarization at the zinc side can be appeared and would lead to a huge overpotential.
6. The other issue that led to bad electrochemical performance could be the inappropriate cell geometry. Since three working electrodes had been placed on top of each other, it was probable that the electrodes kinked or got displaced. Another possibility was the contact between the working electrodes and the zinc foil which would lead to short circuit.
7. Another problem was due to the Plexiglas cell plate. In order to have a compact battery cell, the battery compartments should be pressed strongly together. With the mentioned design, there was a mechanical limitation due to the Plexiglas material.
8. It was difficult to control the amount of pumped electrolyte through the battery with the mentioned procedure. In other words, it was not possible to make sure that the distribution of the electrolyte at the last chamber was the same as for the first one. Furthermore, it was unclear whether with the used pumping speed, the air was completely removed from each chamber.

Since the main goal of reaching 1 Wh battery had remained, it was important to design a new cell by considering the aforementioned problems. For this purpose, a cell with the given design as shown in Fig. 8-4 was proposed. As it is clear from Fig. 8-4, the Plexiglas cell plate was replaced by a Polyoxymethylene (POM) sheet to prevent any mechanical limitation. In addition, we tried to improve the cell from a geometrical point of view. Thereby, an internal frame with a depth of 0.2 mm had been cut from the main frame. In this version of the cell, instead of five chambers, four chambers with smaller dimensions had been designed. Furthermore, the metallic connectors for pumping electrolyte were only placed on one side of the cell plate and during electrolyte pumping, each two adjacent chambers were connected with each other. The surface of the internal frame was covered by a foam rubber (colored with grey in the image below) to avoid any electrolyte leakage and to prevent an internal short circuit. It is important to mention that in the previous designed version, the foam rubber had the same thickness as the frame depth but after tightening the cell, the leakage of the electrolyte occurred again. Therefore, in the latest design, we did not change the thickness of the foam rubber and it kept at 1 mm to prevent major thickness deformation due to the mechanical force upon tightening. Another change in the latest design was the bipolar plates. The bipolar plates had smaller dimensions and thickness (0.6 mm) than the previous design and they only covered the area which the internal frame had been placed. Extra POM plates were placed after graphite plates in order to hold them in their

positions and to prevent any drifting. At last, the cell was closed and sealed with the stainless-steel plates and screws.

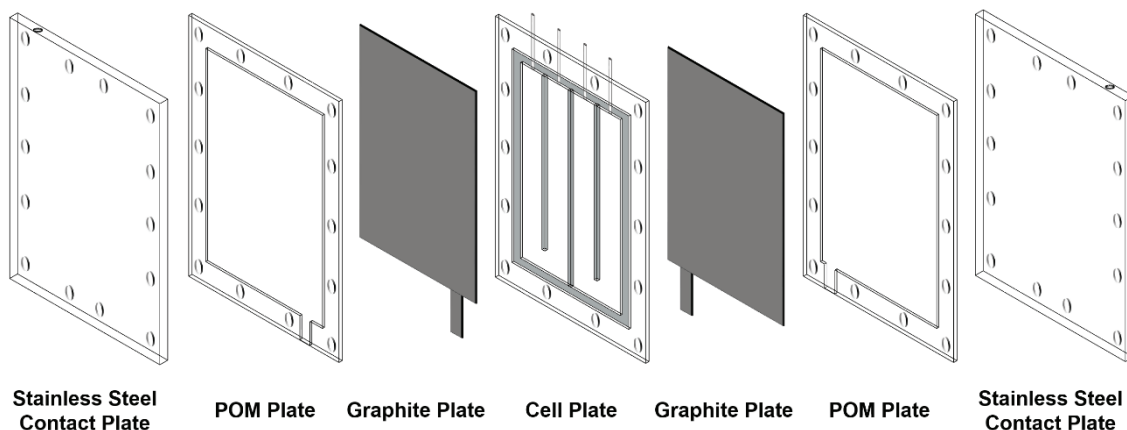


Figure 8-4. Schematic design of the second full cell battery.

Since in this design the size of each chamber was smaller (1×8.8 cm) than the previous design, six cell plates were employed to reach 1 Wh battery. Before running the measurement, around 13.5 g of standard CuHCF was synthesized and was painted equally on 24 carbon cloth stripes. Each chamber consisted of one carbon cloth covered with active material, three separators and one zinc foil. The cell plates were located between the bipolar plates. Thereafter, all cells had been assembled as it was discussed above. To avoid any internal short circuit between layers, each cell plate had been filled up with electrolyte separately (Fig. 8-5a). After filling up the cell completely, the inlet and outlet at each cell plate was connected to each other to avoid any electrolyte loss and overpressure.

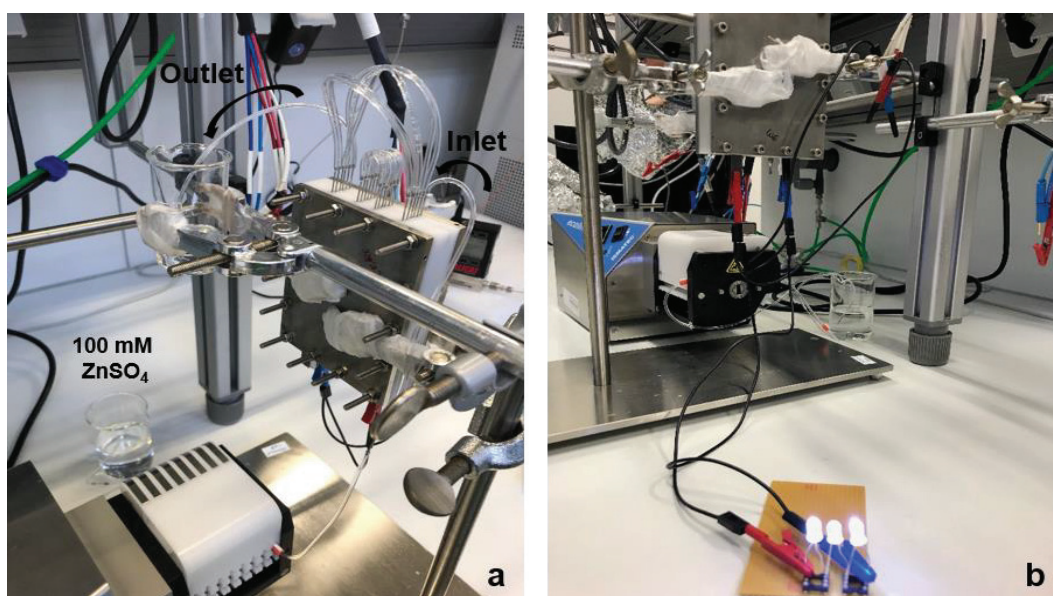


Figure 8-5. The aqueous zinc-ion full cell battery with second design (a) illustrating the pumping procedure at one cell plate, (b) potential of the battery for lightening the LEDs.

Since the six cell plates were connected in series, the potential range for GCPL had been limited from 7 to 12.5 V vs. Zn/Zn²⁺. In this design the bipolar plates had an extra tail to the outside of the cell frame. This tail was established to facilitate the connection at each cell plate and enabled cycling each cell plate separately. The potential at each cell plate had been checked and was around 1.6 V vs. Zn/Zn²⁺, while having an OCV of 9.92 V vs. Zn/Zn²⁺. The battery had been charged with the current rate of C/10. The cell was able to oxidize till 12.2 V and afterwards it dropped till 10.7 V (Fig. 8-6). As a proof of principle, the cell had been connected to three light-emitting diodes (LED) which were connected in series (Fig. 8-5b). Each LED needed a potential of 3.2 V to illuminate. Although the cell did not reach 12.5 V it was still able to light the LEDs. The reason for the potential drop during oxidation is not completely clear. It can be related to the active material or the zinc anode. Afterwards, the potential at each layer was checked and one of them had a low potential of ~1.2 V. Chronoamperometry technique was applied to increase the potential of this specific layer to higher values, but in a short time its potential dropped drastically again. Probably an internal short circuit occurred in this layer and damaged the active material. Thereafter, the battery had been cycled with the left over five cell plates. Unfortunately, the cell could not reach the potential that was set at the BioLogic software and it led to a huge overpotential.

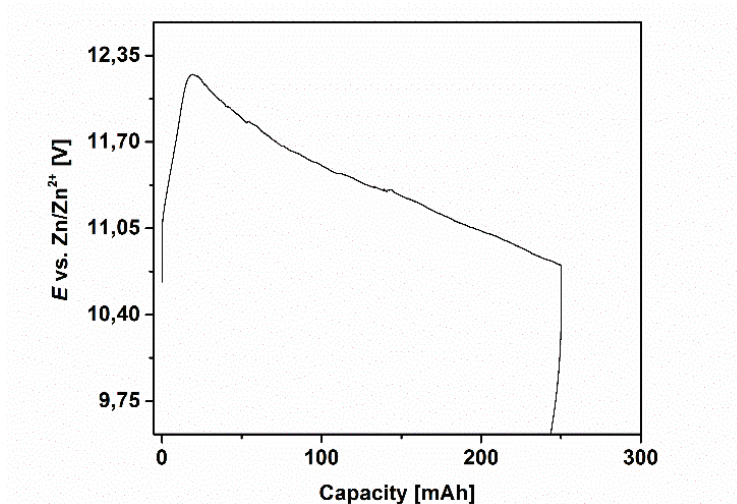


Figure 8-6. The potential profile of the aqueous zinc-ion full cell battery performed in the second designed cell.

In order to find the sources of these problems the cell was disassembled. There were several grey spots on the separators (Fig. 8-7a) and their former white color changed to yellow (iron traces). On the side of the bipolar plates which were in contact with standard CuHCF, a copper layer was formed (Fig. 8-7b) and we assumed that hydrogen evolution at graphite happened. On the surface of the zinc foils, zinc dendrites were formed, which is accompanied by hydrogen evolution.

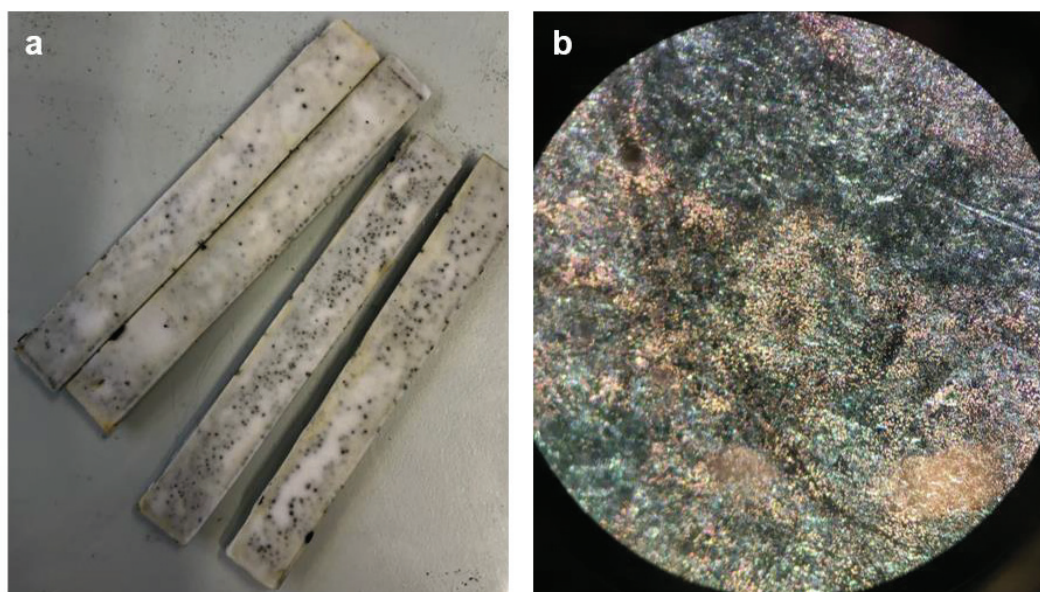


Figure 8-7. (a) Separators after cycling and (b) the surface of the bipolar plate under an optical microscope.

With this design, we tried to overcome contact issues of the previous version by reducing the number of cathodes in each chamber, replacing the Plexiglas with the POM material, and covering the frame with foam rubber to prevent electrolyte leakage and any internal short circuits. However, several drawbacks after the experiment had been revealed. It was found that the internal short circuit issue was not fully solved. There were leakages at the connections of the metallic connectors to the frame of POM. Gluing the connectors to the POM material was difficult and in contact with humidity they broke. Although the new design of bipolar plates with lower thickness allowed each cell plate to be cycled separately, they got deformed due to the tightening of the cell and furthermore the extra tail for the connection got damaged after several attempts of connecting with a crocodile clip. A huge overpotential had been observed which corresponded to the zinc dendrite formation and hydrogen evolution at the zinc anode side. In addition, the active material degraded and copper was deposited on the bipolar plates. Additionally, there were iron traces on the separators. At last all these problems led to a poor and unstable electrochemical performance of the full cell battery.

Although the second design had fewer drawbacks than the first version, still more developments are needed to reach a 1 Wh battery. There are several important aspects that can be considered for further optimizations. Employing one big electrode chamber instead of several chambers in each cell plate can be one solution. The procedure of pumping electrolyte needs optimization, may it be in a way to control the distribution of the electrolyte at each chamber or to make the equal amounts of electrolyte in each cell plate. Another way can be adding the electrolyte during the cell assembling by wetting the separators with the desired electrolyte. In this case no extra rubber for blocking the electrolyte is needed and the metallic connectors for the electrolyte

supply no longer are needed. Furthermore, the material of the cell plate can be replaced with a flexible one, such as silicone rubber gasket, which can provide sufficient sealing. Moreover, silicon rubber can prevent leakage between different substrate sections and have excellent resistivity at high and low temperatures. Another important property of silicone is that it usually does not react with most of the chemicals and can be used in a wide range of applications. Since the zinc foil anode undergoes a zinc dendrite formation and lead to an internal short circuit, it is critical to overcome or limit this problem. For this purpose, one can use a zinc electrode by painting a slurry containing zinc powder mixed with additives and binder on the carbon cloth current collector.

9. Conclusions and Outlook

As the value of EESs is increasing due to the worldwide energy demand, studying and developing reliable, stable, low-cost and high energy efficient energy storage systems for integrating renewables into the electricity grid and grid integration of electric mobility is a matter of importance. Among EESs, batteries as an electrochemical energy storage system can be the best candidate for integrating renewable resources.

Kundu et al.^[106] estimated that the cost of ZIBs is lower than US\$65 per kWh. This value is much lower than that of LIBs with US\$300 per kWh and close to that of lead-acid and Ni-Fe batteries.^[62,235,236] Therefore, focusing on aqueous metal-ion batteries such as zinc-ion battery that became an attractive candidate with high potentials for large-scale batteries to support electrical grid, is critical. In this Ph.D. work different battery systems were reviewed and the main focus was laid on aqueous zinc-ion batteries based on standard CuHCF and its derivatives. In addition, several attempts and experiments have been performed in this study to achieve a stable active material with high energy retention and long life cycle, as a positive electrode for ZIB. A new cathode material with high energy efficiency has been successfully developed. This material can enable a zinc-ion battery system to be stable up to 1500 cycles and reach the performance of a classic high power LIB. This study provided a wide range of new ideas and perspectives to overcome the challenges in the pursuit of stable cathode and anode materials with long lifetime and investigating a compatible aqueous electrolyte which is compatible with the electrodes.

Here several suggestions for future work on this specific battery system are proposed. For having a better insight during the electrochemical experiments, synchrotron techniques or in-situ/in-operando techniques for material characterizations during battery cycling could help to understand and characterize the phase transformation mechanism. A more sophisticated cell design in combination with an in-situ technique compatible with aqueous medium can offer a better overview on the performance of the battery as well as increasing the kinetics of the system. Furthermore, one can study different co-ion intercalations through CuHCF structure and investigate their kinetic and thermodynamic effects on the electrochemical performances of CuHCF. Since the main goal is to reach a battery with high life cycle (10000 cycles), it would be a good idea to construct a pouch cell battery pack and study the performance of the full cell battery. In addition, the results of this work showed that the synthesis parameters have an enormous effect on the electrochemical performance of CuHCF. Therefore, further studies on the synthesis conditions and parameters are important. As the argon gas has higher solubility (62 mg L^{-1}) in water, at 20°C and pressure of 1 bar, than nitrogen gas (20 mg L^{-1}),^[237] it is probable that the argon gas during synthesis procedure has been dissolved in the solutions.

Accordingly, it is interesting to study whether employing nitrogen gas instead of argon gives a sample with better electrochemical performance. Moreover, one can study the possible ion-exchange when the CuHCF is soaked in different concentrations of zinc sulfate, while controlling the immersing time. This goal can be achieved with the help of post-mortem analysis.

It is crucial for energy storage development that besides attempts for lowering the final costs of a battery (utilizing cheap materials and electrolytes), to develop a smart model to control every single occurrence at a battery during cycling. This model in addition to detect any system failure could predict the performance of a system and allows the operator to fix and regulate those weaknesses. Besides the direct control of a system, the model can also provide power during peak demand, storing power peaks during overproduction in a backup storage, and regulate/smooth the output of renewable energy sources. By merging a smart model with an energy storage system such as batteries it will be possible to fully integrate renewables into a sustainable energy system and to fulfill the worldwide energy demand.

10. References

- [1] S. Chu, Y. Cui, N. Liu, *Nat. Mater.* **2017**, *16*, 16.
- [2] M. Z. Jacobson, M. A. Delucchi, *Energy Policy* **2011**, *39*, 1154.
- [3] *International Energy Outlook*, U.S. Energy Information Administration, **2016**.
- [4] “PVX Spot Market Price Index Solar PV Modules,” can be found under <http://go.nature.com/2fHdydjV>, **2016**.
- [5] J. P. Barton, D. G. Infield, *IEEE Trans. Energy Convers.* **2004**, *19*, 441.
- [6] Z. Yang, J. Zhang, M. C. W. Kintner-Meyer, X. Lu, D. Choi, J. P. Lemmon, J. Liu, *Chem. Rev.* **2011**, *111*, 3577.
- [7] V. S. Arunachalam, E. L. Fleischer, *MRS Bull.* **2011**, *33*, 264.
- [8] D. Ginley, M. Green, R. Collins, *MRS Bull.* **2008**, *33*, 355.
- [9] J. P. Holdren, *Science* **2007**, *315*, 737.
- [10] X. Li, H. Zhang, Z. Mai, H. Zhang, I. Vankelecom, *Energy Environ. Sci.* **2011**, *4*, 1147.
- [11] C. P. Grey, J. M. Tarascon, *Nat. Mater.* **2016**, *16*, 45.
- [12] “Technology Roadmap: Electric and Plug-in Hybrid Electric Vehicles,” can be found under http://www.oecd-ilibrary.org/energy/technology-roadmap-electric-and-plug-in-hybrid-electric-vehicles_9789264088177-en, **2009**.
- [13] M. Beaudin, H. Zareipour, A. Schellenberglabe, W. Rosehart, *Energy Sustain. Dev.* **2010**, *14*, 302.
- [14] Lazard, *Lazard’s levelized cost storage - version 3.0* **2017**, 1.
- [15] P. T. Moseley, J. Garche, Eds. , *Electrochemical Energy Storage for Renewable Sources and Grid Balancing*, International Lead Zinc Research Org. Inc., Durham, NC, USA, **2014**.
- [16] G. Fuchs, B. Lunz, M. Leuthold, D. U. Sauer, in *Electrochem. Energy Storage Renew. Sources Grid Balanc.*, Elsevier B.V., **2014**, pp. 89–102.
- [17] O. Palizban, K. Kauhaniemi, *J. Energy Storage* **2016**, *6*, 248.
- [18] S. P. S. Badwal, S. S. Giddey, C. Munnings, A. I. Bhatt, A. F. Hollenkamp, *Front. Chem.* **2014**, *2*, 1.
- [19] P. Kurzweil, in *Electrochem. Energy Storage Renew. Sources Grid Balanc.*, Elsevier B.V., **2014**, pp. 269–307.
- [20] S. Matteson, E. Williams, *Energy Policy* **2015**, *85*, 71.
- [21] B. Zakeri, S. Syri, *Renew. Sustain. Energy Rev.* **2015**, *42*, 569.
- [22] H. Chen, T. N. Cong, W. Yang, C. Tan, Y. Li, Y. Ding, *Prog. Nat. Sci.* **2009**, *19*, 291.
- [23] G. L. Kyriakopoulos, G. Arabatzi, *Renew. Sustain. Energy Rev.* **2016**, *56*, 1044.
- [24] *Meeting the Energy Needs of Future Warriors*, Committee On Soldier Power/Energy Systems, Board On Army Science And Technology, National Research Council Of The Nation Academies, Washington (DC), **2004**.
- [25] “WebElements,” can be found under <http://www.webelements.com>, **2018**.
- [26] P. C. K. Vesborg, T. F. Jaramillo, *RSC Adv.* **2012**, *2*, 7933.
- [27] W. M. Brown, *The Meaning of Scarcity in the 21st Century : Drivers and Constraints to the Supply of Minerals Using Regional , National and Global Perspectives*, **2002**.
- [28] C. J. Barnhart, S. M. Benson, *Energy Environ. Sci.* **2013**, *6*, 1083.
- [29] “Chemicool,” can be found under <http://www.chemicool.com>, **2018**.
- [30] “Leonland,” can be found under http://www.leonland.de/elements_by_price/en/list, **2018**.
- [31] D. Linden, T. B. Reddy., Eds. , *Handbook of Batteries*, McGraw-Hill, **2002**.
- [32] I. Landa-Medrano, C. Li, N. Ortiz-Vitoriano, I. Ruiz De Larramendi, J. Carrasco, T. Rojo, *J. Phys. Chem. Lett.* **2016**, *7*, 1161.
- [33] J. F. DeCarolis, D. W. Keith, *Energy Policy* **2006**, *34*, 395.
- [34] M. A. Delucchi, M. Z. Jacobson, *Energy Policy* **2011**, *39*, 1170.
- [35] Y. C. Lu, B. M. Gallant, D. G. Kwabi, J. R. Harding, R. R. Mitchell, M. S. Whittingham, Y. Shao-Horn, *Energy Environ. Sci.* **2013**, *6*, 750.

- [36] H. D. Yoo, E. Markevich, G. Salitra, D. Sharon, D. Aurbach, *Mater. Today* **2014**, *17*, 110.
- [37] N. Singamsetti, S. Tosunoglu, *8th Int. Symp. Manag. Eng. Informatics, MEI 2012* **2012**.
- [38] D. G. Enos, in *Adv. Batter. Mediu. Large-Scale Energy Storage*, Elsevier Ltd., **2015**.
- [39] D. Bresser, E. Paillard, S. Passerini, in *Adv. Batter. Mediu. Large-Scale Energy Storage*, Elsevier Ltd., **2015**.
- [40] G. Soloveichik, *Annu. Rev. Chem. Biomol. Eng.* **2011**, *2*, 503.
- [41] A. M. Vassallo, in *Adv. Batter. Mediu. Large-Scale Energy Storage*, Elsevier Ltd., **2015**, pp. 587–607.
- [42] H. Lee, M. Yanilmaz, O. Toprakci, K. Fu, X. Zhang, *Energy Environ. Sci.* **2014**, *7*, 3857.
- [43] M. Sathiya, G. Rouse, K. Ramesha, C. P. Laisa, H. Vezin, M. T. Sougrati, M. L. Doublet, D. Foix, D. Gonbeau, W. Walker, A. S. Prakash, M. Ben Hassine, L. Dupont, J. M. Tarascon, *Nat. Mater.* **2013**, *12*, 827.
- [44] X. Ji, K. T. Lee, L. F. Nazar, *Nat. Mater.* **2009**, *8*, 500.
- [45] M. S. Whittingham, W. M. S., *Chem. Rev.* **2004**, *104*, 4271.
- [46] C. K. Chan, H. Peng, G. Liu, K. McIlwrath, X. F. Zhang, R. A. Huggins, Y. Cui, *Nat. Nanotechnol.* **2008**, *3*, 31.
- [47] D. Lin, Y. Liu, Z. Liang, H. W. Lee, J. Sun, H. Wang, K. Yan, J. Xie, Y. Cui, *Nat. Nanotechnol.* **2016**, *11*, 626.
- [48] Y. Wang, W. H. Zhong, *ChemElectroChem* **2015**, *2*, 22.
- [49] F. R. Kalhammer, B. M. Kopf, D. H. Swan, V. P. Roan, M. P. Walsh, *Electr. Power Res. Institute, Palo Alto, CA* **2007**.
- [50] Z. Huang, G. Du, in *Adv. Batter. Mediu. Large-Scale Energy Storage*, **2015**, pp. 74–90.
- [51] F. Cheng, J. Liang, Z. Tao, J. Chen, *Adv. Mater.* **2011**, *23*, 1695.
- [52] D. Ryu, C. Park, H. Ahn, B. Kim, E. Lee, *U.S. Patent Application*, **2007**.
- [53] C.-W. Park, J.-H. Ahn, H.-S. Ryu, K.-W. Kim, H.-J. Ahn, *Electrochem. Solid-State Lett.* **2006**, *9*, A123.
- [54] J. Coetzer, R. Galloway, R. Bones, D. Teagle, P. Moseley, *DE Patent*, **1983**.
- [55] C. X. Li, Ponce de Léon, F. C. Walsh, R. G. A. Wills, D. Pletcher, in *Adv. Batter. Mediu. Large-Scale Energy Storage*, **2015**.
- [56] H. Zhang, in *Adv. Batter. Mediu. Large-Scale Energy Storage*, Elsevier Ltd., **2015**, pp. 317–327.
- [57] M. Skyllas-Kazacos, J. F. McCann, in *Adv. Batter. Mediu. Large-Scale Energy Storage*, Elsevier Ltd., **2015**, pp. 329–386.
- [58] A. Z. Weber, M. M. Mench, J. P. Meyers, P. N. Ross, J. T. Gostick, Q. Liu, *J. Appl. Electrochem.* **2011**, *41*, 1137.
- [59] *EPRI-DOE Handbook of Energy Storage for Transmission & Distribution Applications*, U.S. Department Of Energy, Washington, **2003**.
- [60] “Electrical Storage Association,” can be found under <http://electricitystorage.org/ESA/technologies>, **2018**.
- [61] “Electropaedia, Energy Sources and Energy Storage, Battery and Energy Encyclopaedia and History of technology,” can be found under <https://www.mpoweruk.com/performance.htm>, **2005**.
- [62] J. O. G. Posada, A. J. R. Rennie, S. P. Villar, V. L. Martins, J. Marinaccio, A. Barnes, C. F. Glover, D. A. Worsley, P. J. Hall, *Renew. Sustain. Energy Rev.* **2017**, *68*, 1174.
- [63] Y. Li, J. Lu, *ACS Energy Lett.* **2017**, *2*, 1370.
- [64] G. Girishkumar, B. McCloskey, A. C. Luntz, S. Swanson, W. Wilcke, *J. Phys. Chem. Lett.* **2010**, *1*, 2193.
- [65] K. M. Abraham, Z. Jiang, *J. Electrochem. Soc.* **1996**, *143*, 1.
- [66] T. Ogasawara, A. Débart, M. Holzapfel, P. Novák, P. G. Bruce, *J. Am. Chem. Soc.* **2006**, *128*, 1390.
- [67] P. G. Bruce, S. A. Freunberger, L. J. Hardwick, J.-M. Tarascon, *Nat. Mater.* **2012**, *11*, 19.
- [68] B. D. Adams, C. Radtke, R. Black, M. L. Trudeau, K. Zaghbi, L. F. Nazar, *Energy*

- Environ. Sci.* **2013**, *6*, 1772.
- [69] L. Johnson, C. Li, Z. Liu, Y. Chen, S. A. Freunberger, P. C. Ashok, B. B. Praveen, K. Dholakia, J. M. Tarascon, P. G. Bruce, *Nat. Chem.* **2014**, *6*, 1091.
- [70] N. B. Aetukuri, B. D. McCloskey, J. M. García, L. E. Krupp, V. Viswanathan, A. C. Luntz, *Nat. Chem.* **2015**, *7*, 50.
- [71] Y. Chen, S. A. Freunberger, Z. Peng, O. Fontaine, P. G. Bruce, *Nat. Chem.* **2013**, *5*, 489.
- [72] B. J. Bergner, A. Schürmann, K. Peppler, A. Garsuch, J. Janek, *J. Am. Chem. Soc.* **2014**, *136*, 15054.
- [73] H. D. Lim, H. Song, J. Kim, H. Gwon, Y. Bae, K. Y. Park, J. Hong, H. Kim, T. Kim, Y. H. Kim, X. Leprö, R. Ovalle-Robles, R. H. Baughman, K. Kang, *Angew. Chemie - Int. Ed.* **2014**, *53*, 3926.
- [74] Z. Peng, S. A. Freunberger, Y. Chen, P. G. Bruce, *Science* **2012**, *337*, 563.
- [75] M. M. Ottakam Thotiyil, S. A. Freunberger, Z. Peng, Y. Chen, Z. Liu, P. G. Bruce, *Nat. Mater.* **2013**, *12*, 1050.
- [76] T. Liu, M. Leskes, W. Yu, A. J. Moore, L. Zhou, P. M. Bayley, G. Kim, C. P. Grey, *Encycl. Soils Environ.* **2005**, *350*, 170.
- [77] J. Lu, Y. J. Lee, X. Luo, K. C. Lau, M. Asadi, H. H. Wang, S. Brombosz, J. Wen, D. Zhai, Z. Chen, D. J. Miller, Y. S. Jeong, J. B. Park, Z. Z. Fang, B. Kumar, A. Salehi-Khojin, Y. K. Sun, L. A. Curtiss, K. Amine, *Nature* **2016**, *529*, 377.
- [78] H. K. Lim, H. D. Lim, K. Y. Park, D. H. Seo, H. Gwon, J. Hong, W. A. Goddard, H. Kim, K. Kang, *J. Am. Chem. Soc.* **2013**, *135*, 9733.
- [79] C. W. Lee, K. Sathiyarayanan, S. W. Eom, M. S. Yun, *J. Power Sources* **2006**, *160*, 1436.
- [80] S.-H. Lee, Y.-J. Jeong, S.-H. Lim, E.-A. Lee, C.-W. Yi, K. Kim, *J. Korean Electrochem. Soc.* **2010**, *13*, 45.
- [81] G. E. Gilligan, D. Qu, in *Adv. Batter. Mediu. Large-Scale Energy Storage*, **2015**, pp. 441–461.
- [82] P. K. Nayak, L. Yang, W. Brehm, P. Adelhelm, *Angew. Chemie - Int. Ed.* **2018**, *57*, 102.
- [83] H. Lee, Y.-I. Kim, J.-K. Park, J. W. Choi, *Chem. Commun.* **2012**, *48*, 8416.
- [84] Y. You, X.-L. Wu, Y.-X. Yin, Y.-G. Guo, *Energy Environ. Sci.* **2014**, *7*, 1643.
- [85] X. Yao, Z. Zhu, Q. Li, X. Wang, X. Xu, J. Meng, W. Ren, X. Zhang, Y. Huang, L. Mai, *ACS Appl. Mater. Interfaces* **2018**, *10*, 10022.
- [86] J. B. Goodenough, H. Y. Hong, J. A. Kafalas, *Mat. Res. Bull.* **1976**, *11*, 203.
- [87] A. K. Padhi, K. S. Nanjundaswamy, C. Masquelier, J. B. Goodenough, *J. Electrochem. Soc.* **1997**, *144*, 2581.
- [88] B. L. Ellis, L. F. Nazar, *Curr. Opin. Solid State Mater. Sci.* **2012**, *16*, 168.
- [89] J. Yang, H. Wang, P. Hu, J. Qi, L. Guo, L. Wang, *Small* **2015**, *11*, 3744.
- [90] F. Sauvage, L. Laffont, J. M. Tarascon, E. Baudrin, *Inorg. Chem.* **2007**, *46*, 3289.
- [91] Y. Cao, L. Xiao, W. Wang, D. Choi, Z. Nie, J. Yu, L. V. Saraf, Z. Yang, J. Liu, *Adv. Mater.* **2011**, *23*, 3155.
- [92] Y. Lu, L. Wang, J. Cheng, J. B. Goodenough, *Chem. Commun.* **2012**, *48*, 6544.
- [93] T. Matsuda, M. Takachi, Y. Moritomo, *Chem. Commun.* **2013**, *49*, 2750.
- [94] M. Pasta, R. Y. Wang, R. Ruffo, R. Qiao, H.-W. Lee, B. Shyam, M. Guo, Y. Wang, L. A. Wray, W. Yang, M. F. Toney, Y. Cui, *J. Mater. Chem. A* **2016**, *4*, 4211.
- [95] J. Y. Liao, Q. Hu, B. K. Zou, J. X. Xiang, C. H. Chen, *Electrochim. Acta* **2016**, *220*, 114.
- [96] D. A. Stevens, J. R. Dahn, *J. Electrochem. Soc.* **2001**, *148*, A803.
- [97] M. M. Doeff, M. M. Doeff, Y. Ma, Y. Ma, S. J. Visco, S. J. Visco, L. C. De Jonghe, L. C. De Jonghe, *J. Electrochem. Soc.* **1993**, *140*, 169.
- [98] D. Stevens, J. R. Dahn, *J. Electrochem. Soc.* **2000**, *147*, 1271.
- [99] S. Il Park, I. Gocheva, S. Okada, J. Yamaki, *J. Electrochem. Soc.* **2011**, *158*, A1067.
- [100] H. Xiong, M. D. Slater, M. Balasubramanian, C. S. Johnson, T. Rajh, *J. Phys. Chem. Lett.* **2011**, *2*, 2560.
- [101] V. L. Chevrier, G. Ceder, *J. Electrochem. Soc.* **2011**, *158*, A1011.
- [102] Y. J. Kim, W. Wu, S.-E. Chun, J. F. Whitacre, C. J. Bettinger, *Proc. Natl. Acad. Sci.*

- 2013**, 110, 20912.
- [103] J. Liu, J. G. Zhang, Z. Yang, J. P. Lemmon, C. Imhoff, G. L. Graff, L. Li, J. Hu, C. Wang, J. Xiao, G. Xia, V. V. Viswanathan, S. Baskaran, V. Sprenkle, X. Li, Y. Shao, B. Schwenzer, *Adv. Funct. Mater.* **2013**, 23, 929.
- [104] J. Liu, G. Cao, Z. Yang, D. Wang, D. Dubois, X. Zhou, G. L. Graff, L. R. Pederson, J. G. Zhang, *ChemSusChem* **2008**, 1, 676.
- [105] P. Butler, J. L. Miller, P. a Taylor, *Energy Storage Opportunities Analysis Phase II Final Report, A Study for the DOE Energy Storage Systems Program*, **2002**.
- [106] D. Kundu, B. D. Adams, V. Duffort, S. H. Vajargah, L. F. Nazar, *Nat. Energy* **2016**, 1.
- [107] F. Beck, P. Rüetschi, *Electrochim. Acta* **2000**, 45, 2467.
- [108] V. Renman, D. O. Ojwang, M. Valvo, C. P. Gómez, T. Gustafsson, G. Svensson, *J. Power Sources* **2017**, 369, 146.
- [109] C. Xia, J. Guo, P. Li, X. Zhang, H. N. Alshareef, *Angew. Chemie - Int. Ed.* **2018**, 57, 3943.
- [110] S. H. Lapidus, N. N. Rajput, X. Qu, K. W. Chapman, K. A. Persson, P. J. Chupas, *Phys. Chem. Chem. Phys.* **2014**, 16, 21941.
- [111] N. Alias, A. A. Mohamad, *J. Power Sources* **2015**, 274, 237.
- [112] W. Li, W. R. Mckinnon, J. R. Dahn, *MRS Proc.* **1994**, 369, 69.
- [113] P. He, X. Zhang, Y.-G. Wang, L. Cheng, Y.-Y. Xia, *J. Electrochem. Soc.* **2008**, 155, A144.
- [114] J. Y. Luo, W. J. Cui, P. He, Y. Y. Xia, *Nat. Chem.* **2010**, 2, 760.
- [115] M. Zhao, B. Zhang, G. Huang, H. Zhang, X. Song, *J. Power Sources* **2013**, 232, 181.
- [116] L. Suo, O. Borodin, W. Sun, X. Fan, C. Yang, F. Wang, T. Gao, Z. Ma, M. Schroeder, A. von Cresce, S. M. Russell, M. Armand, A. Angell, K. Xu, C. Wang, *Angew. Chemie - Int. Ed.* **2016**, 55, 7136.
- [117] L. Suo, O. Borodin, T. Gao, M. Olguin, J. Ho, X. Fan, C. Luo, C. Wang, K. Xu, *Sci. Mag.* **2015**, 350, 938.
- [118] D. Kundu, E. Talaie, V. Duffort, L. F. Nazar, *Angew. Chemie - Int. Ed.* **2015**, 54, 3432.
- [119] N. Yabuuchi, K. Kubota, M. Dahbi, S. Komaba, *Chem. Rev.* **2014**, 114, 11636.
- [120] J. Qian, C. Wu, Y. Cao, Z. Ma, Y. Huang, X. Ai, H. Yang, *Adv. Energy Mater.* **2018**, 1702619, 1.
- [121] J. F. Whitacre, A. Tevar, S. Sharma, *Electrochem. commun.* **2010**, 12, 463.
- [122] Z. Li, D. Young, K. Xiang, W. C. Carter, Y.-M. Chiang, *Adv. Energy Mater.* **2013**, 3, 290.
- [123] X. Wu, M. Sun, Y. Shen, J. Qian, Y. Cao, X. Ai, H. Yang, *ChemSusChem* **2014**, 7, 407.
- [124] A. Paolella, C. Faure, V. Timoshevskii, S. Marras, G. Bertoni, A. Guerfi, A. Vijh, M. Armand, K. Zaghbi, *J. Mater. Chem. A* **2017**, 5, 18919.
- [125] Y. J. He, J. F. Peng, W. Chu, Y. Z. Li, D. G. Tong, *J. Mater. Chem. A* **2014**, 2, 1721.
- [126] S. Liu, G. L. Pan, G. R. Li, X. P. Gao, *J. Mater. Chem. A* **2015**, 3, 959.
- [127] A. Eftekhari, P. Corrochano, *Sustain. Energy Fuels* **2017**, 1, 1246.
- [128] S. Liu, J. J. Hu, N. F. Yan, G. L. Pan, G. R. Li, X. P. Gao, *Energy Environ. Sci.* **2012**, 5, 9743.
- [129] Y. Liu, S. Sang, Q. Wu, Z. Lu, K. Liu, H. Liu, *Electrochim. Acta* **2014**, 143, 340.
- [130] G. A. Elia, K. Marquardt, K. Hoepfner, S. Fantini, R. Lin, E. Knipping, W. Peters, J. F. Drillet, S. Passerini, R. Hahn, *Adv. Mater.* **2016**, 28, 7564.
- [131] F. Wang, F. Yu, X. Wang, Z. Chang, L. Fu, Y. Zhu, Z. Wen, Y. Wu, W. Huang, *ACS Appl. Mater. Interfaces* **2016**, 8, 9022.
- [132] D. Kundu, S. Hosseini Vajargah, L. Wan, B. Adams, D. Prendergast, L. F. Nazar, *Energy Environ. Sci.* **2018**, 11, 881.
- [133] C. Xia, J. Guo, Y. Lei, H. Liang, C. Zhao, H. N. Alshareef, *Adv. Mater.* **2018**, 30, 1.
- [134] C. Xu, B. Li, H. Du, F. Kang, *Angew. Chemie Int. Ed.* **2012**, 51, 933.
- [135] C. Xu, Y. Chen, S. Shi, J. Li, F. Kang, D. Su, *Sci. Rep.* **2015**, 5, 14120.
- [136] B. Zhang, Y. Liu, X. Wu, Y. Yang, Z. Chang, Z. Wen, Y. Wu, *Chem. Commun.* **2014**, 50, 1209.

- [137] H. Pan, Y. Shao, P. Yan, Y. Cheng, K. S. Han, Z. Nie, C. Wang, J. Yang, X. Li, P. Bhattacharya, K. T. Mueller, J. Liu, *Nat. Energy* **2016**, *1*.
- [138] T. Gao, H. Fjellvåg, P. Norby, *Anal. Chim. Acta* **2009**, *648*, 235.
- [139] P. He, Y. Quan, X. Xu, M. Yan, W. Yang, Q. An, L. He, L. Mai, *Small* **2017**, *1702551*, 1.
- [140] L. Zhang, L. Chen, X. Zhou, Z. Liu, *Adv. Energy Mater.* **2014**, *5*.
- [141] L. Zhang, L. Chen, X. Zhou, Z. Liu, *Sci. Rep.* **2015**, *5*.
- [142] R. Trócoli, F. La Mantia, *ChemSusChem* **2015**, *8*, 481.
- [143] S. Higashi, S. W. Lee, J. S. Lee, K. Takechi, Y. Cui, *Nat. Commun.* **2016**, *7*, 1.
- [144] T. Gupta, A. Kim, S. Phadke, S. Biswas, T. Luong, B. J. Hertzberg, M. Chamoun, K. Evans-lutterodt, D. A. Steingart, *J. Power Sources* **2016**, *305*, 22.
- [145] A. Bani Hashemi, G. Kasiri, J. Glenneberg, F. Langer, R. Kun, F. La Mantia, *ChemElectroChem* **2018**, *5*, 2073.
- [146] A. Bani Hashemi, G. Kasiri, F. La Mantia, *Electrochim. Acta* **2017**, *258*, 703.
- [147] Y. Xu, S. Zheng, H. Tang, X. Guo, H. Xue, H. Pang, *Energy Storage Mater.* **2017**, *9*, 11.
- [148] A. G. Sharpe, *London; New York Acad. Press* **1976**.
- [149] K. R. Dunbar, R. A. Heintz, *Chemistry of Transition Metal Cyanide Compounds: Modern Perspectives*, **1997**.
- [150] J. Woodward, *Philos. Trans.* **1724**, *33*, 15.
- [151] J. Brown, *Philos. Trans. R. Soc. London* **1724**, *33*, 17.
- [152] H. Holtzman, *Ind. Eng. Chem.* **1945**, *37*, 855.
- [153] Elisabeth West Fitzhugh, Ed. , *Artists' Pigments: A Handbook of Their History and Characteristics*, **1986**.
- [154] A. Ludi, H. U. Güdel, *Inorg. Chem.* **1973**, *14*, 1.
- [155] H. J. Buser, D. Schwarzenbach, W. Petter, A. Ludi, *Inorg. Chem.* **1977**, *16*, 2704.
- [156] M. B. Robin, P. Day, *Adv. Inorg. Chem. Radiochem.* **1968**, *10*, 247.
- [157] A. Ludi, H. U. Güdel, M. Ruegg, *Inorg. Chem.* **1970**, *9*, 2224.
- [158] F. Grandjean, L. Samain, G. J. Long, *Dalt. Trans.* **2016**, *45*, 18018.
- [159] Y. Li, Y. Lu, C. Zhao, Y. S. Hu, M. M. Titirici, H. Li, X. Huang, L. Chen, *Energy Storage Mater.* **2017**, *7*, 130.
- [160] V. D. Neff, *J. Electrochem. Soc.* **1978**, *125*, 886.
- [161] G. Zampardi, S. V. Sokolov, C. Batchelor-McAuley, R. G. Compton, *Chem. - A Eur. J.* **2017**, *23*, 14338.
- [162] V. Jassal, U. Shanker, S. Shankar, *J. Environ. Anal. Chem.* **2015**, *2*, 1000128.
- [163] A. A. Karyakin, *Electroanal.* **2001**, *13*, 813.
- [164] J. E. Huheey, E. A. Keiter, R. L. Keiter, *Anorganische Chemie*, Walter De Gruyter Verlag, Berlin, **1988**.
- [165] D. O. Ojwang, J. Grins, D. Wardecki, M. Valvo, V. Renman, L. Häggström, T. Ericsson, T. Gustafsson, A. Mahmoud, R. P. Hermann, G. Svensson, *Inorg. Chem.* **2016**, *55*, 5924.
- [166] C. Zhang, Y. Xu, M. Zhou, L. Liang, H. Dong, M. Wu, Y. Yang, Y. Lei, *Adv. Funct. Mater.* **2017**, *27*, 1604307.
- [167] S. M. Chen, *Electrochim. Acta* **1998**, *43*, 3359.
- [168] S. M. Chen, M. F. Lu, K. C. Lin, *J. Electroanal. Chem.* **2005**, *579*, 163.
- [169] R. Garjonyte, A. Malinauskas, *Sensors Actuators, B Chem.* **1999**, *56*, 93.
- [170] V. Ganesh, D. Latha Maheswari, S. Berchmans, *Electrochim. Acta* **2011**, *56*, 1197.
- [171] M. E. Ghica, R. C. Carvalho, A. Amine, C. M. A. Brett, *Sensors Actuators, B Chem.* **2013**, *178*, 270.
- [172] R. Y. Wang, C. D. Wessells, R. a. Huggins, Y. Cui, *Nano Lett.* **2013**, *13*, 5748.
- [173] R. Y. Wang, B. Shyam, K. H. Stone, J. N. Weker, M. Pasta, H. W. Lee, M. F. Toney, Y. Cui, *Adv. Energy Mater.* **2015**, *5*, 1401869.
- [174] C. D. Wessells, S. V. Peddada, R. a. Huggins, Y. Cui, *Nano Lett.* **2011**, *11*, 5421.
- [175] C. D. Wessells, R. a. Huggins, Y. Cui, *Nat. Commun.* **2011**, *2*, 550.
- [176] C. D. Wessells, S. V. Peddada, M. T. McDowell, R. A. Huggins, Y. Cui, *J. Electrochem. Soc.* **2012**, *159*, A98.

- [177] M. Pasta, C. D. Wessells, R. a. Huggins, Y. Cui, *Nat. Commun.* **2012**, *3*, 1149.
- [178] C. D. Wessells, M. T. McDowell, S. V. Peddada, M. Pasta, R. a. Huggins, Y. Cui, *ACS Nano* **2012**, *6*, 1688.
- [179] Y. Mizuno, M. Okubo, E. Hosono, T. Kudo, K. Oh-ishi, A. Okazawa, N. Kojima, R. Kurono, S. Nishimura, A. Yamada, *J. Mater. Chem. A* **2013**, *1*, 13055.
- [180] X. Wu, Y. Cao, X. Ai, J. Qian, H. Yang, *Electrochem. commun.* **2013**, *31*, 145.
- [181] V. D. Neff, *J. Electrochem. Soc.* **1985**, *132*, 1382.
- [182] E. W. Grabner, S. Kalwellis-Mohn, *J. Appl. Electrochem.* **1987**, *17*, 653.
- [183] S. Kalwellis-Mohn, E. W. Grabner, *Electrochim. Acta* **1989**, *34*, 1265.
- [184] M. Pasta, C. D. Wessells, N. Liu, J. Nelson, M. T. McDowell, R. A. Huggins, M. F. Toney, Y. Cui, *Nat. Commun.* **2014**, *5*, 1.
- [185] C. J. Du, F. X. Bu, D. M. Jiang, Q. H. Zhang, J. Sen Jiang, *CrystEngComm* **2013**, *15*, 10597.
- [186] A. Bani Hashemi, F. La Mantia, *Anal. Chem.* **2016**, *88*, 7916.
- [187] A. J. Bard, L. R. Faulkner, *Electrochemical Methods: Fundamentals and Applications*, Wiley, **2000**.
- [188] W. Wang, X. Wei, D. Choi, X. Lu, G. Yang, C. Sun, in *Adv. Batter. Mediu. Large-Scale Energy Storage*, Elsevier Ltd., **2015**.
- [189] D. R. Lide, *CRC Handbook of Chemistry and Physics*, CRC Press, 85th Edition, **2005**.
- [190] J. Newman, K. E. Thomas-Alyea, *Electrochemical Systems*, John Wiley & Sons, **2004**.
- [191] R. Guduru, J. Icaza, *Nanomaterials* **2016**, *6*, 41.
- [192] M. C. Lin, M. Gong, B. Lu, Y. Wu, D. Y. Wang, M. Guan, M. Angell, C. Chen, J. Yang, B. J. Hwang, H. Dai, *Nature* **2015**, *520*, 325.
- [193] Y. Waseda, E. Matsubara, K. Shinoda, *X-Ray Diffraction Crystallography*, **2011**.
- [194] W. Zhou, Z. L. Wang, Eds., *Scanning Microscopy for Nanotechnology*, **2007**.
- [195] G. Kasiri, R. Trócoli, A. B. Hashemi, F. La Mantia, *Electrochim. Acta* **2016**, *222*, 74.
- [196] R. Trócoli, G. Kasiri, F. La Mantia, *J. Power Sources* **2018**, *400*, 167.
- [197] J. B. Goodenough, K. S. Park, *J. Am. Chem. Soc.* **2013**, *135*, 1167.
- [198] M. Tang, W. C. Carter, Y.-M. Chiang, *Annu. Rev. Mater. Res.* **2010**, *40*, 501.
- [199] C. Liu, Z. G. Neale, G. Cao, *Mater. Today* **2016**, *19*, 109.
- [200] R. Huggins, *Advanced Batteries: Materials Science Aspects*, Springer Science & Business Media, **2008**.
- [201] E. Madej, E. Ventosa, S. Klink, W. Schuhmann, F. La Mantia, *Phys. Chem. Chem. Phys.* **2014**, *16*, 7939.
- [202] A. Dostal, B. Meyer, F. Scholz, U. Schröder, A. M. Bond, F. Marken, S. J. Shaw, *J. Phys. Chem.* **1995**, *99*, 2096.
- [203] A. K. Bonnette, S. E. Gandy, *J. Chem. Educ.* **1981**, *58*, 355.
- [204] N. F. Zakharchuk, N. Naumov, R. Stösser, U. Schröder, F. Scholz, H. Mehner, *J Solid State Electrochem* **1999**, *3*, 264.
- [205] A. Widmann, H. Kahlert, H. Wulff, F. Scholz, *J Solid State Electrochem* **2005**, *9*, 380.
- [206] S. J. Reddy, A. Dostal, F. Scholz, *J. Electroanal. Chem.* **1996**, *403*, 209.
- [207] D. Schwudke, R. Stößer, F. Scholz, *Electrochem. commun.* **2000**, *2*, 301.
- [208] Z. Jia, B. Wang, Y. Wang, *Mater. Chem. Phys.* **2015**, *149–150*, 601.
- [209] A. B. Lavand, Y. S. Malghe, *J. Asian Ceram. Soc.* **2015**, *3*, 305.
- [210] M. Saliani, R. Jalal, E. Kafshadre. Goharshadi, *Jundishapur J. Microbiol.* **2015**, *8*.
- [211] X. Luo, J. Wang, M. Dooner, J. Clarke, *Appl. Energy* **2015**, *137*, 511.
- [212] A. L. Patterson, *Phys. Rev.* **1939**, *56*, 978.
- [213] Y. Yang, Y. X. Min, W. Hong, X.-Z. Liao, Z.-F. Ma, *Meet. Abstr.* **2016**, *1*, 113.
- [214] H. Inoue, T. Nakazawa, T. Mitsuhashi, T. Shirai, E. Fluck, *Hyperfine Interact.* **1989**, *46*, 723.
- [215] C. Aparicio, L. Machala, Z. Marusak, *J. Therm. Anal. Calorim.* **2012**, *110*, 661.
- [216] *International Energy Outlook Executive Summary*, U.S. Energy Information Administration, **2017**.
- [217] F. Díaz-González, A. Sumper, O. Gomis-Bellmunt, R. Villafafila-Robles, *Renew.*

- Sustain. Energy Rev.* **2012**, *16*, 2154.
- [218] J. I. San Martín, I. Zamora, J. J. San Martín, V. Aperribay, P. Eguía, *Int. Conf. Renew. Energies Power Qual.* **2013**, *1*, 1.
- [219] F. A. Farret, M. G. Simoes., *Integration of Alternative Sources of Energy*, John Wiley & Sons, **2006**.
- [220] I. Hadjipaschalis, A. Poullikkas, V. Efthimiou, *Renew. Sustain. Energy Rev.* **2009**, *13*, 1513.
- [221] *Review of Electrical Energy Storage Technologies and Systems and of Their Potential for the UK*, **2004**.
- [222] A. Du Pasquier, I. Plitz, S. Menocal, G. Amatucci, *J. Power Sources* **2003**, *115*, 171.
- [223] M. Kamibayashi, D. K. Nichols, T. Oshima, *IEEE/PES Transm. Distrib. Conf. Exhib.* **2002**, *3*, 1664.
- [224] S. M. Schoenung, *Energy Storage Systems Cost Update: A Study for the DOE Energy Storage Systems Program*, **2011**.
- [225] T. Yamamura, X. Wu, S. Ohta, K. Shirasaki, H. Sakuraba, I. Satoh, T. Shikama, *J. Power Sources* **2011**, *196*, 4003.
- [226] J. McDowall, *J. Power Sources* **2006**, *162*, 959.
- [227] J. Baker, *Energy Policy* **2008**, *36*, 4368.
- [228] M. G. Molina, in *Dyn. Model.* (Ed.: A. Brito), **2010**.
- [229] “Electricity storage technology comparison. Electricity Storage Association (ESA),” can be found under http://www.electricitystorage.org/technology/storage_technologies/technology_comparison, **2013**.
- [230] J. Kondoh, I. Ishii, H. Yamaguchi, A. Murata, K. Otani, K. Sakuta, N. Higuchi, S. Sekine, M. Kamimoto, *Energy Convers. Manag.* **2000**, *41*, 1863.
- [231] L. Barote, R. Weissbach, C. Marinescu, M. Cirstea, in *11th Int. Conf. Optim. Electr. Electron. Equip., IEEE*, **2008**, pp. 407–412.
- [232] G. Pistoia, *Electric and Hybrid Vehicles: Power Sources, Models, Sustainability, Infrastructure and the Market*, Elsevier, **2010**.
- [233] P. L. P. Li, *IEEE Nanotechnol. Mag.* **2008**, *2*, 13.
- [234] D. Rastler, *Energy Storage Technology Status, EPRI Renewable Council Meeting*, **2011**.
- [235] M. Song, H. Tan, D. Chao, H. J. Fan, *Adv. Funct. Mater.* **2018**, *1802564*, 1802564.
- [236] O. Schmidt, A. Hawkes, A. Gambhir, I. Staffell, *Nat. Energy* **2017**, *2*.
- [237] “Lenntech: Water Treatment and Purification,” can be found under <https://www.lenntech.com/>, **2018**.

11. Appendix

11.1. Influence of other Synthesis Parameters

In addition to the mentioned syntheses and the performances in the previous chapters, several other methods have been also tested but did not derive any good results. In tables below the synthesis procedure of some is noted.

Table 11-1. Different synthesis methods for CuHCF.

Precursor 1	Precursor 2	Water	Temperature	Washing step	Drying temperature
120 mL of 100 mM Cu(NO ₃) ₂ · 3H ₂ O	120 mL of 100 mM K ₃ Fe(CN) ₆	60 mL H ₂ O	Room temperature	Wash with HNO ₃ + KNO ₃ followed by distilled water	Dry at 60°C
	120 mL of 100 mM K ₄ Fe(CN) ₆	60 mL H ₂ O	Room temperature	Wash with HNO ₃ + KNO ₃ followed by distilled water	
	120 mL of 50 mM K ₄ Fe(CN) ₆	60 mL H ₂ O	Room temperature	Wash with HNO ₃ + KNO ₃ followed by distilled water	
	120 mL of 50 mM K ₄ Fe(CN) ₆	60 mL H ₂ O	70°C	Wash with HNO ₃ + KNO ₃ followed by distilled water	
	120 mL of 50 mM K ₃ Fe(CN) ₆	60 mL H ₂ O	Room temperature	Wash with distilled water	
	120 mL of 50 mM K ₃ Fe(CN) ₆	60 mL H ₂ O + C65 (HNO ₃)	Room temperature	Wash with distilled water	
	120 mL of 50 mM K ₃ Fe(CN) ₆	60 mL H ₂ O	Room temperature, synthesis in sonication bath	Wash with distilled water	
	120 mL of 50 mM K ₃ Fe(CN) ₆	60 mL H ₂ O	Room temperature, synthesis in sonication bath	Wash with HNO ₃ + KNO ₃ followed by distilled water	
	120 mL of 50 mM K ₃ Fe(CN) ₆	60 mL H ₂ O	70°C	Wash with HNO ₃ + KNO ₃ followed by distilled water	
	120 mL of 50 mM K ₃ Fe(CN) ₆	60 mL KNO ₃ (1 M)	70°C	Wash with HNO ₃ + KNO ₃ followed by distilled water	
120 mL of 50 mM K ₃ Fe(CN) ₆	No H ₂ O	Room temperature	Wash with distilled water		

Precursor 1	Precursor 2	Water	Temperature	Washing step	Drying temperature
120 mL of 100 mM $\text{Cu}(\text{NO}_3)_2 \cdot 3\text{H}_2\text{O}$	120 mL of 50 mM $\text{K}_3\text{Fe}(\text{CN})_6$	60 mL H_2O	Room temperature	Wash with $\text{Cu}(\text{NO}_3)_2$ + HNO_3 followed by distilled water	Dry at 60°C
		60 mL H_2O	Room temperature	Wash with $\text{Zn}(\text{NO}_3)_2$ + HNO_3 followed by distilled water	
		60 mL H_2O	Room temperature	Wash with $\text{Cu}(\text{NO}_3)_2$ followed by distilled water	
		60 mL H_2O	Room temperature	Wash with $\text{Zn}(\text{NO}_3)_2$ followed by distilled water	
		60 mL H_2O	Under Argon, Room temperature, pumping speed 0.5 mL min^{-1}	Wash with HNO_3 + KNO_3 followed by distilled water	

Table 11-2. Different synthesis methods for ZnHCF .

Precursor 1	Precursor 2	Precursor 3	Water	Temperature	Washing step	Drying temperature
100 mL of 20 mM ZnCl_2	100 mL of 20 mM $\text{K}_3\text{Fe}(\text{CN})_6$	-	200 mL H_2O	100°C		
40 mL of 100 mM $\text{Na}_4\text{Fe}(\text{CN})_6 \cdot 10\text{H}_2\text{O}$	60 mL of 100 mM $\text{Zn}(\text{NO}_3)_2 \cdot 6\text{H}_2\text{O}$	-	-	100°C		
100 mL of 20 mM ZnCl_2	100 mL of 20 mM $\text{K}_3\text{Fe}(\text{CN})_6$	-	200 mL H_2O	Room temperature, synthesis in sonication bath		
100 mL of 10 mM ZnCl_2	100 mL of 10 mM MnCl_2	100 mL of 200 mM $\text{K}_3\text{Fe}(\text{CN})_6$	100 mL H_2O	100°C		Dry at 60°C
120 mL of 100 mM ZnSO_4	120 mL of 100 mM $\text{K}_3\text{Fe}(\text{CN})_6$	-	60 mL H_2O	Room temperature	Wash with distilled water	
120 mL of 100 mM ZnSO_4	120 mL of 50 mM $\text{K}_3\text{Fe}(\text{CN})_6$	-	60 mL H_2O	Room temperature		
100 mL of 100 mM ZnSO_4	100 mL of 50 mM $\text{K}_4\text{Fe}(\text{CN})_6$	-	50 mL H_2O	60°C		
100 mL of 100 mM ZnSO_4	100 mL of 50 mM $\text{K}_3\text{Fe}(\text{CN})_6$	-	50 mL H_2O	60°C		Dry at 70°C
200 mL of 10 mM ZnSO_4	200 mL of 10 mM $\text{K}_3\text{Fe}(\text{CN})_6$	-	-	Room temperature, stir 24 h		Dry at room temperature

11.2. List of Figures

Figure 1-1. Schematic of the electrical energy storage systems classification (adapted from [6]).....	- 2 -
Figure 1-2. Ragone plot comparing different energy storage technologies with regard to their gravimetric power density and gravimetric energy density including their charge times (adapted from [24]).....	- 3 -
Figure 1-3. Relative abundance of chemical elements in the earth’s cluster. Alkali metals and alkaline earth metals are shown in green, transition-metals in orange, and main group elements in blue (extracted and modified from [11,25]).....	- 4 -
Figure 1-4. Schematic representation of a Li-ion battery (adapted from [42]).	- 7 -
Figure 1-5. Schematic representation of a redox flow battery (adapted from [58]).	- 11 -
Figure 1-6. Crystal structure of α -MnO ₂ (adapted from [138]).	- 20 -
Figure 1-7. Schematic representation of a zinc-ion battery cell with CVO as the cathode, zinc metal as the anode, and a zinc containing electrolyte (adapted from [109]).....	- 21 -
Figure 1-8. Crystal structure of Zn _{0.25} V ₂ O ₅ ·nH ₂ O nanobelts along (110) direction (adapted from [106]).	- 21 -
Figure 1-9. Crystal structure of layered V ₃ O ₇ along (010) direction (adapted from [132]).	- 22 -
Figure 1-10. Crystal structure of different ZnHCF polyhedrons (adapted from [141]).	- 23 -
Figure 1-11. Unit cell crystal structures of soluble and insoluble PB. Water hydrogens are not shown in the insoluble structure for the sake of clarity (adapted from [158]).....	- 25 -
Figure 1-12. Framework of copper hexacyanoferrate (CuHCF).....	- 26 -
Figure 2-1. Standard CuHCF synthesis procedure.	- 33 -
Figure 2-2. Coated carbon cloth current collector with active material.	- 35 -
Figure 2-3. (a) Flooded three-electrode cell and (b) DEMS-EIS cell utilized for electrochemical measurements.....	- 36 -
Figure 2-4. Schematic illustration of an aqueous ZIB in a zinc-based electrolyte (standard CuHCF as the positive electrode and zinc foil as the negative electrode).	- 37 -
Figure 2-5. The potential range of a ZIB based on standard CuHCF cathode and Zn anode vs. SHE by considering thermodynamic stability window of water.	- 43 -
Figure 3-1. Potential profiles of CuHCF (solid line) and a Zn film (dashed line) at a rate of 1C in 20 mM ZnSO ₄ (extracted from [142]).....	- 46 -
Figure 3-2. Long-term cycling of standard CuHCF at a rate of 1C in 20 mM of (a) ZnSO ₄ , (b) Zn(ClO ₄) ₂ , (c) ZnF ₂ , and (d) Zn(NO ₃) ₂ aqueous solutions.	- 47 -
Figure 3-3. Potential profiles of standard CuHCF (solid line) and Zn foil (dashed line) at a rate of 1C in 20 mM of (a) ZnSO ₄ , (b) Zn(ClO ₄) ₂ , (c) ZnF ₂ , and (d) Zn(NO ₃) ₂ aqueous solutions.	- 48 -
Figure 3-4. (a) Long-term cycling and (b) coulombic efficiencies of standard CuHCF at a rate of 1C in 100 mM ZnSO ₄ and 100 mM Zn(ClO ₄) ₂ , respectively.....	- 50 -
Figure 3-5. (a,b) Potential profiles of standard CuHCF (solid line) and Zn foil (dashed line) at a rate of 1C in 100 mM ZnSO ₄ and Zn(ClO ₄) ₂ , respectively. (c,d) Differential specific charge profiles at different numbers of cycles for standard CuHCF measured at a rate of 1C in 100 mM ZnSO ₄ and Zn(ClO ₄) ₂ , respectively.....	- 51 -
Figure 3-6. The intensities and potential locations of the cathodic and anodic peaks of the differential specific charge profiles of standard CuHCF in (a,c) 100 mM ZnSO ₄ and (b,d) 100 mM Zn(ClO ₄) ₂ , respectively. The blue circles indicate the first redox couple and the black circles show the second one.	- 52 -
Figure 3-7. (a,b) Thermodynamic and (c,d) kinetic effects observed for standard CuHCF in 100 mM ZnSO ₄ and 100 mM Zn(ClO ₄) ₂ , respectively. The blue circles indicate the first redox couple and the black circles identify the second one.	- 54 -
Figure 3-8. X-ray diffraction patterns of uncycled standard CuHCF electrode, cycled standard CuHCF electrodes in 20 mM and 100 mM Zn(ClO ₄) ₂ , and uncycled as-prepared ZnHCF electrode.....	- 55 -
Figure 3-9. X-ray diffraction patterns for the conductive additive carbon black (C65) and carbon cloth current collector.	- 56 -
Figure 3-10. Potential profiles of standard CuHCF in 20 mM and 100 mM Zn(ClO ₄) ₂ at the 500 th cycle.....	- 56 -
Figure 3-11. (a) Long-term cycling and (b) coulombic efficiencies of standard CuHCF at 5C and 10C current rates in 100 mM ZnSO ₄	- 57 -
Figure 3-12. (a,b) Potential profiles of standard CuHCF (solid line) and Zn foil (dashed line) at 5C and 10C current rates in 100 mM ZnSO ₄ , respectively. (c,d) Differential specific charge profiles at different numbers of cycles for standard CuHCF measured at 5C and 10C current rates in 100 mM ZnSO ₄ , respectively.....	- 58 -

Figure 3-13. (a,b) Thermodynamic and (c,d) kinetic effects observed for the standard CuHCF in 100 mM ZnSO₄ at 5C and 10C currents, respectively. The blue circles indicate the first redox couple and the black circles represent the second one. - 59 -

Figure 3-14. (a) Hypothetical aging mechanism for standard CuHCF during the intercalation of zinc ions. σ , σ' represent the active material phases, ε is the electrolyte solution phase, V indicates the vacancies in the lattice. (b) A schematic model of CuHCF illustrating the reversible zinc ion hopping between 8c and 4a crystallographic sites in the cavity and [Fe(CN)₆] voids. Color coding: Zn-purple, Fe-yellow, Cu-blue, N-green, C-grey, and H₂O-light blue (extracted from [108]). - 61 -

Figure 4-1. X-ray diffraction pattern of the standard CuHCF powder. - 63 -

Figure 4-2. X-ray diffraction patterns of (a) pristine ZnO and mixture of ZnO with standard CuHCF powder and other CuZnHCF mixtures. (b) A zoom-in of X-ray diffraction patterns for mixture of ZnO with standard CuHCF powder and CuZnHCF mixtures, between 17° and 18° 2 θ - 65 -

Figure 4-3. SEM and EDX elemental mapping (nitrogen, oxygen, potassium, copper, and iron) of standard CuHCF powder. - 66 -

Figure 4-4. SEM and EDX elemental mapping (nitrogen, oxygen, potassium, copper, iron, and zinc) of the Cu_{0.98}Zn_{0.02}HCF mixture powder. - 67 -

Figure 4-5. SEM and EDX elemental mapping (nitrogen, oxygen, potassium, copper, iron, and zinc) of the Cu_{0.95}Zn_{0.05}HCF mixture powder. - 67 -

Figure 4-6. SEM and EDX elemental mapping (nitrogen, oxygen, potassium, copper, iron, and zinc) of the Cu_{0.93}Zn_{0.07}HCF mixture powder. - 68 -

Figure 4-7. SEM and EDX elemental mapping (nitrogen, oxygen, potassium, copper, iron, and zinc) of the Cu_{0.9}Zn_{0.1}HCF mixture powder. - 68 -

Figure 4-8. SEM and EDX elemental mapping (nitrogen, oxygen, potassium, copper, iron, and zinc) of the Cu_{0.85}Zn_{0.15}HCF mixture powder. - 69 -

Figure 4-9. SEM images of (a) standard CuHCF powder, CuZnHCF mixture powders with Cu:Zn ratio of (b) 98:2, (c) 95:5, (d) 93:7, (e) 90:10, and (f) 85:15, scale bar 1 μ m. - 69 -

Figure 4-10. Long-term cycling of standard CuHCF and different CuZnHCF mixtures at a 1C current rate in (a) 20 mM and (b) 100 mM ZnSO₄ after 500 cycles. - 70 -

Figure 4-11. Potential profiles of CuZnHCF mixtures with Cu:Zn ratio of (a) 85:15, (b) 90:10, (c) 93:7, (d) 95:5, (e) 98:2, (f) standard CuHCF (solid line) and Zn foil (dashed line) at a rate of 1C in 20 mM ZnSO₄, respectively. - 71 -

Figure 4-12. Differential specific charge profiles at different number of cycles of CuZnHCF mixtures with Cu:Zn ratio of (a) 85:15, (b) 90:10, (c) 93:7, (d) 95:5, (e) 98:2, and (f) standard CuHCF measured at 1C current rate in 20 mM ZnSO₄, respectively. - 72 -

Figure 4-13. Specific energy, charge, and average potential provided by CuZnHCF mixtures with Cu:Zn ratio of (a) 85:15, (b) 90:10, (c) 93:7, (d) 95:5, (e) 98:2, and (f) standard CuHCF at 1C current rate in 20 mM ZnSO₄ at different number of cycles, respectively. - 73 -

Figure 4-14. Potential profiles of CuZnHCF mixtures with Cu:Zn ratio of (a) 85:15, (b) 90:10, (c) 93:7, (d) 95:5, (e) 98:2, (f) standard CuHCF (solid line) and Zn foil (dashed line) at a rate of 1C in 100 mM ZnSO₄, respectively. - 74 -

Figure 4-15. Differential specific charge profiles at different number of cycles of CuZnHCF mixtures with Cu:Zn ratio of (a) 85:15, (b) 90:10, (c) 93:7, (d) 95:5, (e) 98:2, and (f) standard CuHCF measured at 1C current rate in 100 mM ZnSO₄, respectively. - 75 -

Figure 4-16. Specific energy, charge, and average potential provided by CuZnHCF mixtures with Cu:Zn ratio of (a) 85:15, (b) 90:10, (c) 93:7, (d) 95:5, (e) 98:2, and (f) standard CuHCF at 1C current rate in 100 mM ZnSO₄ at different number of cycles, respectively. - 76 -

Figure 5-1. (a) Long-term cycling and (b) coulombic efficiencies of standard CuHCF and the Cu_{0.93}Zn_{0.07}HCF mixture at a 1C current rate in 20 mM ZnSO₄. - 78 -

Figure 5-2. Potential profiles of (a) standard CuHCF (solid line) and (b) Cu_{0.93}Zn_{0.07}HCF mixture (solid line) at a 1C current rate in 20 mM ZnSO₄, potential profiles of the Zn foil counter electrode is shown with dashed line in both graphs. (c,d) Differential specific charge profiles at different numbers of cycles for standard CuHCF and the Cu_{0.93}Zn_{0.07}HCF mixture measured at a 1C current rate in 20 mM ZnSO₄, respectively. - 79 -

Figure 5-3. Specific energy, charge, and average potential provided by (a) the standard CuHCF and (b) the Cu_{0.93}Zn_{0.07}HCF mixture, at 1C current rate in 20 mM ZnSO₄ at different numbers of cycles. - 80 -

Figure 5-4. Ragone plot of the Cu_{0.93}Zn_{0.07}HCF/ZnSO₄/Zn battery. The power and energy densities were calculated based on the mass of the CuZnHCF active material. - 81 -

Figure 5-5. Comparison of specific powers and energies of different energy storage devices and the introduced aqueous zinc-ion battery based on $\text{Cu}_{0.93}\text{Zn}_{0.07}\text{HCF}$ (adapted from ^[211]). - 82 -

Figure 5-6. X-ray diffraction patterns of the (a) standard CuHCF electrode and (b) $\text{Cu}_{0.93}\text{Zn}_{0.07}\text{HCF}$ electrode before cycling (black) and after 1000 cycles (blue) at a 1C rate in 20 mM ZnSO_4 - 83 -

Figure 5-7. SEM images of the (a) standard CuHCF electrode and (b) $\text{Cu}_{0.93}\text{Zn}_{0.07}\text{HCF}$ electrode before cycling, with a scale bar of 20 μm - 84 -

Figure 5-8. (a) SEM image of standard CuHCF electrode after 1000 cycles at a 1C rate in 20 mM ZnSO_4 with exemplary EDX point measurements, (b) exemplary EDX spectrum of the cubic morphology (green crosses) with calculated average composition (phase 1-1), and (c) exemplary EDX spectrum of the cubic morphology (orange crosses) with calculated average composition (phase 1-2). - 85 -

Figure 5-9. (a) SEM image of standard CuHCF electrode after 1000 cycles at a 1C rate in 20 mM ZnSO_4 with exemplary EDX point measurements, (b) exemplary EDX spectrum of the non-cubic morphology (blue cross) with calculated average composition (phase 2-1), (c) exemplary EDX spectrum of the non-cubic morphology (green crosses) with calculated average composition (phase 2-2), and (d) exemplary EDX spectrum of the non-cubic morphology (orange crosses) with calculated average composition (phase 2-3). - 86 -

Figure 5-10. (a) SEM image of $\text{Cu}_{0.93}\text{Zn}_{0.07}\text{HCF}$ electrode after 1000 cycles at a 1C rate in 20 mM ZnSO_4 with exemplary EDX point measurements, (b) exemplary EDX spectrum of the cubic morphology (green crosses) with calculated average composition (phase 1-1), and (c) exemplary EDX spectrum of the cubic morphology (orange crosses) with calculated average composition (phase 1-2). - 88 -

Figure 5-11. (a) SEM image of $\text{Cu}_{0.93}\text{Zn}_{0.07}\text{HCF}$ electrode after 1000 cycles at a 1C rate in 20 mM ZnSO_4 with exemplary EDX point measurements, (b) exemplary EDX spectrum of the non-cubic morphology (orange crosses) with calculated average composition (phase 2-1), and (c) exemplary EDX spectrum of the non-cubic morphology (green crosses) with calculated average composition (phase 2-2). - 89 -

Figure 5-12. (a) Long-term cycling and (b) coulombic efficiencies of standard CuHCF and the $\text{Cu}_{0.93}\text{Zn}_{0.07}\text{HCF}$ mixture at a 1C current rate in 100 mM ZnSO_4 - 91 -

Figure 5-13. (a,b) Potential profiles of the (a) standard CuHCF (solid line), (b) $\text{Cu}_{0.93}\text{Zn}_{0.07}\text{HCF}$ mixture (solid line) at a 1C current rate in 100 mM ZnSO_4 , potential profiles of the Zn foil counter electrode is shown with dashed line in both graphs. (c,d) Differential specific charge profiles at different numbers of cycles for the standard CuHCF and $\text{Cu}_{0.93}\text{Zn}_{0.07}\text{HCF}$ mixture measured at a 1C current rate in 100 mM ZnSO_4 , respectively. - 92 -

Figure 5-14. Specific energy, charge, and average potential provided by the (a) standard CuHCF and (b) $\text{Cu}_{0.93}\text{Zn}_{0.07}\text{HCF}$ mixture at a 1C current rate in 100 mM ZnSO_4 at different numbers of cycles. - 93 -

Figure 5-15. X-ray diffraction patterns of (a) standard CuHCF electrode and (b) $\text{Cu}_{0.93}\text{Zn}_{0.07}\text{HCF}$ electrode before cycling (black) and after 1000 cycles (blue) at 1C rate in 100 mM ZnSO_4 - 94 -

Figure 5-16. X-ray diffraction patterns of (a) standard CuHCF electrode and (b) $\text{Cu}_{0.93}\text{Zn}_{0.07}\text{HCF}$ electrode before cycling (black) and after 1000 cycles (blue) at 1C rate in 100 mM ZnSO_4 between 16° and 40° 2θ angle. - 95 -

Figure 5-17. (a) SEM image of standard CuHCF electrode after 1000 cycles at a 1C rate in 100 mM ZnSO_4 with exemplary EDX point measurements, (b) exemplary EDX spectrum of the cubic morphology (orange crosses) with calculated average composition (phase 1-1), (c) exemplary EDX spectrum of the cubic morphology (green crosses) with calculated average composition (phase 1-2), and (d) exemplary EDX spectrum of the cubic morphology (blue crosses) with calculated average composition (phase 1-3). - 97 -

Figure 5-18. (a) SEM image of standard CuHCF electrode after 1000 cycles at a 1C rate in 100 mM ZnSO_4 with exemplary EDX point measurements, (b) exemplary EDX spectrum of the needle shaped morphology (orange crosses) with calculated average composition (phase 3-1), and (c) exemplary EDX spectrum of the needle shaped morphology (green crosses) with calculated average composition (phase 3-2). - 98 -

Figure 5-19. (a) SEM image of standard CuHCF electrode after 1000 cycles at a 1C rate in 100 mM ZnSO_4 with exemplary EDX point measurements, (b) exemplary EDX spectrum of plate shaped morphology (green crosses) with calculated average composition (phase 4-1), and (c) exemplary EDX spectrum of plate shaped morphology (orange crosses) with calculated average composition (phase 4-2). - 99 -

Figure 5-20. (a) SEM image of $\text{Cu}_{0.93}\text{Zn}_{0.07}\text{HCF}$ electrode after 1000 cycles at a 1C rate in 100 mM ZnSO_4 with exemplary EDX point measurements, (b) exemplary EDX spectrum of the cubic morphology (orange crosses) with calculated average composition (phase 1-1), (c) exemplary EDX spectrum of the cubic morphology (green crosses) with calculated average

composition (phase 1-2), and (d) exemplary EDX spectrum of the cubic morphology (blue crosses) with calculated average composition (phase 1-3).....	- 101 -
Figure 5-21. (a) SEM image of $\text{Cu}_{0.93}\text{Zn}_{0.07}\text{HCF}$ electrode after 1000 cycles at a 1C rate in 100 mM ZnSO_4 with exemplary EDX point measurements, (b) exemplary EDX spectrum of needle shaped morphology (orange crosses) with calculated average composition (phase 3-1), (c) exemplary EDX spectrum of needle shaped morphology (green crosses) with calculated average composition (phase 3-2), and (d) exemplary EDX spectrum of needle shaped morphology (blue crosses) with calculated average composition (phase 3-3).....	- 102 -
Figure 5-22. (a) SEM image of $\text{Cu}_{0.93}\text{Zn}_{0.07}\text{HCF}$ electrode after 1000 cycles at a 1C rate in 100 mM ZnSO_4 with exemplary EDX point measurements, (b) exemplary EDX spectrum of spike shaped morphology (green crosses) with calculated average composition (phase 5-1), and (c) exemplary EDX spectrum of spike shaped morphology (orange crosses) with calculated average composition (phase 5-2).....	- 103 -
Figure 5-23. SEM image of the ZnSO_4 parasitic phase appeared in standard CuHCF and $\text{Cu}_{0.93}\text{Zn}_{0.07}\text{HCF}$ electrodes after 1000 cycles at a 1C rate in 100 mM ZnSO_4	- 104 -
Figure 5-24. Schematic presentation of standard CuHCF morphology before and after cycling in ZnSO_4 solutions.....	- 106 -
Figure 5-25. Schematic presentation of $\text{Cu}_{0.93}\text{Zn}_{0.07}\text{HCF}$ morphology before and after cycling in ZnSO_4 solutions.....	- 107 -
Figure 6-1. X-ray diffraction patterns of CuHCF powder synthesized with moderate dropping speed (black line), slow dropping speed (blue line), and fast dropping speed (red line).....	- 109 -
Figure 6-2. Potential profiles of CuHCF (solid line) and zinc foil (dashed line) synthesized with (a) 0.5 mL min^{-1} and (b) 2 mL min^{-1} pumping speed at 1C current rate in 100 mM ZnSO_4 , respectively.....	- 109 -
Figure 6-3. Specific energy, charge, and average potential provided by CuHCF synthesized with (a) slow pumping speed and (b) fast dropping speed, in 100 mM ZnSO_4 at different number of cycles, respectively.....	- 110 -
Figure 6-4. X-ray diffraction patterns of CuHCF powder synthesized at room temperature (black line), low temperature (blue line), and high temperature (red line).....	- 112 -
Figure 6-5. Potential profiles of CuHCF (solid line) and zinc foil (dashed line) synthesized at (a) low temperature and (b) high temperature at 1C current rate in 100 mM ZnSO_4 , respectively.....	- 112 -
Figure 6-6. Specific energy, charge, and average potential provided by CuHCF synthesized at (a) low temperature and (b) high temperature, in 100 mM ZnSO_4 at different number of cycles, respectively.....	- 114 -
Figure 6-7. X-ray diffraction patterns of CuHCF powder synthesized under air atmosphere at room temperature (black line), under argon at room temperature (green line), under argon at low temperature (blue line), and under argon at high temperature (red line).....	- 115 -
Figure 6-8. Potential profiles of CuHCF (solid line) and zinc foil (dashed line) synthesized (a) under argon at low temperature, (b) under argon at room temperature, and (c) under argon at high temperature, respectively.....	- 116 -
Figure 6-9. Specific energy, charge, and average potential provided by CuHCF synthesized at (a) under argon at low temperature, (b) under argon at room temperature, and (c) under argon at high temperature, in 100 mM ZnSO_4 at different number of cycles, respectively.....	- 118 -
Figure 6-10. SEM and EDX elemental mapping (nitrogen, oxygen, potassium, copper, and iron) of new CuHCF powder synthesized under argon at room temperature.....	- 119 -
Figure 7-1. The level of technological maturity against the anticipated RD&D investment for variety of energy storage technologies (adapted from ^[234]).....	- 126 -
Figure 8-1. Schematic design of the first full cell battery.....	- 127 -
Figure 8-2. The aqueous zinc-ion full cell battery based on the first design.....	- 128 -
Figure 8-3. The potential profile of the aqueous zinc-ion full cell battery performed in the first designed cell.....	- 129 -
Figure 8-4. Schematic design of the second full cell battery.....	- 131 -
Figure 8-5. The aqueous zinc-ion full cell battery with second design (a) illustrating the pumping procedure at one cell plate, (b) potential of the battery for lightening the LEDs.....	- 131 -
Figure 8-6. The potential profile of the aqueous zinc-ion full cell battery performed in the second designed cell.....	- 132 -
Figure 8-7. (a) Separators after cycling and (b) the surface of the bipolar plate under an optical microscope.....	- 133 -

11.3. List of Tables

Table 1-1. Brief comparison of the energy storage technologies. ^[12,13,22,23,14-21]	- 2 -
Table 1-2. Abundance of chemical elements in the earth's crust. ^[25,29,30]	- 4 -
Table 1-3. Manufacturing costs and cycle life of different Li-ion batteries (LIBs). ^[34,49]	- 9 -
Table 1-4. Overview of the potential batteries for utility applications. ^[5,6,59-62]	- 12 -
Table 1-5. Overview of certain aqueous batteries based on PBAs (adapted from [108,140,142,174,175,180-184]).	- 29 -
Table 2-1. List of the materials and chemicals used in this thesis.	- 31 -
Table 2-2. List of devices used in this thesis.	- 32 -
Table 2-3. Molar conductivities of certain employed ions at 25°C in this study. ^[189]	- 40 -
Table 2-4. Comparison of standard redox potentials, densities, ionic and hydrated ionic radii for monovalent and multivalent cations. ^[120]	- 42 -
Table 3-1. The percentages of capacity retentions and coulombic efficiencies of standard CuHCF after 200 cycles in various 20 mM zinc salt solutions.	- 47 -
Table 3-2. Variation of concentration of iron (ΔC_{Fe}), copper (ΔC_{Cu}), and specific charge fading (ΔQ) after 200 cycles in 20 mM of different electrolytes, as calculated by ICP-MS analysis.	- 49 -
Table 3-3. The percentages of capacity retentions and coulombic efficiencies of standard CuHCF after 400 cycles in 100 mM ZnSO ₄ and 100 mM Zn(ClO ₄) ₂	- 50 -
Table 3-4. The percentages of capacity retentions and coulombic efficiencies of standard CuHCF after 1000 cycles in 100 mM ZnSO ₄ , at the 5C and 10C current rates.	- 57 -
Table 4-1. Percentages of energy and charge retention for standard CuHCF and CuZnHCF mixtures at a 1C rate after 500 cycles in 20 mM and 100 mM of ZnSO ₄	- 70 -
Table 5-1. Percentages of energy and charge retention and the coulombic efficiency values for the standard CuHCF and Cu _{0.93} Zn _{0.07} HCF mixture at a 1C rate after 500 and 1000 cycles in 20 mM ZnSO ₄	- 78 -
Table 5-2. Ratios of potassium to iron and zinc at each composition with a cubic morphology for cycled standard CuHCF electrode in 20 mM ZnSO ₄	- 85 -
Table 5-3. The ratio of potassium to iron, copper, and zinc at each composition with a non-cubic morphology for cycled standard CuHCF electrode in 20 mM ZnSO ₄	- 87 -
Table 5-4. The ratio of potassium to iron and zinc at each composition with a cubic morphology for the cycled Cu _{0.93} Zn _{0.07} HCF electrode in 20 mM ZnSO ₄	- 87 -
Table 5-5. Ratios of potassium to iron, copper, and, zinc at each composition with a non-cubic morphology for the cycled Cu _{0.93} Zn _{0.07} HCF electrode in 20 mM ZnSO ₄	- 89 -
Table 5-6. Percentages of energy and charge retention for the standard CuHCF and Cu _{0.93} Zn _{0.07} HCF mixture at a 1C rate after 500 and 1000 cycles in 100 mM ZnSO ₄	- 91 -
Table 5-7. The ratio of potassium to iron and zinc for each composition with a cubic morphology for cycled standard CuHCF electrode in 100 mM ZnSO ₄	- 98 -
Table 5-8. The ratio of iron to copper, and zinc for each composition with needle shaped morphology for cycled standard CuHCF electrode in 100 mM ZnSO ₄	- 99 -
Table 5-9. The ratio of iron to copper and zinc for each composition with a plate shaped morphology for cycled standard CuHCF electrode in 100 mM ZnSO ₄	- 100 -
Table 5-10. The ratio of potassium to iron and zinc at each composition with a cubic morphology for cycled Cu _{0.93} Zn _{0.07} HCF electrode in 100 mM ZnSO ₄	- 101 -
Table 5-11. The ratio of iron to copper and zinc at each composition with a needle shaped morphology for cycled Cu _{0.93} Zn _{0.07} HCF electrode in 100 mM ZnSO ₄	- 103 -
Table 5-12. The ratio of potassium to iron and zinc at each composition with spike shaped morphology for cycled Cu _{0.93} Zn _{0.07} HCF electrode in 100 mM ZnSO ₄	- 104 -
Table 6-1. Percentage of energy and charge retention for CuHCF synthesized with different pumping speed at 1C rate in 100 mM ZnSO ₄	- 110 -
Table 6-2. Percentage of energy and charge retention for CuHCF synthesized at different temperatures at 1C rate in 100 mM ZnSO ₄	- 113 -

Table 6-3. Percentage of energy and charge retention for CuHCF synthesized under argon at different temperatures at 1C rate in 100 mM ZnSO ₄	- 117 -
Table 7-1. An overview of the determined morphologies and their probable compositions by SEM-EDX for standard CuHCF and Cu _{0.93} Zn _{0.07} HCF electrodes after 1000 cycles in 20 mM ZnSO ₄	- 123 -
Table 7-2. An overview of the determined morphologies and their probable compositions by SEM-EDX for standard CuHCF and Cu _{0.93} Zn _{0.07} HCF electrodes after 1000 cycles in 100 mM ZnSO ₄	- 124 -
Table 7-3. Summary of the percentages of energy and charge retention for different active materials cycled at 1C rate in 100 mM ZnSO ₄	- 124 -
Table 7-4. Merit of certain electrical energy storage systems. ^[211]	- 125 -
Table 11-1. Different synthesis methods for CuHCF.....	- 144 -
Table 11-2. Different synthesis methods for ZnHCF.....	- 145 -

11.4. Abbreviations & Symbols

Abbreviation	
AC/PPy	Activated Carbon/Polypyrrole
ALE	Aqueous Liquid Electrolyte
ARLB	Aqueous Lithium-Ion Battery
BG	Berlin Green
BTU	British Thermal Unit
C65	Amorphous Carbon Black
CAES	Compressed Air Energy Storage
CE	Counter Electrode
CHP	Combined Heat and Power
CoHCF	Cobalt Hexacyanoferrate
CSP	Concentrated Solar Power
CuHCF	Copper Hexacyanoferrate
CuNiHCF	Copper-Nickel Alloy Hexacyanoferrate
CuZnHCF	Copper Zinc Hexacyanoferrate Mixture
CVO	Calcium Based Bronze Structure
C-ZnHCF	Cubooctahedron Zinc Hexacyanoferrate
DEC	Diethyl Carbonate
DEMS-EIS	Differential Electrochemical Mass Spectrometry - Electrochemical Impedance Spectroscopy
DMC	Dimethyl Carbonate
DoD	Depth of Discharge
DOE	Department of Energy
EC	Ethylene Carbonate
EDL	Electrical Double Layer
EDX	Energy Dispersive X-Ray Spectroscopy
EES	Electrical Energy Storage
EMC	Ethyl Methyl Carbonate
EV	Electric Vehicle
FES	Flywheel Energy Storage
FWHM	Full Width at Half Maximum
GCPL	Galvanostatic Cycling With Potential Limitation
GE	Gel Electrolyte
GHG	Greenhouse Gas
HD Zn	Hyper-Dendritic Zinc
HEV	Hybrid Electric Vehicle
ICP-MS	Inductively Coupled Plasma Mass Spectrometry
ILE	Ionic Liquid Electrolyte
ISE	Inorganic Solid Electrolyte
JCPDS	Joint Committee on Powder Diffraction Standards
LAB	Lead Acid Battery
LCB	Lead-Carbon Ultra-Battery
LCO	Lithium Cobalt Oxide
LED	Light-Emitting diode
LFP	Lithium Iron Phosphate
LIB	Lithium-Ion Battery
LiTFSI	Lithium Bis(Trifluoromethane Sulfonyl)Imide
LMO	Lithium Manganese Oxide
LTO	Lithium Titanate

Abbreviation	
M.W.	Molar Weight
MC	Manufacturing Costs
MOF	Metal-Organic Frameworks
NaCuHCF	Na-Rich Copper Hexacyanoferrate (II)
Na-S battery	Sodium-Sulfur Battery
NASICON	Sodium Super Ionic Conductor
NCA	Nickel Cobalt Aluminium Oxide
NCB	Nickel-Cadmium Batteries
Ni-Cd battery	Nickel Cadmium Battery
Ni-Fe battery	Nickel Iron Battery
Ni-H₂ battery	Nickel Hydrogen Battery
NiHCF	Nickel Hexacyanoferrate
NiHCFRu	Nickel Hexacyanoruthenate
Ni-MH	Nickel Metal Hydride
NiOOH	Nickel Oxide Hydroxide Battery
Ni-Zn battery	Nickel Zinc Battery
NMC	Nickel Manganese Cobalt Oxide
NMP	1-Methyl-2-Pyrrolidinone
OCV	Open Circuit Voltage
OER	Oxygen Evolution Reaction
OLE	Organic Liquid Electrolyte
ORR	Oxygen Reduction Reaction
O-ZnHCF	Octahedron Zinc Hexacyanoferrate
PB	Prussian Blue
PBA	Prussian Blue Analogues
PC	Propylene Carbonate
PHES	Pumped Hydroelectric Energy Storage
POM	Polyoxymethylene
PSB	Polysulfide Bromine Flow Battery
PV	Photovoltaic
PVDF	Polyvinylidene Fluoride
PW	Prussian White
PY	Prussian Yellow
RD&D	Research, Development and Demonstration
RE	Reference Electrode
RFB	Redox Flow Battery
SCES	Supercapacitors
SEI	Solid-Electrolyte Interphase
SEM	Scanning Electron Microscopy
SFG6	Graphite
SHE	Standard Hydrogen Electrode
SIB	Sodium Ion Battery
SOC	State of Charge
SPE	Solid Polymer Electrolyte
TES	Thermal Energy Storage
T-ZnHCF	Truncated Octahedron Zinc Hexacyanoferrate
UPHES	Underground Pumped Hydroelectric Energy Storage
V2G	Vehicle to Grid
VRB	Vanadium Redox Flow Battery
WE	Working Electrode
XRD	X-Ray Diffraction

Abbreviation	
Zebra	Zeolite Battery Research Africa
ZIB	Zinc-Ion Battery
ZnBr battery	Zinc Bromine Flow Battery
ZnHCF	Zinc Hexacyanoferrate
ZVO	Zinc Pyrovandate

Symbols	
ΔE_{eq}	Equilibrium Cell Voltage
ΔE_{eq}°	Standard Equilibrium Voltage
E_a	Anodic Potential
E_{anode}	Potential at the Anode
E_c	Cathodic Potential
$E_{cathode}$	Potential at the Cathode
$E_{eq,anode}^{\circ}$	Standard Equilibrium Potential at the Anode
$E_{eq,cathode}^{\circ}$	Standard Equilibrium Potential at the Cathode
E_t	Thermodynamic Equilibrium Potential
R_{int}	Ohmic Internal Resistance
i_0	Exchange Current Density
t_i	Transport Number of Ion i
z_i	The Ionic Charge
Λ_m	Molar Conductivity
η_{bu}	Bubble Overpotential
η_{cr}	Crystallization Overpotential
η_{ct}	Charge Transfer Overpotential
η_{mt}	Mass Transport Overpotential
η_{nu}	Nucleation Overpotential
η_o	Ohmic Overpotential
λ_i	Molar Ionic Conductivity of Ion i
ν_i	Number of Ion i in the Formula Unit of the Electrolyte
ΔE	Total Cell Voltage
ΔE°	Standard Cell Voltage
ΔG	Gibbs Free Energy
C_t	Theoretical Capacity
d	Distance Between the Atomic Layers in a Crystal
E	Cell Potential
E°	Standard Potential
E_t	Thermodynamic Equilibrium Potential
F	Faraday Constant
G°	Standard Free Gibbs Energy
i	Applied Current
n	Number of Transferred Electrons Per Mole of Reactant During the Electrochemical Reaction
R	Gas Constant
T	Absolute Temperature
u_i	Mobility of Ion i
ΔC_{Cu}	Variations in the Concentrations of Copper
ΔC_{Fe}	Variations in the Concentrations of Iron
ΔQ	Specific Charge Fading
K	Shape Factor
λ	Wavelength of the Incident X-Ray Beam
α	Charge Transfer Coefficient
β	Full Width at Half Maximum
η	Overvoltage
η	Kinetic Overpotential by Eq. 3.2.2
θ	Bragg Angle
τ	Average Crystalline Size

12. Publications and Conference Contributions

12.1. Published peer-reviewed Papers

1. **G. Kasiri**, J. Glenneberg, A.B. Hashemi, R. Kun, F. La Mantia, “Electrochemical Studies of Mixed Copper-Zinc Hexacyanoferrates as Cathode Materials for Aqueous Zinc-Ion Batteries”, accepted in *Energy Storage Materials* 19, 360-369 (2019).
2. J. Glenneberg, **G. Kasiri**, I. Bardenhagen, F. La Mantia, M. Busse, R. Kun, “Investigations on morphological and electrochemical changes of an all-solid-state thin film battery cell under dynamic stress conditions”, *Nano Energy* 57, 549-557 (2019).
3. R. Trócoli, **G. Kasiri**, F. La Mantia, “Phase transformation of copper hexacyanoferrate (KCuFe(CN)₆) during zinc insertion: Effect of co-ion intercalation”, *Journal of Power Sources*, 400, 167-171 (2018).
4. A.B. Hashemi, **G. Kasiri**, J. Glenneberg, R. Kun, F. La Mantia, “Electrochemical and Morphological Characterization of Zn-Al-Cu Layered Double Hydroxides as a Negative Electrode in Aqueous Zinc-Ion Batteries”, *ChemElectroChem* 5, no. 15, 2073-2079 (2018).
5. A.B. Hashemi, **G. Kasiri**, F. La Mantia, “The effect of polyethyleneimine as an electrolyte additive on zinc electrodeposition mechanism in aqueous zinc-ion batteries”, *Electrochimica Acta*, 258, 703-708 (2017).
6. **G. Kasiri**, R. Trócoli, A.B. Hashemi, F. La Mantia, “An electrochemical investigation of the aging of copper hexacyanoferrate during the operation in zinc-ion batteries”, *Electrochimica Acta*, 222, 74-83 (2016).
7. R. Trócoli, **G. Kasiri Bidhendi**, F. La Mantia, “Lithium recovery by means of electrochemical ion pumping: a comparison between salt capturing and selective exchange”, *Journal of Physics: Condensed Matter* 28, 114005 (2016).

12.2. Oral Presentations at International Conferences

1. **G. Kasiri**, A.B. Hashemi, J. Glenneberg, R. Kun, F. La Mantia, “Synthesis and Characterization of New Improved Copper Hexacyanoferrate Nanoparticles for Zinc-Ion Batteries”, 22nd Topical Meeting of the International Society of Electrochemistry (ISE), Japan, April 2018.
2. **G. Kasiri**, A.B. Hashemi, J. Glenneberg, R. Kun, F. La Mantia, “Stable Cathodic Material for Zinc-Ion Batteries Based on Prussian Blue Derivatives for Stationary Applications”, 6th Regional Symposium on Electrochemistry of South-East Europe (6th RSE-SEE), Hungary, June 2017.

3. A.B. Hashemi, **G. Kasiri**, F. La Mantia, “The Effect of Additive on Zinc Electrodeposition Mechanism in Zinc-ion Batteries”, European Spring Meeting of Materials Research Society (E-MRS), France, May 2017.
4. A.B. Hashemi, **G. Kasiri**, F. La Mantia, “On the Way of Improving Zinc-Ion Batteries Based on Copper Hexacyanoferrate for Grid-Scale Energy Storage”, Electrochemistry 2016, Goslar, September 2016.

12.3. Posters at International Conferences

1. **G. Kasiri**, A.B. Hashemi, J. Glenneberg, R. Kun, F. La Mantia, “Stable Cathodic Material for Zinc-Ion Batteries Based on Prussian Blue Derivatives”, European Spring Meeting of Materials Research Society (E-MRS), France, May 2017.
2. **G. Kasiri**, R. Trócoli, A.B. Hashemi, F. La Mantia, “The Effect of Electrolyte Concentration on the Aging of Copper Hexacyanoferrate in Zinc-ion Batteries”, 67th Annual Meeting of the International Society of Electrochemistry (ISE), Netherlands, August 2016.
3. J. Glenneberg, **G. Kasiri**, I. Bardenhagen, F. La Mantia, R. Kun, “Electrochemical and morphological changes of solid-state batteries under mechanical stress”, The 19th International Meeting on Lithium Batteries (IMLB), Japan, June 2018.

Declaration

The work presented in this Ph.D. thesis was carried out during my doctoral studies from November 2015 to September 2018 in the group of Prof. Fabio La Mantia, Energy Storage and Energy Conversion Systems (ESECS), University Bremen.

Here I confirm that:

- The work was carried out without any unauthorized third-party assistance,
- No other sources or aids than the ones specified have been used,
- Those works/text passages which have been included word by word or by content accordingly from other sources have been indicated.
- In this dissertation the results from the supervision of the following students' works are included.

Student work with the title of “*Konstruktion einer 1 Wh-Zink-Ionen-Batterie und Auswertung der Leistungsfähigkeit bei Stromnetzanwendungen*”.

Name of students:

Mona Leuchters, Sascha Stallmann, Mathias Wielki, Patrick Thom, Bock Jakob (WISE 2016/2017).

Louis Klotz, Florian Haberland, Johannes Nitsch (WISE 2017/2018).

Date of submission: 29.10.2018

Ghoncheh Kasiri Bidhendi